5TH INTERNATIONAL EXCHANGE AND INNOVATION CONFERENCE ON ENGINEERING & SCIENCES

PROCEEDINGS AND PROGRAM

24-25TH OCTOBER 2019

INTERDISCIPLINARY GRADUATE SCHOOL OF ENGINEERING SCIENCES (IGSES)

KYUSHU UNIVERSITY, FUKUOKA, JAPAN

Welcome message from the Conference Committee

On behalf of the organizing committee, I am delighted to welcome all the participants to the 5th International Exchange and Innovation Conference on Engineering & Sciences (IEICES 2019) which is scheduled to take place on October 24-25, 2019 at Fukuoka, Japan.

This academic conference brings together academics, researchers and students to share the latest developments and researches in the fields of materials, energy and environmental engineering & sciences. The organizing committee is going to develop an exciting program to give participants an opportunity to present their academic works, concepts and new discoveries. Moreover, participants will have a chance to get to know one another closely.

We are looking forward to meeting you and ensuring that you will have an appealing and exciting experience on your participation during the conference in the beautiful city of Fukuoka.

Osama Eljamal

IEICES 2019 Chairman

IEICES 2019 Scientific Committee

Prof. Hideharu Nakashima
Conference honorary chairman,
Dean of Interdisciplinary Graduate School of Engineering Sciences,
Kyushu University

Prof. Seigi Mizuno
Conference Advisor,
Vice Dean of Interdisciplinary School of Engineering Sciences,
Kyushu University

Prof. Akira Harata
Conference Advisor,
Interdisciplinary Graduate School of Engineering Sciences,
Kyushu University

Prof. Jun Tanimoto
Conference Advisor,
Interdisciplinary Graduate School of Engineering Sciences,
Kyushu University

Prof. Aya Hagishima
Conference Advisor,
Interdisciplinary Graduate School of Engineering Sciences,
Kyushu University

IEICES 2019 Organizing Committee

Assoc. Prof. Osama Eljamal

Conference Chairman,
Interdisciplinary Graduate
School of Engineering Sciences,
Kyushu University

Mr. Shahrul Hisyam Marwan
Conference Organizer
Kyushu University

Mr. Solli D. Murtyas
Conference Organizer
Kyushu University

Mr. Ibrahim M.A. Maamoun
Conference Organizer
Kyushu University

Mr. Sneh Kumar
Conference Organizer
Kyushu University

Mr. Md. Ahsan Habib
Conference Organizer
Kyushu University

Mr. Ramadan Eljamal
Conference Organizer
Kyushu University

Ms. Sitti Subaedah
Conference Organizer
Kyushu University

Mr. Md. Khalid Hossain
Conference Organizer
Kyushu University

Mr. Jaedeok Ko
Conference Organizer
Kyushu University

Ms. Farhana Jesmin Tuli
Conference Organizer
Kyushu University

Ms. Bensaida Khaoula
Conference Organizer
Kyushu University

IEICES 2019 Co-organizers

- **Prof. Muhammad Azmi Ayub**, Dean of Faculty of Mechanical Engineering, Universiti Teknologi MARA, Malaysia
- **Dr. Abdul Halim Abdullah**, Faculty of Mechanical Engineering, Universiti Teknologi MARA, Malaysia
- **Dr. Ahmad Hussein Abdul Hamid**, Faculty of Mechanical Engineering, Universiti Teknologi MARA, Malaysia
- **Dr. Mohd Hafiz Mohd Noh**, Faculty of Mechanical Engineering, Universiti Teknologi MARA, Malaysia
- **Dr. Helmi Rashid**, Faculty of Mechanical Engineering, Universiti Teknologi MARA, Malaysia
- **Assoc. Prof. Dr. Aidah Jumahat**, Faculty of Mechanical Engineering, Universiti Teknologi MARA, Malaysia

Conference Program

International Exchange and Innovation Conference on Engineering & Sciences IEICES 2019

Oct. 24th (Thursday)

	Chikushi Hall, C-CUBE Building, Chikushi Campus, Kyushu University	
09:00 – 09:30	Registration (Lobby, C-CUBE Building)	
09:30 – 09:35	Welcome Speech: **Assoc. Prof. Osama Eljamal** IEICES 2019 Chair *Interdisciplinary Graduate School of Engineering Sciences, Kyushu University*	
09:35 – 09:45	Opening Remark: **Prof. Hideharu Nakashima** IEICES 2019 Scientific Committee *Dean of Interdisciplinary Graduate School of Engineering Sciences, Kyushu University*	
09:45 – 10:05	About the IGSES, Kyushu University: **Prof. Seigi Mizuno** IEICES 2019 Scientific Committee *Vice Dean of Interdisciplinary Graduate School of Engineering Sciences, Kyushu University*	
10:05 – 10:20	Photo Session / Coffee Break	
	Special Session 1 (Chikushi Hall)	
Session Chair Co-chair	Assoc. Prof. Andrew Spring Ibrahim Maamoun	
10:20 – 10:50	Keynote Speech 1: **Assoc. Prof. Hooman Farzaneh** *Interdisciplinary Graduate School of Engineering Sciences, Kyushu University, Japan*	
10:50 – 11:20	Keynote Speech 2: **Assoc. Prof. Solehuddin Shuib** *Faculty of Mechanical Engineering, Universiti Teknologi MARA, Malaysia*	
11:20 – 11:40	Coffee Break	
	Session 1 Civil Engineering 1 (Chikushi Hall)	Session 2 Environmental Engineering 1 (Room 303)
Session Chair Co-chair	Sahabuddin Sitti Subaedah Solli Murtyas	Md. Ahsan Habib Sneh Kumar
11:40 – 11:42	**Rilya Rumbayan** *Manado State Polytechnic*	**Ibrahim Maamoun** *Kyushu University*
11:42 – 11:54	**Achmad Gufron** *Universitas Gadjah Mada*	**Tamer Shubair** *Kyushu University*
11:54 – 12:06	**Nor Aiman Nor Izmin** *Universiti Teknologi MARA*	**Frantisek Miksik** *Kyushu University*
12:06 – 13:40	Lunch	
	Special Session 2	

	(Chikushi Hall)	
Session Chair Co-chair	Assoc. Prof. Osama Eljamal Bensaida Khaoula	
13:40 – 14:10	Keynote Speech 3: **Mr. Ryo Sato** *Research Management Solution Consultant Elsevier Japan*	
14:10 – 14:20	Coffee Break	
	Session 3 Material Science 1 (Chikushi Hall)	Session 4 Electrical, Computer, Aerospace Engineering and Material Science 2 (Room 303)
Session Chair Co-chair	Solli Murtyas Sahabuddin Sitti Subaedah	Sneh Kumar Md. Ahsan Habib
14:20 – 14:32	**Nor Hafiez Mohamad Nor** *Universiti Teknologi MARA*	**Faheem Abass** *Mawyah Abdullah Al-Bkheet-Estal-Hasa*
14:32 – 14:44	**Ji-Hwoan Lee** *Kyushu University*	**Suziana Binti Ahmad** *Kyushu University*
14:44 – 14:56	**Seung-Hyeon Kim** *Kyushu University*	**Aneeka Wasim** *University of Gujrat*
14:56 – 15:08	**Paradee Kwanmuang** *Kasetsart University*	**Mohd Hafiz Mohd Noh** *Universiti Teknologi MARA*
15:08 – 15:20	**Mohd Muzamir Mahat** *Universiti Teknologi MARA*	**Farhana Jesmin Tuli** *Kyushu University*
15:20 – 15:44	Coffee Break	
	Session 5 Mechanical Engineering 1 (Chikushi Hall)	Session 6 Civil Engineering 2, Environmental Engineering 2, and Mechanical Engineering 2 (Room 303)
Session Chair Co-chair	Ramadan Eljamal Ibrahim Maamoun	Khaoula Bensaida Jaedeok Ko
15:44 – 15:56	**Jannatul Fardous** *Kyushu University*	**Hamidun Bin Mohd Noh** *Universiti Tun Hussein Onn Malaysia*
15:56 – 16:08	**Nor Fazli Adull Manan** *Universiti Teknologi MARA*	**Do Yeon Kim** *Kumoh National Institute of Technology*
16:08 – 16:20	**Ahmad Hussein Abdul Hamid** *Universiti Teknologi MARA*	**Nur`Ain Idris** *Universiti Tun Hussein Onn Malaysia*
16:20 – 16:32	**Shahrul Hisyam Marwan** *Kyushu University*	**Relebohile Mokete** *Kyushu University*
16:32 – 16:44	**Helmi Bin Rashid** *Universiti Teknologi MARA*	**Mohd Suhairil Meon** *Universiti Teknologi MARA*
16:44 – 17:00	Closing Remark	

Oct. 25th (Friday)

	Special Session 3 (Chikushi Hall)	
Session Chair Co-chair	Assoc. Prof. Osama Eljamal Bensaida Khaoula	
09:30 – 10:00	Keynote Speech 4: **Dr. Hadi Farabi-Asl** *International Institute for Carbon-Neutral Energy Research, Kyushu University, Japan*	
10:00 – 10:24	Coffee Break	
	Session 7 **Energy Sciences** **(Chikushi Hall)**	**Session 8** **Optoelectronics** **(Room 303)**
Session Chair Co-chair	M. Khalid Hossain Shahrul Hysyam Marwan	Jaedeok Ko Farhana Jesmin Tuli
10:24 – 10:36	**Wasim Abass** *Mawyah Abdullah Al-Bkheet-Estal-Hasa*	**Yu Han** *Kyushu University*
10:36 – 10:48	**Sampad Ghosh** *Kyushu University*	**Zan Hui Chen** *Kyushu University*
10:48 – 11:00	**M. L. Palash** *Kyushu University*	**Satoshi Ogawa** *Kyushu University*
11:00 – 11:12	**Tahmid Hasan Rupam** *Kyushu University*	**Li Wenying** *Kyushu University*
11:12 – 11:24	**Syed Fahad Zamir** *Nora Cooling EST*	**Shingo Murakami** *Kyushu University*
11:24 – 13:24	Lunch	
	Session 9 **Mechanical Engineering 2** **(Chikushi Hall)**	**Session 10** **Environmental Engineering 3** **(Room 303)**
Session Chair Co-chair	Shahrul Hysyam Marwan M. Khalid Hossain	Farhana Jesmin Tuli Jaedeok Ko
13:24 – 13:36	**Kaiser Ahmed Rocky** *Kyushu University*	**Sami Alkhudhayri** *Kyushu University*
13:36 – 13:48	**J. B. Saedon** *Universiti Teknologi MARA*	**Khaoula Bensaida** *Kyushu University*
13:48 – 14:00	**S. Shawal** *Universiti Teknologi MARA*	**Ramadan Eljamal** *Kyushu University*
14:00 – 14:12	**Mohammad Azeeb Mazlan** *Universiti Teknologi MARA*	**Omar Falyouna** *Kyushu University*
14:12 – 14:24	**Wan Fatimatul Aifaa Wan Fadzil** *Universiti Teknologi MARA*	**Md. Mariar Rahman** *Kyushu University*
14:24 – 14:40	Coffee Break	

14:40 – 16:30	Poster session (3rd floor C-cube building)
	Closing Remark & Best Presenter Award
16:30 – 17:00	Prof. Seigi Mizuno *Vice Dean of Interdisciplinary Graduate School of Engineering Sciences, Kyushu University*

List of presented papers

Page	Theme: Civil and Environmental Engineering
1-3	**A Study on the Utiliization of Local Coconut Timber Waste as Sustainable Building Material** Rilya Rumbayan, Meita Rumbayan *Manado State Polytechnic*
4-8	**Study on Effect of Reinforcement using Helical Bars on Circular RC Columns under Cyclic Lateral Load** Do Yeon Kim, Ja-Eun Shin, Seong-Kyum Kim, Il-Young Jang *Kumoh National Institute of Technology*
9-11	**Effect of Nano Zero Valent Iron Delivery Method into Porous Media on Phosphorus Removal from Groundwater** Ibrahim Maamoun, Osama Eljamal, Ramadan Eljamal, Omar Falyouna, Yuji Sugihara *Kyushu University*
12-15	**The Stability of Water Molecular Bridges in Ombrotrophic Peatland Soil** Frantisek Miksik, Štěpánka Freithová, Josef Kotlík, Jiří Kučeřík, Alasdair MacLeod *Brno University of Technology, Kyushu University*
16-18	**Analogy of Iron-Copper and Iron-Silver Bimetals during the Corrosion Process** Relebohile Mokete, Osama Eljamal *Kyushu University*
19-21	**Thermodynamic Effect on Boron Removal from Aqueous Solutions by MgAl-Layered Double Hydrotalcite** Sami Alkhudhayri, Osama Eljamal, Ibrahim Maamoun, Ramadan Eljamal *Kyushu University*
22-23	**Effect of Bimetallic Zero Valent Iron Nanoparticles Ag/NZVI on Bacterial Growth** Khaoula Bensaida, Osama Eljamal, Ramadan Eljamal, Relebohile Mokete, Yuji Sugihara *Kyushu University*
24-25	**Upgrading of Aerobic Sequencing Batch Reactor System with Adding Nanoscale Zero Valent Iron for Wastewater Treatment** Ramadan Eljamal, Osama Eljamal, Ibrahim Maamoun, Yuji Sugihara *Kyushu University*
26-27	**Removal of Cesium from Contaminated Waters by Employing Iron-based Nanoparticles and Nanocomposites** Omar Falyouna, Osama Eljamal, Ibrahim Maamoun *Kyushu University*
28-29	**Factorial Experimental Design for Optimization of Cesium Removal from Aqueous Solutions** Md. Mariar Rahman, Shamal C. Karmaker, Animesh Pal, Osama Eljamal, Bidyut Baran Saha *Kyushu University*

Page	Theme: Energy Sciences
30-31	**Thermoelectric Properties of Graphene and Carbon Nanotube** Sampad Ghosh, Sivasankaran Harish, Bidyut Baran Saha *Kyushu University*
32-33	**Investigation of Surface Energy of Porous Adsorbents** M. L. Palash, Animesh Pal, Bidyut Baran Saha *Kyushu University*
34-35	**Adsorption Characterization of Aluminum Fumarate Metal-organic Framework** Tahmid Hasan Rupam, M.L. Palash, Israt Jahan, Bidyut Baran Saha *Kyushu University*
36-38	**Occupancy Rate and Water Utility Effect on Energy Consumption of Commercial Building: Case Study Grand Inna Malioboro Hotel in Indonesia** Solli Murtyas, Mohammad Ridwan, Rachmawan Budiarto *Kyushu University*
39-43	**Dynamic Simulation of a Thermal Management System Consisting of a CO2 Heat Pump and a Water-loop** Jaedeok Ko, Nobuo Takata, Kyaw Thu, Takahiko Miyazaki *Kyushu University*
Page	Theme: Material and Mechanical Engineering
44-46	**Development of 3D Printed Socket for Transtibial Prosthetic Leg** Wan Fatimatul Aifaa Wan Fadzil, Mohammad Azeeb Mazlan, Fazah Akhtar Hanapiah, Abdul Halim Abdullah *Universiti Teknologi MARA*
47	**Characterization on Microstructural Evolution of Y2O3 Fabricated by Spark Plasma Sintering** Ji-Hwoan Lee, Byung-Nam Kim, Byung-Koog Jang *Kyushu University*
48	**The Effect of Vanadium Addition on the Microstructure and Mechanical Properties of Indefinite Chilled Cast Iron** Seung-Hyeon Kim, Eung-Ryul Baek, Byung-Koog Jang *Kyushu University*
49-52	**Synthesis of a Novel Sensor Based on Orcinol-dansyl Derivative for Fluoride Ion Detection** Paradee Kwanmuang, Apisit Songsasen, Boontana Wannalerse *Kasetsart University*
53-57	**Morphological, Structural and Electrochemical Studies of Conductive Polyaniline Coated Polyester Fabrics** Mohd Muzamir Mahat, Nazreen Che Roslan, Muhammad Asyrap Kamarudin, Siti Nurzatul Ikma Omar, Mohamed Izzharif Abdul Halim, Rosmammuhamadani Ramli, Mohd Muzamir Mahat *Universiti Teknologi MARA*
58-59	**Interfacial Magnetic Properties of Fe Deposited on MoS2 Flakes** Farhana Jesmin Tuli, Mohammad Tawheed Kibria, Takeshi Nakagawa, Seigi Mizuno *Kyushu University*

60-62	**Biomechanical Analysis of Hypertrophic Cardiomyopathy Behavior of Human Heart using Dynamic Finite Element Method** Shahrul Hisyam Marwan, Mitsugu Todo *Kyushu University*
63-66	**Modelling Low-Velocity Impact on Composite Laminate Considering Inter and Intralaminar Damage** Mohd Suhairil Meon, N.H. Mohamad Nor, S. Shawal, J.B. Saedon, M.N. Rao, K.-U. Schröder *Universiti Teknologi MARA*
67-69	**Adsorption Characteristics of CO2 onto Carbon Nanotube for Adsorption Cooling/Capturing Applications** Kaiser Ahmed Rocky, Animesh Pal, Bidyut Baran Saha *Kyushu University*
70-72	**Preparation and Characterization of Yttrium Doped Barium-Zirconates at High Temperature Sintering** M. Khalid Hossain, Kenichi Hashizume *Kyushu University*
73-76	**Coupling Approach of Lattice Boltzmann Fluid Simulation and Finite Element Analysis of Geophysical Properties: Application to Natural Rock Fracture in Geothermal Area** Kazuki Sawayama, Takeshi Tsuji, Yasuhiro Fujimitsu *Kyushu University*
77-79	**Integrating 3D-Printing Technology in Assistive Adaptive Device Prescription in Rehabilitation Medicine: A Conceptual Framework** Natiara Binti Mohamad Hashim, NAC Zakaria, S Shukor, MZ Amin, NS Mahdzir, NM Mustafah, NF Aroslan *Universiti Teknologi MARA*
80	**Non-uniform Sintering Behavior of Y2O3 Ceramics** Ji-Hwoan Lee, Byung-Nam Kim, Byung-Koog Jang *Kyushu University*
81-83	**Propagation Mode Retention Using Strongly Coupled Multi-Core Fiber** Mahmoud Nasef, Kantaro Fujimoto, Haisong Jiang, Kiichi Hamamoto *Kyushu University*
84-86	**The Effect of Post Treatment in Pore Development of Activated Carbon Prepared from Rice Husk** Chairunnisa, Kyaw Thu, Takahiko Miyazaki, Jin Miyawaki, Koji Nakabayashi, Muhammad Hamid Mahmood, Muhammad Sultan *Kyushu University*
87-88	**Design & Analysis of 3D Printed Prosthetic Hand for Symbrachydactyly Patients** Mohammad Azeeb Mazlan, Wan Fatimatul Aifaa Wan Fadzil, Helmi Rashid, Abdul Halim Abdullah *Universiti Teknologi MARA*
89-92	**Effects of Varus & Valgus Implant Malposition in Resurfacing Hip Arthroplasty** Nor Aiman Nor Izmin, Mitsugu Todo, Abdul Halim Abdullah *Universiti Teknologi MARA, UiTM*

93-96	**Feasibility Study of Theophylline Solution in Water and Sodium Carboxy-methylcellulose** Jannatul Fardous, A H M Saifuddin, Sultana Amena, Sakina Sultana *Kyushu University*
Page	Theme: Electrical Engineering and Optoelectronics
97-99	**Comparison of LCL and LCLC Compensation Circuit for Capacitive Power Transfer System** Suziana Binti Ahmad, Aam Muharam, Reiji Hattori *Kyushu University*
100-102	**Significant Propagation Loss Reduction on Silicon High-Mesa Waveguides Using Thermal Oxidation Technique** Yu Han, Wenying Li, Haisong Jiang, Kiichi Hamamoto *Kyushu University*
103-104	**Compact and Highly Sensitive Methane Sensor Based on Two tTngent Air Hole Structure** Zan Hui Chen, Wenying Li, Haisong Jiang, Kiichi Hamamoto *Kyushu University*
105-106	**Proposal of 1×N Optical Mode Switch Based on Spatial Single Dimensional Mode** Satoshi Ogawa, Haisong Jiang, Kiichi Hamamoto *Kyushu University*
107-108	**Compact Breath Sensing using Amplifier Assisted CRDS (Cavity Ring-down Spectroscopy)** Li Wenying, Yu Han, Zanhui Chen, Haisong Jiang, Kiichi Hamamoto *Kyushu University*
109-110	**Observation of 60 GHz and 20 GHz Multiple Photon-Photon Resonances Using Active Multimode Interferometer Laser Diodes** Shingo Murakami, Bingzhou Hong, Haisong Jiang, Kiichi Hamamoto *Kyushu University*
Page	Theme: Others
111-115	**Transition of Initiative from Ubiquitous City to Sustainable Smart City by Korea: Focusing on the Case of Songdo City** MyungHee Kim *Smith College, Sahmyook University*
116-117	**"Can People Detect Dilemma Strength in A 2 Player 2 Strategy Game?": A Survey** Md. Ahsan Habib *Kyushu University*

Conference Venue

Chikushi Hall, C-CUBE Building,
Chikushi Campus, Kyushu University,
6-1 Kasuga-koen, Kasuga, Fukuoka, 816-8580, Japan

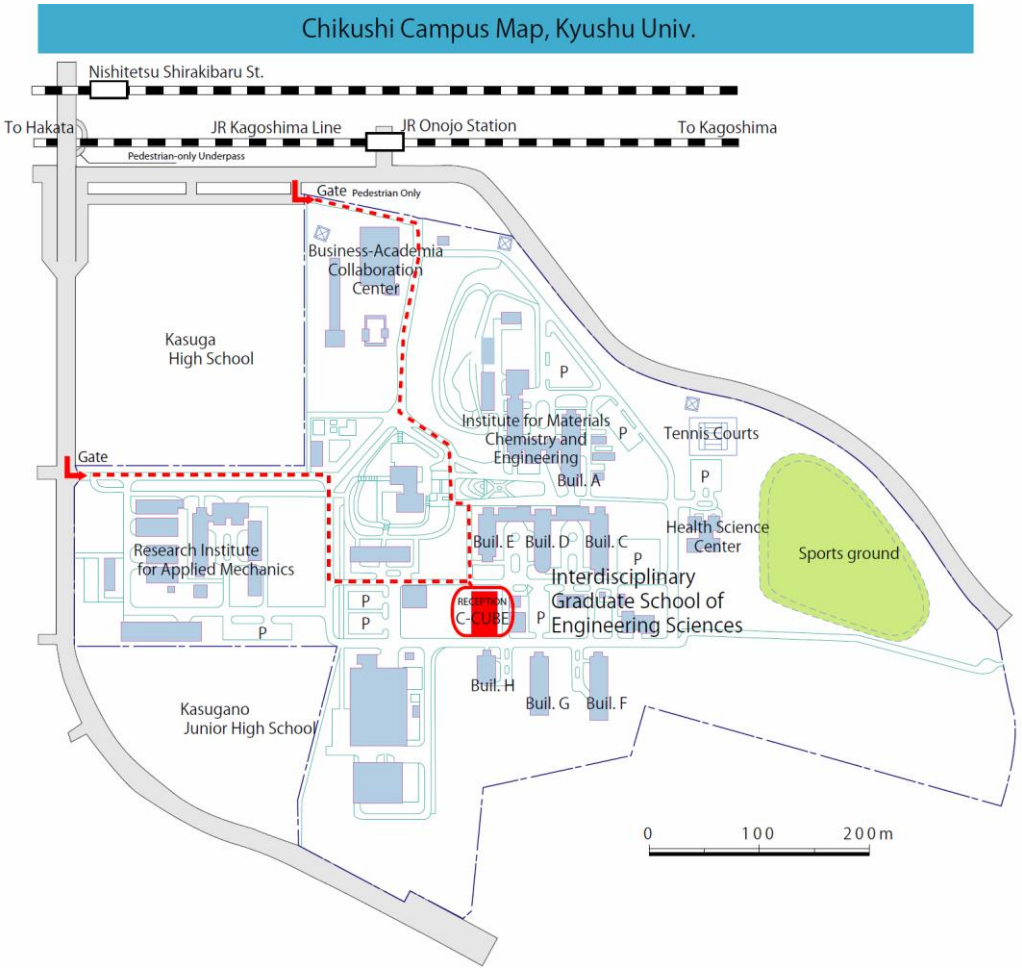

■ Chikushi Campus Access

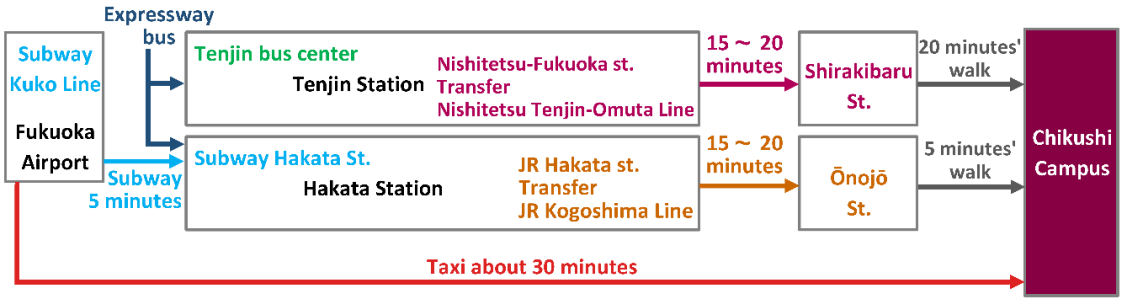

Keynote Speaker

Hooman Farzaneh
Associate Professor,
Inter/Transdisciplinary Energy Research,
Interdisciplinary Graduate School of Engineering Sciences
Kyushu University
Email: farzaneh.hooman.961@m.kyushu-u.ac.jp

Short Biography

Hooman Farzaneh is an associate professor at Kyushu University, Japan. He obtained his Ph.D. degree in energy systems engineering from the science and research branch of Azad University, Tehran, Iran. His research interests span both quantitative and qualitative studies, focusing on developing research patterns of low carbon energy scenarios and policy implementations designed to tackle air pollution problems at both regional and local scales. Much of his work has been on improving the understanding and designing of sustainable energy systems, through data mining, statistics and developing different tools and modeling approaches. Before joining Kyushu University, Hooman worked at the Institute of Advanced Energy, Kyoto University and the United Nations University. Dr. Farzaneh has more than ten years' experience teaching energy-science-related subjects at various universities in Iran and Japan and is currently the principal investigator of a funded research project entitled "Clean Energy Development in Asia-Pacific Cities" at the Kyushu University Platform of Inter/Transdisciplinary Energy Research. He is also serving as the head of the Energy and Environmental Systems (EES) laboratory at the Interdisciplinary Graduate School of Engineering Sciences (IGSES).

Multiple Benefits Assessment of the Low Emission Development Strategies in Asian cities

Abstract:
Cities throughout Asia have experienced an unprecedented economic development over the past decades. In many cases, this has contributed to their rapid and uncontrolled growth and has resulted in multiple problems, which include a rapid population increase, enhanced environmental pollution, collapsing traffic systems, dysfunctional waste management, as well as a rapid increase in the consumption of energy, water, and other resources. The twin challenges of global climate change and energy insecurity in Asian cities can only be solved with rapid devising of clean energy strategies, both for energy supply and energy efficiency. Moreover, this rapid development is needed globally. The big challenges concerning the clean energy development in Asian cities spring from the lack of awareness at the local government level and the limited institutional capacities and arrangements. Comprehensive policies focused on clean energy and mitigation do not currently exist at the city level in Asia, and only a minority of developed countries such as Japan and Korea have started formulating such policies. Development processes in Asian cities have generated many social and economic benefits in the last decades, but the patterns of urban development have shown themselves to be deficient in a number of areas. Consequently, urban areas in Asia contribute increasingly to climate change, as well as suffering many of its impacts.
The objective of this research is to demonstrate a new strategic planning mechanism for achieving multiple energy, environmental, public health, and economic benefits of clean energy development strategies in the selected megacities in Asia, together with a robust analytical framework that can be used to assess those benefits during the development and implementation process. By evaluating potential clean energy policies with criteria that cut across the multiple benefits, localities can select options that facilitate the achievement of multiple goals and avoid options that may impede key priorities. This research is financially supported by the Japan Society for the Promotion of Science (JSPS), the Asia-Pacific Network (APN) and the Hitachi Global Foundation. The research findings were collected in the following book:
"Hooman Farzaneh, Devising a clean energy strategy for Asian cities, Springer, 2018"

Keynote Speaker

Solehuddin Shuib
Assoc. Professor, Mechanical Engineering
Universiti Teknologi MARA, Shah Alam, Selangor, Malaysia
Email: solehuddin2455@uitm.edu.my

Short Biography

Solehuddin Shuib is Assoc. Professor of Mechanical Engineering at the Universiti Teknologi MARA. He holds a BSc in Mechanical Engineering from the University of Alabama, Birmingham, USA, MS in Mechanical Engineering from the University of Toledo-Ohio, USA, and Ph.D in Biomechanical Engineering from Universiti Putra Malaysia. Currently, he is the Head of Center for Post Graduate Studies, Faculty of Mechanical Engineering, Universiti Teknologi MARA. His specific research interests are in Computer-aided modelling, optimization and simulation with applications to Biomedical Engineering, Bio-inspired Wing, and Medical devices design. He has supervised more than 10 graduate students (of which 5 are PhDs) in these fields and his graduate students all obtain good jobs in industry and in academia. He has been funded for several research projects from government and industry worth more than RM2.6 Million. He has more than 40 journal articles, 70 proceedings, and 10 book chapters, and has been an invited speaker on numerous occasions at academic institutions throughout the world and at national and international conferences. The recognition he has garnered nationally and internationally were the appointment as an editorial board of Journal of Applied Sciences and Archives of Orofacial Sciences , Executive editor of Journal of Mechanical Engineering, and as panel reviewer on the Journal of Industrial Technology(SIRIM), Journal of Applied Sciences(JAS), Information Technology Journal(ITJ) and Asian Journal of Scientific Research(AJSR), and Expert panel for National grant evaluation by Ministry of Energy, Science, Technology, Environment and Climate Change (MESTECC), Malaysia. His consultancy services have earned a good reputation in the private sector. Within the 20 years service with University, he had the opportunities to participate more than 10 consultancy works worth approximately RM4.4million.

Influence of Dental Implant Designs on Stress Distribution and Micromotion Of Mandibular Bone

Abstract

The significant effects of biomechanical dental implant designs have been realised by some researchers, however, the studies were restricted on the discrete invariability of designs and geometries of dental implants on the primary stability of immediately loaded implants. Moreover, restricted procedure and limited software ability to develop a comprehensive 3D model of mandibular bone make the in vitro studies on dental implants relatively unreliable. This research was conducted to provide a feasible method for reconstructing the 3D model of mandibular bone to undergo finite element analysis. This study also examines several design features of dental implants based on commercially available products. Then, the highest performance dental implant design was evaluated, and the significant design parameters were studied in order to determine the optimal combination of design parameters. Computerised Tomography scan was conducted to generate head images for bone reconstruction process. MIMICS software 8.0 and 3-matic software were used to develop the 3D mandibular model. The reconstructed mandibular model was then assembled with five different 3D models of dental implants. Feasible boundary conditions and material properties were assigned to the developed muscle areas and joints. The results of the maximum von Mises stresses, shear stresses and deformations were analysed, and the best design was selected. Next, grey based Taguchi method was used to identify several design parameters influences such as conical hollow height, thread thickness, cutting-edge angle and cutting-edge depth. The second model appeared to exhibit the highest performance in this bone remodelling prediction simulation. Lastly, the optimal combination of design parameters calculated in this study were 5 mm of conical hollow height, 0.3 mm of thread thickness, 30° of cutting-edge angle and 6 mm of cutting-edge depth. In conclusion, this research provides a systemic approach to develop segmented 3D mandibular bones with quality meshing in order to prevent error in finite element analysis. Based on this study, the suggested optimal combination had improved the dental implant and bone performance.

Keynote Speakers

Ryo Sato
Solution Consultant, Research Intelligence
Elsevier Japan K.K.
Email: r.sato@elsevier.com

Short Biography

Ryo Sato is a Solution Consultant of Research Intelligence Solution at Elsevier Japan K.K. He supports research assessment, planning, and marketing activities of many universities and companies in Japan by providing training and consultation of analytical solutions such as Scopus, SciVal, and PlumX. Scopus is a source-neutral abstract and citation database curated by independent subject matter experts. It places powerful discovery and analytics tools in the hands of researchers, librarians, institutional research managers and funders. SciVal is a web-based analytics solution with unparalleled power and flexibility that provides comprehensive access to the research performance of over 14,000 research institutions and their associated researchers from 230 nations worldwide by analyzing data in Scopus. PlumX provides insights into the ways people interact with individual pieces of research output (articles, conference proceedings, book chapters, and many more) in the online environment and integrated to Scopus.

Recent use cases of bibliometric data and metrics in Japan to evaluate impact of scholarly output

Abstract

How bibliometric data and metrics are being used to evaluate impact of scholarly output is changing rapidly in Japan. For instance, metrics based on academic citations are recently used for assessment of research activities because the Government of Japan is asking for EBPM (Evidence Based Policy Making) for universities and academic communities in their latest Science and Technology Basic Plan. Besides, new data and metrics to evaluate impact of scholarly output have been developed to overcome the limitations of assessment by academic citations. The aim of this presentation is to share these recent use cases of bibliometric data and metrics in Japan to evaluate impact of scholarly output. This presentation consists of two parts. In the first part, I will introduce recent use cases of data and metrics of academic citations in Scopus. For instance, Field Weighted Citation Impact (FWCI) is used to compare the impact of scholarly output among different subject areas. CiteScore is used not only to assess journal impact but also to estimate citation impact of recent publications in the future. In the second part, I will discuss new use cases of non-academic citations and other impact metrics in PlumX. For instance, citations by patents and media mentions are adopted to evaluate economic and societal impact of scholarly output. Moreover, the number of views and downloads of publications are used as reference for forecasting citation impact of recent publications in the future.

Keynote Speakers

Hadi Farabi-Asl
Researcher, Energy systems analysis
Research Institute for Humanity and Nature, Kyoto, Japan
E-mail: farabi@chikyu.ac.jp

Short Biography

Hadi Farabi-Asl is a Researcher in Research Institute for Humanity and Nature (RIHN) in Kyoto, Japan. He is a member of Supply Chain project in RIHN, aiming to assess the environmental impacts of the global supply chains with quantitate methods.
Before joining RIHN, Hadi was a Postdoctoral Research Associate in International Institute for Carbon-Neutral Energy Research (I²CNER), Kyushu University. His research in Energy Analysis Division (EAD) of I²CNER, was related to modeling the energy systems in national and global scales, considering deep-decarbonization targets. He has a background in Mechanical Engineering. Results of his studies are published in journal papers and presented in conferences, including an award-winning paper in 4th International Conference of Grand Renewable Energy in Yokohama, Japan.

Energy Systems Analysis under Deep-decarbonization Constraints

Abstract

Low-carbon transitions of energy systems are required globally under the Paris Agreement for the United Nations Framework of Convention of Climate Change (UNFCCC). It important to understand how transitions in supply and demand structure of energy system help to realize the low-carbon energy system? On the other hand, quantitative analyses are necessary for the policy recommendations.
In order to achieve the ambitious target of an 80% CO_2 emission reduction in Japan by 2050 (compared to 2013 levels), various low-carbon sources on the supply side, and efficient technologies on the demand side of the energy system must be deployed at a reasonable cost. In this study, we investigate the possibility of achieving the emission reduction targets in Japan using the TIMES-Japan framework, which employs a least cost optimization approach. Results of the analysis reveals the significant importance of hydrogen import on the supply side at the same time with renewable power generation, and electrification of steel-making furnaces on the demand side for obtaining feasible scenarios. The minimum amount of carbon capture and storage (CCS) capacity is calculated for each scenario and the results vary between 5 and 150 million tons of CO_2 by 2050. Based on the results of our analysis, a moderate scenario is proposed to engender desirable future actions.

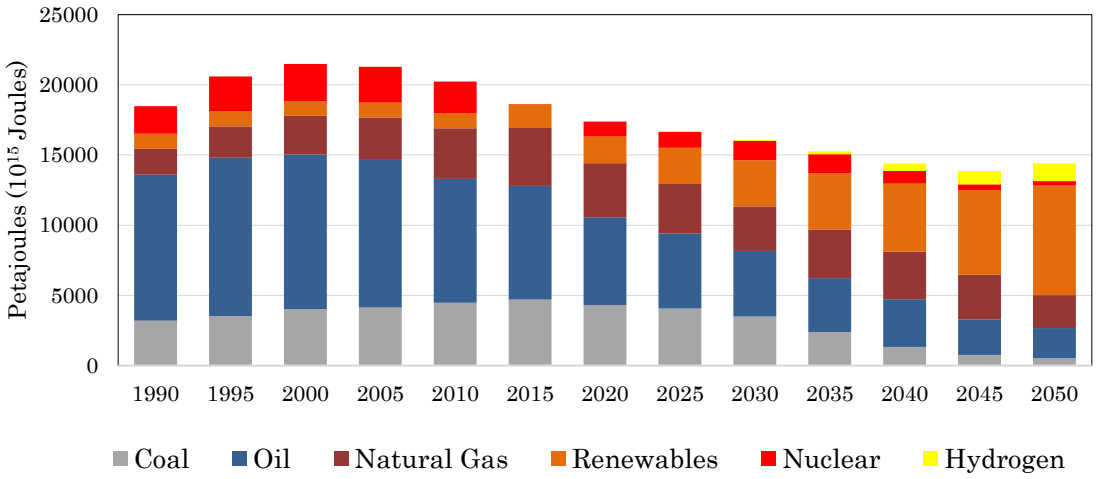

Fig. 1 Primary energy in Japan (1990 – 2050) in one of the scenarios of study

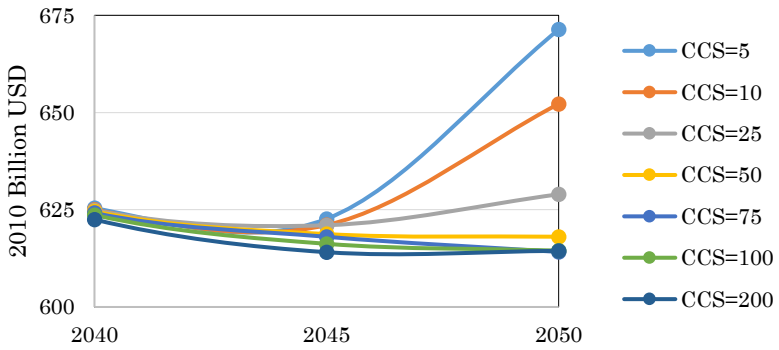

Fig. 2 Relationship between energy system cost and CCS capacity (million tons of CO_2) in a group of scenarios

Documentations

Opening session by IEICES 2019 Chairman Assoc. Prof. Osama Eljamal

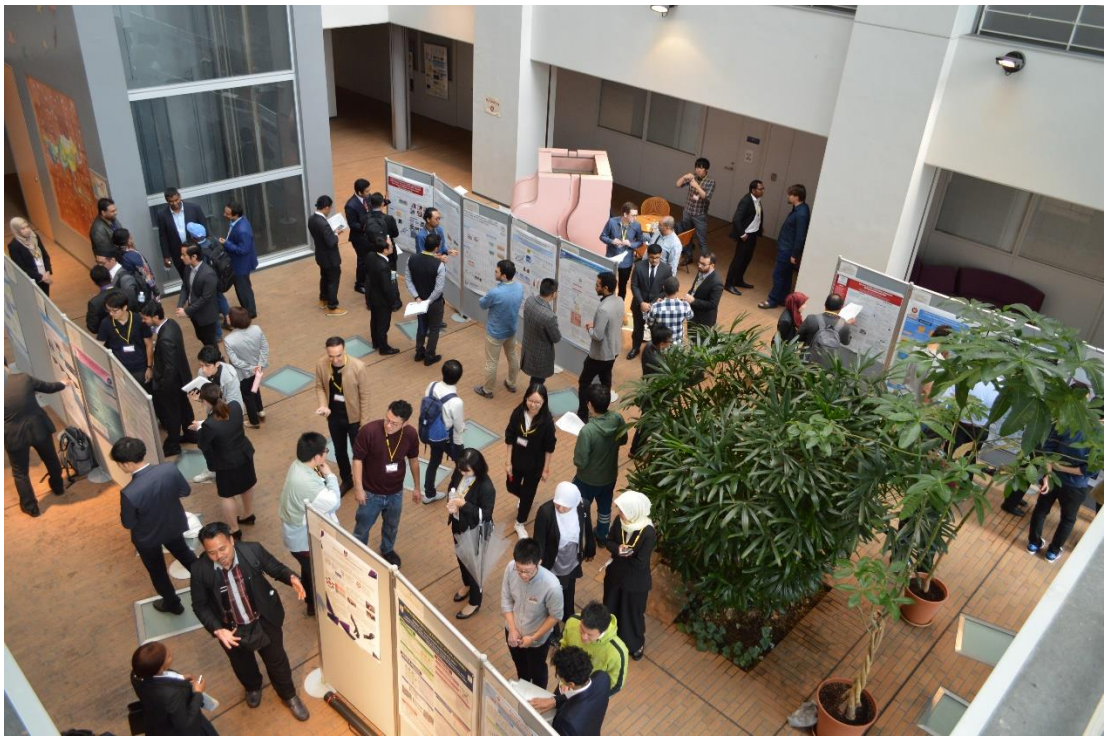

Poster session of IEICES 2019

IEICES 2019

A Study on The Utilization of Local Coconut Timber Waste as Sustainable Building Material

Rilya Rumbayan[1], Meita Rumbayan[2]
[1]Manado State Polytechnic, [2]Sam Ratulangi University.
rilya.rumbayan@gmail.com

Abstract: *This paper performs a study into the use of local coconut timber waste as an alternative building material to build earthquake-resistant timber house in Indonesia. The goals of this research are: (1) to design a model of earthquake-resistant house made of local coconut timber waste, and (2) to present structural analysis of the house under earthquake load. Research methods include design of an earthquake-resistant local-timber house, estimation of the dimensions of structural elements of earthquake-resistant local-timber house; and analysis of the performance of the timber house under earthquake load with structural software for building analysis and design. Outcomes from this study are expected to promote the beneficial usage of the potentially of local timber waste as construction material for timber house in an effort to mitigate the risk of earthquake hazard.*

Keywords: Local coconut timber; earthquake-resistant; building material, design and analysis

1. INTRODUCTION

Indonesia is located on the Pacific Ring of Fire that has a high degree of tectonic activity. North Sulawesi Province is one of the regions in Indonesia that has a high risk of earthquake. Based on the map of earthquake regions used as a reference for structural building design, the province is located in Earthquake Region 5 which is categorized as a high-risk zone with earthquake scale between 5-7 Richter.

Building construction made of timber presents many advantages such as relatively higher structural stability and integration. This is due to the fact that timber has higher strength-to-weight ratio compared to steel and concrete. This weight or mass of construction has a linear correlation to the lateral force sustained by the construction. These characteristics have caused timber to become an alternative building material for earthquake prone areas such as North Sulawesi [1].

According the Indonesian standard about the quality and dimensions of construction timber, SNI 03-3527-1994 [2], timber can be classified into 5 strength classes based on the physical properties, flexural strength and compressive strength as shown in Table 1.

Table 1. Mechanical properties of timber

Strength Class	Air-dry Density	Flexural Strength (Kg/cm^2)	Compressive Strength (Kg/cm^2)
I	≥ 0.90	≥ 1100	≥ 650
II	0.90 – 0.60	1100 – 725	650 – 425
III	0.60 -0.40	725 – 500	425 – 300
IV	0.40 – 0.30	500 -360	300 – 215
V	≤ 0.30	≤ 360	≤ 215

The long-term goal of this study is to produce a prototype of earthquake-resistant timber house made of coconut-timber. The particular objectives of this research are to design a model of earthquake-resistant house made of local coconut timber waste, and to present structural analysis of the house under earthquake load.

This study is significant as an effort to utilize the use of local timber waste as a construction material to build earthquake-resistant timber house. Additionally, results of this study are believed to support the utilization of potential sustainable local natural resources.

2. MATERIALS

Coconut is one of the many potential plantation crops commodities grown in North Sulawesi. The main waste from the rejuvenation of coconut trees are the trunks from old coconut trees aged over 50 years and needed rejuvenation because of their decreasing fruit productivity. Utilization of the unproductive coconut trees as a building material for timber house can be an alternative solution to the handling of coconut tree trunks after the rejuvenation, which will be useful to the local communities [1].

The characteristics of coconut-timber are different to the characteristics of other hardwoods. There is no cambium in a coconut tree therefore the diameter of the tree does not increase. Moreover, coconut trees do not form the annual circle because there is no annual growth to the diameter of the trunk and coconut trees do not have branches, which means that they are free of knots. In addition, coconut-timber also cannot regenerate, which can be observed from the existing footholds made during the harvesting of coconut that never disappear [3].

In previous study by the author was obtained the mechanical properties of coconut timber as shown in Table 2 [1]. The timber waste was obtained from unproductive coconut trees from Minahasa Selatan region in North Sulawesi. It was found that conform the SNI 03-3527-1994 classification, the strength class of coconut-timber can be used as structural construction timber, of which usage requires the calculation of load. Results from the previous study were used as references in design stage of a 8m x 12m model of timber house.

Table 2. The mechanical properties of coconut timber

No.	Characteristics of coconut-timber	Test result
1	Modulus of Elasticity (kg/cm^2)	67000
2	Flexural strength (kg/cm^2)	458.66
3	Compressive strength parallel to grain (kg/cm^2)	399.3
4	Compressive strength perpendicular to grain (kg/cm^2)	179.79
5	Shear strength parallel to grain (kg/cm^2)	65.13
6	Density (gr/cm^3)	0.9
7	Moisture content (%)	15.95
8	Tensile strength – parallel to the grain (kg/cm^2)	44760.1
9	Toughness (kgf)	424.74

3. RESEARCH METHOD

Research methods include design of an earthquake-resistant local-timber house, estimation of the dimensions of structural elements of earthquake-resistant local-timber house; and analysis of the performance of the timber house under earthquake load with structural software for building analysis and design as shown in Figure 1.

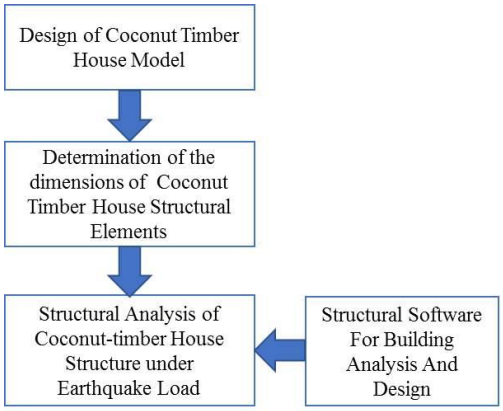

Fig.1. Research Method

The design phase of the coconut timber house model includes the drawing of design plan of the timber house and calculation of timber structural elements. The design phase was implemented principles and standards of building model by considering earthquake load. The dimension determination of the house structural elements including beam, column, floor panel, wall panel and roof. Simulation of structural performance test was done by analysis of the structure under earthquake load using structural software for building analysis and design.

4. RESULTS DAN DISCUSSION

Results of structural design of a coconut-timber house with a floor plan size of 8m x 12m are shown in Figure 2. The result of the design of a coconut-timber house model is shown in Figure 3.

Structural calculation of coconut-timber house includes roof frame structure, ceiling structure: main beam, secondary beam, floor beam and floor board, floor structure: main beam, secondary beam, floor beam and floor board, and columns. Determination of the dimensions of coconut-timber house structural elements was performed in accordance to design principles, standards and implementation methods building model construction by considering earthquake load. Design results of dimensions of the timber house structural elements are presented in Table 3.

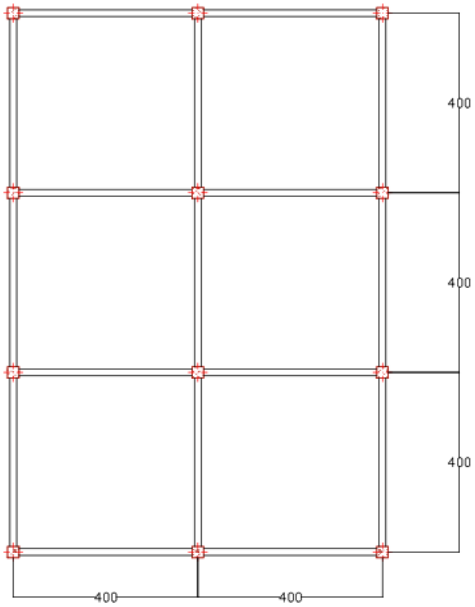

(a)

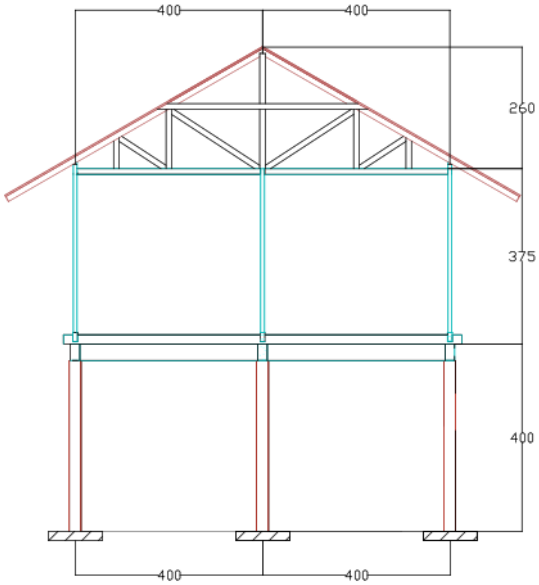

(b)

Fig.2. Design of coconut-timber house (a). Floor Plan; (b) Portal Frame

Structural performance test is done by analysis of structure under earthquake load with simulation of structural model. The software used for this simulation process is ETABS (Structural software for building analysis and design). The sway mode caused by earthquake on the frame structure of coconut-timber house generated by ETABS software can be seen in Figure 4. Results from the structural analysis of the coconut-timber house frame structure under earthquake

loading using ETABS software show that the house is safe.

Fig.3. Design drawing and model of timber house

Table 3. Calculation result of the dimensions of coconut-timber house structural elements

No.	Construction	Element	Dimension
1	Ceiling	Main beam	b=8 cm and h=15 cm
2	Floor	Main beam	b=15 cm and h=25 cm
		Secondary beam	b=12 cm and h=20 cm
3	Upper columns		b=12 cm and h=12 cm
4	Lower columns		b=20 cm and h=20 cm

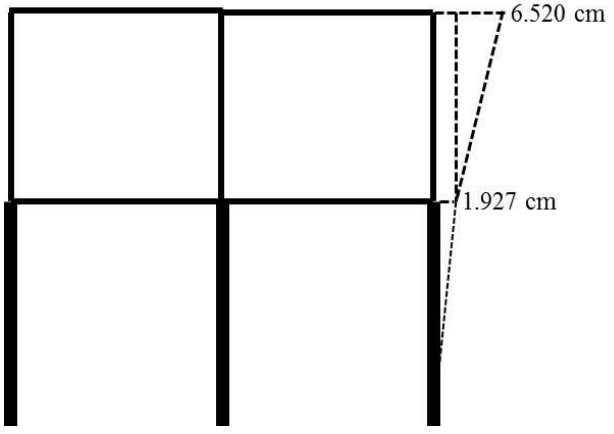

Figure 4. Sway mode due to earthquake load acting on the frame structure of coconut-timber house (generated with ETABS).

Outcomes from this study are expected to promote the beneficial usage of the potentially of local timber waste as construction material for timber house in an effort to mitigate the risk of earthquake hazard.

5. ACKNOWLEDGEMENTS

The authors would like to acknowledge the support for this study from Directorate of Research and Development – Ministry of Research, Technology and Higher Education (Ristekdikti), Indonesia.

6. REFERENCES

[1] R. Rumbayan, D. Taju, R. Mait, An investigation on Coconut-timber waste as construction material for earthquake resistant wooden house in North Sulawesi, Indonesia, Toward the Future of Asia: My Proposal Vol. 4 (2019) 185-190

[2] SNI 03-3527-1994. Mutu Kayu Bangunan. Badan Standarisasi National.

[3] V.K. Sule, Asian and Pacific Coconut Community, Proceedings of the Workshop for Policy Makers (1990), Zamboanga, Philippines.

Study on Effect of Reinforcement using Helical Bars on Circular RC Columns under Cyclic Lateral Load

Do-Yeon Kim[1], Ja-Eun Shin[2], Seong-Kyum Kim[3], Il-Young Jang[4]
[1,2,3,4] Department of Civil Engineering, Kumoh National Institute of Technology, Korea
correspondence should be addressed to Il-Young Jang; jbond@kumoh.ac.kr

Abstract: *To improve an earthquake-resistance of highway bridge constructed in South Korea before 1992, in this study, it was conducted quasi-static test according to the displacement-controlled (strain control) method on RC columns reinforced helical bar. In the experiment, fracture behavior of the circular column and its lateral load-displacement was investigated using three types of reinforcing bar, which has 6, 8 and 10 mm of the diameter. As a result, it was confirmed that seismic performance was dependent on reinforcement of helical bar and its size. During the test, the specimen reinforced using helical bar with 8 mm in the diameter was highest in maximum lateral load, of which the value accounted for 130.9 kN. For a diameter of 10 mm, however, it showed an over-reinforcement effect. Therefore, it would be cautious in reinforcing the helical bar, considering the given conditions including cross-section of a pier, amounts of steel bar in the pier and requirement of seismic performance.*

Keywords: Quasi-static test, Helical bar, Seismic reinforcement, Circular column, Spiral reinforcement

1. INTRODUCTION

It has been evaluated South Korea as a safe zone from earthquakes, but the frequency of the disaster is increasing recently [1]. From the survey and analysis of observation records, additionally, it is confirmed that approximately 70 times occurred annually in South Korea from 1999 to 2018 since the observation was started from 1988 [2]. Although there have been no accidents such as collapse and failure of reinforced concrete (herein RC) structures due to the earthquakes with various magnitudes in recent years, it could not be excluded the possibility of an occurrence of earthquakes causing damage to the structures in South Korea.

In South Korea, the seismic design was firstly introduced in 1992 and legally required for the RC structures [3]. This seismic design was applied to newly constructed facilities, but most of the structures built in the previous introduction of the earthquake-resistant design in 1992 were designed and constructed without considering the effects of an earthquake. Also, the structures have been aged due to an extended period. As a result, the majority of the bridges constructed in South Korea before 1992 do not satisfy current seismic design criteria.

In the plastic zone of the bridge piers, lateral reinforced steel prevents buckling of longitudinal rebars and a loss of compressive strength of the concrete during earthquakes [4]. Simultaneously, it plays a vital role as shear reinforcement, which increases the shear strength of the piers [5]. After completion of construction by the initial design, however, it is challenging to enhance the performance of the piers; by increasing the amounts of rebars and/or varying the section of the concrete. Therefore, various types of materials and its reinforcing methods are used to increase cross-sectional force for seismic performance [6].

In this study, it was conducted the quasi-static method using a specimen fabricated with quarter-scale for bride pier according to the design before 1992 in South Korea. At that time, the lateral load according to the displacement ratio of the pier was input by the displacement control method. After reinforcing the circular pier outside using the helical bar to increase the resistance to earthquakes, it was analyzed the fracture behavior and characteristics of load-displacement through a laboratory test.

2. EXPERIMENTAL WORKS

2.1 Materials

The deformed rebar with a yield strength of 400 MPa and concrete with a design strength of 25 MPa were used in this study. The concrete mix design is given in Table 1. Also, in order to improve the performance of the specimen against-earthquake, in terms of the lateral load, it was used reinforcement in a specified section outside the column. As organic materials may result in separation and spalling from the concrete, inorganic material with similar physical properties of the conventional reinforcement was adopted [7]. A helical bar used as the reinforcing material originates from nickel-chrome alloy and has high resistance against corrosion. Moreover, the reinforcement possessing spirally twisted shape exhibits an enhanced ductility and tensile strength, of which the strength accounts for about 1,100 MPa, compared to the rounded form [8]. These properties can produce the increased binding force to external force, and simultaneously not be easily cut off due to high elongation rate [8]. Therefore, it is expected to show excellent performance as a reinforcing material by resistance to earthquake. The helical bar with different types of diameter was used in the present works, and its schematic diagram is shown in Fig. 1.

Table 1. Mix properties of concrete

Strength (MPa)	Slump (mm)	W/B (%)	s/a (%)	Quantity of material per unit volume of concrete (kg/m^3)			
				W	C	S	G
24	120±25	514	49.1	148	288	857	899

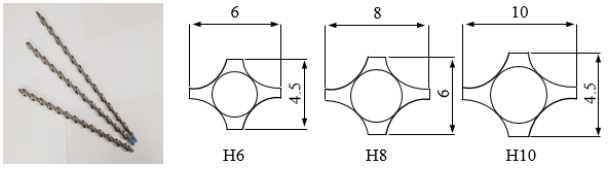

Figure 1. Helical bar and section

2.2 Specimen preparation

The specimen with a quarter-scale of the circular pier was designed dividing into a foundation part and a column one. The former was fabricated with formwork (1,200×600×600 mm in length) using normal rebars to ensure a restraining force when loaded laterally to the circular column, and the latter was manufactured with a transverse reinforcement ratio of 0.25% and an aspect ratio of 3.0, which equals to a height of 1,250 mm and a diameter of 400 mm. Fig. 2 shows the detail and picture of the RC specimen, respectively.

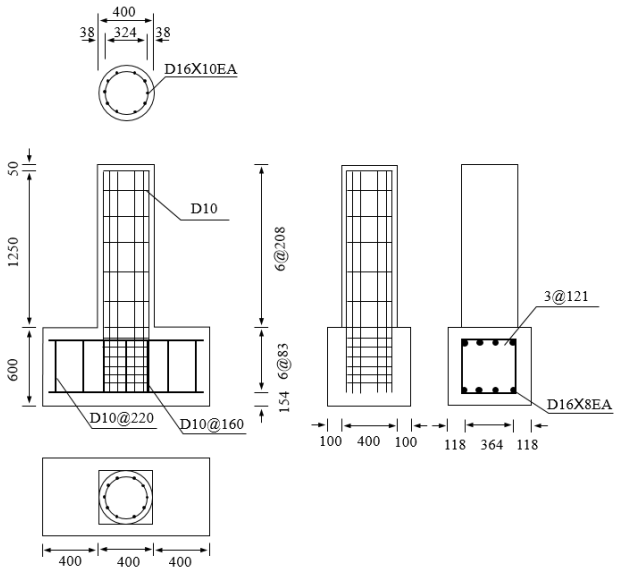

Figure 2. Design section and arrangement of specimens

After removing the concrete cover of about 20-30 mm from the surface of the RC specimen, the helical bar was installed along the furrow. Then, ends of the reinforcement were fixed in a hole of 50 mm using high strength epoxy as if a vertical anchor to achieve sufficiently restraining force. In turn, the buried space was filled out using rapid hardening grout with a strength of 40 MPa, followed by an adhesive agent was used for enable to behave integrally between old and new cross section. Reinforcing the helical bar in the column is shown in Fig. 3 as schematic diagram.

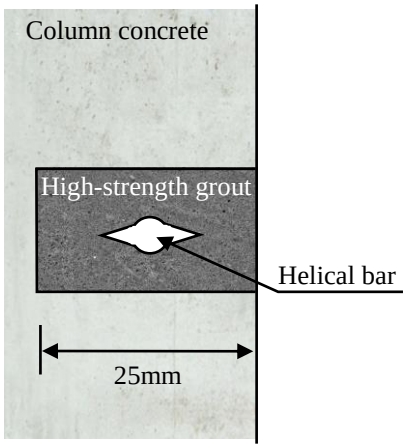

Figure 3. Reinforced section of setting helical bar

2.3 Plan to lateral force loading

To determine the load ratio in lateral force to the RC specimen, the yield displacement was verified through the control specimen, of which a value of the displacement(δy) was 22 mm. Based on the result, the drift level (δ/ δy) was 0.25% (5.5 mm), 0.5% (11 mm), 0.75% (16.5 mm), 1.0% (22 mm), 1.5% (33 mm), 2.0% (44 mm), 2.5% (55 mm), 3.0% (66 mm), 4.0% (88 mm) and 5.0% (110 mm). Fig. 4 show an experimental setup for cyclic loading adopted in this study.

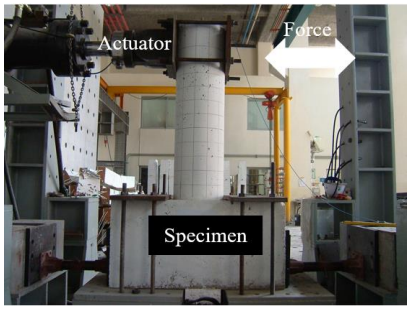

Figure 4. Experimental setup for cyclic loading test

3. EXPERIMENTAL RESULTS

3.1 Failure behavior by load stages

In all experiments, the same environmental conditions were maintained. During the course of the experiment, interesting surfaces of the specimens were focused and observed at every 100 mm from the base - column junction to the upper direction. All of the specimens were destroyed in the plastic hinge section and showed typical bending-shear failure behavior. There was a difference in the size and degree of the final failure depending on the presence of reinforcement and the variables of each experiment. However, in general, the cracks tended to be uniformly distributed throughout the initial period after the start of the experiment, and in the latter period, the cracks rapidly concentrated on the plastic hinge region, leading to the decline of the concrete covering and the detachment of the deep concrete. In the case of circular column specimens with reinforcement, the stiffness was increased due to the increase of lateral confining force of

the column members due to the effect of stiffeners until the middle of the experiment, which was confirmed by increasing the ultimate displacement and decreasing the lateral displacement. The following is a summary of behavioral characteristics of each specimen.

Control specimen After flexing up to 109.6 kN of the maximum lateral load with a non-reinforced specimen, concrete sheath was removed from the test specimen at a height of 500 mm from the base joint, the section of the plastic hinge after 2.5% of the drift level, and rebars were exposed and severely bent in the same direction as the loading direction. In other words, due to the loss of concrete, some resistance to transverse loads was lost, and only the capitulation of axial rebar and the core concrete resisted. After the drift level 3.0%, the core restraint concrete inside the axial rebars was destroyed due to severe cracks, and its resistance to transverse loads was reduced rapidly. Since the large amount of core concrete loss occurred, the axial rebar has decreased its bonding performance with the concrete, causing a slip behavior, and showed the severe rebars buckling in the plastic hinge region, which is a 200 mm height section from the base joint. Fig. 5 shows specimen destroyed after the experiment.

Figure 5. Control specimen experimental result

H6 specimen The specimen is spiral-reinforced with a 6 mm diameter helical bar that extends the danger cross section from the base joint to a height of 500 mm. The spacing of the reinforcing helix is 100 mm. During the test, the maximum lateral load applied to the specimen was 105.2 kN, and after the drift level 3.0%, the helical bar was first cut by lateral load, and then the reinforcement was severely cut off. Due to the lateral confinement loss as a stiffener, it showed a drastic decrease in performance as in the case of unreinforced specimens. In this test condition, the sectional force of 6 mm diameter helical bar is weaker than that of unreinforced specimen in order to obtain high lateral load resistance. Fig. 6 shows specimen destroyed after the experiment.

H8 specimen It is a specimen reinforced up to 500 mm, the dangerous section, with a spiral gap of the column of 100 mm using a helical bar of 8 mm in diameter. The maximum lateral load of the specimen during the test was 130.9 kN. After the drift level 3.0%, the first reinforcing bar, helical bar, was cut by lateral load, but unlike the 6 mm diameter reinforcement, no additional cuts occurred elsewhere. Because of the reinforcement of the spiral, it

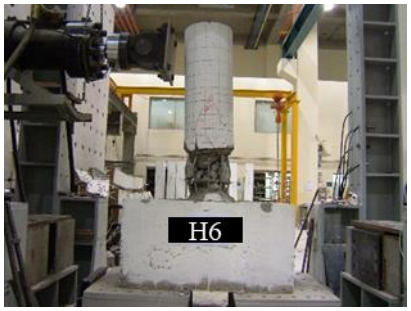

Figure 6. H6 specimen experimental result

is considered that even if the reinforcement is cut in one section, it does not cause severe damage to the entire reinforcement effect. Therefore, the remaining sheath showed less failure due to cracks, and the energy absorption capability for the lateral load even to the end of the experiment was demonstrated without the loss of lateral resistance. It is shown that the lateral load strength is reduced from 3.0% of the drift level and 60 mm of displacement, but is not sudden and is decreased smoothly. Fig. 7 shows specimen destroyed after the experiment.

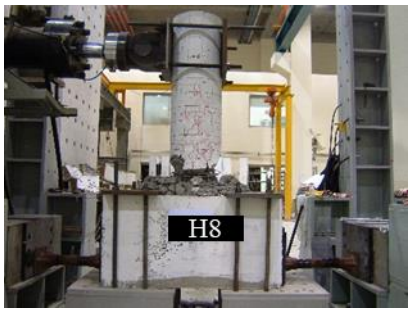

Figure 7. H8 specimen experimental result

H10 specimen It is a specimen reinforced up to 500 mm, the dangerous section, with a spiral gap of the column of 100 mm using a helical bar of 10 mm in diameter. It is a reinforcement to be used when a relatively large reinforcing performance is required, and it has a disadvantage that it is difficult to construct due to a high sectional force and is expensive. The maximum lateral load of the specimen during the test was 123.1 kN. It shows high energy absorption at more than 4.0% of the drift level. However, due to the use of reinforcement having too large section force relative to the performance of existing members, the main reinforcement was cut from the drift level lower than in the case of H8 due to its high lateral binding force. Fig. 8 shows specimen destroyed after the experiment.

Figure 8. H10 specimen experimental result

In H6 and H8, there was no amputation of the rebar. Because of the low lateral confinement force, concrete and steel bars did not behave at all during plastic deformation and slip behavior occurred. It is judged that the lateral binding force is applied from 8mm in diameter. Only H10, of all reinforced specimens other than H6, did not have a helical bar-section cut. When reinforcing material with a diameter of 10 mm was used, the shape was maintained until the subject reached failure and the axial rebars were cut inside the column, and sudden failure of the reinforced bar was shown compared to the degree of external failure. The fracture of the cast iron was found to be at a drift level of 4.0%, which is faster than the other specimens. As the lateral binding force due to reinforcement increases, it is believed that the strength development of the confined concrete has improved, thus failing to induce ductile behavior and resulting in brittle fracture. Table 2 shows the results of the characteristics of each specimen by each loading cycle.

Table 2. Behavior property of entire specimens

Drift Level (%)	Specimens: Control	H6	H8	H10
0.25	◎	◎	◎	◎
0.5	●○	●		●■
0.75	■	■	●○	
1.0		○	■	○□
1.5	□		□	◇
2.0		□		
2.5	◆	◇		◆
3.0		☆◆	☆◆	
4.0				★
5.0			★	

◎ : Initial crack
● : Shear crack
○ : Diagonal crack
◆ : Axial main reinforcement exposure
★ : Axial main reinforcement cut-off
□ : Concrete cover fall-off
■ : Column joint crack
◇ : Helical bar exposure
☆ : Helical bar cut-off

3.2 Load-displacement envelope

The envelope was created by deriving the maximum lateral load for each displacement from the load - displacement curves obtained through the experiment. The area formed with the x-axis below the graph is considered to be the ductile strength of a structure that can absorb external energy in the event of an earthquake, at a envelope consisting of displacement of the transverse axis and lateral load of the longitudinal axis. It can be seen that the performance is drastically degraded from the drift level of 2.5% (55 mm) as compared with the Control specimen which is not reinforced. All of the reinforced specimens show a difference in magnitude, but generally show an improvement in reinforcing performance after this section. Fig. 9 is the load-displacement envelope of the entire specimen displayed on one coordinate. At the load-displacement envelope obtained when the reinforcement diameter is variable, with all the reinforcement spacing of 100 mm, the performance of the 8 mm diameter reinforcement was best demonstrated. It is shown that the reinforcement spacing of the 8 mm diameter reinforcing materials with the best performance is different from the reinforcing spacing in the envelope test to improve both stiffness and ductility.

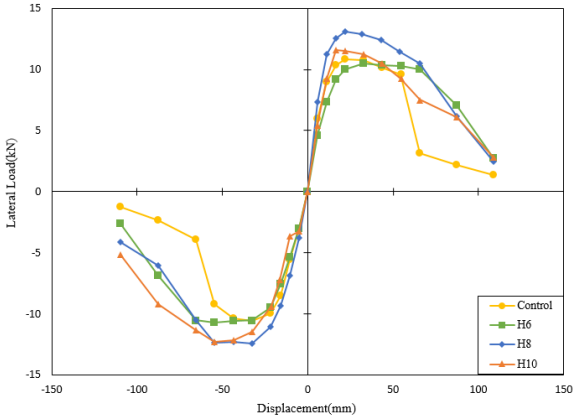

Figure 9. Lateral load – Displacement envelope of all specimens

4. CONCLUSIONS

The seismic performance for the specimen simulated circular bridge pier was evaluated by quasi-static experiments after reinforcement using helical bar. The conclusions of the present works are summarized as follows.

(1) Reinforcement of the helical bar to piers effectively inhibited the spalling of cover concrete arising from the failure by increasing the lateral displacement of the column (i.e., Drift level). Due to this phenomenon, the core restraint effect of the concrete was continued at a certain level after the column failure (109.6 kN), and eventually the specimen was collapsed when the lateral load reached at 130.9 kN.

(2) The actual failure of RC specimens with the helical bar appeared within the reinforced section of the pier (500 mm from the foundation), which would induce the ductile failure of the column due to the reinforcing effect. The further reinforcement for the broad area of the bridge piers seems to improve the resistance against earthquake by preventing the non-uniform loading, but it can result in an uneconomical and oversized design.

(3) For effective seismic reinforcement, it is necessary to select an appropriate level for reinforcement using a helical bar, considering the

amounts of longitudinal steels in the pier. The specimen using the helical bar with a diameter of 6 mm exhibited a lower ductility, while the case of 10 mm diameter showed an over-reinforcement effect. It should be cautious in the use of the helical bar for reinforcing bridge piers due to behavior of brittle fracture resulted from over-reinforcement.

5. REFERENCES

[1] Lee, H. M., Baek, K. L., Kim, J. H., Earthquake Occurrence Frequency and Magnitude Analysis for South Korea on the Basis of Ground-Observed Data, Journal of the Korean Society of Hazard Mitigation, 14 (2015) 268-268.

[2] Korea Meteorological Administration website : http://www.weather.go.kr/weather/earthquake_volcano/domestictrend.jsp (accessed 19.06.29).

[3] Design Code for Highway Bridges in Korea, Ministry of Land, Transport and Maritime Affairs, 2010.

[4] Anil K. Chopra, “dynamic of structures theory and application to earthquake engineering”, Prentice Hall, Pakistan, 2001.

[5] Chung, Y. S., Park, J. H., Park, H. S., Seismic Performance Evaluation and Enhancement of Circular Reinforced Concrete Bridge Piers by Pseudo Dynamic test, Journal of the Korean Society of Civil Engineers, KSCE, 22 (2002) 499-509.

[6] M. J. N. Priestley, F. Seible, G. M. Calvi., Seismic Design And Retrofit Of Bridges, John Willey and Sons, Inc., New York, 1996.

[7] Chung, Y. S., Park, J. H., Park, H. S., Seismic Performance Evaluation and Enhancement of Circular Reinforced Concrete Bridge Piers by Pseudo Dynamic test, Journal of the Korean Society of Civil Engineers, KSCE, 22 (2002) 499-509.

[8] Kim, J. B., Won, Y. S., Cho, C. H., An Experimental Study on the Structural Behavior of Reinforced Concrete Columns Rehabilitated with Epoxy-Bonded Steel Plates, Journal of the Korea Institute for Structural Maintenance and Inspection, KSMI, 3(3) (1999) 269-277.

Effect of Nano Zero Valent Iron Delivery Method into Porous Media on Phosphorus Removal from Groundwater

Ibrahim Maamoun[1], Osama Eljamal[1*], Ian P. Thompson[2], Ramadan Eljamal[1], Omar Falyouna[1], Yuji Sugihara[1]
[1] Department of Earth System Science and Technology, Interdisciplinary Graduate School of Engineering Sciences, Kyushu University, Fukuoka, Japan
[2] Department of Engineering Science, University of Oxford, Parks Road, Oxford, OX1 3PJ, UK
*Corresponding author email: osama-eljamal@kyudai.jp

Abstract: *The main aim of this study is to investigate the effect of the delivery method of nano zero valent iron (NZVI) into porous media on the removal of phosphorus from groundwater. Different column experiments were conducted considering injection and permeable reactive barrier (PRB) approaches using sand-packed column with 65 cm length and 10 cm inner diameter. Results revealed that Injecting 10 g of NZVI into C4 resulted in the highest sorption capacity and average removal efficiency of 25 mg/L phosphorus concentration over 14 days with 197.76 mg-P/g-NZVI and 84.8% respectively. The dissolved oxygen levels in the effluent samples of the NZVI column were declined due to the oxidation process of NZVI, which was accompanied by a lower ORP values.* The *change of the delivery methodology of NZVI into porous media affected its capacity to remove phosphorus, revealing that injection could be better than PRB in terms of the reactive performance.*

Keywords: Phosphorus; nano zero valent iron; permeable reactive barrier; injection; delivery method.

1. INTRODUCTION

Phosphorus (P) is one of the major nutrients and it is essential element for all forms of life. However, the excessive use of fertilizers and the uncontrolled discharge of untreated sewage could increase the phosphorous concentration in groundwater [1,2]. Correspondingly, the migration of such contaminated groundwater into water bodies could be one of the possible factors in speeding up eutrophication [3]. Therefore, phosphorus removal from groundwater plays a significant role in decreasing the harmful impact of eutrophication on the aquatic systems and the drinking water quality as well [4,5]. Meanwhile, nano zero valent iron (NZVI) has been widely used as an efficient adsorbent for phosphorus removal from water, because of its unique core-shell structure which increases its reactivity towards several water pollutants [6,7]. In addition, its nano-size features lead to larger specific surface area which provides more available sorption sites on the surface. Moreover, owing to its position in the chemical reactivity series it can react with most of the soluble contaminants in water. When it comes to applying NZVI into in-situ groundwater remediation applications, there are two main methodologies that has been widely used. The first one is injecting NZVI solution into the porous media using screened wells which penetrates the medium to the desired contamination depth. The second approach is the PRB, which basically conducted by digging a trench into porous media in which NZVI is packed to Intersect the contaminated plume [8]. Therefore, the main objectives in this study are; a) conducting column experiments to determine the best delivery method of NZVI into porous media, and b) investigating the effect of the delivery method on the reactivity and longevity of NZVI towards phosphorus.

2. MATERIALS & METHODOLOGY

2.1 NZVI Synthesis

Chemical reduction method of ferric chloride ($FeCl_3$) by the drop-wisely injected sodium borohydride ($NaBH_4$) was used to synthesize NZVI [9]. To prepare 1 g of NZVI, the two solutions ($FeCl_3$/$NaBH_4$: 5/3.5) were mixed mechanically at 250 RPM and at constant temperature of 25 ± 0.5° C. Nitrogen purging was provided for all the prepared solutions before use and also during the whole synthesis steps to ensure the anaerobic environment. After 20 min aging time the black precipitates of NZVI were collected using vacuum filtration and washed by DIW.

2.2 Column Experiments

Different column experiments were conducted in order to investigate the effect of the NZVI delivery method into porous media on phosphorus removal from groundwater. In our experiments, three NZVI delivery methods were considered: a) supporting NZVI on sand using a PRB layer of NZVI/Sand mixture (mixing mass ratio of Fe/Sand: 1/100), b) Bare NZVI using a PRB layer of pure NZVI, and c) Injecting NZVI solution. The same dosage of 10 g NZVI was considered in the three approaches for a reasonable and fair comparison. Moreover, the injection rate of NZVI solution into the column was 2 g/day distributed over the experiment time.

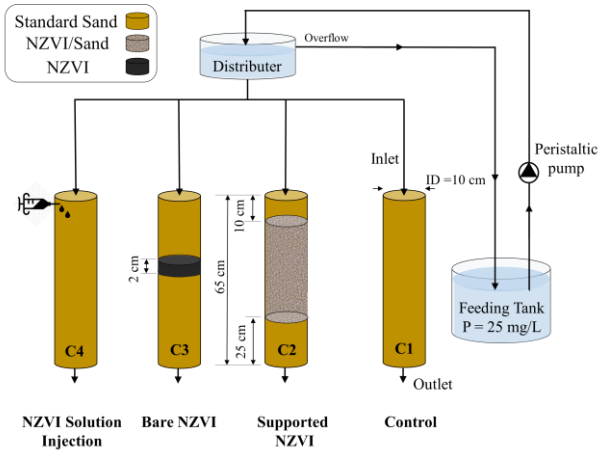

Fig. 1. Schematic of column experiment configurations.

A Plexiglas column (65 cm height and 10 cm inner diameter), packed with standard sand as the main porous medium, was used in the column experiments. Four columns (C1-C4) were considered including the three delivery methods to be investigated as well as the control column. The configurations of the 4 columns are shown in detail in Fig. 1. Feeding phosphorus solution with initial concentration of 25 mg-P/L was pumped downward into the column at 15 mL/min flowrate. The initial geochemical measurements of the inlet solution are; pH = 7 ± 0.5, oxygen reduction potential (ORP) = -25 mV and dissolved oxygen (DO) = 8 mg/L. Effluent samples and samples along the column height were collected for phosphorus analysis over 14 days of experiment time. Samples were directly analyzed using UV-Vis spectrophotometer (DR3900, HACH, USA) for phosphorus concentration.

3. RESULTS & DISCUSSION

3.1 Sorption Capacity & Removal Efficiency

Sorption capacity and removal efficiency were calculated using Eq. 1 and 2 respectively based on the phosphorus concentration in the effluent samples. Results are plotted with respect to experiment days as shown in Fig. 2 and 3.

$$q_e\ (mg/g) = \frac{(C_o - C_e)\,V}{m} \quad (1)$$

$$R\ (\%) = \frac{(C_o - C_e)}{C_o} \times 100 \quad (2)$$

Where; C_o and C_e (mg/L) are inlet and effluent phosphorus concentration, m (g) is NZVI dosage, and V (L) is accumulated inflow volume.

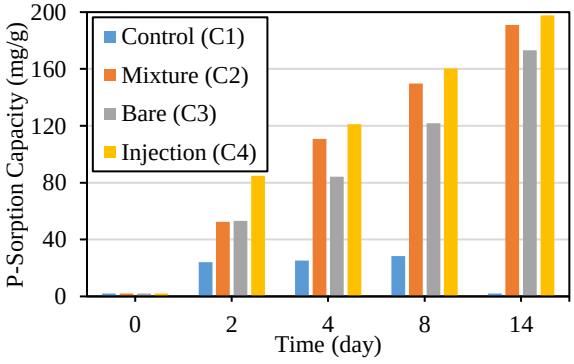

Fig. 2. Effect of delivery method on NZVI sorption capacity towards phosphorus.

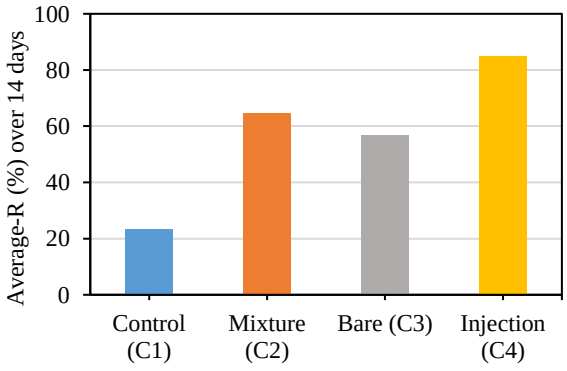

Fig. 3. Average phosphorus removal efficiency (R %) over the 14 days experiment time.

Sorption capacity gradually increased for C2, C3 and C4 to reach its maximum values after 14 days of the experiment of 190.94, 173.12 and 197.76 mg-P/g-NZVI respectively. Whereas, the maximum sorption capacity in the control column was around 28.42 mg-P/g-NZVI. Results showed an obvious enhancement in the sorption capacity for the injection column (C4) comparing to the PRB columns (C2 and C3). However, it is worth to be said that the performance of the supported NZVI in C2 was comparable to C4. Meanwhile, the results of the average removal efficiency of phosphorus were consistent with what have been concluded. Injecting NZVI into C4 resulted in an average removal efficiency of 84.8% which was the highest comparing with the other two PRB columns (C2 and C3) with 64.4% and 56.8% respectively.

3.2 Geochemical Measurements

Over the experiment time, geochemical measurements (pH, ORP and DO) of the effluent samples were recorded, as presented in Fig. 4.

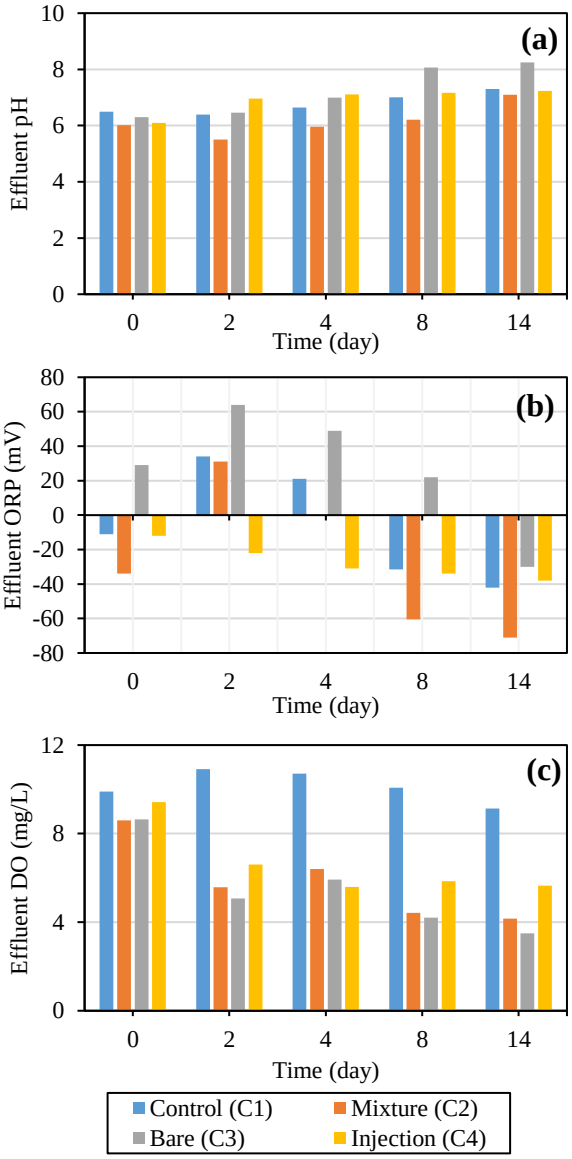

Fig. 4. Effect of NZVI delivery methods in the effluent's geochemical values of: (a) pH, (b) ORP, and (c) DO.

Results showed that there was no significant difference in the pH values at the effluent of the 4 columns.

However, there was a slight increase in case of bare NZVI in C3 comparing to the supported one in C2 to reach pH value above 8 at the later stages of the experiment, which could be attributed to the easy oxidation of the bare NZVI which accompanied with the release of iron oxides (Fe^{2+} and Fe^{3+}) and OH^- anions:

$$2Fe^0 + 4H^+ + O_2 \rightarrow 2Fe^{2+} + 2H_2O \quad (3)$$

$$2Fe^{2+} + 2H_2O \rightarrow 2Fe^{3+} + 2H_2 + 2OH^- \quad (4)$$

ORP measurements was fluctuated for all the columns except for the injection column (C4), in which it had a clear trend with a final value of -38 mV, which is not so far from the initial value. Meanwhile, DO levels significantly decreased in the effluent of the three NZVI columns (C2-C4) comparing to that in the control column (C1), indicating the oxygen consumption which occurred by the presence of NZVI within the medium.

3.3 P-Profiles

Phosphorus concentration along the column's height at the 14th day of the experiment time are shown in Fig.5. Results depicted that phosphorus concentration in case of injecting NZVI into the column decreased dramatically comparing to that of the other columns. That could be attributed to both the fresh state of the injected (as-synthesized) NZVI slurry in addition to the possible rapid surface oxidation of the packed-NZVI particles during the packing process in C2 and C3.

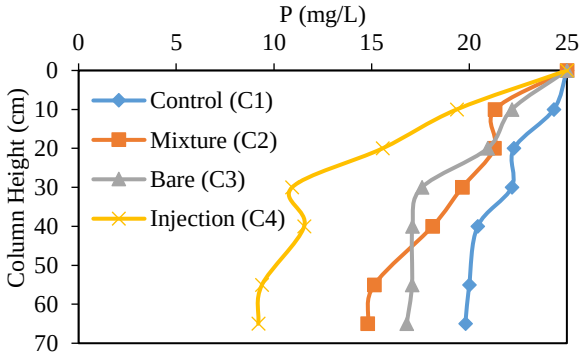

Fig. 5. Phosphorus profiles along the columns at the end of the experiment.

4. CONCLUSIONS

In this study, different delivery approaches of NZVI into porous media were investigated through a set of laboratory column experiments for a better performance in groundwater treatment. Results implied that injecting the solution of the as-synthesized NZVI into porous media showed superiority over packing it as a PRB layer. Injecting 10 g of NZVI into C4 resulted in the highest sorption capacity and average removal efficiency of 25 mg/L phosphorus concentration over 14 days with 197.76 mg-P/g-NZVI and 84.8% respectively. Meanwhile, mixing NZVI with sand as a PRB material showed a comparable performance to the injection method. Geochemical measurements were consistent with the obtained results showing the decline in the dissolved oxygen levels in the effluent samples due to the oxidation process of NZVI, which was accompanied by a lower ORP values. Generally, it could be concluded that the change of the delivery methodology of NZVI into porous media affected its capacity to remove phosphorus, revealing that injection could be better than PRB in terms of the reactive performance. However, further investigation is needed on the use of NZVI/Sand mixture as PRB material because of its comparable depiction. Also, it is important to conduct a feasible comparison between Injection and PRB in terms of the installation and operating costs, which represents a crucial factor in the real field applications.

5. REFERENCES

[1] T. Almeelbi, A. Bezbaruah, Aqueous phosphate removal using nanoscale zero-valent iron, in: Nanotechnol. Sustain. Dev., Springer, 2012: pp. 197–210.

[2] J. Wei, J. Ge, A.A. Rouff, X. Wen, X. Meng, Y. Song, Phosphorus recovery from wastewater using light calcined magnesite, effects of alkalinity and organic acids, J. Environ. Chem. Eng. 7 (2019) 103334. doi:https://doi.org/10.1016/j.jece.2019.103334.

[3] I. Maamoun, O. Eljamal, A.M.E. Khalil, Y. Sugihara, N. Matsunaga, Phosphate Removal Through Nano-Zero-Valent Iron Permeable Reactive Barrier; Column Experiment and Reactive Solute Transport Modeling, Transp. Porous Media. 125 (2018) 395–412. doi:10.1007/s11242-018-1124-0.

[4] O. Eljamal, J. Okawauchi, K. Hiramatsu, M. Harada, Phosphorus sorption from aqueous solution using natural materials, Environ. Earth Sci. 68 (2013) 859–863. doi:10.1007/s12665-012-1789-6.

[5] O. Eljamal, J. Okawauchi, K. Hiramatsu, Product rich in phosphorus produced from phosphorus-contaminated water, in: Adv. Mater. Res., Trans Tech Publ, 2014: pp. 261–265.

[6] I. Maamoun, O. Eljamal, N. Matsunaga, Enhancement of Nanoscale Zero-Valent Iron Stability in Aqueous Solution Via Metal Hydroxide Coating, (2018).

[7] I. Maamoun, O. Eljamal, T. Shubair, H. Noutsuka, B.B. Saha, N. Matsunaga, Integrating nano-scale zero valent iron (nZVI) in phosphorus removal from aqueous solution through porous media: packed-column experiment, Proc. Int. Exch. Innov. Conf. Eng. Sci. 3 (2017) 25–30.

[8] T. Tosco, M.P. Papini, C.C. Viggi, R. Sethi, Nanoscale zerovalent iron particles for groundwater remediation: a review, J. Clean. Prod. 77 (2014) 10–21.

[9] R. Eljamal, O. Eljamal, A.M.E. Khalil, B.B. Saha, N. Matsunaga, Improvement of the chemical synthesis efficiency of nano-scale zero-valent iron particles, J. Environ. Chem. Eng. 6 (2018) 4727–4735. doi:https://doi.org/10.1016/j.jece.2018.06.069.

The stability of water molecular bridges in ombrotrophic peatland soil

František Mikšík[1,2], Štěpánka Freithová[1], Josef Kotlík[1], Jiří Kučeřík[1], Alasdair MacLeod[3]
[1]Institute of Environmental Chemistry, Faculty of Chemistry, Brno University of Technology, Purkyňova 464/118, Brno 612 00, Czech Republic, [2]Interdisciplinary Graduate School of Engineering Sciences IGSES, Kyushu University, Kasuga-koen 6-1, Kasuga-shi, Fukuoka 816-8580, Japan, [3]Lews Castle College, University of Highlands and Islands, HS2 0XR Stornoway, Isle of Lewis, United Kingdom
miksik@kyudai.jp

Abstract: *The stability of water molecular bridges (WaMB) is investigated on the ombrotrophic organic peatland type soil. The samples of the soil collected in the north part of Scotland (UK) near the city of Stornoway. The temperature dependence of the WaMB breaking point was measured through differential scanning calorimetry and shows how much are the organic structures inside the peat type soil susceptible to drying. The deeper peatland soil in this work shows much lower temperature values of WaMB breaking of around T* ~ 47 °C compared to the top layer where the middle temperature of WaMB breakage is T* ~ 58 °C, comparable to regular soil types. This temperature dependence shows higher susceptibility of the studied peal soil for drying and therefore higher sensitivity to changes in the water table levels and disturbance of the top layers of the soil system.*

Keywords: Peatland; Soil; Water; Water Molecular Bridges; Ombrotrophic.

1. INTRODUCTION

The latest estimates give peatland ground around 3 % of the globe's total land area[1] and according to the analysis of Yu et al.[2] the peat bogs across the world have accumulated approximately 530 – 694 Gt of carbon. However, some estimates believe that almost 50 % of the soil carbon deposits (soil carbon pool) are contained in the peatlands, which would be approximately around 1 600 – 1 700 Gt of carbon[3], in the northern regions only. That would be, technically, twice the amount of carbon in the atmosphere in a form of CO_2 (considering the concentration of 400 ppm). And truly, looking at the world map in Fig. 1, the majority of the peatland areas are located in the colder north climate region with a considerable amount of peatland stabilized in the permafrost of Russian's Siberia and North America[3]. Because of the amount of stored and relatively stabilized carbon, the peatland ecosystems are very important for sustaining and control of natural carbon cycle as disruption of those ecosystems can result in a significant release of CO_2 into the atmosphere.

The problematic of the rapid release of CO_2 from peatlands is often mentioned in connection to the underground peat fires in tropical regions[4]. However, the CO_2 and CH_4 release from peatland is a complicated process and can be also triggered by disruption of the water table and temperature changes as well. The release of CO_2 from a drained peatland in Southeast Asia was studied by Hooijer et al.[5] describing serious carbon emission due to the peatland decomposition in the magnitude of 355 Mt to 855 Mt p.a. Recently, the temperature effects on boreal fen were examined by Laine et al.[6] observing that temperature itself has only limited impact and concluding that water table levels are

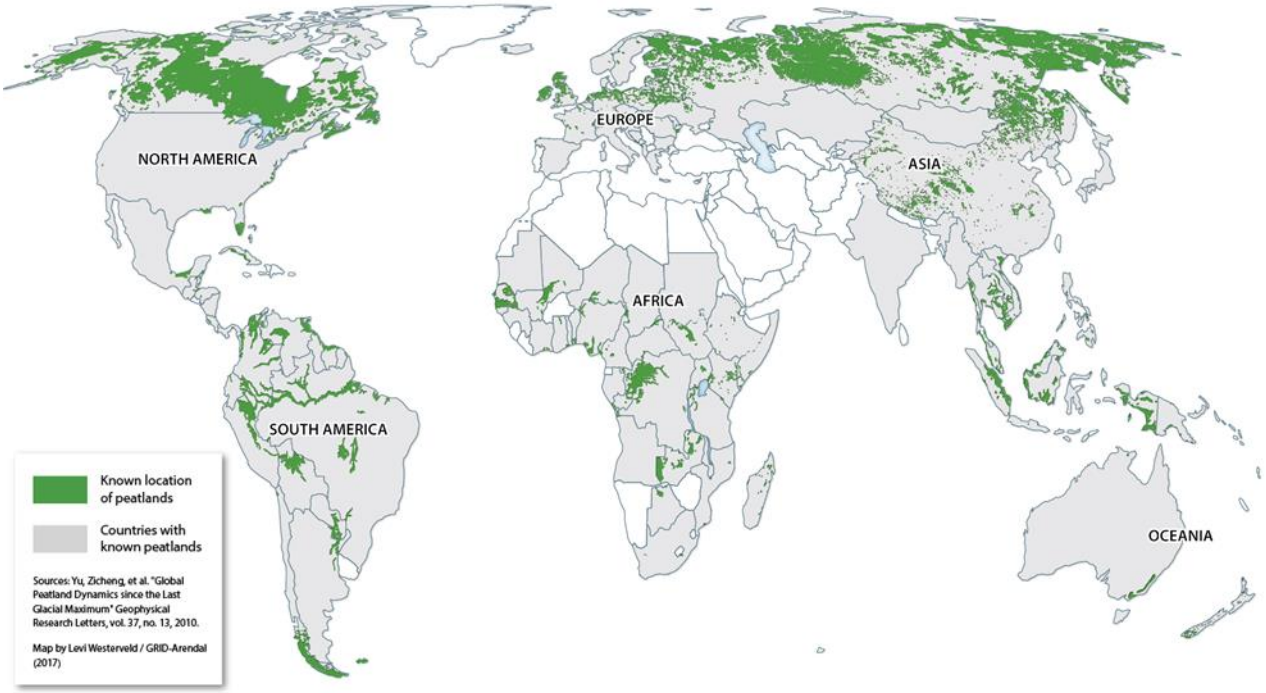

Fig. 1. Global distribution of peatlands[12]

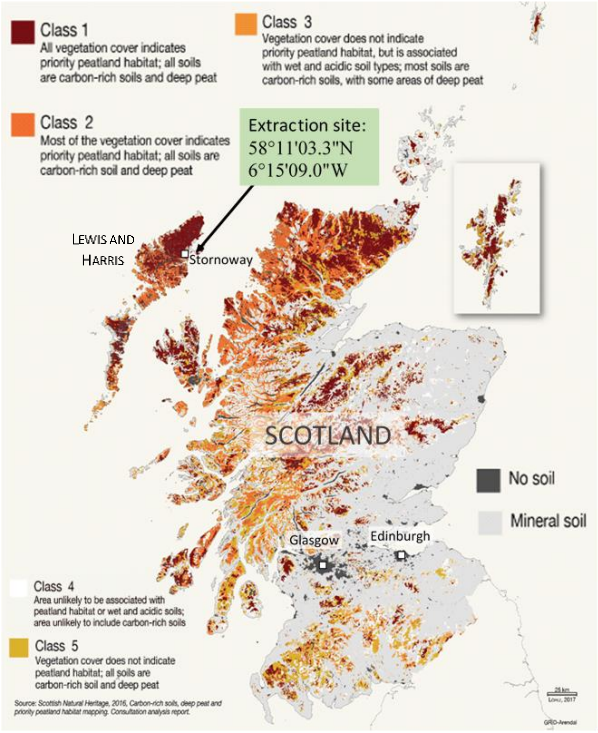

Fig. 2. Extraction location and peatland habitat coverage of Scotland, UK (original map from[13], adjusted)

a more serious matter for northern regions, thus similarly to the finding of Hooijer et al.[5] in case of hot regions of Southeast Asia. Accordingly, based on those findings we can assume that water levels and water retention capabilities of peat bogs and fens will play an important role in the future sustainability of the peatlands.

Sustainable water levels are naturally mostly connected to the prevalent water transportation mechanism at a given location, however, the water retention mechanisms of the particular soil type play an important role in its tolerance for sudden changes in the water level over short periods of time. One way how to describe the peat macromolecular stability is its dependence on temperature in polymer or polymer-like materials is the determination of water molecular bridges (WaMB). The water molecular bridges connect hydrophilic functional ends of the present macromolecular organic compounds thus stabilizing them inside the peat matrix. Consequently, the increased crosslinking of the structure better binds the water inside the organic matrix. Therefore, the presence of WaMBs is usually connected to the actual material stability and depending on the composition of the given peat soil type we can assume a correlation to the endurance against water shortage as well. Here, we study stability of the peat soil through the determination of the energy of WaMB as the temperature of the decomposition of water molecular bridges structures. The water molecular bridges were extensively studied by Shuman at el.[7, 8] trying to explain the effect of the WaMB on the biochemical and hydrological processes inside peat soil. In this work, the focus is given to the quality of the WaMB and its analytical importance on the water retention capabilities of examined peat samples.

2. EXPERIMENTAL

2.1 Location and sample treatment

Samples were collected on the Outer Hebrides' island Lewis and Hariss in Scotland, the United Kingdom near

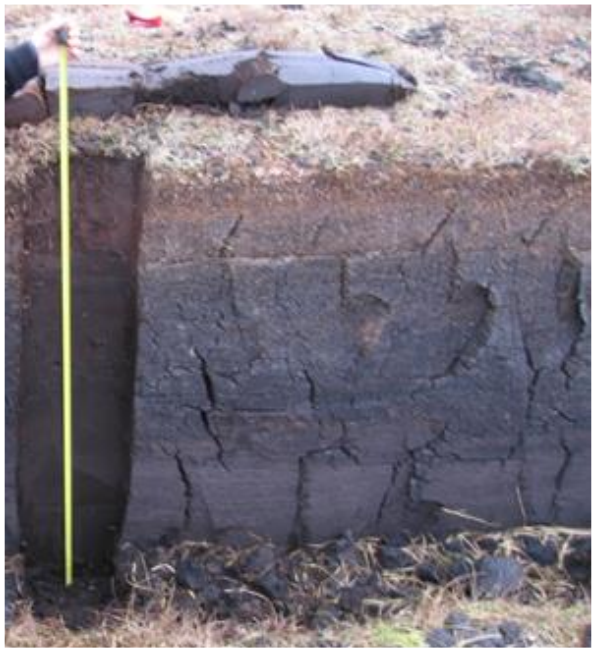

Fig. 3. Extraction site inside the peat bog – uncovering of the fresh layers of peat

the harbour city Stornoway. The exact location is shown in Fig. 2 together with the peat classifications of the soil types associated with peat formation. The sampling was conducted in March before the start of a new vegetation period.

The sample was taken from inside an active peat bog area at the full depth from the top vegetation layer down to the solid bedrock as shown in Fig. 3. To obtain a fresh sample first 10 - 20 cm of the weathered peat was removed prior to the actual sampling to uncover undisturbed peat layers. The full length of the sample of 120 cm was vertically separated into 18 equally sized rectangular blocks of thickness around 3 cm and length of 6-7 cm. The individual blocks of the samples were then dried slowly inside an exicator at 20 °C and 43 % humidity until no weight loss was observed any more. After the drying, the samples were ground in a standard laboratory agate mortar to be homogenized and easier to analyse.

2.2 Methods

The main method to study the breaking point of the water molecular bridges was used the Differential Scanning Calorimetry (DSC). For the measurement was used instrument Discovery DSC 2500 (TA Instruments, US) equipped with an automatic handler and cooling system RSC90. The temperature program was set in the first phase to cooling from ambient temperature to -40 °C with the gradient of 10 °C/minute and then heating to 110 °C again at the rate of 10 °C/min. the amount of the sample was in the range 2-8 mg inside a standard aluminium pan. The purge gas was nitrogen with a flow of 50 ml/min. The DSC was acquired at least twice for each sample type.

The dry mass (water content) was measured for both treated and untreated samples by thermogravimetry (TG). The weight of the dry mass was acquired at the point where the mass change d*w* was equal to 0 °C in the temperature range from 100 °C to 150 °C. The temperature range was selected in respect to the thermally unstable component which started to influence the mass change typically beyond the 150 °C mark. The

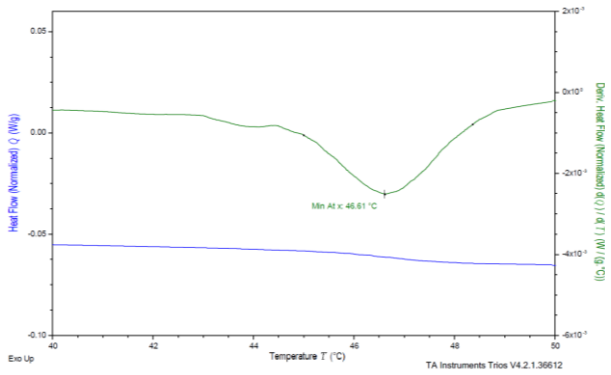

Fig. 4. Establishing of WaMB breakage point

measurement was repeated three times for each type of sample, always with a fresh sample.

Values of pH were established on the untreated samples due to the better wettability of the material and therefore better access and mobility of water and creation of hydronium cations as the basic measure for acidity. 130-200 mg of the raw peat was mixed with 60 ml of distilled and deionized water and after 15 minutes the pH was measured as a direct consumption of NaOH solution until neutral pH was achieved. The measurement was conducted on automatic titration stand Schott, TitroLine alpha plus (SI Analytics, Germany). The freshly prepared NaOH solution was calibrated by a standard solution of oxalic acid. The pH meter was calibrated as well by a precise laboratory buffer solution of pH = 7.00±0.05 (Sigma Aldrich, Germany). The measurement was repeated twice for each sample type.

3. RESULTS AND DISCUSSION

The amount of carboxylic acids contained in individual peat layers lowers the value of pH depending on the concentration and type, therefore the measured pH value gives us some basic information about the peat type and composition. The top layer of the extracted peat is only slightly acidic (pH ~6) allowing the existence of more diverse botanical environment rather than predominant *Sphagnum* moss as in case of more acidic peat bogs [9]. The pH then drops with the depth reaching the minimum of pH = 5.1 at the utmost bottom. Although the actual composition of the organic acid composition was not analysed typical humic substances such as humic and fulvic acids can be expected. The increase in acidity is apparently connected to the dominant transport mechanism of nutrients in the observed peat column (rainfall) when the smaller and better soluble fulvic acids

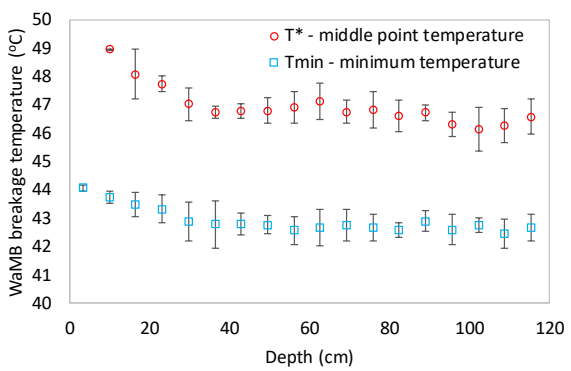

Fig. 6. Temperature of the collapse of the WaMB

Fig. 5. pH dependence of the peat on the depth

Table 1. pH, dry mass share and separation temperature of the WaMB (the numerical part of the sample's names represents median of its depth range in centimeters from the top)

Sample	pH	Dry mass (fresh) w_F/(%)	Dry mass (prepared) w_P/(%)	WaMB break temp. T_{WaMB}/(°C)
D3	6.3	23.1	86.5	58.5
D10	6.1	15.8	87.9	49.0
D17	6.0	15.8	87.5	48.1
D23	5.8	13.2	88.1	47.7
D30	5.7	14.0	89.9	47.0
D36	5.6	15.4	89.3	46.7
D43	5.5	13.9	88.4	46.8
D50	5.4	15.7	88.7	46.8
D56	5.3	17.0	88.1	46.9
D63	5.4	18.0	88.9	47.1
D69	5.3	18.2	90.4	46.8
D76	5.4	16.2	88.3	46.8
D83	5.3	15.4	89.2	46.6
D89	5.3	14.4	87.5	46.7
D96	5.2	16.5	88.0	46.3
D102	5.3	15.9	88.3	46.1
D109	5.3	17.4	88.2	46.3
D116	5.1	35.0	87.4	46.6

are transported to the lower layers. From the results shown in Fig. 5 are apparent two zones, one with a rapid change of acidity down to around 50 cm of depth and slow a change zone all the way down to the bedrock. This boundary may suggest a change in the transport process and water permeation. Once we compare the actual peat layers, as can be seen in Fig. 3, we can see that around the 50 cm mark the soil colour and consistency start to change rapidly turning into much more compact and highly decomposed peat. Even though that the actual water content stays almost constant through the peat layers as they are listed in the Table 1., the consistency changes significantly from the top with roots and many herbal residues to the bottom layers which behave more like a paste-type material without any traces of original organic material. This stratification is, of course, typical for peat bogs, although the ratio of individual layers is dependent on the stage of ageing of the peat. The pH measurement was also attempted on treated and homogenized samples (dried) as well, however, the results showed no change of pH over the whole depth of the peat samples. The reasons for this measurement fail can be several, however, one of the more probable ones is the hydrophobic change of dried peat described in the literature on several occasions [10], as well as showed by our direct observation.

The temperatures at which the water molecular bridges break apart are shown in Fig. 6 where the middle pint temperature of the process is signed as T^* and the starting or minimum temperature for the bridges to start collapsing is marked as T_{min}. If we compare the utmost top layer with the lower layers we can see that the difference is not dramatic but, similarly to the pH, two zones can be distinguished this time around the 40 cm mark. This time the visual change is more apparent in Fig. 3. The change in colour and consistency is mostly caused by the presence of active root system of the herbs living on the surface together with the *Sphagnum* moss. If we compare the values of the peat from this work with other

soil types we can see that the regular soil has much higher values for the breaking of the water molecular bridges 50 - 70 °C[11], and that it stabilizes with depth as the peat becomes more compact and regular. This means that the water is actually connected to the peat structures only poorly and peat type of soil is more endangered by lack of water and the process of drying can be much faster than usually expected.

4. CONCLUSION

The breaking temperature of the water molecular bridges is highest in the top layers of the examined peat column at T_{WaMB} = 58.5 °C and drops with the increasing depth. This shows higher susceptibility to drying when the top layers are removed or damaged.

Significant complications are brought by the problematic of the low rewetting ability of once dried peat which requires a long time for regeneration.

The temperature of the WaMB collapse is significantly smaller for peat than for regular soil, therefore the synergic effect of the drying process and reduced rewetting ability makes the peatland more sensitive to sudden changes in the water cycle.

5. REFERENCES

[1] RYDIN, H. et al., "Peatlands around the world", The Biology of Peatlands, Oxford University Press (2006) 216–238.

[2] YU, Z. et al., Global peatland dynamics since the Last Glacial Maximum, Geophysical Research Letters **37** *13* (2010) 1–5.

[3] TARNOCAI, C. et al., Soil organic carbon pools in the northern circumpolar permafrost region, Global Biogeochemical Cycles **23** *2* (2009).

[4] HIRANO, T. et al., Carbon dioxide emissions through oxidative peat decomposition on a burnt tropical peatland, Global Change Biology **20** *2* (2014) 555–565.

[5] HOOIJER, A. et al., Current and future CO 2 emissions from drained peatlands in Southeast Asia, Biogeosciences **7** *5* (2010) 1505–1514.

[6] LAINE, A.M. et al., Warming impacts on boreal fen CO 2 exchange under wet and dry conditions, Global Change Biology **25** *6* (2019) 1995–2008.

[7] SCHAUMANN, G.E. et al., Do water molecules bridge soil organic matter molecule segments?, European Journal of Soil Science **59** *3* (2008) 423–429.

[8] SCHAUMANN, G.E. et al., Combined proton NMR wideline and NMR relaxometry to study SOM-water interactions of cation-treated soils, Journal of Hydrology and Hydromechanics **61** *1* (2013) 50–63.

[9] ROBICHAUD, A. et al., Development of a raised bog over 9000 years in Atlantic Canada, Mires and Peat **5** *04* (2009) 1–19.

[10] DEKKER, L.. et al., Wetting patterns and moisture variability in water repellent Dutch soils, Journal of Hydrology **231**–**232** (2000) 148–164.

[11] KUČERÍK, J. et al., Formation of Water Molecule Bridges Governs Water Sorption Mechanisms in Soil Organic Matter, Langmuir **34** *40* (2018) 12174–12182.

[12] WESTERVELD, L., Distribution of Global Peatlands, Smoke on Water, http://www.grida.no/resources/12546.

[13] IZQUIERDO, N.L., Carbon and Peatland in Scotland, Smoke on Water, http://www.grida.no/resources/12544.

Analogy of iron-copper and iron-silver bimetals during the corrosion process

Relebohile Mokete, Osama Eljamal*
Department of Earth System Science and Technology (ESST), Interdisciplinary Graduate School of Engineering Sciences, Kyushu University, 6-1 Kasuga – Koen Kasuga, Fukuoka 816-8580, Japan
Corresponding author email: osama-eljamal@kyudai.jp

Abstract: *Because of their strong magnetic properties, the Fe based nanomaterials have successfully been used in order to remediate environmental contamination. The synthesis of the bimetallic nanoparticles was done following chemical reduction of ferric chloride with sodium borohydride then deposition of the respective bimetal. This study was conducted to determine the concentration influence on the dissolution of iron in the presence of the bimetallic nanoparticles along with determining the role of FeCu and FeAg bimetals during iron corrosion. The results showed that the higher the dosage, the higher the iron dissolution due to increased surface area hence reactivity. Also, the bimetals improved the reactivity of iron.*

Keywords: Nanoscale Zero Valent Iron (NZVI); Bimetal; Dissolution; Oxidation.

1. INTRODUCTION

The quality of air, soil and water has currently been depleted by human development activities such as industrialization which exposes contaminants to the environment [1]. Because of their strong magnetic properties, the Fe based nanomaterials have successfully been used in order to remediate environmental contamination [2]. Particularly, Nanoscale Zero-Valent Iron (NZVI) has proven to be the most effective and increasingly used nanomaterial due to adsorptiveness, high reactivity as a result of surface area exposure, eco-friendliness as well as cost-effectiveness [1, 3]. NZVI has a capability of contaminant removal through sorption, precipitation, complexation and surface reduction [4, 5, 6, 7]. However, the performance of NZVI has been limited by the nanoparticles' agglomeration influenced by high surface energy charges, as a result, metal-doped nanoparticles have successfully been used in order to solve this problem. The properties of metal-doped nanoparticles include enhanced reactivity owing to minimized oxidation and improved reduction due to physical properties' alteration [3, 8]. In terms of characterization, Scanning Electron Microscopy (SEM) is used to analyze the size and structure of the nanoparticles whereas the elemental composition and crystal structure are analyzed using the Transmission Electron Microscopy with Energy Dispersive X-ray (TEM-EDX) and X-ray diffraction (XRD) respectively [9]. The method of chemical reduction of ferric chloride using sodium borohydride was used to synthesize NZVI, FeCu and FeAg nanoparticles in this study and the effect of concentration on the nanoparticles' reactivity as well as the role of the bimetals during reactivity were studied.

2. MATERIALS AND METHODS

2.1 Materials

The NZVI nanoparticles were synthesized using Ferric chloride ($FeCl_3$), Sodium borohydride ($NaBH_4$) whereas the bimetals were correspondingly synthesized using silver nitrate and copper (II) chloride. FerroVer and Ferrous reagents were used for total iron and ferrous ions analysis respectively. Nitrogen gas (N_2) was purged in the Deionized (DI) water to maintain anoxic conditions and the pH was adjusted using 0.1M HCl, 5M NaOH.

2.2 Synthesis procedure

2.2.1 NZVI nanoparticles synthesis

Two solutions of 200ml and 100ml deoxygenated (10 minutes N_2 purging) DI water that was respectively mixed with 5g ferric chloride ($FeCl_3$) and 2.2g sodium borohydride (NaBH4) were prepared. Inside a 500ml round bottom flask with 4 holes which was immersed in a 30°C water bath, the sodium borohydride solution was added dropwise (pump speed 10 RPM – 16 ml/min) to the ferric chloride solution and the continuous N^2 purging as well as vigorous overhead stirring (400 RPM) conditions were maintained. The reaction was given 5 minutes aging time after which the synthesized nanoparticles were filtered, washed with 250ml deoxygenated DI water then vacuum dried for about 20 minutes. The reaction involved in the synthesis of NZVI is according to E1 [10]:

$$2Fe\ Cl_3{\cdot}6H_2O + 6NaBH_4 + 6H_2O \rightarrow 2Fe^0 + 21H_2 + 6B(OH)_3 + 6NaCl \quad \text{E1}$$

2.2.2 NZVI bimetallic nanoparticles synthesis

With respect to the aforementioned NZVI synthesis procedure, the respective FeCu and FeAg bimetallic nanoparticles were synthesized through the addition of 1% (wt/wt) $CuCl_2$, and $AgNO_3$ into reactor immediately after 5 minutes aging time and the reaction was allowed to further proceed for the following 30 minutes. The synthesized nanoparticles were therefore filtered, washed with 250ml deoxygenated DI water then vacuum dried for about 20 minutes and stored in a N_2 rich atmosphere to avoid oxidation. The main process involved in the formation of bimetallic nanoparticles is reduction then deposition and E2-E3 represent the overall equations involved [10, 11]:

$$Cu^{2+} + Fe^0 \rightarrow Cu^0 + Fe^{2+} \quad \text{E2}$$
$$Ag^{2+} + Fe^0 \rightarrow Ag^0 + Fe^{2+} \quad \text{E3}$$

2.3 Batch experiments

The 300ml Erlenmeyer flasks with three-hole, valve controlled stoppers were used as the batch experiments reactors. The activity of the bimetallic nanoparticles concentrations of 1g/L, 2g/L, 3g/L was studied. The initial conditions of the batch experiments were: pH 7, 200ml DI water, anoxic condition (10 minutes N_2 purging), 25ºC temperature and the system was kept closed throughout. The sampling time was during the first 3 hours where the first sample was taken within the first 10 minutes of the reaction whereas the rest of samples were taken within the at the 30 minutes' interval since the commencement of the experiment. After 3 hours, the samples were taken daily for a duration of 7 days.

2.4 Analysis

The 5ml samples were withdrawn by the 10ml syringe pump after which they were filtered by 0.45µm syringe filters. The total iron and ferrous iron content were analyzed using UV–visible spectrophotometer (DR 3900, Hach Co., USA). Before analysis, the samples were diluted and their pH was adjusted in accordance with the spectrophotometer requirements. FerroVer and ferrous ion reagents were used to analyze the total iron and ferrous ions respectively.

3. RESULTS AND DISCUSSION

3.1 Nanoparticles' concentration

The results of three concentration ranges (1g/L, 2g/L and 3g/L) are shown in Fig. 1. It can be noted from the results that the total iron concentration was recorded during the first 3 hours at 30 minutes' interval with the exception of the first sample that was take within the 10 minutes' period of the reaction then the rest of the results were recorded for the overall period of 7 days (168 hours) at the 1 day (24 hours) interval. Fig. 1a shows the results of FeCu bimetal where the 3g/L dosage resulted in the highest iron concentration with the maximum concentration of 32.08mg/L during the first 10 minutes of the reaction followed by the rapid decrease up to an equilibrium state at around 1 hour. The total iron concentrations of 2g/L and 1g/L followed a similar trend to that 3g/L with respective maximum values of 8.05g/L and 7.67g/L during 10 minutes' interval. After 24 hours, all the total iron concentrations increased to 6.74mg/L, 12.46mg/L and 9.04mg/L in respective dosages of 1g/L, 2g/L, 3g/L, however, the concentration of 2g/L surpassed that of 3g/L after 24 hours due to rapid precipitation and aggregation of nanoparticles. Regarding FeAg nanoparticles (Fig. 1b), the maximum total iron concentration was still attained at 10 minutes' period in all the dosages of 3g/L, 2g/L and 3g/L respectively after which equilibrium were reached around 1 hour. Similarly, the concentrations in all the dosages increased at 24 hours' period before the second equilibrium state was attained.

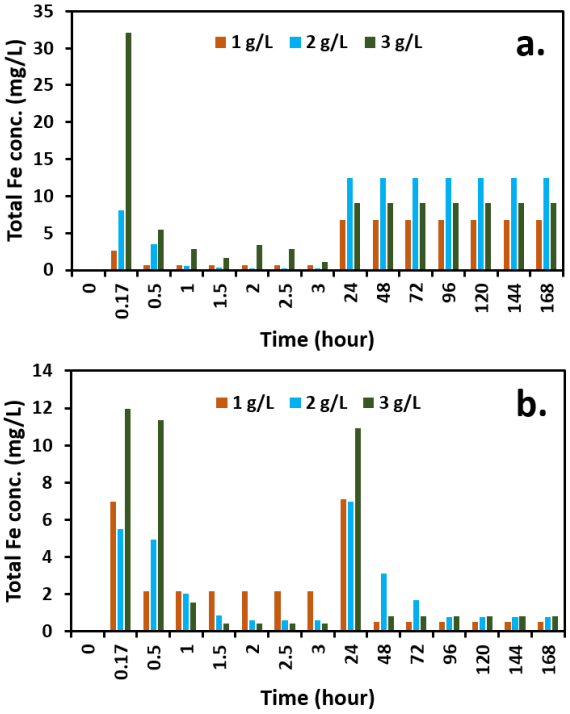

Fig. 1: FeCu (a) and FeAg (b) dosage for 168 hours (7 days) [Conditions: dosage = (1, 2, 3) g/L, anoxic condition, temperature = 25ºC, pH = 7]

The NZVI alone during the period of 3 hours (Fig. 2) also showed a similar trend where the concentration of 3g/L attained the greatest dissolution of iron followed respectively by 2g/L and 1g/L. In overall, it can be noted from all the nanoparticles' results that the highest concentration of total iron was generally attained in the 3g/L dosage because of the increased number on nanoparticles that avail the surface area hence the active sites for reaction thus increasing the iron concentration [12]. The governing equations involved during the dissolution of iron are E4-E7 whereas those attributed to precipitation process are with respect to E8-E9 [5, 10, 13].

$$Fe^0 \rightarrow Fe^{2+} + 2e^- \quad \text{E4}$$

$$Fe^0 + 2H_2O \rightarrow Fe^{2+} + H_2 + 2HO^- \quad \text{E5}$$

$$Fe^0 + 2Fe^{3+} \rightarrow 3\,Fe^{2+} \quad \text{E6}$$

$$2Fe^{2+} + 2H_2O \rightarrow 2Fe^{3+} + H_2 + 2OH^- \quad \text{E7}$$

$$Fe^{3+} + 3H_2O \rightarrow Fe(HO)_{3(s)} + 3H^+ \quad \text{E8}$$

$$Fe^{2+} + 2OH^- \rightarrow Fe(OH)_{2(s)} \quad \text{E9}$$

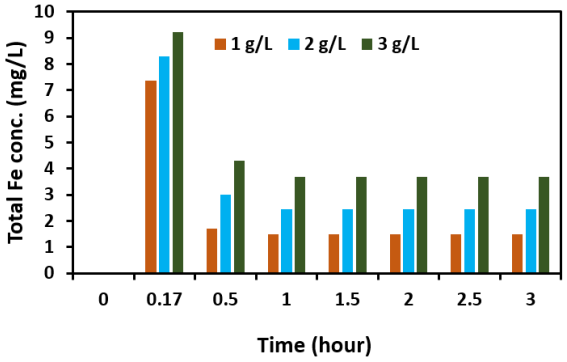

Fig. 2: NZVI dosage for 168 hours (7 days) [Conditions: dosage = (1, 2, 3) g/L, anoxic condition, temperature = 25ºC, pH = 7]

3.2 The role of bimetals

Although all the results revealed that the respective trend of iron dissolution from highest to lowest under similar conditions was according to 3g/L, 2g/L and 1g/L for all the nanoparticles, it is evident that the highest dissolution was attained by the bimetallic nanoparticles (Fig. 1a and b) whereas the least was attained by NZVI alone (Fig. 2). Therefore, taking 3g/L for instance, the highest total iron concentrations of 9.22mg/L, 11.98mg/L and 32.08mg/L were correspondingly accomplished by NZVI, FeAg and FeCu particularly within the first 10 minutes of the reaction. Thus it is clear that the dissolution of iron was increased in the presence of the bimetallic nanoparticles where FeCu showed the best performance. According to the corresponding explanation, the bimetallic nanoparticles play a role in increasing the surface area thus reactivity as well as immobilizing the nanoparticles through the creation of a discontinuous layer that disconnects the nanoparticles [14]. As a result, the bimetallic nanoparticles act as reaction catalysts that increase the reduction process [3, 8].

4. CONCLUSIONS AND RECOMMENDATIONS

The higher the dosage of the bimetallic nanoparticles, the higher the iron dissolution. Furthermore, bimetallic nanoparticles increase the reaction process due to their catalytic nature. In comparison, FeCu bimetallic nanoparticles attained the highest iron dissolution as opposed to FeAg bimetallic nanoparticles and NZVI. Generally, the reactivity is improved in the presence of the bimetals. It must be noted however that although the highest dosage of the nanoparticles leads to increase reactivity, too much of it in the real-life application might result in environmental toxicity hence its application must be with respect to the water standard limits.

5. REFERENCES

[1] A. Singh, S. Ahmad, A. Ahmad, Green Extraction Methods and Environmental Applications of Carotenoids - a review, RSC Adv. 5 (2015) 62358–62393.

[2] A. V. B. Reddy, Z. Yusop, J. Jaafar, Y. V. M. Reddy, A. B. Aris, Z. Abdul Majid, J. Talib, G. Madhavi, Recent progress on Fe-based nanoparticles: Synthesis, properties, characterization and environmental applications, Journal of Environmental Chemical Engineering 4 (2016) 3537–3553.

[3] F. Zhu, L. Li, S. Ma, Z. Shang. Effect factors, kinetics and thermodynamics of remediation in the chromium contaminated soils by nanoscale zero valent Fe/Cu bimetallic particles. Chemical Engineering Journal, 302 (2016) 663-669.

[4] Z. Wen, Y. Zhang, C. Dai. Removal of phosphate from aqueous solution using nanoscale Zerovalent iron (nZVI). Colloids and Surfaces A: Physicochem. Eng. Aspects, 457 (2014) 433–440.

[5] T. Harada, T. Yatagai, and Y. Kawase, Hydroxyl Radical Generation Linked with Iron Dissolution and Dissolved Oxygen Consumption in Zero-Valent Wastewater Treatment Process, Chemical Engineering Journal 303 (2016) 611 – 620.

[6] Y. Zhang, Y. Jing, J. Zhang, L. Su, X. Quan. Performance of a ZVI-UASB reactor for azo dye wastewater treatment. Journal of Chemical Technology and biotechnology, 86 (2011) 199-204.

[7] Y. Zhang, W. Chen, C. Dai, C. Zhou, X. Zhou, Structural Evolution of Nanoscale Zero-Valent Iron (nZVI) in anoxic Co2+ solution: Interactional performance and mechanism, Sci. Rep. 5 (2015) 13966.

[8] K. Sridharan, T. Endo, S.Cho, J. Kim, T. Joo Park, R. Philip. Single step synthesis and optical limiting properties of Ni–Ag and Fe–Ag bimetallic nanoparticles. Optical Materials, 35 (2013) 860-867.

[9] Y. Li, X. Li, D. Han, W. Huang, C. Yang. New insights into the role of Ni loading on the surface structure and the reactivity of nZVI toward tetrabromo- and tetrachlorobisphenol A. Chemical Engineering Journal, 311 (2017) 173–182.

[10] R. Mokete, K. Chen, O. Eljamal, N. Matsunaga. Inspection of Iron-Copper Bimetal Performance in Chemically Altered Atmosphere. Proceedings of International Exchange and Innovation Conference on Engineering & Sciences (IEICES). 4, pp.66-69, 2018-10-18. Interdisciplinary Graduate School of Engineering Sciences, Kyushu University.

[11] H. Wang, W. Huang, P. Peng, D. E. Fennell. Rapid dechlorination of 1,2,3,4-TCDD by Ag/Fe bimetallic particles. Chemical Eng. Journal 2015 (273) 465-471.

[12] Y. Yu, Z. Huang, D. Deng, Y. Ju, L. Ren, M. Xiang, L. Li, H. Li. Synthesis of millimeter-scale sponge Fe/Cu bimetallic particles removing TBBPA and insights of degradation mechanism. Chemical Engineering Journal, 325 (2017) 279-288.

[13] R. Mokete, H. Yifan, O. Eljamal, N. Matsunaga, Investigations of Nanoscale Zero Valent Iron interactions in aqueous solution, Proceedings of International Exchange and Innovation Conference on Engineering & Sciences (IEICES). 3, pp.149-152, 2017-10-19.

[14] Y. Wu, Q. Yue, Y. Gao, Z. Ren, B. Gao. Performance of bimetallic nanoscale zero-valent iron particles for removal of oxytetracycline. Journal of Environmental Sciences, 69 (2018) 173-182.

Thermodynamic Effect on Boron Removal from Aqueous Solutions by MgAl-Layered Double Hydrotalcite

Sami Alkhudhayri, Osama Eljamal*, Ibrahim Maamoun, Ramadan Eljamal
Earth System Science and Technology, Interdisciplinary Graduate School of Engineering Sciences, Kyushu University, 6-1 Kasuga-Koen Kasuga, Fukuoka, 816-8580, Japan
*osama-eljamal@kyudai.jp

Abstract: *Boron is an element of requirement for the growth of plants, animals and humans. Though environmental issues and health hazards are related to its applications in various industries; such as plants' growth retardation and the effect on humans' nerve system. In this research adsorption capabilities of Mg-Al Layered Double Hydrotalcite (LDH) on boron were tested to remove it from aqueous solutions. Experiments were conducted with variety of temperatures, and initial boron concentration; thus finding the most optimum factors and conditions. Results showed that with high temperatures faster removing rate of the contaminant from aqueous solutions was achieved. Moreover, thermodynamic analysis depicted that the adsorption process of boron on Mg-Al LDH is endothermic and involves both physisorption and chemisorption.*

Keywords: Boron; Mg-Al; Layered-Double-Hydrotalcite; Adsorption.

1. INTRODUCTION

Being used in many industries, boron is in demand for the production of various fertilizers, insecticides, corrosion inhibitors in anti-freeze formulations for motor vehicles and other cooling systems, buffers in pharmaceutical and dyestuff production, bleaching solutions in paper industries and in detergents. As well as glass, ceramics, electronics and detergents [1, 2]. Although boron is an element needed for plants but only in controlled amounts, otherwise it could result in growth retardation [3]; which was observed in arid and semi-arid areas in South Australia, Turkey [4]. Humans' nerve system is also affected by consumption of large amounts of boron. Regulations have recently been set by the World Health Organization (W.H.O.) to determine the maximum concentration limits for boron in drinking water to be less than 2.4 mg/L [5]. Many methods were tested for the removal of boron [6] and one of the common practices is adsorption process using hydrotalcite or hydrotalcite-like materials; in this paper Mg-Al LDH adsorption properties are investigated with boron. A range of different temperatures is applied to investigate the thermal effect on the removal process. Furthermore, thermodynamics analysis is conducted to study the nature of the adsorption process of the Mg-AL LDH.

2. MATERIALS AND METHODS:

2.1 Preparation of Mg-Al bimetallic:

The hydrotalcite-like material was synthesized for Mg-Al bimetallic Oxide. The materials used for the synthesis are $Mg(NO_3)_2{\cdot}6H_2O$, $Al(NO_3)_3{\cdot}9H_2O$, NaOH [7, 8]. Synthesis was carried out in the duration of three days [9]; 700 mL aqueous solution containing 0.1 mmol (25.6406 g) of $Mg(NO_3)_2{\cdot}6H_2O$ and 0.05 mmol (18.7565 g) of $Al(NO_3)_3{\cdot}9H_2O$. Then, it was added drop wise to 1500 mL of 2 M NaOH solution stirred vigorously with a mechanical mixer at 400 rpm. The temperature was kept at 45± 3 ℃ during the process. Slurry obtained was then heated for 2 hours (T=85± 3 ℃) under slow mixing 200 rpm. The solution was kept in room temperature for 12 h. Next day; The solid product was separated by centrifugation and washed with deionized water several times until pH reached 10-11 and conductivity was constant. The solids were drying at 60℃ for 48. Part of the product was calcined at 550℃ for 4 h. The solids were dry enough to be crushed into powder-like form and measured. Then it was kept in a concealed container.

2.2 Batch preparation:

Boron stock solution was prepared using H_3BO_3, 500mg/L. For every experiment 100 mL of solutions were used with boron concentration of 5, 10, 20 mg/L, Initial pH at 9 and Mg-Al LDH dosage of 2 g/L was found to be the optimum pH condition for boron removal according to our previous study [9]. The separation of samples is conducted with syringe filters 2 µm. UV-vis spectrophotometer was used for boron concentration measurement in samples; BoroVer 3 Boron Reagent Powder Pillow, Sulfuric Acid, concentrated, ACS and Deionized water were used.

2.3 Removal effect:

In this test a dosage of 2g/L of Mg-Al LDH were used on boron contaminated stocks with initial concentrations of (5, 10, 20) mg/L; to study the removal efficiency of Mg-Al LDH on boron. Removal efficiency was calculated using the following formula [10-12]:

$$Removal\ efficiency\ (\%) = \frac{C_o - C_e}{C_o} \times 100 \qquad (1)$$

Where; C_o and C_e are initial and equilibrium boron concentrations respectively.

2.4 Temperature effect:

Temperature experiment was conducted to study the effects of different temperatures (T= 25, 40, 55, 70 ℃) in the removal of boron with initial concentration of 20 mg/L. Mg-Al LDH were added to the flasks with boron solution. Stirring with 25 ℃ for 24 hours. Samples were taken in (10min, 3hrs, 6hrs, 12hrs, 18hrs, 24hrs).

3. RESULTS AND DISCUSSION:

3.1 Removal efficiency:

Although the dosage remained similar in all the batches (2g/L) successful removal of boron was achieved with all. The higher the initial concentration was the longer it took for Mg-Al LDH to adsorb the contaminant Fig. 1. Where the 5 and 10 mg/L of initial B concentration reached maximum at less than 10 hours the 20mg/L sample took over 24 to reach maximum.

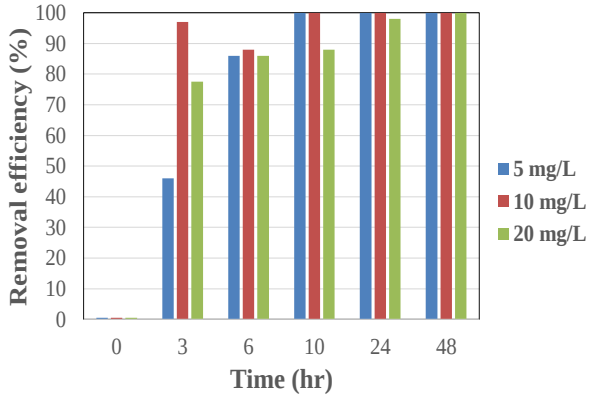

Fig. 1 removal efficiency with different initial boron conc. samples over time.

3.2 Temperature effect:

This test showed the removal rate of the Mg-Al LDH is effected with temperature. The higher the temperature got the faster the removal of the contaminant; as shown in the Fig. 2 at temperature 70 ℃ removal rate reached equilibrium at about 6 hours whereas the other temperatures have not reached the maximum rate even at 24 hours.

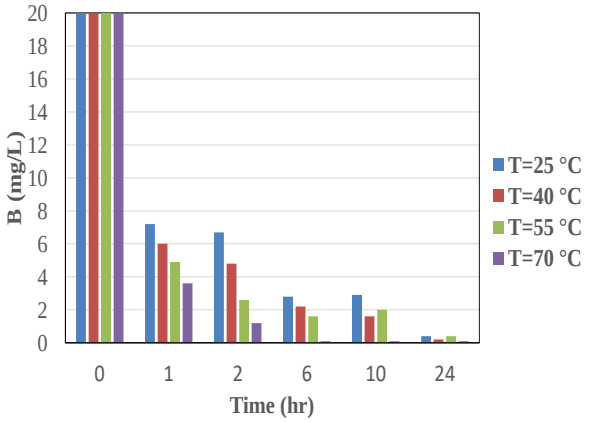

Fig. 2 effect of different temperatures on boron adsorption process.

3.3 Thermodynamic analysis:

Thermodynamic analysis was conducted on the adsorption data using the following equations:

$$\Delta G° = -RT\ ln\ K \qquad (2)$$

$$lnK = -\frac{\Delta H°}{RT} + \frac{\Delta S°}{R} \qquad (3)$$

Whereas R is the Universal Gas constant (8.314 J/mol K), K is Adsorption equilibrium constant, $\Delta G°$ is change in Gibbs free energy (KJ/mol), T is temperature (Kalvin), $\Delta S°$ is change in entropy (J/mol K) and $\Delta H°$ is change in enthalpy (KJ/mol).

The values of these thermodynamics parameters were evaluated by plotting lnK vs 1/T, and knowing the slope and the interception values.

Temp.°C	ΔG (KJ/mol)	ΔH (KJ/mol)	ΔS (J/mol K)
25	-26.77019421	104.0469778	432.0369254
40	-29.94807013		
55	-33.28740924		
70	-47.96147746		

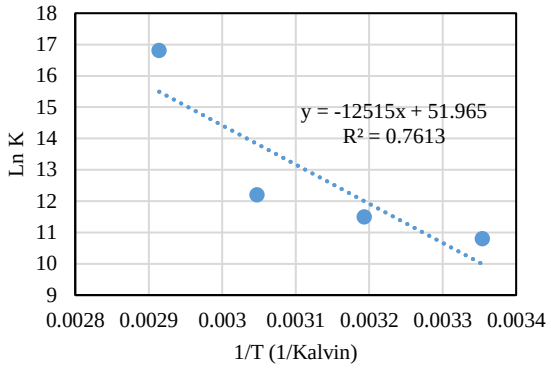

Fig. 3 Linear plot of thermodynamic analysis.

The negative value of $\Delta G°$ indicates the endothermic nature of the removal of boron by MgAl-LDH indicating the enhancement in boron removal by raising the operating temperature. Moreover, the positive value of entropy change indicates that the randomness of the solid/liquid interaction increases within the adsorption process of Boron. The magnitude of enthalpy change (104.04 KJ/mol) and The magnitudes of the change of the free energy indicate that boron removal by MgAl-LDH involves both physisorption and chemisorption processes.

4. CONCLUSION:

Mg-Al LDH showed promising results in removing boron contamination from aqueous solutions. Temperature has high effectivity on the removal rate; at 70 ℃ equilibrium was achieved at about six hours of mixing with a nearly full removal of the 20 mg/L boron concentration, whereas it took longer time to reach equilibrium with the other temperatures. Even with high initial boron concentration (20 mg/L), Mg-Al LDH had removed almost 99.9 % of the contaminant. Thermodynamic analysis showed that the adsorption mechanism of boron by Mg-Al LDH was endothermic in nature and involves both of physisorption and chemisorption.

5 REFERENCES

[1] Grigori Z., Raphael S., 2013, Boron removal from water and its recovery using iron (Fe^{3+}) oxide/hydroxide-based nanoparticles (NanoFe) and NanoFe-impregnated granular activated carbon as adsorbent. Desalination, pp. 107-117 (333).

[2] Ahmet Nedim Ay, Birgül Zümreoglu-Karan, Abidin Temel, 2007, Boron removal by hydrotalcite-like, carbonate-free Mg–Al–NO_3-LDH and a rationale on the mechanism, Microporous and Mesoporous Materials, 98(1-3):1-5.

[3] Wang, B., Guo, X., Bai, P., 2014. Removal technology of boron dissolved in aqueous solutions A review. Colloids Surf. A (444) 338-344.

[4] F.S. Kot, 2009, Boron sources, speciation and its potential impact on health Rev. Environ. Sci. Biotechnol., 8, pp. 3-28.
[5] Boron in drinking-water, Background document for development of WHO Press, World Health Organization, 20 Avenue Appia, 1211 Geneva 27, Switzerland (2009).
[6] Zhimin G., Jiafei L., Peng B., Xianghai G., 2015. Boron removal from aqueous solutions by adsorption — A review. Desalination, pp. 29-37 (383).
[7] Ulibarri M.A., Pavlovic I., Barriga C., Hermosin M.C., Cornejo J., 2001 Adsorption of anionic species on hydrotalcite-like compounds: effect of interlayer anion and crystallinity Appl Clay Sci., 18, pp. 17-27.
[8] S. Moriyama, K. Sasaki, T. Hirajima, 2014 Effect of calcination temperature on Mg–Al bimetallic oxides as sorbents for the removal of F^- in aqueous solutions Chemosphere, pp. 597-603 (95).
[9] Alkhudhayri, S., Eljamal, O., Eljamal, R., 2018, Removal of boron from aqueous solutions using MgAl composition. Proceedings of International Exchange and Innovation Conference on Engineering & Sciences (IEICES), pp. 45-55 (4).
[10] Maamoun, I., Eljamal, O., Matsunaga, N., 2018, Enhancement of Nanoscale Zero-Valent Iron Stability in Aqueous Solution Via Metal Hydroxide Coating. Proceedings of International Exchange and Innovation Conference on Engineering & Sciences (IEICES), pp. 82-83 (4).
[11] Maamoun, I., Eljamal, O., Khalil, A., Sugihara, Y., Matsunaga, N., 2018, Phosphate Removal Through Nano-Zero-Valent Iron Permeable Reactive Barrier; Column Experiment and Reactive Solute Transport Modeling. Transport in Porous Media, pp. 395–412 (125).
[12] Eljamal, R., Eljamal, O., Khalil, A., Saha, B. B., Matsunaga, N., 2018, Improvement of the Chemical Synthesis Efficiency of Nano-scale Zero-valent Iron Particles. Journal of Environmental Chemical Engineering, pp. 4727–4735; 6(4).

Effect of Bimetallic Zero Valent Iron Nanoparticles Ag/NZVI on Bacterial Growth

Khaoula Bensaida, Osama Eljamal*, Ramadan Eljamal, Relebohile Mokete, Yuji Sugihara
* Department of Earth System Science and Technology, Interdisciplinary Graduate School of Engineering Sciences, Kyushu University, Fukuoka, Japan
*Corresponding author email: osama-eljamal@kyudai.jp

Abstract: *In this study, a 13-day operation was conducted in order to investigate the effect of Ag-Fe nanoparticles on bacterial growth. To do so, three samples (S1, S2, S3) made of freshly domestic wastewater were treated under anaerobic conditions. S1 was considered as the control batch while 50mg/L of zero valent iron nanoparticles (NZVI) and Ag-Fe bimetallic nanoparticles were added to S2 and S3, respectively. Results showed that the addition of NZVI was effective in activating the bacterial growth. However, Ag-Fe nanoparticles inhibited the bacterial growth. A comparison of the chemical oxygen demand COD of the three samples confirmed the obtained results.*

Keywords: Ag-Fe nanoparticles; zero valent iron; bacterial growth; COD.

1. INTRODUCTION

Recently, population growth and modernization have extensively raised the global demand for clean energy and water [1,2]. Around the world, 1.3 billion people lack access to electricity and 783 million people lacking access to clean water [3]. The electrical energy generation through Microbial Fuel Cells (MFCs) using microorganisms is a renewable and sustainable approach. It creates truly an efficient technology for power production and wastewater treatment. The most important part of MFC is the microbes.

Using Nano zero-valent Iron NZVI technique was successfully applied in degrading the chemical pollutants and cleaning wastewater. However, the use of NZVI for enhancing the bacterial growth is still not confirmed yet.

The reactivity of NZVI can be substantially improved by impregnating with a second metal, typically Ni, Ag, or Cu to form so-called bimetallic nanoparticles [4].

A considerable number of investigations have evaluated the effect of NZVI on bacterial growth. In [5], results showed a negative impact of NZVI on Bacillus cereus growth capability, consistent with the entrance of cells in an early sporulation stage, observed by TEM. In [6], the impact exerted by NZVI nanoparticles on bacteria population highlights that toxicity should be dose and species dependent. The objective of this research is to investigate the feasibility of using bi-metallic iron nanoparticles NIZVI/Ag to wastewater to promote the bacterial growth.

2. MATERIALS & METHODOLOGY

2.1 Preparation of NZVI and Ag/NZVI nanomaterials

Zero valent iron nanoparticles were prepared by the chemical reduction of 0.093 M ferric chloride hexahydrate ($FeCl_3.6H_2O$, 99.0%, Junsei Chemical Co., Japan) by 0.58 M sodium borohydride ($NaBH_4$, 98.0%, Sigma–Aldrich Inc., USA) within anaerobic conditions provided by continues nitrogen purging [7,8]. NZVI precipitates were formed by the 400 RPM vigorous mixing during the whole synthesis time at 30 ± 0.5 °C. Vacuum filtration was used for the particles separating after washing with deionized water (DIW). The Ag/NZVI bimetallic particles used in this study were prepared by adding silver nitrate $AgNO_3$ to the FeCl3·6H2O solution (5% Ag) before dropping the reducing reagent of $NaBH_4$.

2.2 Wastewater source

The wastewater samples used in this study were obtained from Mikasagawa domestic wastewater purification center located in the city of Fukuoka, Japan. The wastewater was saved under 4^0C in order to inhibit the bacterial all along the period of experiments.

2.3 Batch experiments

Batch experiments were conducted using three bottles S1, S2, and S3 filled with 100 mL of wastewater. The samples were saved at 37 °C under anaerobic conditions for 13 days. S1 was the control batch without any additives. NZVI and NZVI/Ag nanoparticles were added to S2 and S3 respectively, with a concentration of 50mg/L.

2.4 Measuring Microbial growth

Plate count method was adopted for bacterial growth counting. To do so, 0.5 ml of the saved sample is diluted five times. Then, 1 ml of each dilution is placed in the center of a petri dish. 15 ml of melted agar was poured and well mixed. The plate was saved for 24 hours at 37 °C. Each growth colony is carefully counted and represented a colony forming unit CFU.

3. RESULTS & DISCUSSION

3.1 Effect of NZVI and Ag/NZVI on Bacterial growth

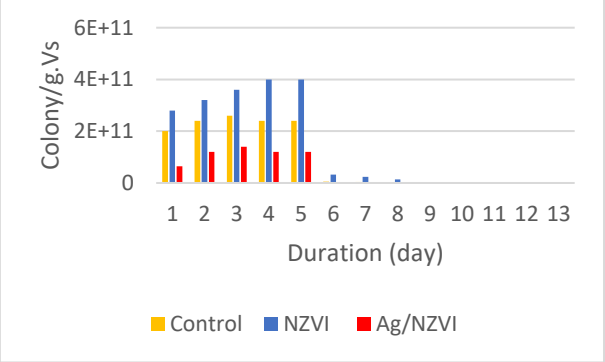

Fig. 1. Effect of NZVI and Ag/NZVI particles on bacterial growth.

For a 13-day operation, cell colonies were counted, and the number of cells were plotted over time as it is presented in figure1.

Results show that adding iron nanoparticles to the medium had a positive effect on bacterial growth. The maximum number of cells was 3.6 E+11colonies /g.Vs for the S2 while 2.6 E+11colonies /g.Vs for S1.

Therefore, using NZVI particles activates the bacterial growth, thus the digestion of organic matter is enhanced. However, Ag/NZVI had a toxic effect as it inhibited the growth of bacterial colonies. The maximum number of cells was just 1.4 E+11 colonies /g.Vs.

3.2 Impact of NZVI and Ag/NZVI particles on COD

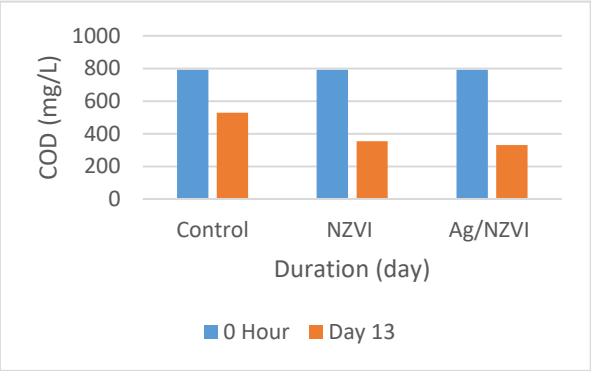

Fig. 2. Impact of NZVI and Ag/NZVI particles on COD.

The chemical oxygen demand was calculated in order to check the effect of adding nanoparticles on the bacterial activation thus, on the organic matter degradation.

At 0 hour, the COD concentration was 792 mg/l. After 13 days of operation, the COD of the three samples S1, S2 and S3 were 529, 354, 331 mg/L, respectively. Therefore, using NZVI particles enabled the bacterial growth and activation during the period of experiments. However, bacterial communities could be active only since the COD decreased (during the operating days), but their growth was limited as it was presented in figure1.

4. CONCLUSIONS

In this study, the microbial growth was subjected to the treatments of NZVI particles and Ag/NZVI bimetallic nanoparticles with concentration of 50 mg/L for 13 days. When treated directly with NZVI particles under anaerobic condition, bacterial growth capability was improved. However, no growth was observed for bacterial communities when they were treated with Ag/NZVI.

5. REFERENCES

[1] Call TP, Carey T, Bombelli P, Lea-Smith DJ, Hopper P, Howe CJ, Torrisi F, Platinium-free, graphene based anodes and air cathodes for single chamber microbial fuel cells. J mater Chem, 2017;523:872-86.

[2] Y. Zhang, L. Liu, B. Bruggen, Nanocarbon based composite electrodes and their application in microbial fuel cells, J mater Chem,2017;512673-98.

[3] A. Devi Sekar, T. Jayabalan, H. Muthukumar, N. I. Chandrasekaran, S. N. Mohamed, M. Matheswaran, Enhancing power generation and treatment of dairy waste water in microbial fuel cell using Cu-doped iron oxide nanoparticles decorated anode, / Energy 172 (2019) 173-180.

[4] Y. Lv, Z. Niu, Y. Chen, Y. Hu, Bacterial effects and interfacial inactivation mechanism of NZVI/Pd on Pseudomonas putida strain, Water Research 115 (2017) 297-308.

[5] C. Fajardoa, M.L. Saccàa,b, M. Martinez-GomarizM. Martinez-Gomarizc, G. Costaa, M. Nandea, M. Martin, Transcriptional and proteomic stress responses of a soil bacteriumBacillus cereusto nanosized zero-valent iron (nZVI) particles, Chemosphere 93 (2013) 1077–1083.

[6] Fajardoa,⇑, L.T. Ortíza, M.L. Rodríguez-Membibrea, M. Nandea, M.C. Lobob, M. Martin, Assessing the impact of zero-valent iron (ZVI) nanotechnology on soil microbial structure and functionality: A molecular approach, Chemosphere 86 (2012) 802–808.

[7] R. Eljamal, O. Eljamal, A.M.E. Khalil, B.B. Saha, N. Matsunaga, Improvement of the chemical synthesis efficiency of nano-scale zero-valent iron particles, Journal of Environmental Chemical Engineering 6 (2018) 4727-4735.

[8] I. Maamoun, O. Eljamal, N. Matsunaga, Enhancement of Nanoscale Zero-Valent Iron Stability in Aqueous Solution Via Metal Hydroxide Coating, (2018).

Upgrading of Aerobic Sequencing Batch Reactor System with Adding Nanoscale Zero Valent Iron for Wastewater Treatment

Ramadan Eljamal[1], Osama Eljamal[1]*, Ian P. Thompson[2], Ibrahim Maamoun[1], Yuji Sugihara[1], Gulsum Yilmaz[3]
[1]Department of Earth System Science and Technology, Interdisciplinary Graduate School of Engineering Science, Kyushu University, Fukuoka, Japan
[2]Department of Engineering Science, University of Oxford, Parks Road, Oxford, OX1 3PJ, UK
[3]Department of Environmental Engineering, Faculty of Engineering, Istanbul University-Cerrahpasa, 34320 Avcilar, Istanbul, Turkey
*Corresponding author email: osama-eljamal@kyudai.jp

Abstract: *The aim of this study was to investigate the effect of nano-scale zero-valent iron (nZVI) on the performance of aerobic sequencing batch reactors (SBRs) in terms of COD, phosphate removal and microbial species growth. Two lab scale SBRs were operated simultaneously for sixty days with and without adding nZVI. The reactors were fed with synthetic wastewater and acclimated with seed sludge which was taken from a full-scale municipal wastewater treatment plant in Istanbul. As a result, next generation sequencing technology analysis confirmed that the addition of nZVI in R2 promoted some bacterial types such as Xanthomonadales and inhibited others such as Clostridiales, confirming that the effect of nZVI on the bacterial growth was genera dependent. In addition, the phosphate and COD were completely removed at the end of the study and slightly enhanced with 15 % after the addition of nZVI in R2.*

Keywords: wastewater treatment; nanoscale zero valent iron; Aerobic reactors; bacterial growth

1. INTRODUCTION

Wastewater is known as water that has been struck in quality by the generated pollutants from domestic use, agricultural and industrial activities [1]. Nutrient elements of nitrate and phosphorus are among the most found elements in wastewater [2]. Exceeding the concentration of nutrient elements in wastewater to more than the acceptable levels could adversely affect human health, environment, and agriculture sector [3]. Therefore, several efforts have been made to recover the quality of household wastewater by removing the undesired elements such as nitrate, phosphorus, ammonia and COD. Biological treatment is the most used method for the remediation of household wastewater either using aerobic or anaerobic strategies. Specifically, aerobic granular sludge (AGS) has been emerged and successfully applied for the contaminates removal from wastewater [4]. Comparing with the anaerobic treatment that can cause odor problems and the formation of secondary pollutants [5], aerobic granules brought the attention of researchers over the last 10 years, due to the increased microbial growth and the superior decomposition or settling ability [6]. Therefore, the objective of this study was to investigate the effect of nano-scale zero valent iron (nZVI) on the performance of the sequencing batch reactor system (SBR) in terms of nutrient and COD removal. In addition, detect the effect of nZVI on the bacterial growth species.

2. MATERIALS & METHODS

2.1 Experimental set-up and reactor operation

Tow sequencing batch reactor were operated in sequencing batch mode with a cycle time of 6 hours divided into four phases: 60 minutes of anaerobic static feeding of the synthetic wastewater from the bottom of the reactor; 283 minutes of aeration; 2 minutes of settling; and 15 minutes for discharging. Tow liters of the seed sludge were added in each reactor and the reactors were fed with the synthetic wastewater that had the following initial substrate; COD, 500 mg L^{-1}; NH_4-N, 40 mg L^{-1}; PO_4^{3}-P, 8 mg L^{-1}.

2.2 Analytical methods

Samples were analyzed using T60UV-Visble Spectrophotometer for chemical oxygen demand (COD), nitrate (NO^{3-} , nitrite (NO_2^-–N), orthophosphate (PO_4^{3-}–P). In addition, Next Generation Sequencing (NGS)–Based Metagenomics were carried out to determine microbial community at the end of this study.

3. RESULTS & DISCUSSION

3.1 COD removal

COD was monitored in the SBR1 and SBR2 over the whole study as shown in Fig. 1. The reactors had an excellent performance in terms of reducing the concentration of COD. However, after the addition of nZVI in the influent of the SBR2 with 10 mg/L on day 24th , the removal of COD measured in the effluent of SBR2 was much better than that COD concentration in the effluent of SBR1, confirming that nZVI had a positive effect on the removal of COD.

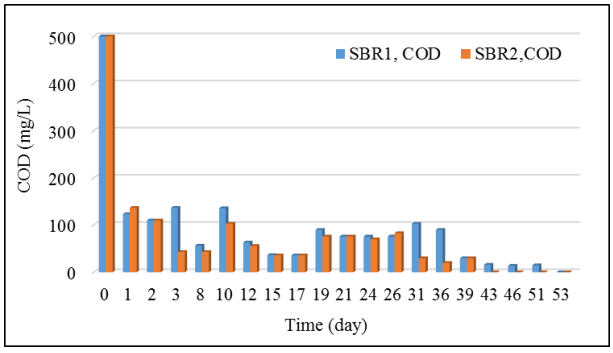

Fig. 1. Performance of the SBR1 and SBR2 in removing COD during the whole period of the study.

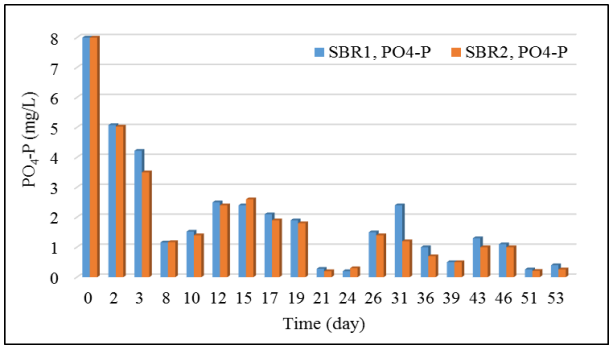

Fig. 2. Performance of the SBR1 and SBR2 in removing phosphate during the whole period of the study.

3.2 Phosphate removal

Phosphate removal was tracked in the effluent of the reactors over the entire study as shown in Fig.2. As a result, biological treatment with aerobic granulation system effectively removes phosphate from wastewater. As it observed in Fig. 2, phosphate removal progressively improved with time in the reactors. Almost a complete removal was seen the reactors at the end of the study. Phosphate removal was slightly better in the effluent of the SBR2. It was proved that the nZVI particles are one of the most efficient adsorbent materials for the removal of phosphate from water [7-10]. Additionally, nZVI particles promoted the growth of bacteria in the reactors which in turn improved their phosphate removal ability.

3.2 Bacterial growth

Bacterial growth species were estimated in the used seed sludge, SBR1and SBR2 at the end of the study. In total 38 order that commonly found in the wastewater plants [11, 12], six orders were found in the seed sludge and in the aerobic granules taken from the SBR1 and SBR2. These orders were presented in Table 2 including Rhizobiales (Rh), Clostridiales (Cl), Sphingobacteriales (Sp), Actinomycetales (Ac), Burkholderiales (Bu) and Xanthomonadales (Xa). These types of bacteria were found with different ration either in the used seed sludge or in the reactors. Next generation sequencing technology analysis showed that the growth of some bacterial species was increased in the reactors compared to the used seed sludge expect the growth of Clostridiales. The elevated microbial growth in the reactors ascribed to the trace elements in the wastewater that service as food for bacteria. However, it was noted that there is a difference in the bacterial growth in the reactors. Some orders were stimulated in the SBR2 that nZVI was added and some other were inhabited (refer to Table 1), confirming that the effect of nZVI on the bacterial growth was genera dependent.

Table: 1 Microbial population in seed sludge, R1 and R2 sludges at the end of the study.

Seed Sludge		**R1**		**R2**	
Order	**%**	**Order**	**%**	**Order**	**%**
Rh	14.7	*Rh*	23.9	*Rh*	25.1
Cl	11.1	*Cl*	6.2	*Cl*	3.6
Sp	8.1	*Sp*	1.2	*Sp*	1.2
Ac	7.6	*Ac*	8.8	*Ac*	7.5
Bu	5.3	*Bu*	5.1	*Bu*	4.9
Xa	4.9	*Xa*	12	*Xa*	13.5

4. CONCLUSIONS

This study investigated the efficiency and the visibility of the sequencing batch reactor system in the treatment of wastewater. In addition, this work investigated the effect of nZVI on the performance of the sequencing batch reactor in terms of COD and phosphate removal. we concluded that the reactors and aerobic granules had an excellent performance in removing of COD and phosphate where almost a complete removal of COD and phosphate was observed at the end of the study. The results of microbial community analysis proved that the effect of nZVI on the bacterial growth was genera dependent.

2. REFERENCES

[1] A.I. Al-Zarah, Assessment of Trace Elements in Wastewater Effluent in Al-Hassa Eastern Province of the Kingdom of Saudi Arabia, Research Journal of Environmental Sciences 8 (2014) 405-421.

[2] O. Eljamal, J. Okawauchi, K. Hiramatsu, Removal of phosphorus from water using marble dust as sorbent material, Journal of Environmental Protection 3 (2012) 709.

[3] I. Maamoun, O. Eljamal, A.M. Khalil, Y. Sugihara, N. Matsunaga, Phosphate removal through nano-zero-valent iron permeable reactive barrier; column experiment and reactive solute transport modeling, Transport in Porous Media 125 (2018) 395-412.

[4] J. Wagner, L. Guimarães, T. Akaboci, R. Costa, Aerobic granular sludge technology and nitrogen removal for domestic wastewater treatment, Water Science and Technology 71 (2015) 1040-1046.

[5] J. Beun, M. Van Loosdrecht, J. Heijnen, Aerobic granulation in a sequencing batch airlift reactor, Water Research 36 (2002) 702-712.

[6] Y. Liu, J.-H. Tay, State of the art of biogranulation technology for wastewater treatment, Biotechnology advances 22 (2004) 533-563.

[7] R. Eljamal, O. Eljamal, A.M. Khalil, B.B. Saha, N. Matsunaga, Improvement of the chemical synthesis efficiency of nano-scale zero-valent iron particles, Journal of environmental chemical engineering 6 (2018) 4727-4735.

[8] S. Takami, O. Eljamal, A.M. Khalil, R. Eljamal, N. Matsunaga, Development of continuous system based on nanoscale zero valent iron particles for phosphorus removal, Journal of JSCE 7 (2019) 30-42.

[9] O. Eljamal, A.M. Khalil, N. Matsunaga, Experimental and modeling column study of phosphorus removal by permeable reactive materials, Int J Environ Agric Res 3 (2017) 62-70.

[10] O. Eljamal, R. Mokete, N. Matsunaga, Y. Sugihara, Chemical pathways of nanoscale zero-valent iron (NZVI) during its transformation in aqueous solutions, Journal of environmental chemical engineering 6 (2018) 6207-6220.

[11] X. Ren, Y. Chen, L. Guo, Z. She, M. Gao, Y. Zhao, M. Shao, The influence of Fe2+, Fe3+ and magnet powder (Fe3O4) on aerobic granulation and their mechanisms, Ecotoxicology and environmental safety 164 (2018) 1-11.

[12] H.-L. Jiang, J.-H. Tay, Y. Liu, S.T.-L. Tay, Ca 2+ augmentation for enhancement of aerobically grown microbial granules in sludge blanket reactors, Biotechnology letters 25 (2003) 95-99.

Removal of Cesium from Contaminated Waters by Employing Iron-Based Nanoparticles and Nanocomposites

Falyouna O[1], Eljamal O[1], Maamoun I[1]
[1] Department of Earth System Science and Technology, Interdisciplinary Graduate School of Engineering Sciences, Kyushu University, 6-1 Kasuga-Koen Kasuga, Fukuoka 816-8580, Japan.
osama-eljamal@kyudai.jp (O. Eljamal).

Abstract: *Radioactive cesium $^{137}C^{+}$ is one of the most dangerous radionuclides that exists in radioactive wastewater. Fast, low-cost, efficient and environmentally friendly adsorbents are in need to remove $^{137}C^{+}$ from the affected waters in order to protect the environment from the adverse effects of $^{137}C^{+}$. Based on two well-known remedial adsorbents namely, nanoscale zerovalent iron (NZVI) and zeolite, nine nanoparticle and nanocomposites were synthesized and tested toward the removal of cesium from contaminated waters. The performance of nanoparticles (NZVI, Cu/Fe, Ni/Fe and Ag/Fe) was disappointing because their removal efficiencies could not exceed 10%. On the other hand, zeolite and its magnetic nanocomposites Ze/Fe, Ze/Fe-Cu, Ze/Fe-Ni and Ze/Fe-Ag were effectively able to recover the cesium from contaminated water by 99.92%, 61.25%, 53.95%, 37.68% and 53.92%, respectively.*

Keywords: Radioactive cesium; Nanoscale zerovalent iron; Zeolite; Ionic exchange; Adsorption

1. Introduction

A wide range of industries, in particular, nuclear power industry, generate huge amounts of radioactive waste due to the utilization of radionuclides in their processes[1]. This kind of waste is very dangerous and should be carefully handled as it contains radioelements that persist in the environment for a long time and adversely severely affect the environment as well as the living organisms[2]. Due to its extended half-life (30.2 years), high emissions of gamma (γ) rays and beta (β) particles, high solubility and mobility in the environment as well as susceptibility of causing lethal diseases such as cancer, radioactive cesium $^{137}Cs^{+}$ is nominated to be the most hazardous radionuclide existed in radioactive wastes[3]. Therefore, a broad spectrum of techniques has been developed previously and recently in order to effectively recover the radioactive cesium $^{137}Cs^{+}$ from contaminated waters. Ionic exchange and adsorption by nanoparticles and nanocomposites are getting the attention of the researchers for radioactive decontamination because they are simple, fast, cost-effective and efficient[4]. Nanoscale zerovalent Iron (NZVI) and zeolite (Ze) as excellent remedial materials are widely applied to remove different contaminants from contaminated waters, such as nitrate, phosphorous, heavy metals and radionuclides[5]. Therefore, in this study, nine different nano-adsorbents based on NZVI and Ze were synthesized in laboratory in order to investigate their performance in removing cesium from contaminated waters.

2. Materials and Methods

2.1 Materials

Ferric chloride hexahydrate (JUNSEI, 99.0%), sodium borohydride (Sigma Aldrich, ≥ 98%), copper(II) chloride (Sigma Aldrich, 99.9%), nickel(II) chloride hexahydrate (Wako, 99.9%), silver nitrate (JUNSEI, 99.8%) and zeolite (Sigma Aldrich) were used to prepared the iron-based nanoparticles (NP) and nanocomposites (NC). Cesium chloride (Wako, 99.9%) was used to prepare cesium stock solutions. Deoxygenated deionized water (Purging time: 15 mins) was used in all experiments of this study. Furthermore, all chemicals were analytical of grade and used without any prior treatment.

2.2 Synthesis of iron-based nanoparticles and nanocomposites

Nanoscale zerovalent iron (NZVI) was prepared in laboratory by chemical reduction method and based on the optimization conditions of previous research[6]. Bimetallic copper-nanoscale zerovalent iron (Cu/Fe^{0}), bimetallic nickel-nanoscale zerovalent iron (Ni/Fe^{0}) and bimetallic silver-nanoscale zerovalent iron (Ag/Fe^{0}) were prepared following the same previous method, but with the addition of specific amounts of noble metals (Doping ratio = 5%) before the beginning of the reduction process. Zeolite powder was purchased from Sigma Aldrich and used directly in the batch experiments. On the other hand, four iron-zeolite based nanocomposites namely, Ze/Fe^{0}, $Ze/Cu\text{-}Fe^{0}$, $Ze/Ni\text{-}Fe^{0}$ and $Ze/Ag\text{-}Fe^{0}$ were prepared following the previously reported procedures[7].

2.3 Design of batch experiments

Several batch experiments were conducted in order to investigate and define the best adsorbent to remove cesium from contaminated waters. The adsorption experiment was conducted in 300 mL conical flask by adding 200 mL of deoxygenated cesium stock solution with initial concentration of 1 mg/L and 1 g of adsorbent (Adsorbent dosage = 5g/L). The initial pH of the solution wasn't controlled and remained between 5.5 to 6. However, the adsorption temperature was controlled to be 25 °C during the adsorption process. The solution was magnetically stirred (Stirring speed = 1000 rpm) for 120 minutes. 4 samples with a volume of 0.5 mL were taken at different specific time intervals (10 min, 30 min, 60 min and 120 min) and filtered by 0.2 µm disposable membrane filter. Inductively coupled plasma mass spectrometry (ICPM-8500, Shimadzu Co.) was used to determine the residual concentration of cesium after the adsorption. The samples were diluted by deionized water (Dilution Factor= 40) prior the analysis of ICP-MS. All

experiments were conducted in duplicate and the average value was presented in the results.

The removal efficiency of each adsorbent after the interaction with the adsorbate for 120 minutes was calculated using the following equation:

$$Removal\ Efficiency\ (\%) = \frac{C_0 - C_t}{C_0} \times 100\% \quad (1)$$

where C_0 (mg/L) is the initial concentration of cesium and C_t (mg/L) is the concentration of cesium at a given time t.

3. Results and Discussion

3.1 Performance of nanoparticles

Figure (1) illustrates the performance of nanoparticles in removing cesium from contaminated water. It can be shown from **figure (1)** that the performance of NZVI is very poor as it can approximately remove ***6.5%*** of cesium. On the other hand, doping a noble metal such as Cu, Ni or Ag on the surface of NZVI to synthesis bimetallic nanoparticles could enhance the efficiency of NZVI. This was the case with bimetallic Cu/Fe^0 as the removal efficiency slightly increased from ***6.5%*** to ***7%***. However, the efficiency of bimetallic Ni/Fe^0 and Ag/Fe^0 deteriorated to ***4.9%*** and ***0%***, respectively. Overall, the performance of iron-based nanoparticles is imperfect compared with most of the reported adsorbents and can't be applied in the real applications where the concentration of cesium is very low compared with the background concentrations of cations.

3.2 Performance of nanocomposites

Figure (2) summarizes the removal efficiencies of nanocomposites. The decontamination performance of zeolite powder is outstanding as the removal efficiency is approximately 100%. However, the separation of zeolite after the adsorption of cesium is very hard as a result of its colloidal property. Magnetization was introduced to zeolite by incorporating it with NZVI with a mass ratio of 1:1 (Ze/Fe) in order to improve its separation after the reaction. As shown in **figure (2)**, the recovery rate of cesium by Ze/Fe drastically decreased by 40% compared with zeolite. This maybe due to the exhaustion of the ionic exchange capacity of zeolite by the presence of sodium borohydride in the synthesis process. Interestingly, the performance of nanocomposites Ze/Fe-Cu, Ze/Fe-Ni and Ze/Fe-Ag was unsatisfying and the removal efficiencies were 53.95%, 37.68 and 53.92%, respectively.

4. Conclusions

Nine different adsorbents were examined in a series of batch experiments to remove cesium from contaminated waters. The iron-based nanoparticles (NZVI, Cu/Fe, Ni/Fe and Ag/Fe) failed to effectively recover the cesium as the efficiencies were below ***10%***. On the contrary, zeolite powder exhibited excellent decontamination efficiency which reached to almost ***100%***. However, the prepared composites (Ze/Fe, Ze/Fe-Cu, Ze/Fe-Ni and Ze/Fe-Ag) were able to recover less than ***60%*** of cesium.

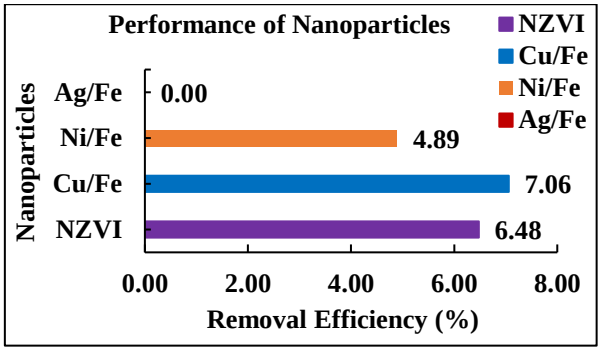

Figure (1): Performance of nanoparticles. Adsorption conditions: initial concentration of cesium = 1mg/L, adsorbent dosage = 5g/L, initial pH = (5.5 to 6), initial temperature = 25°C and contact time = 120 minutes.

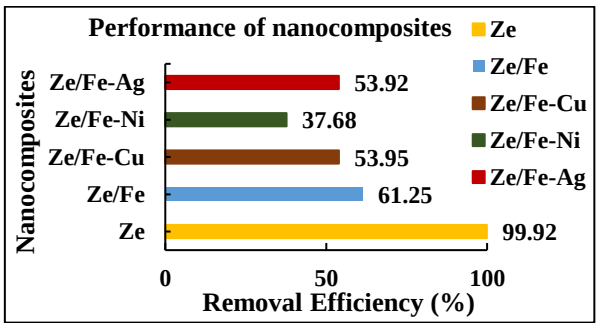

Figure (2): Performance of nanocomposites. Adsorption conditions: initial concentration of cesium = 1mg/L, adsorbent dosage = 5g/L, initial pH = (5.5 to 6), initial temperature = 25°C and contact time = 120 minutes.

5. References

1. Faghihian, H., et al., Evaluation of a new magnetic zeolite composite for removal of Cs+ and Sr2+ from aqueous solutions: Kinetic, equilibrium and thermodynamic studies. Comptes Rendus Chimie, 2014. 17(2): p. 108-117.
2. Shubair, T., et al., Novel application of nanoscale zero valent iron and bimetallic nano-Fe/Cu particles for the treatment of cesium contaminated water. Journal of Environmental Chemical Engineering, 2018. 6(4): p. 4253-4264.
3. Hwang, K.S., et al., Highly efficient removal of radioactive cesium by sodium-copper hexacyanoferrate-modified magnetic nanoparticles. Colloids and Surfaces a-Physicochemical and Engineering Aspects, 2017. 516: p. 375-382.
4. Lee, K.Y., et al., Novel application of nanozeolite for radioactive cesium removal from high-salt wastewater. Water Research, 2016. 95: p. 134-141.
5. Khalil, A.M.E., et al., Performance of nanoscale zero-valent iron in nitrate reduction from water using a laboratory-scale continuous-flow system. Chemosphere, 2018. 197: p. 502-512.
6. Eljamal, R., et al., Improvement of the chemical synthesis efficiency of nano-scale zero-valent iron particles. Journal of Environmental Chemical Engineering, 2018. 6(4): p. 4727-4735.
7. Wang, W., et al., Novel NaY zeolite-supported nanoscale zero-valent iron as an efficient heterogeneous Fenton catalyst. Catalysis Communications, 2010. 11(11): p. 937-941.

Factorial Experimental Design for Optimization of Cesium Removal from Aqueous Solutions

Md. Matiar Rahman[1,2,3], Shamal C. Karmaker[1,3], Animesh Pal[2], Osama Eljamal[4], Bidyut Baran Saha[1,2,*]
[1]Mechanical Engineering Department, Kyushu University, 744 Motooka, Nishi-ku, Fukuoka 819-0395, Japan
[2]International Institute for Carbon-Neutral Energy Research (WPI-I2CNER), Kyushu University,
744 Motooka, Nishi-ku, Fukuoka 819-0395, Japan
[3]Department of Statistics, University of Dhaka, Dhaka-1000, Bangladesh
[4]Interdisciplinary Graduate School of Engineering Sciences, Kyushu University
Kasuga-koen6-1, Kasuga-shi, Fukuoka 816-8580, Japan
[*]Corresponding Author E-mail: saha.baran.bidyut.213@m.kyushu-u.ac.jp

Abstract:*The effective removal of cesium from aqueous solution is an emerging issue all over the world particularly in Japan after destroyed Daiichi nuclear power plant of Fukushima. To reduce the expended chemicals and reagents in experimental work and number of the experiment, it is required to implement statistical optimization of the factors forthe cesium removal process. In this study, factorial experimental design and multivariate regression technique were employed to evaluate the main effects and interactions among the pH, initial concentration and contact time in the cesium removal process using nZVI-Z as an adsorbent. The study revealed that maximum cesium removaloccurred at pH level 6, initial concentration of 200 mg/L and contact time of 30 minutes.Initial concentration was the statistically significant factor followed by contact time. Moreover, the significant interaction effect was observed between contact time and initial concentration.*

Keywords: Analysis of variance; Cesium removal; Factorial experiment; Interaction effect; Main effect.

1. INTRODUCTION

The earthquake and the resultant Tsunami on 11th March 2011, completely destroyedthe Daiichi Nuclear Power Plant of Fukushima[1]. As a consequence, a vast amount of radioactive materials discharged into groundwater, seawater and surrounding soil [2]. The most common radioactive form of cesium is Cs-137 which is made by nuclear fission. Cesium is regarded as a deadly hazard contaminant material that severely affects our environment and has half-life is 30.17 years[2]. Hence, cesium removal from liquid waste is a major concern. Ion exchange method has become one of the utmost cesium removal techniques due to its simplicity, efficiency, and selectivity. Eljamal et al. [3,4] developed novel nanoscale composites (nZVI-Z and nFe/Cu-Z) for cesium elimination through ion exchange technique followed by liquid-phase reduction. Takami et al.[5]examined the removal of phosphorus from aqueous solutions using nano-scale zero valent iron. Earlier researchers employed the traditional 'one variable at a time' approach. The variables were autonomous to investigate the single effect of numerousaspects on the removalmethod. In fact, this is not true, and in these circumstances, it is required to take into account numerous influences concurrently[6]. The factorial experimentaldesign is a very expedient technique for this purpose, as it gives statistical models which explain the interactions among the factors that have been optimized[7,8]. Moreover, statistical models give an enormous quantity of information, decrease the total number of experiments, time, amount of chemicals, and total research expenses.

In this study, a factorial design has been employed to investigate the influence of several factors and their relations on the efficiencyof cesium removal and then evaluate the optimum conditions for the removal of cesiumusing iron based nanoparticles-zeolite.

2. MATERIALS AND METHODS

The preparation and characterization of nanoscale zero valent iron-zeolite(nZVI-Z) composite was described by Osama Eljamal et. al [3]. Data have been extracted from this article[3]. In this study, 2^3 factorial design is considered and the high and low levels defined for this design are listed in Table 1.

Table 1. Parameters considered for full factorial designs.

Factors (units)	Levels	
	Low	High
pH	6	10
Initial concentration(mg/L)	100	200
Contact time (min)	5	30

3. RESULTS AND DISCUSSION

3.1 Normal probability plot for 2^3 factorial experiment

For the main and interaction effects, a normal plot is an appropriate way for relating the statistically significant and degree of significance of factorial experiments. Every point on the normal plot indicates a factor and the points close to the slant line are less potentials compared to the distant one (Fig. 1). Factors presented by red square symbols describe the significant effect and away from the slant line are regarded as more significant which affects the removal efficiency of cesium. The plot illustrates that the points representing initial concentration (B), contact time (C), the interaction of concentration and time (BC), pH and concentration(AB), and interaction of pH, concentration and time (ABC) lie on the right portion of the slant line. It implies that studied factors have a positive significant effect on the cesium removal. On the contrary, the points that lie on the left portion of the slant line has negative effect. An increase pH might reduce removal of cesium. The initial concentration (B) has a

leading effect due to its point lies farthest from the slant line.

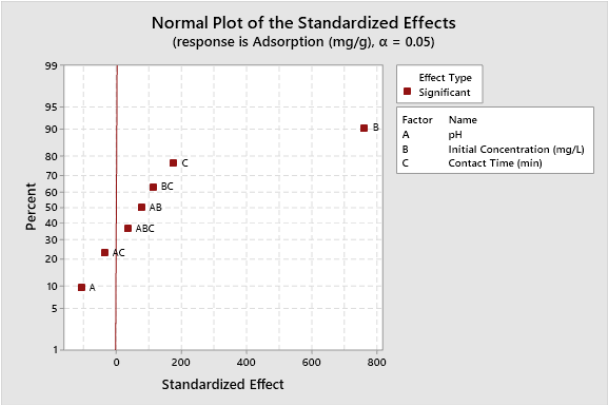

Fig. 1. Normal probability plot of standardized effects.

3.2 Main effects plotof cesium removal

At two levels in the factorial experiment, the main effects plot is adopted to understand the mean differences of each factor. Fig. 2 illustrates a positive relationship between the cesium removal and contact time and each of initial concentration. It means that cesium removal increases if the initial concentration and contact time increase. Instead, there is a negative correlation between pH and cesium removal. It is observed that if pH increases from 6 to 10, the removal of cesium decreases.

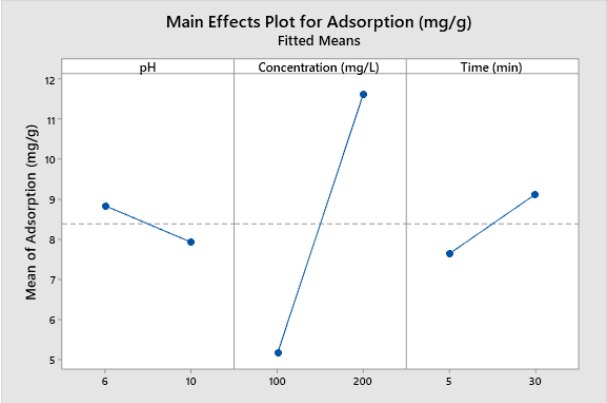

Fig. 2. Main effects plot for cesium adsorption.

3.4 Multivariate regression for the removal of cesium

For more statistical evidence of the adsorption of cesium, statistical analysis containing coefficient of estimated effect, standard error of coefficient, t-value and p-value has been demonstrated in Table 2.

Using the regression coefficient in Table 2 the resulting equation is expressed as equation (1).

$$\eta = 8.382 - 0.456A + 3.232B + 0.744C + 0.329AB - 0.156AC + 0.475BC + 0.143ABC \quad (1)$$

The coefficient expressed in equation (1) represents the effect of the factors as well as interactions. Here, η represents the amount of cesium removal (mg/g). A positive coefficient means that removal of cesium increases with change in the low to high levels. Oppositely, the negative effect reveals a negative correlation with the cesium removal.

Table 2. Estimated effects and coefficients of 2^3 factorial experiment for cesium removal.

Factor	Effect	Coef.	SE	t-value	P-value
Const.		8.382	0.004	1980.04	2E-16
A	-0.912	-0.456	0.004	-107.81	2E-15
B	6.464	3.232	0.004	763.41	2E-16
C	1.488	0.744	0.004	175.78	2E-15
AB	0.659	0.329	0.004	77.87	2E-14
AC	-0.312	-0.156	0.004	-36.85	2E-14
BC	0.950	0.475	0.004	112.30	9E-15
ABC	0.286	0.143	0.004	33.88	2E-14

4. CONCLUSIONS

A 2^3 full factorial experimental design is employed to identify the effect of initial concentration, contact time and pH and their interaction on cesium removal. Moreover, multivariate regression technique is applied to determine the optimum cesium removal process. Statistical analysis results reveals that the initial concentration, contact time and pH have a significant effect to enhance the removal method. Initial concentration is the most potential factor for this removal process followed by contact time, and interaction between initial concentration and contact time.

5. REFERENCES

[1] P. Sylvester, T. Milner, J. Jensen, Radioactive liquid waste treatment at Fukushima Daiichi, J. Chem. Technol. Biotechnol. 88 (2013) 1592–1596.

[2] Y. Koma, A. Shibata, T. Ashida, Radioactive contamination of several materials following the Fukushima Daiichi Nuclear Power Station accident, Nucl. Mater. Energy. 10 (2017) 35–41.

[3] O. Eljamal, T. Shubair, A. Tahara, Y. Sugihara, N. Matsunaga, Iron based nanoparticles-zeolite composites for the removal of cesium from aqueous solutions, J. Mol. Liq. 277 (2019) 613–623.

[4] N.M. Tamer Shubair, Osama Eljamal, Nano-Fe / Cu particles for the remediation of cesium contaminated solutions, Proc. Int. Exch. Innov. Conf. Eng. Sci. 4 (2018) 60–63.

[5] N.M. Seiya TAKAMI, Osama Eljamal, Phosphorus Removal by using Nano-scale Iron Materials, Proc. Int. Exch. Innov. Conf. Eng. Sci. 4 (2018) 70–71.

[6] J.C. Echeverría, I. Zarranz, J. Estella, J.J. Garrido, Simultaneous effect of pH, temperature, ionic strength, and initial concentration on the retention of lead on illite, Appl. Clay Sci. 30 (2005) 103–115.

[7] F. Geyikçi, H. Büyükgüngör, Factorial experimental design for adsorption silver ions from water onto montmorillonite, Acta Geodyn. Geomater. 10 (2013) 363–370.

[8] S. Saadat, A. Karimi-Jashni, Optimization of Pb(II) adsorption onto modified walnut shells using factorial design and simplex methodologies, Chem. Eng. J. 173 (2011) 743–749.

Thermoelectric Properties of Graphene and Carbon Nanotube

Sampad Ghosh[1,2], Sivasankaran Harish[2], and Bidyut Baran Saha[1,2,3,*]
[1]Interdisciplinary Graduate School of Engineering Sciences, Kyushu University, Japan
[2]International Institute for Carbon-Neutral Energy Research (WPI-I2CNER), Kyushu University, Japan
[3]Department of Mechanical Engineering, Kyushu University, Japan
*Corresponding author email: saha.baran.bidyut.213@m.kyushu-u.ac.jp

Abstract: *Graphene (GNP) and carbon nanotube (CNT) filled composites have great potential for making cheaper thermoelectric materials which can be used in building energy harvesting applications. In this paper, the thermoelectric performance of GNP and CNT powders are investigated. The as-received powders were compressed and subsequently cured at room temperature to make it bulk. On bulk samples, the electrical conductivity, Seebeck coefficient and thermal conductivity were measured. Semiconductor like behavior of the electrical conductivity as observed in both samples. As a consequence of high electrical conductivity and Seebeck coefficient, GNP had better result of thermoelectric efficiency. The largest dimensionless figure of merit (ZT) equals to ~0.004 was obtained for the graphene sample.*

Keywords: Carbon nanotube; Energy harvesting; Figure of merit; Graphene; Thermoelectric properties.

1. INTRODUCTION

Depletion of natural fuels and the socio-economic threat to nuclear energy has a quest for alternative sources of energy generation. Thermoelectric (TE) system is very promising for the conversion of heat into electricity which utilizes the temperature gradient. The traditional TE materials such as Bi_2Te_3 exhibits a high figure of merit [1]; however, they are expensive and toxic. Improvement in the figure of merit for structural materials based nanocomposites may be of interesting due to their availability, low cost, non-toxicity and ease of production. Graphene (GNP) and carbon nanotube (CNT) have been considered as promising candidates for various fields like electronic, optical and solar cells due to their outstanding electrical properties. GNP and CNT also have been used as fillers in polymer composites and the electrical conductivities of such composites are of the order of magnitude higher than other polymer composites containing different conductive fillers. These kinds of applications triggered to incorporate GNP and CNT into the structural materials for building energy harvesting. In addition, both GNP and CNT has gained interest in the field of TE materials due to its one dimensional (1D) structure. It has been reported that the lower dimensional, i.e., one or two dimensional TE materials can perform better than bulk materials [2].

The goal of this study was to investigate the thermoelectric properties of graphene and carbon nanotube since they can enhance the TE properties of structural materials when used as a filler. Promising results were obtained which is represented by the figure of merit (ZT) based on thermoelectric properties measurement.

2. EXPERIMENT

In this work, Graphene (H-grade nanoplatelets, average particle diameter 25 µm from XG Sciences, USA), Carbon nanotube (multi-wall, outer diameter : < 8 nm, inner diameter : 2-5 nm from Raymor – Nanotubes for Electronics, Canada), Polyvinyl alcohol (molecular weight - 44.05 g/mol from Kanto Chemical Co., Japan), and deionized water were used. To prepare the graphene (GNP) composite samples, graphene nanoplatelets were loaded in a metallic die and compressed at around 40 MPa pressure (See Fig.1). For carbon nanotube (CNT) composite samples, CNT was mixed with a water-binder solution followed by compressed at about 40 MPa. Finally, the composite samples were dried to remove the water and moisture contents. The thermoelectric properties of the samples were measured by RZ2001i from Ozawa Science, Japan [3] at ambient condition within the temperature range between 25 and 100 °C. The thermal conductivity was studied using the laser flash method. Thermal conductivity value was obtained from thermal diffusivity and specific heat capacity measured by NETZSCH LFA 457 [4] and a differential scanning calorimeter (DSC-60A) [5], respectively.

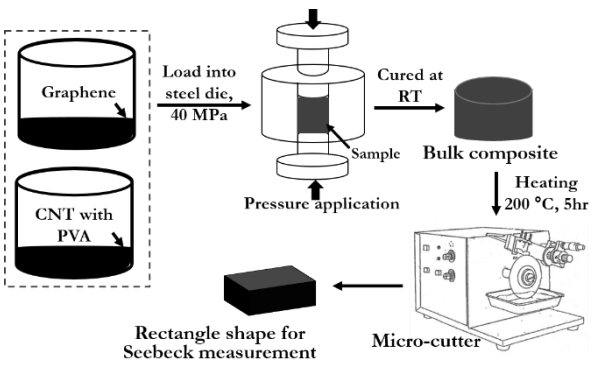

Figure 1 Sample preparation flows

3. RESULTS AND DISCUSSION

The results shown in Fig.2 suggest that the samples derived from graphene exhibited higher electrical conductivity in comparison to the carbon nanotube, with the largest difference of almost two orders of magnitude between GNP and CNT. The electrical conductivity observed on both samples was semiconductor like since conductivity increases with temperature. As shown in Fig.5, the thermal conductivity of CNT was lower than those of GNP, and the difference was 90% which is maintained throughout the temperature range. This would be attributed to a much smaller average particle diameter in CNT. All samples exhibited Seebeck coefficient around 15 μVK^{-1} as seen in Fig.3. The best

result (23 μVK^{-1}) that combined with high conductivity of GNP sample (890 Scm^{-1}) gave a rise to considerable (0.0035) figure of merit. In the case of the CNT, best obtained thermoelectric figure of merit was ~0.2×10^{-3} (Fig.6). The Seebeck coefficient for both samples gradually increased with increase in temperature. However, GNP samples exhibited the highest Seebeck coefficient at around 60 °C. (Fig.3). The Seebeck coefficient values for all samples are positive which confirmed the composites are p-type semiconductor and hole carriers play an important role in them. Power factor (Fig.4) that describes electrical contribution to the ZT shows that GNP was electrically superior to CNT. This gives basis to conclude that higher ZT of the GNP though CNT had lowered thermal conductivity.

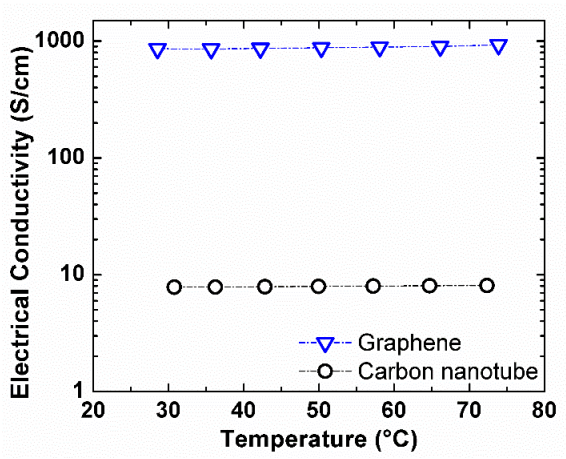

Figure 2 Electrical conductivity

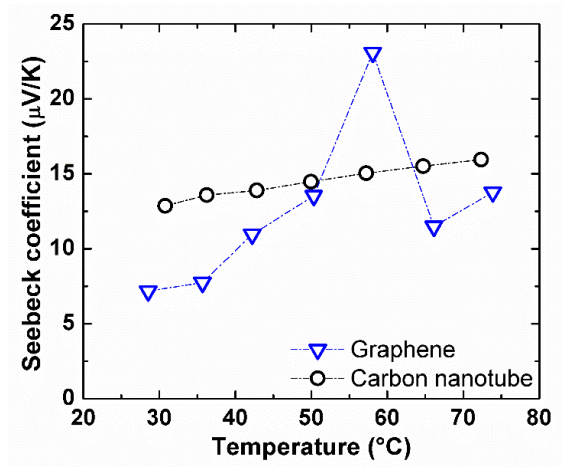

Figure 3 Seebeck coefficient

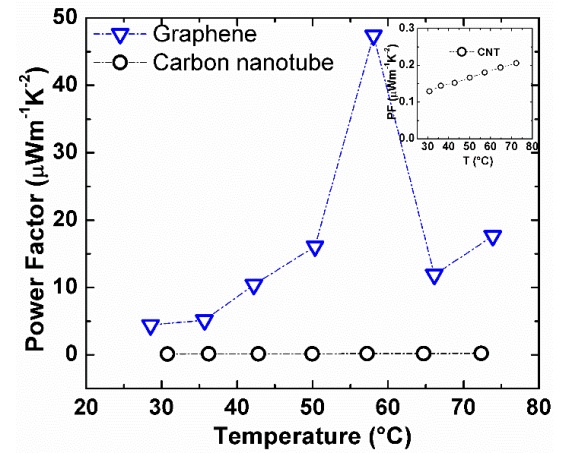

Figure 4 Power factor

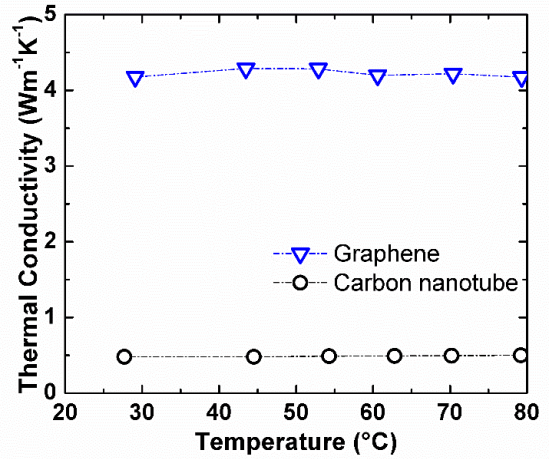

Figure 5 Thermal conductivity

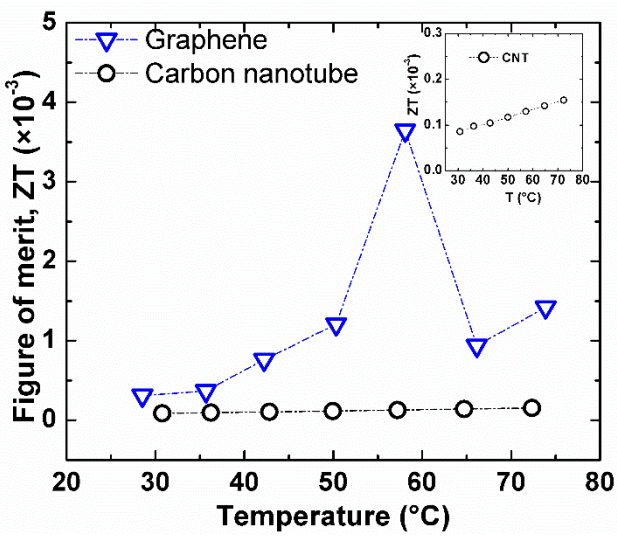

Figure 6 Figure of merit

4. CONCLUSION

Thermoelectric performances of graphene and carbon nanotube were evaluated to use them as nano-filler in the building energy harvesting technology. Graphene exhibits higher values of electrical and thermal conductivity than carbon nanotube. However, their Seebeck coefficient values are comparable. The figure of merit equals to 4×10^{-3} is obtained for graphene samples.

ACKNOWLEDGEMENTS

The authors are grateful to Prof. Michitaka Ohtaki, Mr. Wojciech Klich and Mr. Kaiser Ahmed Rocky from Kyushu University for their helpful discussion during measurements.

REFERENCES

[1] Minnich AJ et. al., Energy Environ Sci 2(2009) 466–79.
[2] Abhijit Dey et. al., Renewable and Sustainable Energy Reviews 53(2016) 653–671.
[3] W. J. Klich et. al., in proc. of IEICES 4 (2018) 84–87.
[4] Md. M. Younes et. al., in proc. of IEICES 3 (2017) 103–104.
[5] Md. A. Islam et. al., in proc. of IEICES 4 (2018) 151–152.

Investigation of Surface Energy of Porous Adsorbents

M. L. Palash[1,2,3], Animesh Pal[3], Bidyut Baran Saha[1,2,3,*]
[1]Green Asia Education Center, Kyushu University, Fukuoka, Japan
[2]Interdisciplinary Graduate School of Engineering Sciences, Kyushu University, Japan
[3]International Institute for Carbon-Neutral Energy Research, Kyushu University, Japan
[*]Corresponding author, e-mail: saha.baran.bidyut.213@m.kyushu-u.ac.jp

Abstract: *Surface energy of adsorbent materials is one of the critical parameters which can be used to understand the insight of the adsorption phenomenon. In this work, a comparative study on surface energies at infinite delusion is presented for activated carbon, silica gel, and carbon fiber. Additionally, ethanol and hexane adsorptions are studied with 0.1 coverage to determine the influence of high energy sites at the adsorption process. The study explicitly explains the possible influence of surface energy on gas adsorption with experimental findings.*

Keywords: Adsorption; Surface energy; Inverse gas chromatography; Porous Adsorbent.

1. INTRODUCTION

The sorption phenomenon of porous adsorbents plays a vital role in various applications in industrial and environmental sectors. One of the conventional ways of understanding this adsorption phenomenon is by measuring adsorption isotherms [1,2]. These adsorption isotherms are the state diagram influenced by adsorbent's pore size distribution, surface energy, site energy distribution, and adsorbate properties. Recently the International Union of Pure and Applied Chemistry (IUPAC) has introduced six types of isotherms with two subcategories [3]. Different models have been addressed for each of the isotherm types, however no universal model yet been proposed. Ng *et al.*, [4] found that if the site energy distribution with their prospective probability function is considered for modeling, then a universal isotherm model can be developed. This finding revealed that surface energy might be the key to understanding the adsorption phenomenon. However, there is a lack of experimental findings which can relate the adsorption phenomenon with the surface energy.

Therefore, in this work, ethanol and hexane adsorption on three different types of adsorbents are studied. To find a connection between the surface energy with the adsorption phenomenon, dispersive and specific surface energies of the mentioned adsorbents were measured using inverse gas chromatography (IGC).

2. EXPERIMENTAL

2.1 Materials

Highly porous activated carbons and silica gel were studied in this work to measure surface energy. Maxsorb III and activated carbon fiber (ACF) are the porous carbons having a very high surface area. On the other hand, porous silica gel, like RD silica gel, contains a moderate surface area. Porous properties of the samples are presented in Table 1.

Table 1. Porous properties of samples [5,6]

Parameter	Maxsorb III	ACF A-20	RD silica gel
Surface area [m^2/g]	3045	1900	798
Pore volume [cm^3/g]	1.7	1.028	0.415
Pore size [nm]	1.12	2.16	2.28

2.2 Apparatus and Procedure

The experiments were conducted with an inverse gas chromatography equipment (SEA-iGC, Surface measurement systems, UK). Here samples/adsorbents were placed in a narrow column of 30 cm length and 3 mm in diameter. Each sample was packed with glass wools. Polar (ethanol, dichloromethane, ethyl acetate, acetone, acetonitrile) and non-polar (hexane, heptane, octane) gases were sent to the column for adsorption; helium was used as a carrier gas. For desorption, helium was flowed through the column with a flow rate of 30 sccm. The schematic of IGC equipment is shown in Fig. 1. Desorbed gases then detected using a flame ionization detector (FID).

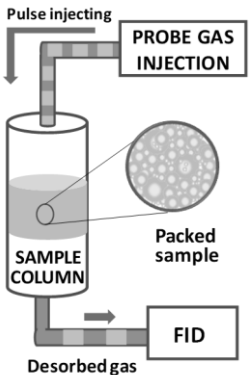

Fig. 1. Schematic of IGC

3. RESULTS AND DISCUSSION

Typically, one IGC experiment provides the information of two retention times, one is for probe molecule (t_R), and another one is for inter gas (t_0). The amount of carrier gas required to remove the adsorbed gas from the adsorbents is termed as retention volume (V_g), which can be obtained by multiplying the net retention time (t_R-t_0). The higher value of retention volume means higher interaction between the probe molecules and adsorbents. In this work, the flow rates were kept constant. Therefore, the higher value of net retention time indicates higher interaction. The relation between these parameters can be presented in equation 1 [7].

$$V_g^0 = \frac{j}{m_s} F_c (t_R - t_0) \frac{273.15}{T} \quad \text{.....(1)}$$

The position of the peaks showed in Fig. 2(a) indicates there is a strong interaction between hexane with the porous carbon samples because this non-polar probe elutes later from the surface of these samples. Furthermore, asymmetric peaks are found for the porous

carbons due to the stronger attraction. On the other hand, polar probe ethanol shows higher affinity with RD silica gel samples (Fig 2(b)). The peak for silica gel is generated significantly later than that for porous carbons. There is a high possibility that the hydroxylated surface of RD silica gel has an additional attraction to the hydroxyl part of ethanol. Carbon samples show very low affinity towards ethanol.

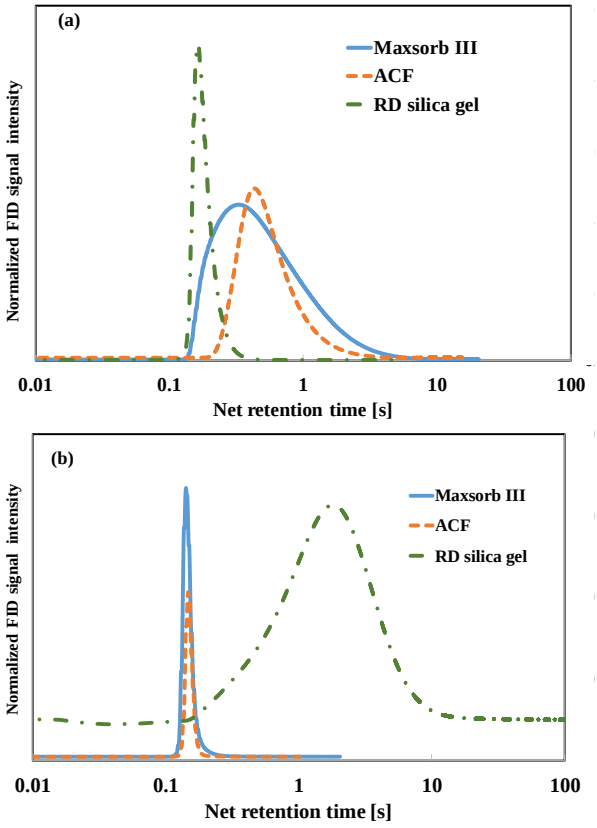

Fig. 2. Experimental chromatograph on different samples at 0.01 surface coverage a) non-polar probe hexane and b) polar probe ethanol.

The total surface energy for each sample was measured using eight different probe materials. It has two components: (i) dispersive and (ii) specific. The source of dispersive surface energy is the weak van der Waals force between surface atoms. Moreover, the specific surface energy is influenced by acid-base interaction, magnetic force etc. The surface energies of the samples are presented in Fig. 3. Dispersive component of surface energy is found higher in the carbon materials. According to this experiment, no direct relationship is found between the surface area and surface energy. For instance, Maxsorb III has a higher surface area, however, it has lower dispersive surface energy than ACF.

The specific component of silica gel is significantly higher than porous carbons. For 0.01 surface coverage, specific surface energy silica gel is 19.87 m^2/g, whereas carbon materials have below 1.5 m^2/g. The low specific surface energy measured with the polar probe indicates these carbon materials have high hydrophobic surfaces.

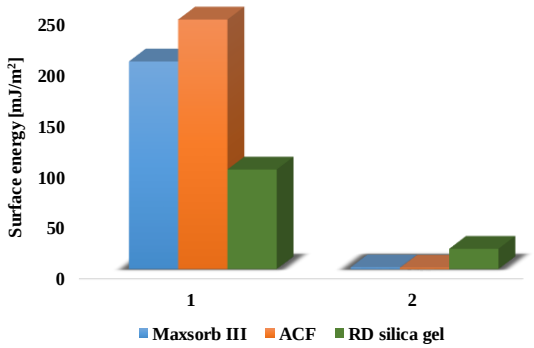

Fig. 3. Surface energy comparison of different samples at infinite dilution.

4. CONCLUSION

The interaction between hexane probe and porous carbon is found more intense than the silica gel surface. However, RD silica gel shows a stronger affinity for ethanol. The total surface energy of ACF is higher than the other samples. Nevertheless, ACF has a lower surface area than Maxsorb III. Surface energy is heavily influenced by the surface of the adsorbents, and the types of adsorbate are used rather than the surface area and pore size distribution.

REFERENCES

[1] A. Pal, S. Mitra, K. Thu, B.B. Saha, Improved adsorption uptake of ethanol and CO2 onto biomass based activated carbons, in: Proc. Int. Exch. Innov. Conf. Eng. Sci., 2017: pp. 127–128.

[2] M.A. Islam, B.B. Saha, S. Jribi, K. Thu, T. Miyazaki, S. Koyama, Adsorption Isotherms and Kinetics of Ethanol onto Powder and Consolidated Activated Carbon, in: Proc. Int. Exch. Innov. Conf. Eng. Sci., Fukuoka, 2016: pp. 21-24.

[3] K.A. Cychosz, M. Thommes, Progress in the Physisorption Characterization of Nanoporous Gas Storage Materials, Engineering. 4 (2018) 559–566.

[4] K.C. Ng, M. Burhan, M.W. Shahzad, A. Bin Ismail, A Universal Isotherm Model to Capture Adsorption Uptake and Energy Distribution of Porous Heterogeneous Surface, Sci. Rep. 7 (2017) 10634.

[5] B.B. Saha, K. Uddin, A. Pal, K. Thu, Emerging sorption pairs for heat pump applications: an overview, JMST Adv. (2019).

[6] M.L. Palash, S. Mitra, S. Harish, K. Thu, B.B. Saha, An approach for quantitative analysis of pore size distribution of silica gel using atomic force microscopy, Int. J. Refrig. (2018).

[7] A. Pal, A. Kondor, S. Mitra, K. Thu, S. Harish, B.B. Saha, On surface energy and acid–base properties of highly porous parent and surface treated activated carbons using inverse gas chromatography, J. Ind. Eng. Chem. (2018).

Adsorption Characterization of Aluminum Fumarate Metal-organic Framework

Tahmid Hasan Rupam[1], M.L. Palash[1,2], Israt Jahan[3], Bidyut Baran Saha[1,2,3,*]
[1]Kyushu University Program for Leading Graduate School, Green Asia Education Center
Kyushu University, Kasuga-koen 6-1, Kasuga-shi, Fukuoka 816-8580, Japan
[2]International Institute for Carbon-Neutral Energy Research (WPI-I2CNER), Kyushu University, 744 Motooka, Nishi-ku, Fukuoka 819-0395, Japan
[3]Mechanical Engineering Department, Kyushu University, 744 Motooka, Nishi-ku,
Fukuoka 819-0395, Japan
[*]saha.baran.bidyut.213@m.kyushu-u.ac.jp

Abstract: *Microporous metal-organic frameworks (MOFs) having higher difference between adsorption and desorption uptake per cycle are considered as one of the most potential adsorbents for future designing of adsorption heat pumps. In this study, the porous properties and water adsorption isotherm of a commercially available MOF- aluminum fumarate were studied. The porous properties confirmed this to microporous material. The obtained water adsorption isotherms were S-shaped. These S-shaped isotherms ensured that the uptake offtake difference was large within a very short range of pressure.*

Keywords: Aluminum fumarate; microporous material; porous properties; water uptake.

1. INTRODUCTION

MOFs are highly crystalline powdered like materials having higher surface area and regular pore geometry than the conventional adsorbents. MOFs can be easily synthesized in their pure form and modifications in MOFs synthesise have made them more stable than ever before. As a result, they become great potential materials for various applications involving microporous materials As the MOFs are known to possess highewr surface area and adequate pore volume, they fulfil one of the primary conditions to be an adsorbent for adsorption chiller [1,2]. Water adsorption has been done on a number of MOFs including MOF-805, MOF-806, Mg-MOF-74, Ni-MOF-74, CAU-10 etc. They showed better performance when compared with silica gel and zeolite [3]. Thus MOFs are becoming more and more popular for water assisted AHT applications. The pore diameter and hydrophilicity plays an important role in water adsorption in an adsorbent. The adsorbents having a pore radious below the critical (10.38 Å) for water, would trigger water adsorption in the pores without condensation. Moreover, hydrophilicity in the pore must be sufficient enough to permit the molecules of water to fill the pores below the relative pressure (P/Ps=0.3) for adsorption heat transfer applications [4].

We have a goal to synthesize aluminum fumarate, a promising MOF water adsorption using a green technology involving water as a solvent instead of DMF (Dimethylformamide). After synthesizing we need to have the commercial sample's adsorption characteristic data to valid our synthesized aluminum fumarate. This study thus focuses on obtaining the adsorption characteristics for the adsorption properties such as porous properties and water uptake isotherms. 3D view of aluminum fumarate is shown in fig. 1.

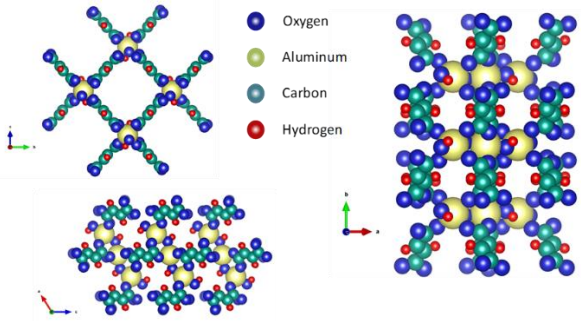

Fig. 1. 3D view of aluminum fumarate

2. EXPERIMENT

The porous properties of the commercial aluminum fumarate was obtained by N_2 adsorption isotherms at 77K. Aluminum fumarate sample was degassed at a temrperature of 120˚C for 3h before N_2 adsorption experiment was perforemed. The N_2 adsorption/desorption isotherm on aluminum fumarate was investigated using volumetric method. 3Flex™ Surface Characterization Analyzer was used to do the experment. NLDFT (Non-localized density functional theory) method was applied on the ontained N_2 adsorption isotherm to investigate about the pore size distribution. The micro-pore volume was determined before the isotherm reaches saturation.macro pores are not filled until saturation. As a result the micro-pore volume is determined appropriately. Near saturation the N_2 adsorption isother has a sharp increase before reaching the limiting uptake value due to macropore filling.This limiting uptake defined the total pore volume of aluminum fumarate.

Water adsorption on aluminum fumarate was measured at different temperature and pressure using thermogrametric method. A thermogrametric analyzer (TGA) was used as it had high accuracy and good control over the temperature and pressure at the time of the experiment. Rubotherm of type MSB-VG-S2 supplied by BEL Japan, Inc is a magnetic suspension adsorption measurement unit which was used for the experiment.

3. RESULTS AND DISCUSSION

Fig. 2. shows the N_2 adsorption-desorption isotherm on commercial aluminum fumarate. Experimental data shows that the volumetric uptake of N_2 gas was 12 mmol/g before reaching the saturated pressure. Near the saturated pressure, the volumetric uptake sharply increases up to approximately 17 mmol/g suggesting macropore filling. This concludes that the material also has macropore besides micro pores. BET analysis and N_2 adsorption isotherms were used to determine the pore size distribution, surface area and pore width. The surface area was found to be 600 m^2g^{-1} and the average pore width is 11 Å. which agrees with the crystallographic data. The pore size distribution is shown in fig. 3.

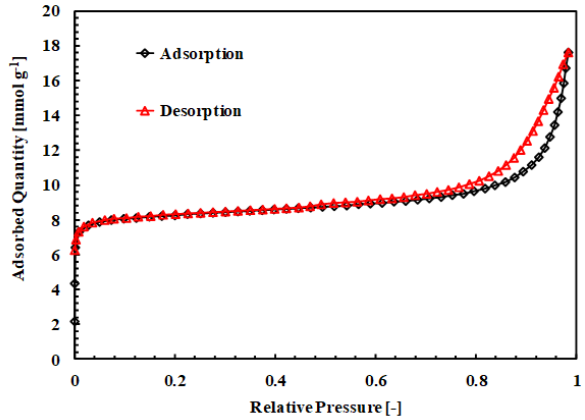

Fig. 2. N_2 adsorption/desorption isotherm at 77 K

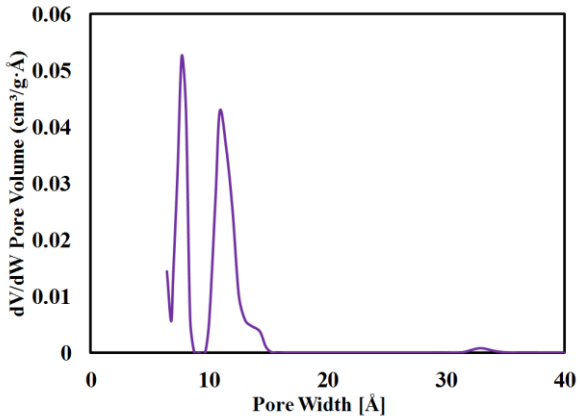

Fig. 3.Pore size distribution of Aluminum fumarate

Water adsorption isotherms were measured for the commercial aluminum fumarate sample at 30 °C, 50 °C and 70 °C. The results are shown in Fig. 4. We obtained S-shaped isotherms in all cases that are the desired one for adsorption chiller application.

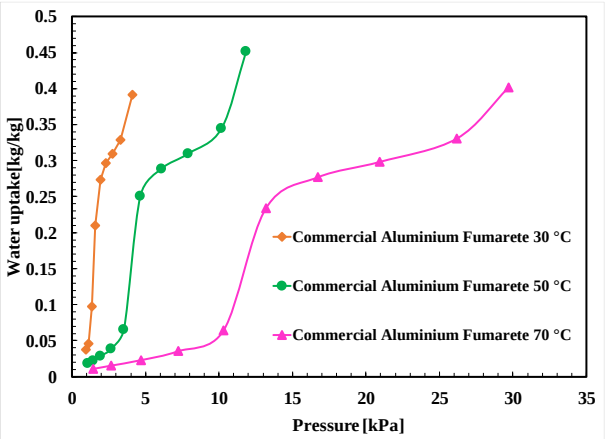

Fig. 4. Water adsorption isotherms o commercial aluminum fumarate

4. CONCLUSION

Water adsorption and porous properties were measured for commercial aluminum fumarate. The average pore width was found 11 Å. the material was mostly microporous. The water adsorption isotherms were all s-shaped. The ultimate goal of this study is to find a green synthesis technique which can produce aluminum fumarate with properties like the commercial one or even better. Then we can apply other MOF medication techniques to make that even better and more aligned to a particular application.

5. REFERENCES

[1] P. Animesh, M. Sourav, T. kyaw, B.B. Saha Improved adsorption uptake of ethanol and CO_2 onto biomass based activated carbons, Proceedings of International Exchange and Innovation Conference on Engineering & Sciences (IEICES), 3 (2017) 127-128.

[2] M.A. Islam, T. kyaw, B.B. Saha, Specific heat capacity of mangrove and waste palm trunk in raw, carbonized and activated form, Proceedings of International Exchange and Innovation Conference on Engineering & Sciences (IEICES), 4 (2018) 151-152

[3] H. Furukawa, F. Gandara, Y. Zhang, J. Jiang, W. L. Queen, M.R. Hudson, O. M. Yaghi, Water Adsorption in Porous Metal–Organic Frameworks and Related Materials, *J. Am. Chem. Soc.*2014136114369-4381

[4] H. W. B. Teo, A. Chakraborty, Y. Kitagawa, S. Kayal, Experimental study of isotherms and kinetics for adsorption of water on Aluminium Fumarate, International Journal of Heat and Mass Transfer, Volume 114, November 2017, Pages 621-627, 2017

Occupancy Rate and Water Utility Effects on Energy Consumption of Commercial Building: Case Study Grand Inna Malioboro Hotel in Indonesia

Solli Murtyas[1*], Mohammad Ridwan[2], Rachmawan Budiarto[3]
[1]Interdisciplinary Graduate School of Engineering Sciences, Kyushu University, Japan
[2,3]Department of Nuclear Engineering and Engineering Physics, Universitas Gadjah Mada, Indonesia
[*]Corresponding author email: murtyas.solli.438@s.kyushu-u.ac.jp

Abstract: *Hotel is the one of the major consumers of the energy for commercial buildings sector that have directly correlated for energy conservation effort. This study emphasizes the correlation of each energy supply such as electricity, fuel and LPG that used to the occupation rate and water consumption in the hotel to utilize the building based on data collection. As Result, electricity was the major energy to use in the hotel with 28985.04 GJ (88%). The other two energy resources were 1900 GJ (6%) for fuel and 1883.2 GJ (6%) for LPG. The behavior of occupants were dominantly affecting the use of electricity than other energy. The use of LPG was tightly correlated with the use of water due to kitchen activity that mainly devices used LPG than electricity or fuel.*

Keywords: Energy Consumption; Electricity; Fuel; LPG; Water consumption.

1. INTRODUCTION

The buildings contributed for 40% of world's energy consumption [1]. Hotel is the one of the major consumers of the energy for commercial buildings sector that have directly correlated for energy conservation effort. In the other hand, average global efficiency of fossil-fueled power generation has remained stagnant for decades at 35% to 37% [2]. Meanwhile, reducing energy consumption will increase energy security of the country [3].

In Indonesia, tourism has been significantly grown in the last decades. Consequently, it stimulated the growing of hotel buildings. This will continue to intersect with the principles of natural balance and energy management as the key roles on conducting sustainable tourism. The government has a role to arrange General Energy Planning based on UU No. 30 year 2007 about energy policy. The goals of government in future based on this, is to create competitive commercial industries based on efficiency of energy, green environment and renewable energy [4]. In the other hand, behavior of the occupants of a building contribute more significant to the energy consumption than specific features of a particular building [5].

This study emphasizes the correlation of each energy supply such as electricity, fuel and LPG that used in the hotel to utilize the building based on data collection in the period of 2011 and 2012. This study applied a statistical measurement to explain the strength or weak relationship among energy resources to the occupants and water utility. In addition, it will explain the use of energy for the building's utilization in conducting operational activities such as electrical equipment, kitchen and portable power generator (power genset). The result will give a benefit to arrange the strategy to increase energy efficiency in the energy supply and usage stage of the hotel as commercial buildings.

2. METHODOLOGY

2.1 Study Area

Grand Inna Malioboro Hotel is located in the heart of Yogyakarta. Its specific location in Jl. Malioboro No. 60 Suryatmajan Danurejan Yogyakarta the Sultan Palace, 42 kilometers from the famous Borobudur Budhist temple, 17 kilometers from the Hindu temple of Prambanan [6]. The hotel consist of two main buildings: main building in the north and extension building in the south. The hotel has 7 floors for each building. Total area of the building is 23792 m^2 and the ground's area is 18000 m^2.

Figure 1. Gran Inna Malioboro hotel [6]

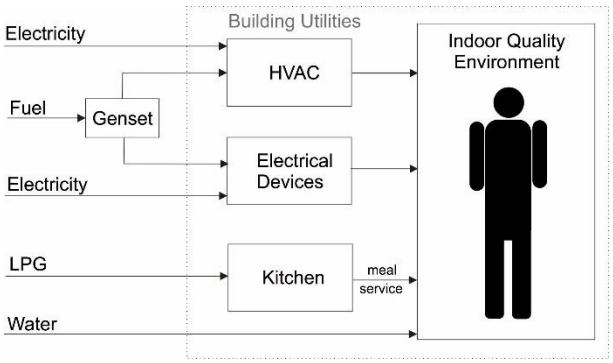

Figure 2. Energy supply model for building hotel of Grand Inna Malioboro

2.2 Energy Supply Schematic

The hotel use energy to achieve the main function in conducting indoor quality environment and operational process including kitchen activity, laundry etc. The main energy supply is electricity provided by National Electricity Company (PT. PLN). The portable power generation (genset) was used supply the electricity in case of power drop occurrence. The main energy resource for genset was fuel. LPG was used to cook meal in the kitchen. The water was the additional resource for laundry activity beside electricity for the washing and iron machine. Schematic of the energy supply model is shown in figure 2.

2.3 Data Collection

Data of energy consumption was collected in the period of 2011 and 2012 based on the documents that the hotel's manager provided. It consisted of data energy consumption from electricity, fuel, LPG and water per month. We included the water as parameter that has direct correlation with the energy consumption especially in some activities including shower, laundry, swimming pool, food and beverage.

3. RESULT AND DISCUSSION

3.1 Energy Consumption Trend

The operation of hotel exhibits some characteristics that have a direct impact on the energy consumption of the building [7]. It operates in basis, which means that services, equipment and several areas in the building were used continuously. The behavior of the building occupants has also a direct impact on the energy consumption record.

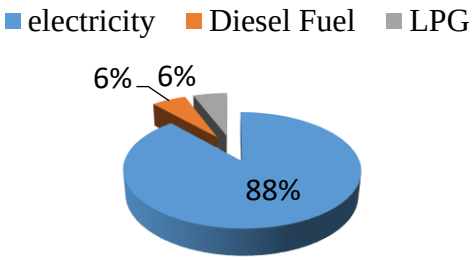

Figure 3. Energy consumption based on type in the period of data collection

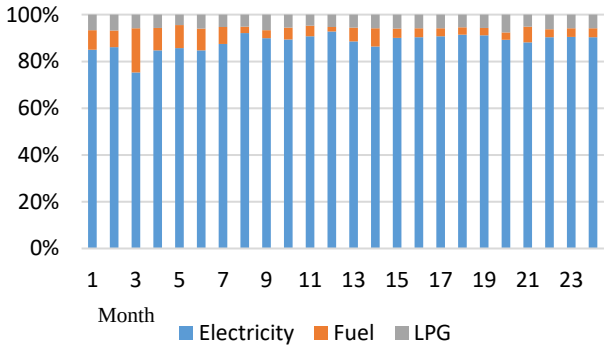

Figure 4. Monthly percentage of energy consumption based on the type

Electricity was the major energy to use in the hotel with 28985.04 GJ (88%). The other two energy resources were 1900 GJ (6%) for fuel and 1883.2 GJ (6%) for LPG. The fuel was used to substitute the electricity when it dropped or extinguished by PLN (National Electricity Company). Therefore, the rate of consumption was not much as the electricity LPG usage was stable every month and it was not significantly affected when the electricity drop. In month 3 (March 2011) there was electricity drop and it showed in figure 4 that fuel consumption was increasing but in the same time electricity consumption decreased.

3.2 Occupation Rate Effect on Energy Consumption

Based on the data, there were various number of occupant for each month. The minimum occupation rate usually conducted on September, it because of lack of holidays at that month. In addition, September is the beginning of rain season. It was the reason for the tourists unwilling to come. In the other side, international tourist come mostly on July-August (summer) and December-January (long holiday). Thus, maximum occupation rate was on November 2011 and January 2012. It is shown in figure 5.

Occupation rate has significant contribution on electricity consumption. It shows on figure 6 that the correlation expressed by R^2 was 0.9126. This positive linear regression also indicates that the number of electricity consumption will increase as the number of occupation increase. In addition, the guest mostly use the devices and services from the hotel that mostly powered by the electricity.

Fuel and LPG have weak correlation with the occupation rate. Fuel had the weakest energy consumption affected by the occupation rate with 0.0093. It because the fuel was only a substitutive energy component instead of electricity. Thus, it was not very significant correlation.

LPG has positive correlation with the occupation rate (0.3608) even though it was not as strong as electricity. LPG was tightly correlated with the meal production in the kitchen. Based on this, we concluded that LPG was the second energy that tightly correlated with the guest of hotel due to it was the main resource energy that used in the kitchen.

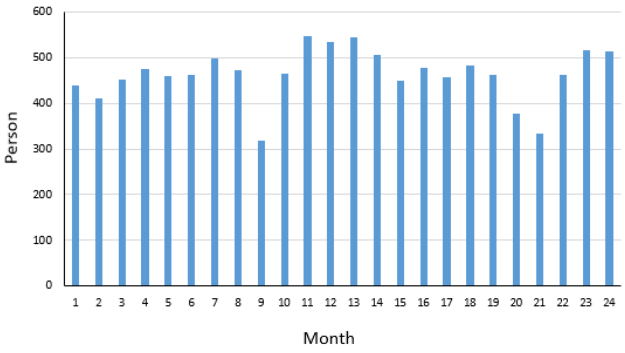

Figure 5. Occupation rate

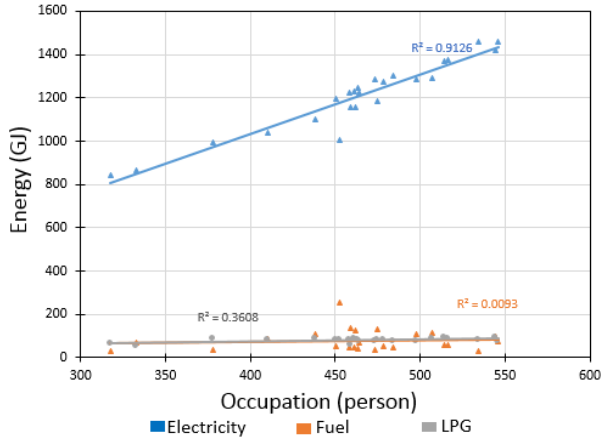

Figure 6. Linear regression between occupation rate and energy consumption by type

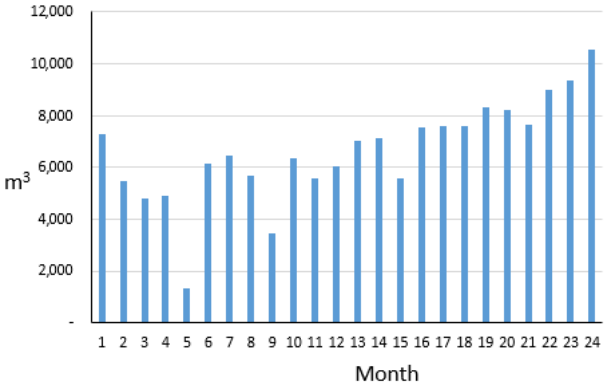

Figure 7. Water consumption

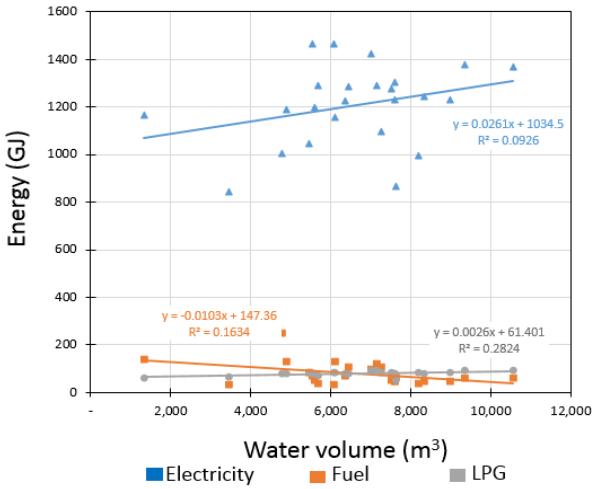

Figure 8. Linear regression between water utility and energy consumption by type

3.3 Water Utility Correlation on Energy Consumption

Water was the one of natural resources that used to kitchen and laundry activity in the hotel. The water supplied by National Water Company (PT. PDAM). The use of water was not strongly affected by the occupation rate ($R^2 = 0.0444$). It indicates that mostly visitor was not using water from the hotel except for limited activities such as laundry and shower.

However, the water usage have different pattern in affecting the use of energy. Kitchen activities consumed more water. It directly correlated to the LPG usage. Thus, the number of R^2 was the highest with 0.2824. The use electricity do not contribute significantly to the water. Some electricity devices that correlated to the water such as heater and laundry machine were directly use the water. Generally, it has small effect to achieve positive correlation between this two more than 10% dependency each other. It was parallel with the correlation the use of water and fuel, even though it was higher value of R^2 than electricity (0.1634). The use of water in portable power supply was in order to cool the machine. It was the only direct correlation between water and fuel consumption in the hotel.

4. CONCLUSION

The energy consumption of Grand Inna Malioboro hotel during 2011 and 2012 consist of electricity, fuel and LPG. The amount electricity consumption is 28985.04 GJ (88%). It was more than the others energy conversions used in the hotel including diesel fuel is 1899.9 GJ (6%) and LPG 1883.2 GJ (6%). In general, electricity as the major energy-consumed and it was increasing 3% during 2011 and 2012. The behavior of occupants were dominantly affecting the use of electricity than other energy. The use of LPG was tightly correlated with the use of water due to kitchen activity that mainly devices used LPG than electricity or fuel.

ACKNOWLEDGEDMENT

A special appreciation was awarded to the engineers of Inna Garuda Hotel including Mr. Suwandono, Mr. Sarjono, Mrs. Ratna and Mr. Wintolo. A lot of efforts and works together with them to get the data of energy from the hotel was a great time for the authors. Hopefully this research will give a significant contribution to make the hotel better in energy management for the future.

5. REFERENCES

[1] Cogeneration and Renewables. Technical Document, International Energy Agency, Paris, Frence, 2011.
[2] Combined Heat and Power a Clean Energy Solution. Technical Document, United States Environmental Protection Agency, U.S Department of Energy, United States of America, 2012.
[3] Farabi-Asl, H. Chapman, A. Itaoka, K. Noorollahi, Y, Zero Emission Buildings and Challenges in Japan, IEICES Proceeding 4 (2018) 96-101
[4] Enshassi, A. Elzebdeh, S. Residential Consumers' Attitudes towards Water and Energy Conservation, IEICES Proceeding 3 (2017) 47-52
[5] Undang-Undang RI No. 30 Tahun 2007 about Energy Policy.
[6] Inna Garuda Hotel.Profile of Inna Garuda. Acessed from http://www.innagaruda.com/profile.php (accessed 13.02.27)
[7] M. Santamouris, C.A. Balaras, E. Dascalaki, A. Argiriou, A. Gaglia. Energy Conservation and Retrofitting Potential in Hellenic Hotels, Energy and Buildings 24 (1996) 65-75.

Dynamic Simulation of a Thermal Management System Consisting of a CO_2 Heat Pump and a Water-Loop

Jaedeok Ko[1]*, Nobuo Takata[1], Kyaw Thu[1,2], Takahiko Miyazaki[1,2]
[1]Interdisciplinary Graduate School of Engineering Sciences, Kyushu University, [2]International Institute for Carbon-Neutral Energy Research, Kyushu University
*ko.jaedeok.980@s.kyushu-u.ac.jp

Abstract: *A dynamic simulation of a thermal management system which combined a CO_2 heat pump with a water-cooling system have been carried out using Simscape™ according with the change of the compressor rotation speed. Simscape™ built-in models are used for each system component. The simulation results demonstrate that the system's behavior and performance are reasonable in terms of the physical senses, however, it needs to be validated experimentally.*

Keywords: Dynamic simulation; Thermal management system, CO_2 (R-744) heat pump

1. INTRODUCTION

Dynamic simulations of refrigeration systems using CO_2 as a refrigerant in multi-physical domain platform have been carried out some researchers. Because, it is convinent to simulate complicate systems which consist of components in different physical-domains. Pfafferott and Schmitz [1] developed a library for CO_2-refrigeration system in Modelica and compared simulation results with their experimental data and they show a good agreement with the experimental results. But the results showed that the refrigerant state at the expansion valve inlet is deviated from its experimental data. In this case it might cause an effect on the dynamic behavior of the system. Shi et al. [2] developed a dynamic model of a transcritical CO_2 for a supermarket refrigeration system in Dymola to investigate the system performance and validated their model with actual field data. Using their model, they investigated the effects of designe parameters in field such as one- and two-dimensional gas cooler models, discretization number for the liquid pipe, and natural convection on the gas cooler.

In the present study, dynamic simulations of an air-to-air thermal management system which combined a CO_2 heat pump with a water-cooling system have been carried out in the MATLAB/Simulink environment, using Simscape™. The system's dynamic behavior and performance are stated corresponding with a changing of compressor speed in this paper.

2. MODEL

Simscape™ provides some physical models, called component block, in the multi-physical domain. Using these blocks, it is possible to build up models of the

Table 1. System component in Simscape™ physical domain.

Actual System	Component	Simscape™ Block model	Physical domain
Heat pump	Compressor	Controlled Mass Flow Rate Source (2P)	Two-Phase Fluid
	IHX	Pipe (2P)	
	Evaporator	Customized	
	Expansion device	Variable Local Restriction (2P)	
Water-cooling system	Pump	Controlled Mass Flow Rate Source (TL)	Thermal Liquid
	Heat exchanger	Pipe (TL)	
Thermal reservoirs		Controlled Temperature Source	Thermal
Air-side convective heat transfer		Convective Heat Transfer	

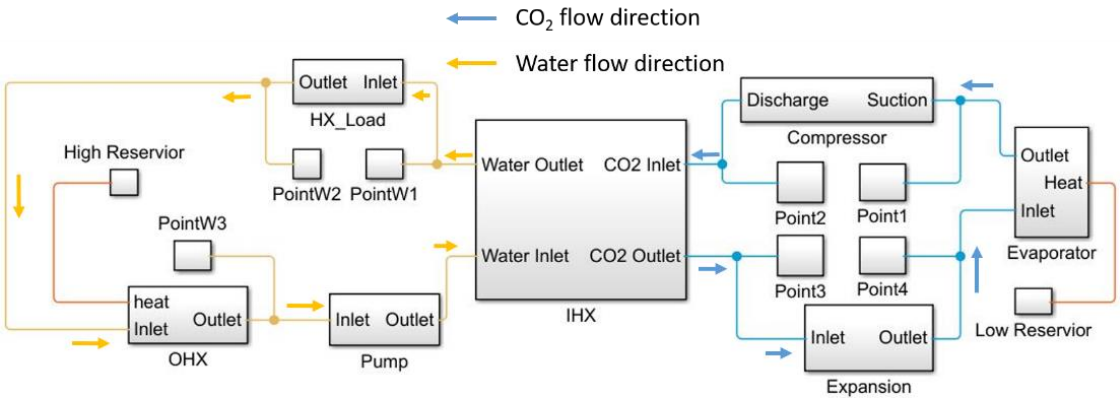

Fig. 1. Schematic of the thermal management system.

physical system and to create customized component blocks or modifying the original built-in blocks by Simscape™ language.

A schematic of the system is shown in Fig. 1. The thermal management system consists of a water-cooling system without phase change and a CO_2 heat pump system. The water-cooling system consists of a pump and three heat exchangers. One is an outdoor heat exchanger (OHX) to reject heat to the high-temperature reservoir, the second is to cool down the 'Load', and the last is an IHX to exchange heat with the heat pump system. The heat pump consists of a compressor, an expansion device, and an evaporator. Table 1 describes component blocks which used to model the present system and what they represent. The detail mathematical models or equations that make up each component block are stated on the Simscape™ Reference [3].

2.1 Compressor

A compressor is set up using 'Controlled Mass Flow Rate Source (2P)' block with the following assumptions:

1. Compression is in isentropic.
2. Heat transfer from or to the surroundings is negligible.

This block gives the specific value of set refrigerant mass flow rate.

2.2 Expansion device

An orifice is set up as an expansion device using 'Variable Local Restriction (2P)' block, under the isenthalpic expansion assumption. By changing the cross-section area of the orifice, the orifice controls pressure loss and refrigerant mass flow rate. The cross-section area of the orifice is controlled by the refrigerant temperature and superheating at the suction.

2.3 Heat exchanger (HX)

2.3.1 Refrigerant-side

Heat transfer and pressure drop of refrigerant flow are calculated based on the mass, momentum, and energy conservation equations using 'Pipe (2P)' block. This block represents a control volume and functions as a unit-segment for calculation. The block works on the following assumptions:

1. One dimensional flow
2. Fully developed flow
3. The gravitational effect is negligible.
4. Change in kinetic and potential energy is negligible.
5. Heat transfer is calculated with respect to the temperature of the fluid bulk.
6. The temperature gradient along the pipe is negligible.

Three conservation equations are as follows:

$$\frac{d}{dt}(\rho V) = \sum_{in}^{out} \dot{m}, \qquad (1)$$

$$\left(-\frac{dP}{dz}\right) = \left(\frac{G^2 dv}{dz}\right) + \left(\frac{f_D G^2 v}{2D_h}\right), \qquad (2)$$

$$\frac{d}{dt}(m\hat{u}) + \sum_{in}^{out} \dot{m}\hat{h} = \dot{Q}, \qquad (3)$$

where, t, ρ, V, $\dot{m}$, G, v, f_D, D_h, z, m, $\hat{u}$, $\hat{h}$, and $\dot{Q}$ represent the time, the refrigerant specific density, the refrigerant volume in the pipe, the refrigerant mass flow rate, the refrigerant mass flux, the refrigerant specific volume, the Darcy friction factor, the hydraulic diameter, the segment length, the refrigerant mass, the specific internal energy, the specific enthalpy, and the heat transfer rate, respectively. This block has only equipped with a condensation correlation for phase change heat transfer coefficient. So, a customized block is newly made for calculation of boiling heat transfer coefficient using Fang [4] model. This customized block is used for the evaporator modeling.

2.3.2 Water-side

Heat transfer and pressure drop of water flow are calculated based on the mass, momentum, and energy conservation equations using 'Pipe (TL)' block. Including 6 assumptions mentioned in the section 2.3.1, this block takes following additional assumptions:

1. Incompressible flow
2. Frictional pressure drop takes into consideration, only.
3. Convective heat transfer is dominant for inner-pipe flows.

2.3.3 Air-side

Convective heat transfer takes into consideration in 'Thermal' domain using 'Convective Heat Transfer' block. This block functions a simple convective heat transfer by a heat transfer area and coefficient as input parameters. Heat transfer coefficient of air-side is manually calculated by a user-defined script file in a fixed temperature using Park and Jacobi [5] model for louver-fin HXs. The dry air properties are obtained from Lemmon et al. [6].

2.4 Pump

'Controlled Mass Flow Rate Source (TL)' block is used for modeling a pump with the following assumptions:

1. Friction loss during pumping procedure is negligible.
2. Heat transfer from or to the surroundings is negligible.

Using this block, the water mass flow rate is controlled.

2.5 Thermodynamic properties

REFPROP ver. 10.0 (Lemmon et al. [6]) is linked with MATLAB. A look-up table of working fluid properties is built at the MATLAB workspace. Properties on this table are parameterized by pressure and normalized specific internal energy. Using 'Two-Phase Fluid Properties (2P)'

block, the properties table is brought into the Simscape™ physical domain. Thermodynamic properties of water are built in 'Thermal Liquid Properties (TL)' block. The water properties in this block are sourced from Coolprop, an open-source fluids database.

Table 2. Geometric specification of each component.

Component	Value
Compressor displacement (cm^3)	4
Expansion device	
Full open diameter (mm)	5
Min. diameter (mm)	5×10^{-4}
Evaporator	
Hydraulic diameter (mm)	1.5
Length (m)	1.3
Number of tubes	46
Total heat transfer area of air-side (m^2)	2.5
OHX	
Hydraulic diameter (mm)	5
Length (m)	1
Number of tubes	34
Total heat transfer area of air-side (m^2)	5
IHX (Double-pipe HX)	
Hydraulic diameter CO_2-side (mm)	10
Hydraulic diameter water-side (mm)	20
Length (m)	10
HX for the Load (Tubular)	
Hydraulic diameter (mm)	10
Length (m)	5
Number of tubes	1

Table 3. Simulation condition.

Content	Value	Remarks
Heat pump system		
High-pressure side		
Initial pressure (MPa)	7	
Initial temperature (K)	300	
Low-pressure side		
Initial pressure (MPa)	5	
Initial temperature (K)	300	
Water-cooling system		
Initial pressure (MPa)	0.101	
Initial temperature (K)	300	
Load (kW)	5	Constant
Thermal reservoir (Dry air)		
High-temperature side		
Temperature (℃)	30	Constant
Mean air velocity (m s^{-1})	17	Constant
Low-temperature side		
Temperature (℃)	20	Constant
Mean air velocity (m s^{-1})	3.5	Constant

2.6 Thermal reservoir

High and low-temperature reservoirs are set up using 'Controlled Temperature Source' and using 'Signal Builder' it is possible to control the temperature of the reservoirs with time. Dry air takes into consideration as a heat transfer medium.

3. SIMULATION

3.1 Conditions

Geometric specifications of each system component are summarized in Table 2. The water mass flow rate is fixed in 0.2 kg s^{-1}. Superheating at the suction keeps more than 3 ℃ and the expansion device opening is controlled by this set superheating. Simulation conditions and initial parameter set-up for each component are summarized in Table 3. For calculation, the 'ode23t', one of implicit variable time-step solvers, is selected. With changing the compressor speed as shown in Fig. 2, the system's behavior and performance are investigated.

3.2 Results

Fig. 3 shows the dynamic behavior of CO_2 heat pump and its performance corresponding with the compressor speed change which mentioned in Fig. 2, for 3 hours (10800 seconds).

In Fig. 3 (a) and (b), when the compressor starts up and it runs on 1500 rpm (revolutions per minute), the system temperature and pressure spread out and reach each steady-state position. After 1000 seconds later the compressor speed decreases to 1000 rpm, the pressure and temperature in the high-pressure side decrease and the pressure and temperature in the low-pressure side increase. After 4000 seconds, the compressor speed changes up and down and the trend of the system pressure and temperature follows up its speed. The system's dynamic behavior is shown in Fig.4 based on the pressure-enthalpy diagram.

The refrigerant mass flow rate is shown in Fig. 3 (c). There are over-shootings in the mass flow rate value when the compressor speed changes abruptly, but the mass flow rate keeps constant during the simulation. Each heat exchanger capacity changes with a change of the compressor speed as shown in Fig. 3 (d). The amount of increase on the IHX capacity is bigger than with that of the evaporator when the compressor speed increases. Because, the increase of the compressor speed results in its power consumption increase as shown in Fig. 3 (e) and the increased power which be input to the heat pump system should be rejected to the water-cooling system by heat transfer at the IHX. Furthermore, because the amount of increase in input power is bigger than the amount of increase in evaporator's cooling capacity, the system performance decrease when the compressor speed increases as shown in Fig. 3 (f).

The simulation results of the water system are shown in Fig. 5. The water temperature increases having a similar trend with that of the CO_2 heat pump system. After the water flows out from the Load, the water temperature increases because it absorbs the heat from the 'Load'. Then this water rejects its heat to the high-temperature thermal reservoir.

4. Limitations

The current air-to-air thermal management system which integrated a CO_2 heat pump with water cooling system demonstrate the dynamic behavior and performance varied with the CO_2 compressor rotation speed. The simulation shows reasonable results on the refrigerant pressure, temperature, heat exchangers capacity and COP corresponding with the change of compressor speed. However, it is not yet validated. Therefore, it is necessary for the simulation results to compare with experimental

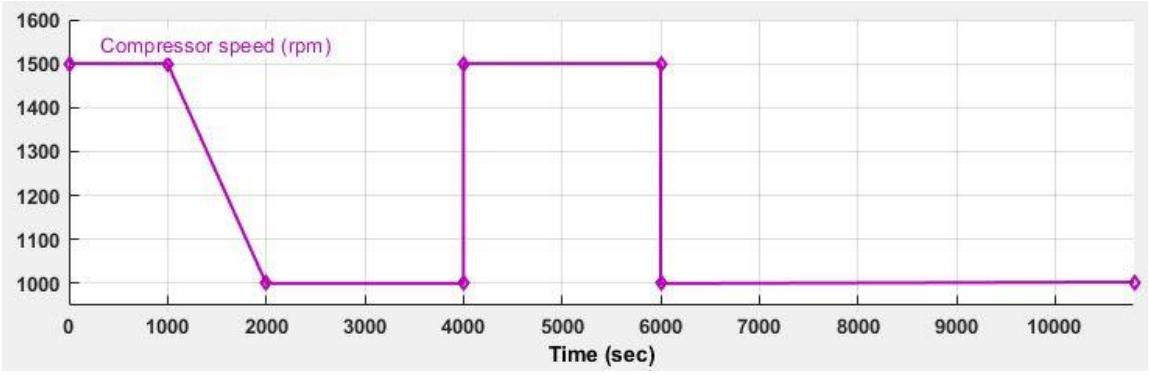

Fig. 2. Variation of the compressor speed.

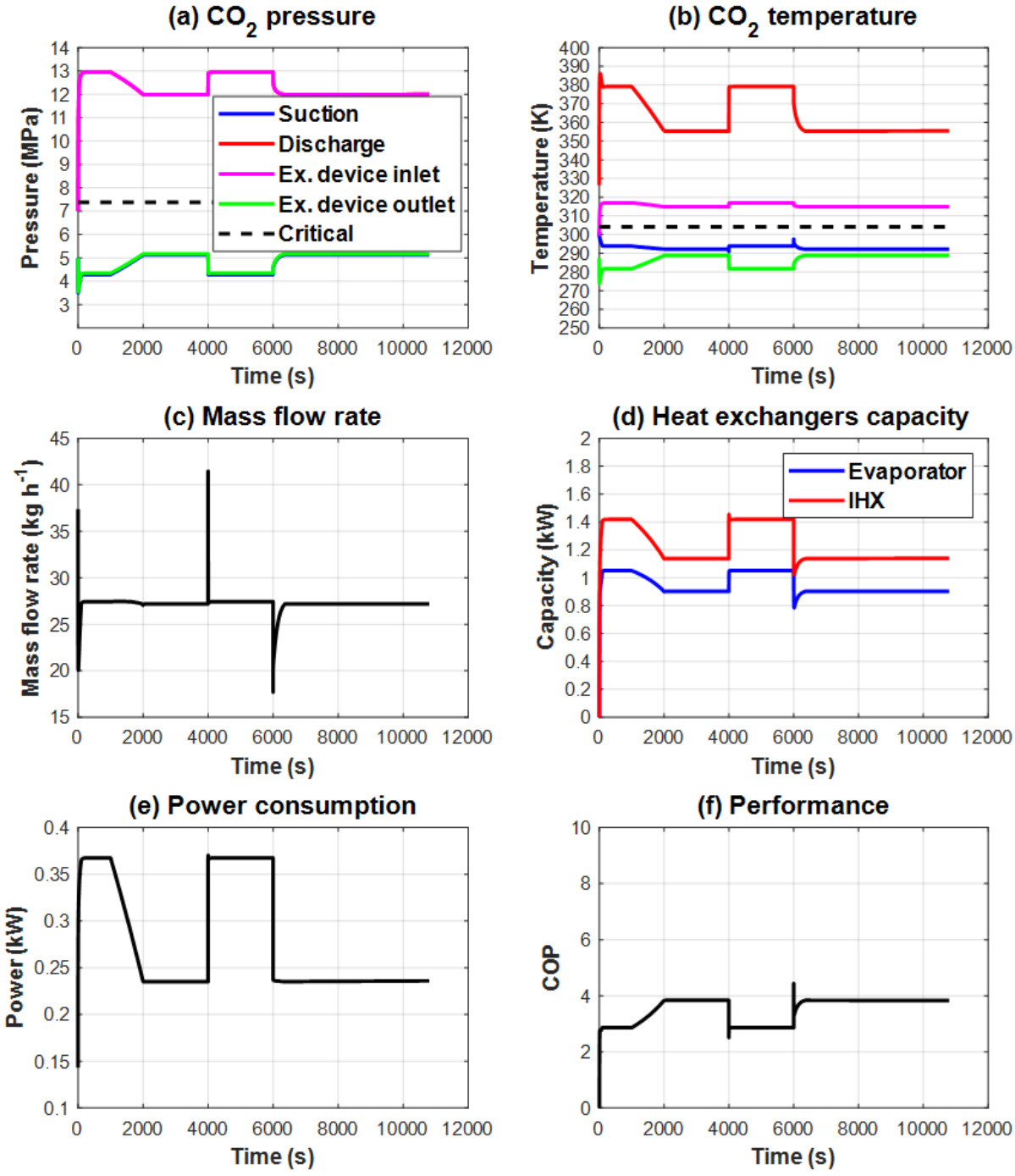

Fig. 3. Simulation results of the CO_2 heat pump system; (a) system pressure, (b) system temperature, (c) refrigerant mass flow rate, (d) heat exchanger capacity, (e) compressor power consumption, (f) system performance.

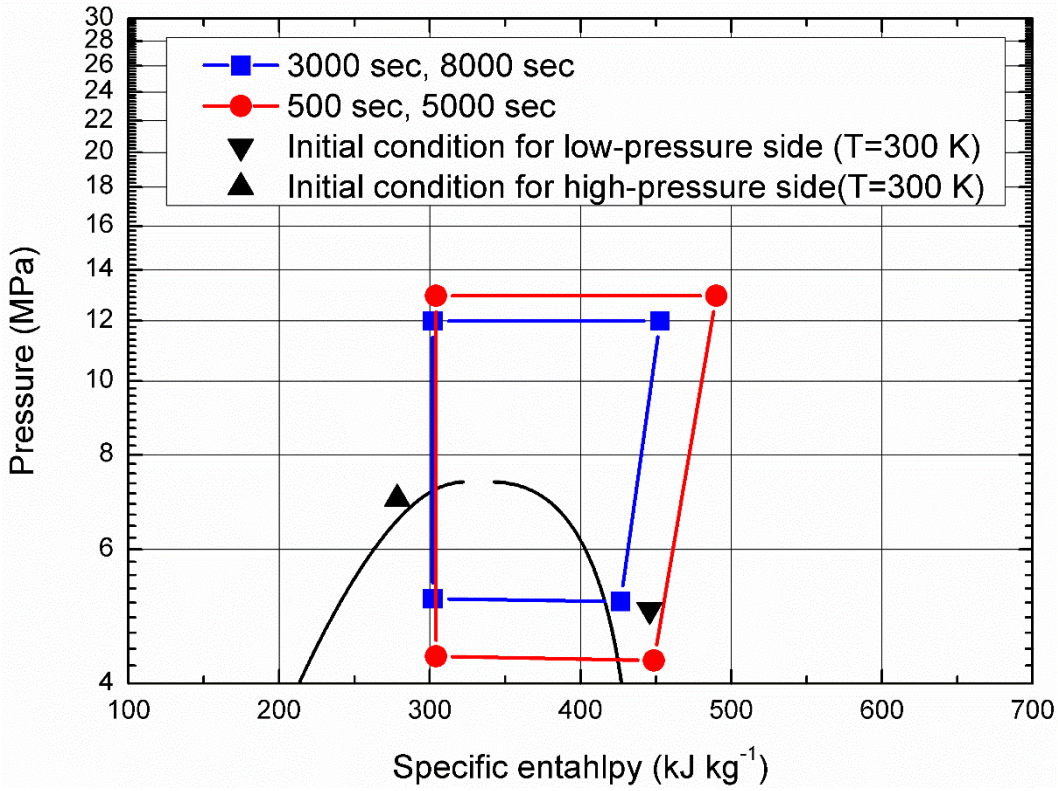

Fig. 4. Pressure-enthalpy diagram of the CO_2 heat pump system.

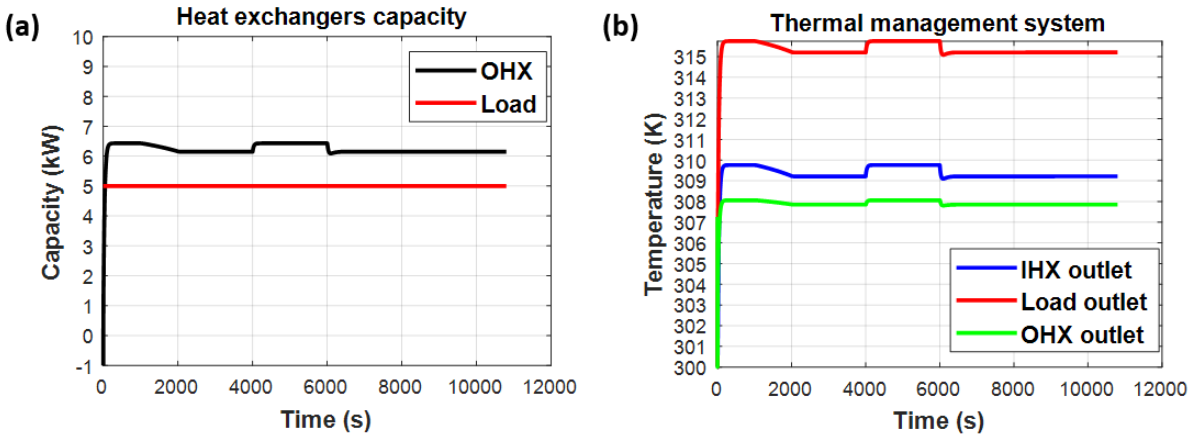

Fig. 5. Simulation results of the water-cooling system; (a) heat exchanger capacity, (b) water temperature.

results of a proper prototype or laboratory scale test-bench.

In the present model, the air-side heat transfer is set up in 'Thermal' domain. So, it is difficult to take into account the flow-dynamic effects caused by air-flow and its distribution. It is necessary to update the air-side of heat exchangers in detail for an air-to-air thermal system. Because the heat transfer rate of air-side has a dominant effect on the total system performance in air-to-air systems.

5. REFERENCES

[1] T. Pfafferott, G. Schmitz, Modelling and transient simulation of CO_2-refrigeration system with Modelica, Int. J. Refrig. 27 (2004) 42-52.

[2] R.F. Shi, D.G. Fu, Y.S. Feng, J.Q. Fan, S. Mijanovic, T. Radcliff, Dynamic modeling of CO2 supermarket refrigeration system. International Refrigeration and Air Conditioning Conference. (2010) 1127.

[3] The MathWorks, Inc., Simscape™ Reference ver. 4.5, Release 2018b.

[4] X. Fang, A new correlation of flow boiling heat transfer coefficients for carbon dioxide, Int. J. Heat Mass Transfer 64 (2013) 802 – 807.

[5] Y.-G. Park, A.M. Jacobi, Air-side heat transfer and friction correlations for flat-tube louver-fin heat exchangers, J. Heat Transfer, 131 (2009), 021801.

[6] E.W. Lemmon, I.H. Bell, M.L. Huber, M.O. McLinden, REFPROP ver. 10.0, NIST Standard Reference Database 23.

Development of 3D Printed Socket for Transtibial Prosthetic Leg

Wan Fatimatul Aifaa Wan Fadzil[1], Mohammad Azeeb Mazlan[1], Fazah Akhtar Hanapiah[2] and Abdul Halim Abdullah[1,*]
[1]Faculty of Mechanical Engineering, Universiti Teknologi MARA, 40450 Shah Alam, Selangor, Malaysia
[2]Faculty of Medicine, Universiti Teknologi MARA, 47000 Sungai Buloh, Selangor, Malaysia
*halim471@uitm.edu.my

Abstract: *The high cost to fabricate a good quality prosthetic leg became a burden to patients especially those with financial constraint. Experienced and specific skills are required to build a customized prosthetic leg and therefore also contribute to time consuming. The socket of the limb prosthesis requires adjustment and modification to accommodate the changes occurred in the residual limb over time. Development of 3D printed of lower limb socket as proposed in this study is expected to be an alternative in the near future. The objectives of this project are to (i) design a lower limb socket for below knee amputees according to size and shape of residual stump, (ii) analyze the performance of the socket at different infill density and (iii) fabricate the lower limb socket using 3D printing technology. The design stage of the project involved four main phases which are data collection and processing, product design, finite element analysis and fabrication of the socket using 3D printing. The analysis findings were discussed based on the resulting von mises stress, shear stress and total displacement. It was suggested that the socket is sufficient to be printed at 60% infill density. In comparable with other infill density percentage, the 60% model experienced only 0.413 MPa of von Mises stress and 0.0067mm of displacement.*

Keywords: Amputation, Lower Limb Socket, Prosthetic Leg, 3D printing, Infill Density

1. INTRODUCTION

Diabetes Mellitus patient usually undergo lower limb amputation due to leg necrosis. There are few types of lower limb amputations for instance hip, knee, ankle and foot amputations. The most common type of lower limb amputation are transtibial amputation, transfemoral and hemipelvic [1]. The risk of serious post-operative complications in a below knee amputation is far less than in a transfemoral amputation. The physical therapist and doctor can work with patients to fit them with the most appropriate device to help maximize their ability to walk. [2]. They may benefit from the skilled services of a physical therapist at different points in time after their amputation. As their stump shape changes, they may require different rehabilitation to keep them strong. They may require different prosthesis from time to time if their size and shape of their stump were changing gradually. That factor also contributes in the substantial amount of constructing prosthetic leg. As the alternative solution to this problem, the Industrial Revolution 4.0 technology and can be utilized and merged with the medical field. The Additive Manufacturing technology which is 3D printing technology and 3D simulation contributed the most in fabricating prosthetic leg [3]. Our objectives will be firstly to design a lower limb socket for a below knee amputation according to shape and size of residual the residual stump. Secondly, analyze the performance of the socket at different infill density and lastly fabricate the lower limb socket using 3D Printing technology.

2. METHODOLOGY

This project involved four main phases which are (i) the data collection and processing, (ii) product design and technology implementation, (iii) analysis and parametric study and (iv) fabrication using 3D printing technology. The phases of the study will be likely the procedure to develop the customized transtibial prosthesis leg.

2.1 Data Collection and Processing

The patient has to undergo 3D scanning to obtain the stump's size and shape [4]. Next, the stump model will be imported to the CAD software to guide the design process of the limb socket. The sample of the 3D scanning process is shown in figure 2.1.

Fig. 2.1 Example of 3D scanning process for the stump [4]

2.2. Product Design and Technology Implementation

The data obtained then undergo three design process which are designing sock layer, inner layer and outer layer. The initial sketches were performed as guidance to design the socket as illustrated in figure 2.2. This process basically will promote the customized prosthesis socket for each patient.

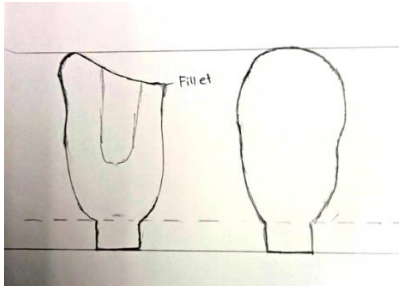

Fig. 2.2 Initial sketches of the socket

2.3. Analyses and Parametric Study

Different settings will have different results in term of energy absorption [5]. In this study, the variety of infill density were defined based on tensile modulus and flexural properties. Table 1 shows the mechanical properties of the PLA at various infill density [6]. Strength analysis was performed on final design according to their variable which is infill density to find von Mises stress, shear stress and total deformation.

Table 1 Material Properties of Polylactic Acid (PLA) at Various Infill Density

Infill Percentage (%)	Tensile Modulus (MPa)	Tensile Strength at Yield (MPa)	Flexural Strength (MPa)	Flexural Modulus (MPa)
20	469.3	9.9	20.6	630
40	938.6	19.8	41.2	1260
60	1407.9	29.7	61.8	1890
80	1877.2	39.6	82.4	2520
100	2346.5	49.5	103	3150

Analysis on infill density that had been tested were 20%, 40%, 60%, 80% and 100% by applying 600N load inside the socket and fixed support at the bottom of the socket as shown in figure 2.3.

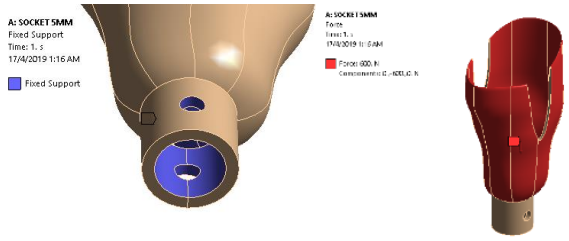

Fig. 2.3 Constraints (left) and loading (right) conditions applied in the analysis

The meshing was assigned to discretize the model into pieces which representing an element each to increase the accuracy of the analysis and to know how it would react in real life [7]. The meshed socket model is shown in figure 2.4

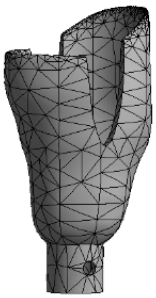

Fig. 2.4 Meshed model of the socket

2.4. Fabrication Using 3D Printing Technology

The fabrication of the model was made using 3D Printing technology by choosing the best design after performed the analysis which are PLA material with 15mm thickness and 60% infill density. The slicing process is visualized in figure 2.5.

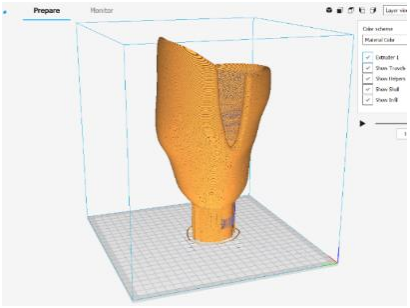

Fig. 2.5 Preparation for printing

3. RESULTS AND DISCUSSION

The infill percentages determined are 20%, 40%, 60%, 80% and 100%.

3.1 Stress Distribution of the Socket at Different Infill Density

The results show that the maximum value of von Mises stress are decreased from 20% infill and it becomes constant from 40% infill to 100% infill. The maximum von Mises stress is measured at 0.440 MPa for 20% infill while constant at the other infill density with 0.413MPa. The maximum von Mises stress in each model are compared to the yield strength of Polylactic Acid (PLA) material to evaluate their performance. All models demonstrate low value as compared to the yield strength of the materials.

For shear stress, the similar trend of von Mises stress results is evaluated. The compressive strength of samples with a 20% to 100% infill density increased significantly [8]. This is expected as the higher of the infill percentage, the greater load it can support thus, the stress is lower. The distribution of maximum Von Mises stress and maximum shear stress results are shown in figure 3.1.

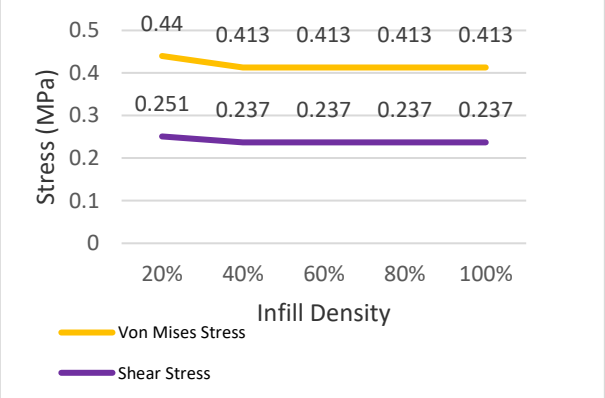

Fig. 3.1 Pattern of stress distribution at different infill density model

3.2 Total Deformation

The total deformation of 20% infill percentage is the highest while the lowest is 100%. Model with 60% infill percentage is chosen to be print as it was sufficient as the model has small value of total deformation. The graph of maximum total deformation results is shown in figure 3.2. From the graph, it shows that the higher the infill density, the greater the load it can support as the deformation decrease.

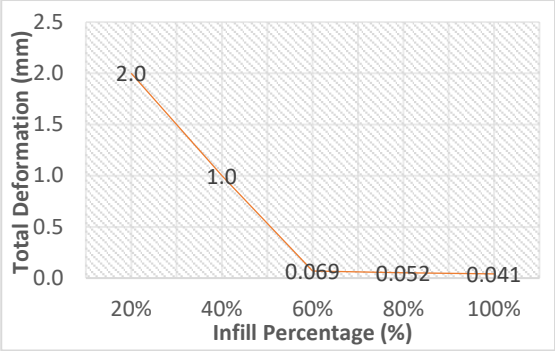

Fig. 3.2 Pattern of total deformation at different infill density

3.3 Fabrication Process

The socket was fabricated using 3D Printing technology with 60% of infill density. The material used was PLA (polylactic acid) filaments and the product is as in figure 3.3.

Fig. 3.3 The fabricated socket

4. CONCLUSION

The most suitable infill density to print the socket is PLA with 60% infill percentage as it is strong, durable and safe enough for the patient to wear it. At 60% infill density, the maximum von Mises stress and shear stress value are 0.413MPa and 0.237MPa, respectively. The higher the infill percentage, the greater load it can support. Set up printing at 60% infill is sufficient for the patient's socket to reduce time and cost consuming.

ACKNOWLEDGMENT

This research was supported by Universiti Teknologi MARA, UiTM under Grant No. 600-IRMI/PERDANA 5/3 BESTARI (103/2018).

5. REFERENCES

[1] Weledji, E. P., & Fokam, P. (2014). Treatment of the diabetic foot - to amputate or not? BMC surgery, 14, 83. doi:10.1186/1471-2482-14-83

[2] Brett Sears, P. (2018, December 30). Types of Lower Extremity Amputations. Retrieved from Very Well Health: https://www.verywellhealth.com/types-of-lower-extremity-amputations-2696172

[3] Cunningham, B. (2015, July 23). The MTC Builds a Simulation App to Optimize 3D Printing. Retrieved from COMSOL BLOG: https://www.comsol.com /blogs/the-mtc-builds-a-simulation-app-to-optimize-3d-printing/

[4] Organization, W. H. (2005). Guidelines for training personnel in developing countries for prosthetics and orthotics services. Geneva.

[5] Zefry Darmawan, Shigeyuki Haruyama, Ken Kaminishi, "Investigate Effect of Thickness and Additional Supporting Frame on Rollover Protective Structure', International Exchange and Innovation Conference on Engineering and Sciences (IEICES), 2017, pp 109-111

[6] Ultimaker. (2018). Technical Data Sheets. UM180821 TDS PLA RB V10.

[7] A. M. M. Ismaiel, S. M. Metwalli, B. M. N. El-Hadidi, "Fatigue Analysis of an Optimized HAWT Composite Blade", International Exchange and Innovation Conference on Engineering and Sciences (IEICES), 2016, pp 49-50.

[8] Abbas, D. F., D. M., & Ali, H. B. (2017). Effect of infill Parameter on compression property in FDM Process. International Journal of Engineering Research and Application, 16-19.

Characterization on Microstructural Evolution of Y_2O_3 Fabricated by Spark Plasma Sintering

Ji-Hwoan Lee[1], Byung-Nam Kim[2], Byung-Koog Jang[1,*]
[1]Interdisciplinary Graduate School of Engineering Science, Kyushu University, Kasuga 816-8580, Japan
[2]Research Center for Functional Materials, National Institute for Materials Science, Tsukuba 305-0047, Japan
*Corresponding author email: jang.byungkoog@kyudai.jp

Abstract: *The Y_2O_3 was fabricated by SPS technique with various heating rates (5, 10, 20, and 50°C/min) and holding times (2, 5, 20, and 60 mins) at 1000°C. In entire sintered bodies, grain size of center was larger than periphery. In case of the sintering loaded high heating rates (20 and 50°C/min) especially, the difference of grain size was significantly large (around 3.5 times on average). There was also a difference in pore distribution. In the uniformly sintered bodies, inter and intra-granular pore existed, but in the non-uniformly sintered bodies, differed pore distributions were observed such as the center (inter granular pore was dominant) and the periphery (inter and intra-granular pore). The porosity of the center dominated by inter-granular pore was higher than that of the periphery. Because there is not any clear mechanism, it is necessary to set the assumption (the mass transfer occurred from center to periphery) to explain for this phenomenon. Due to the endemic characteristics of SPS, the grain boundary mobility has increased with the phenomenon that the vacancies are gathered in center due to the mass transfer from center to periphery [1]. Therefore, there was a difference in the microstructure between the center and the periphery in entire sintered bodies. At the high heating rate (20 and 50°C/min), sintering was completed with lots of defects in sintered bodies and a large amount of coarsening was induced in the center due to dynamic grain growth [2]. The assumption of matter diffusion from the center to the periphery is based on the observation of the density evolution within the samples. The matter diffusion would be induced by the complicated electric current flowing along carbon punches, sheets, mold and powder during SPS. Magnetic fields induced the electric current would also be concerned to the matter diffusion. The details, however, are not clear. The additional experiments are required to demonstrate the assumption set out in this experiment.*

Keywords: Spark Plasma Sintering; Non-uniform Sintering Behavior; Matter Diffusion; Defect Diffusion; Y_2O_3.

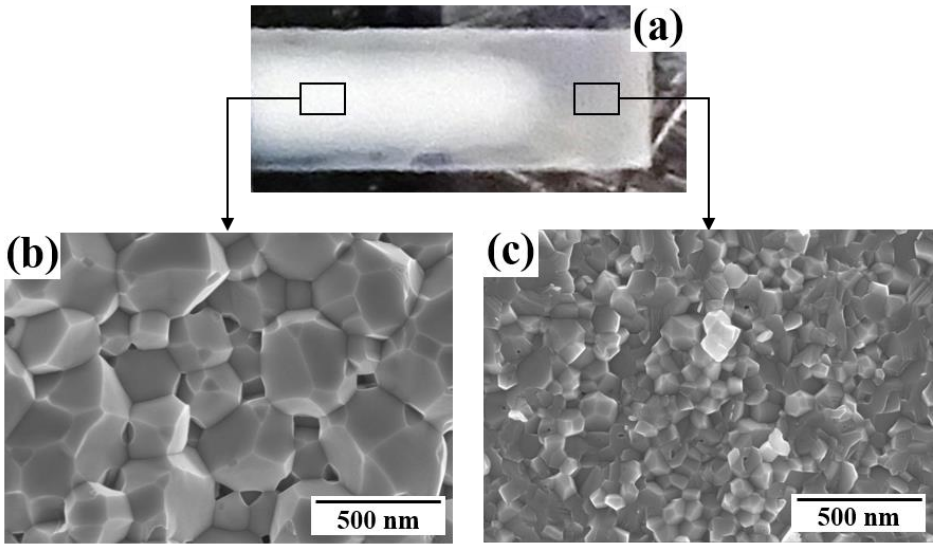

Fig. 1 (a) Cross section of Y_2O_3 sintered for 20 min at 50°C/min; SEM images of (b) center and (c) periphery.

References

[1] B.N. Kim, K. Hiraga, K. Morita, H. Yoshida, Y.J. Park, Y. Sakka, *Scripta Mater.* 80 (2014) 29-32.
[2] S. Grasso, C. Hu, G. Maizza, B.N. Kim, Y. Sakka, *J. Am. Ceram. Soc.* 94 (2011) 1405-1409.

The Effect of Vanadium Addition on the Microstructure and Mechanical Properties of Indefinite Chilled Cast Iron

Seung-Hyeon Kim[1], Eung-Ryul Baek[2], Byung-Koog Jang[1,*]
[1]Interdisciplinary Graduate School of Engineering Science, Kyushu University, Kasuga 816-8580, Japan
[2]Division of Materials Science and Engineering, Yeungnam University, Gyeongsan 38541, Republic of Korea
*Corresponding author email: jang.byungkoog@kyudai.jp

Abstract: *Since the rolled technology is oriented toward technology for the high productivity and high quality of rolled materials, it is required to develop high quality rolls with improved mechanical properties. Indefinite chilled cast iron (ICCI) is a common material which is used on the application of hot strip mill roller that requires a high wear, crack, and thermal resistance. Fatigue cracking occurs when the surface area of the roll with repeated heating and cooling reaches the fatigue limit and parts of the roll material are removed to facilitate wear. In particular, ICCI consists of martensite matrix with good wear resistance. It also secures abrasion resistance by purging more than 25% of Fe_3C. ICCI is very important for improving the material properties of rolls, with organizational factors such as the type, shape, and volume fraction and distribution status of carbide [1]. In this study, the form and distribution of carbide according to the content of the alloy element vanadium were controlled to improve mechanical properties. The addition of vanadium content was presumably able to enhance the wear and crack resistance due to the formation of vanadium carbide which contains high hardness. The base ICCI were added with different content of vanadium to observe the optimum content to resist the wear and crack propagation. Since the toughness can be measured by measuring bending strength, a three-point bending test was performed. After observing the fracture section of the three-point bending test, it was confirmed that the shape of the breaking section of the bending strength test specimen occurred with a small wall surface as the vanadium was added, and that the crack started was Fe_3C [2]. The bending test showed with a 4.3% addition of vanadium possesses highest crack propagation resistance due to a lower size of Fe_3C that formed in the material which followed by others 2.6% and 1.3% addition of vanadium. The wear test was carried out in ball on disk. The relative wear material has a hardness value of 1800Hv as Al_2O_3. The reason for selecting Al_2O_3 is that the relative material for checking the difference in wears for Fe_3C, which is lower in hardness than Al_2O_3. As a result of the wear test, stress is concentrated in Fe_3C and causes wear. The wear test using the ball on disc methods presented a narrower scratch on 4.3% addition compared to 0% addition of vanadium, due to the effect of the high hardness vanadium carbide cause the abrasion marks to narrow.*

Keywords: Indefinite Chilled Cast Iron; Microstructure; Vanadium Carbide; Fe_3C; Bending Test

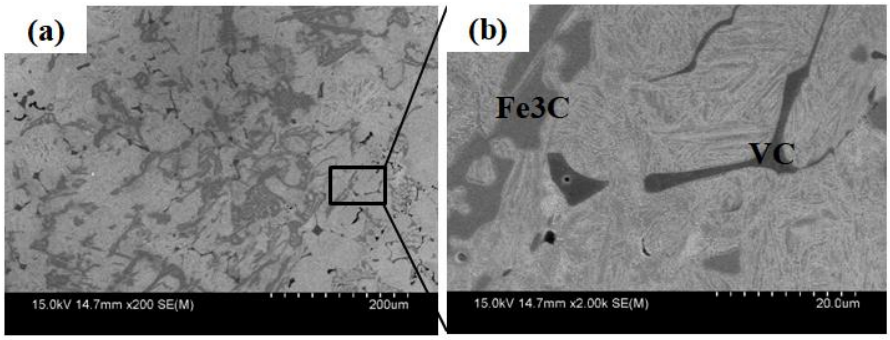

Fig. 1 SEM images of (a) microstructure of indefinite chilled cast iron with vanadium added and (b) Fe_3C and vanadium carbide.

References

[1] G. Huang, Z. Li, J. Tang, and Y. Tian, *ISIJ International*, 51 (2011) 939-944
[2] G. Kwame, W.D. Choi, Y.C. Suh, Y.K. Lee, and Y.J. Oh, *ASM International*, 46 (2015) 4819-4827

Synthesis of a novel sensor based on orcinol-dansyl derivative for fluoride ion detection

Paradee Kwanmuang, Apisit Songsasen, Weekit Sirisaksoontorn and Boontana Wannalerse*
Department of Chemistry and Center of Excellence for Innovation in Chemistry, Faculty of Science, Kasetsart University, Chatuchak, Bangkok, 10900, Thailand
*e-mail: fscibnw@ku.ac.th

Abstract: *A novel chemosensor (PK1) has been designed and synthesized in three steps. The binding ability of sensor PK1 with different anions (F^-, Cl^-, Br^-, $C_6H_5COO^-$, CH_3COO^-, $H_2PO_4^-$) in DMSO was evaluated by using ^1H NMR, UV-vis and fluorescence spectroscopic techniques. Upon addition of fluoride ion, the NH proton of PK1 disappeared because of deprotonation process. The sensor PK1 exhibited the spectral changes of selectivity to fluoride anion (F^-) over other anions, and the new absorption was found at 308 nm due to the internal charge transfer. The fluorescence emission at 415, 438, and 560 nm was quenched due to the complexation of PK1-F^-. The stoichiometric complexation was studies by Job's method as a 1:1 ratio of PK1 with F^-. The association constant between PK1 and fluoride was $4.5x10^4$ M^{-1} in the DMSO solution.*

Keywords: Chemosensor; Dansyl; Fluoride ion.

1. INTRODUCTION

The new chemosensors for anion detection have been extensively developed and gained much attention for several years [1,2]. Anions display in many important aspects such as biochemical, environmental and industrial systems including things in daily life. Fluoride ion (F^-) is mixed in the gradient of toothpaste for protecting caries in human teeth. However, the risk of fluoride ion depends on extreme concentration levels. The excess fluoride level can cause many problems in the human body such as, thyroid problem, bone disease and dental fluorosis [3-4]. According to United States environmental protection agency (USEPA) and world health organization (WHO), the limitation of fluoride in water is 1.5 mg/L (79 µM) [5]. Host-guest chemistry is a simple and fast method for anion detection. The design and synthesis of host molecules have greatly concentrated on the selectivity and sensitivity of binding sites for anion sensing. Generally, chemosensors can interact with anions via hydrogen bonding, electrostatic, or hydrophobic interactions [6]. The dansyl fluorophore is well known due to its high fluorescence quantum yield and tremendous sensitivity to response in its system. Furthermore, dansyl fluorophore is easy to modify the molecule under simple reactions [7]. In this research, we report the synthesized sensor PK1 which consists of the amide moiety as a binding unit and the dansyl group as a signaling unit for fluoride ion detection. The complexation between sensor PK1 and fluoride ion was investigated by ^1H-NMR, UV-visible and fluorescence techniques.

2. EXPERIMENT

2.1 Chemicals and instrumentation

All reagent and solvents were obtained commercially at analytical grade and used without further purification. All the tetrabutylammonium (TBA) salts of various anions (F^-, Cl^-, Br^-, CH_3COO^-, $C_6H_5COO^-$, $H_2PO_4^-$) were purchased from Merck KGaA. The ^1H and ^{13}C NMR spectra were recorded on a Bruker Advance 500 using $CDCl_3$ and $(CD_3)_2SO$ as solvents. FT-IR spectra were taken with Perkin Elmer 2000 using KBr pellet technique in the range of 4000-400 cm^{-1}. High resolution mass spectra (HRMS) were measured on a Bruker microtof-Q III. Elemental analysis of all compounds was examined by SCIENTIFIC AND TECHNOLOGICAL RESEARCH EQUIPMENT CENTER. UV-vis spectra were recorded on a UV-visible spectrophotometer (SHIMADZU UV-1800).

2.2 Synthesis and structural characterization of PK1

The sensor PK1 was successfully prepared by the synthetic route as shown in scheme 1.

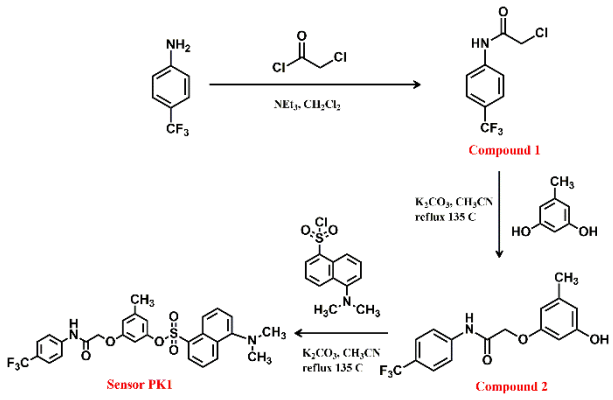

Scheme 1. The synthetic route of sensor PK1

2.2.1 Synthesis of 2-chloro-N-4-(trifluoromethyl)phenyl) acetamide (Compound 1)

4-(trifluoromethyl) aniline (2.5 g, 0.0155 mol) and triethylamine (3.25 mL) in dichloromethane (10 mL) were stirred under nitrogen atmosphere for an hour. The chloroacetyl chloride (4.95 mL) in dichloromethane (2

mL) was added dropwise in ice bath. The mixture was stirred for 24 h. The reaction mixture was poured into water and extracted (3x20 mL) with dichloromethane. The organic layer was dried with anhydrous Na_2SO_4. The CH_2Cl_2 solvent was evaporated by using rotary evaporator. The compound 1 was afforded as a brown solid in yield of 85.03% ^{1}H NMR (400 MHz, $CDCl_3$, ppm): δ = 8.41 (s, 1H), 7.72 (d, J = 8.6 Hz, 2H), 7.65 (d, J = 8.7 Hz, 2H), 4.25 (s, 2H)

2.2.2 Synthesis of 2-(3-hydroxy-5-methylphenoxy)-N-(4-(trifluoromethyl)phenyl)acetamide (Compound 2)

3,5-dihydroxytoluene (1.0448 g, 8.42 mmol) and K_2CO_3 (1.7450 g, 0.0126 mol) in acetonitrile (15 ml) were stirred and refluxed at 135°C under nitrogen atmosphere for an hour. Then, 2-chloro-N-(4-(trifluoromethyl) phenyl) acetamide (2 g, 8.42 mmol) in acetonitrile (15 ml) was added dropwise. The mixture was stirred for 13 h. The reaction mixture was poured into water and extracted with dichloromethane. The organic layer was dried with anhydrous Na_2SO_4. The product was purified by column chromatography using EtOAc/CH_2Cl_2 = 1:9 (v/v) as an eluent to get compound 2 as white solid (26.61%yield). ^{1}H NMR (400 MHz, $CDCl_3$, ppm): δ = 8.39 (s, 1H), 7.75 (d, J = 8.6 Hz, 2H), 7.68 – 7.54 (m, 2H), 6.50 – 6.25 (m, 3H), 5.32 (s, 1H), 4.63 (d, J = 13.0 Hz, 2H), 2.32 (s, 3H).

2.2.3 Synthesis of 3-methyl-5-(2-oxo-2-((4-(trifluoromethyl) phenyl) amino) ethoxy) phenyl 5-(dimethylamino)naphthalene-1-sulfonate (Sensor PK1)

Compound 2 (0.7 g, 2.15 mmol) and K_2CO_3 (0.4461g, 3.23 mmol) in acetonitrile (15 mL) were stirred and refluxed at 135°C under nitrogen atmosphere for an hour. Then, dansyl chloride (0.5805g, 2.15 mmol) in acetonitrile (15 mL) was added dropwise. The mixture was stirred for 7 h. The reaction mixture was poured into water and extracted with dichloromethane. The organic layer was dried with anhydrous Na_2SO_4. The product was purified by column chromatography using CH_2Cl_2 as an eluent to afford sensor PK1 as a yellow solid (77.54%yield). ^{1}H NMR (400 MHz, $CDCl_3$, ppm): δ = 8.66 (d, J = 8.3 Hz, 2H), 8.49 (d, J = 8.6 Hz, 2H), 8.27 (s, 2H), 8.15 (dd, J = 7.3, 1.2 Hz, 2H), 7.77 – 7.66 (m, 6H), 7.63 (d, J = 8.6 Hz, 4H), 7.49 (dd, J = 8.4, 7.5 Hz, 2H), 7.35 – 7.25 (m, 3H), 6.66 (s, 2H), 6.51 (s, 2H), 6.40 (t, J = 2.1 Hz, 2H), 4.37 (s, 4H), 2.96 (s, 12H), 2.23 (s, 6H). ^{13}C NMR (400 MHz, $CDCl_3$, ppm): δ = 165.8, 157.1, 150.3, 141.4, 139.7, 132.1, 131.2, 131.0, 130.1, 129.1, 126.4, 125.3, 123.1, 122.6, 119.4, 116.9, 115.8, 114.2, 106.3, 67.4, 53.4, 45.5, 42.8, 32.2, 29.7, 26.4, 23.4, 21.5. FT-IR (KBr, cm^{-1}): ν = 3369, 1701, 1599, 1533, 1460, 1293,1067; HRMS (ESI): m/z $[M+H]^+$ calc.: $C_{28}H_{25}F_3N_2O_5S$, 559.57, and found: 559.1499; Elemental Analysis : calc. $C_{28}H_{25}F_3N_2O_5S$, %C = 60.21, %H = 4.51, %N = 5.02, and found: %C = 60.61, %H = 4.28, %N = 4.67.

2.3 The preparation of stock solution for binding study between sensor PK1 and various anions

Stock solutions of analytes (F^-, Cl^-, Br^-, CH_3COO^-, $C_6H_5COO^-$, $H_2PO_4^-$ in the form tetrabutylammonium salts) with the concentration of $1x10^{-3}$ M were prepared in DMSO. Sensor PK1 was dissolved in DMSO to give the stock solution with the concentration of $5x10^{-4}$ M.

3. RESULTS AND DISCUSSION

3.1 The binding behavior between sensor PK1 and various anions

3.1.1 ^{1}H NMR study

To investigate the sensing mechanism of sensor PK1 towards various anions, adding 4 equiv anions to PK1 was studied in DMSO-d_6 as a solvent in Fig 1. When adding fluoride ion, the NH proton of sensor PK1 disappeared because of deprotonation process. And also, the deprotonation NH proton of PK1 gave the signal of H_2F^- at 16.07 ppm. [8] Moreover, the aromatic proton shifted to upfield, indicating the increase of electron density. For chloride, bromide, benzoate, acetate and phosphate, the NH signal of PK1 displayed to downfield shift under hydrogen bonding interaction. Meanwhile, thearomatic protons slightly shifted to upfield. These results indicated that the sensor PK1 has high selectivity to the fluoride ion.

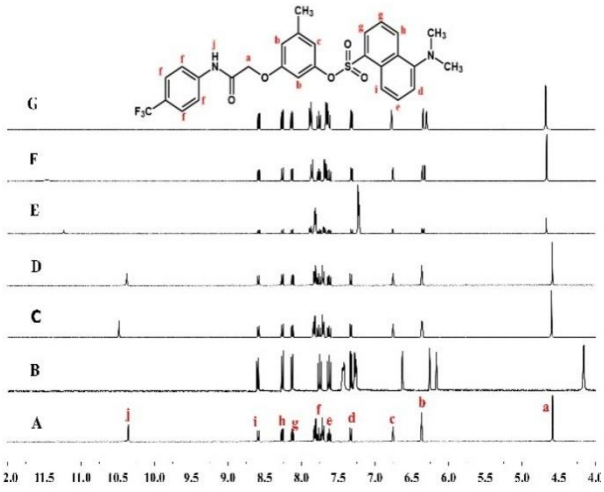

Figure 1. ^{1}H NMR spectra of (A) PK1 = $5x10^{-4}$ M. (B) PK1 + 4 equiv of F^- (C) PK1 + 4 equiv of Cl^- (D) PK1 + 4 equiv of Br^- (E) PK1 + 4 equiv of $C_6H_5COO^-$ (F) PK1 + 4 equiv of CH_3COO^- (G) PK1 + 4 equiv of $H_2PO_4^-$ in DMSO-d_6

3.1.2 UV-vis spectroscopic studies

The anion binding affinity of sensor PK1 with different anions (F^-, Cl^-, Br^-, $C_6H_5COO^-$, CH_3COO^-, $H_2PO_4^-$) was performed by UV-vis absorption spectroscopy. Upon addition of 20 equiv. F^- to PK1 solution, the absorption band at 358 nm was decreased and a new absorption band at 308 nm was found as shown in Fig.2A. The results occurred under internal charge transfer process [9-11]. Moreover, the graph bars exhibited that only F^- ion gave the new band at 308 nm in Fig 2B. Under the

same condition, there was no the absorption band at 308 nm when adding other anions.

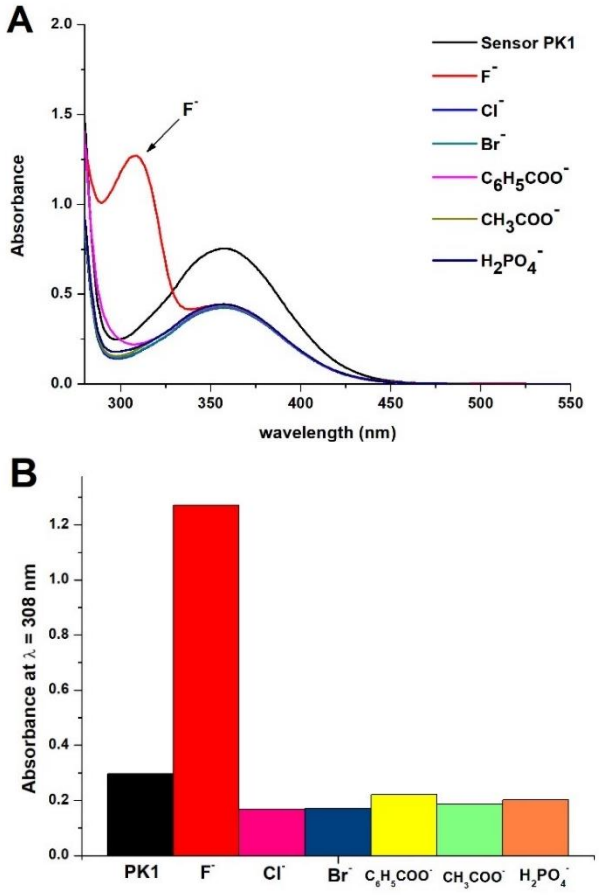

Figure 2. (A) UV-vis absorption spectra of PK1 ($2x10^{-4}$ M) in DMSO/$TBAPF_6$ in the absence and presence of 20 equiv. of various anions: F^-, Cl^-, Br^-, CH_3COO^-, $C_6H_5COO^-$, $H_2PO_4^-$ (B) The graph bars at λ = 308 nm of PK1 and PK1 + various anions.

3.1.3 Fluorescence spectra

The fluorescent sensing properties of sensor PK1 to F^- with different concentrations were performed by the titration experiment in Fig 3.

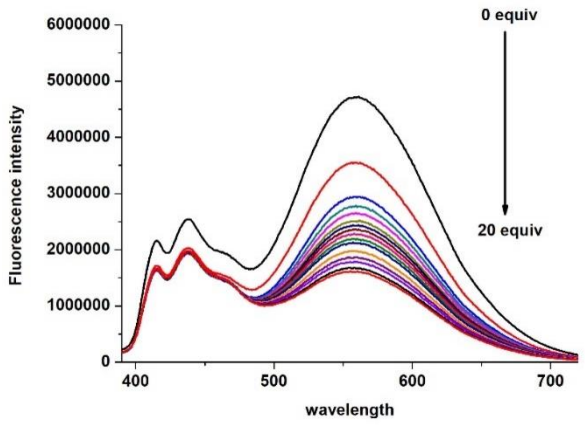

Figure 3. Fluorescence spectra of sensor PK1 (DMSO, $1x10^{-5}$ M.) upon the addition of F^- ion (0-20 equiv.) λ_{ex} = 370 nm.

The fluorescence emission band at 415, 438, and 560 nm were quenched upon the addition of F^- ion. This result indicates the complexation between PK1 and F^- ion in the solution [12]. Moreover, the Job's plot of PK1 and F^- ion suggests that the fluorescence intensity at 558 nm reached the maximum at 0.5 mole fraction (Fig. 4), which was identified as a 1:1 ratio complexation of PK1 and F^-.

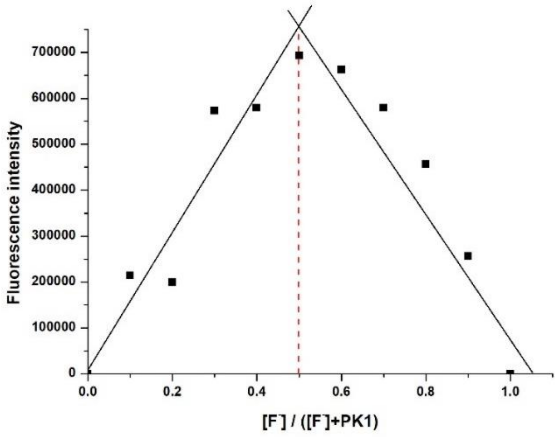

Figure 4. Job's plot of PK1 and fluoride ion in DMSO/$TBAPF_6$. The emission wavelength was 558 nm (λ_{ex} = 370 nm).

3.2 Calculation of the association constant

The association constant can be calculated by using the Benesi-Hildebrand equation [13]. From the relationship between $1/(F-F_0)$ and $1/[F^-]$, a linear plot was obtained with R^2 = 0.9923. The association constant between sensor PK1 and F^- ion was equal to $4.5x10^4$ M^{-1}.

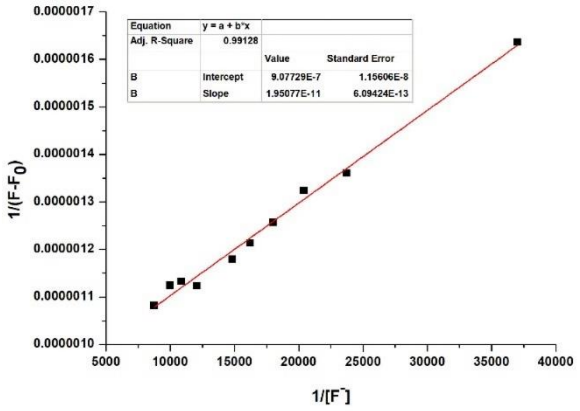

Figure 5. Benesi-Hildebrand plot (λ_{ex} = 370 nm) of $1/(F-F_0)$ vs $1/[F^-]$ based on a 1:1 complexation between PK1 and F^-.

4. CONCLUSION

In summary, we have successfully developed a new orcinol-dansyl derivative (sensor PK1). From ^1H NMR, UV-vis and fluorescence titration studies, the NH proton of PK1 can be deprotonated by F^- ion. It was found that a new absorption band at 308 nm was ascribed to the internal charge transfer. Moreover, the fluorescence emission at 415, 438, and 560 nm was quenched due to complexation between PK1 and F^-.

5.ACKNOWLEGEMENTS

We would like to thank the Thailand Research Fund, Kasetsart University Research and Development Institute, the Department of Chemistry, Faculty of science, Kasetsart University and the Center of Excellent for Innovation in Chemistry (PERCH-CIC), the Ministry of Higher Education, Science, Research and Innovation for financial support.

6. REFERENCES

[1] Chen, C.-F. and Q.-Y. Chen, A tetra-sulfonamide derivative bearing two dansyl groups designed as a new fluoride selective fluorescent chemosensor, Tetrahedron Letters. 45(20)(2004) 3957-3960.

[2] Miao, R., et al, A C-linked peptidocalix[4]arene bearing four dansyl droups: a highly selective fluorescence chemosensor for fluoride ions, Tetrahedron Letter. 45(25)(2004) 4959-4962.

[3] Wu, Y.-C., et al, Design and application of tri-benzimidazolyl star-shape molecules as fluorescent chemosensors for the fast-response detection of fluoride ion, Sensors and Actuators B: Chemical. 237(2016) 865-875.

[4] Kaur, N. and G. Jindal, "Switch on" fluorescent sensor for the detection of fluoride ions in solution and commercial tooth paste, Spectrochimica Acta Part A: Molecular and Biomolecular Spectroscopy. 223(2019) 117361

[5] Gowri, A., et al, A pyrene based colorimetric chemosensor for CO_2 gas detection triggered by fluoride ion, Chemical Physics Letters. 719(2019) 67-71.

[6] Kodlady, S. N., et al, Aromatic aldehyde based chemosensors for fluoride and cyanide detection in organic and aqueous media: Ascertained by characterization, spectroscopic and DFT studies, Inorganic Chimica Acta. 494(2019) 245-255.

[7] Ocak, Ü., et al, Calixarenes with dansyl groups as potential chemosensors, Inorganic Chimica Acta. 381(2012) 44-57.

[8] Liu, S., et al, Distinctive fluoride fluorescent probes with ratiometric characteristics combinate desilylation, hydrogen bond and ESIPT process: Spectral and mechanistic studies, Sensor and Actuators B: Chemical. 255(2018) 401-407.

[9] Yao, K., et al, A novel coumarin-based fluorescent sensor for Ca^{2+} and sequential detection of F^- and its live cell imaging, Spectrochimica Acta Part A: Molecular and Biomolecular Spectroscopy. 216(2019) 385-394.

[10] Niu, Q., et al, A highly selective turn-on fluorescent and naked-eye colorimetric sensor for cyanide detection in food samples and its application in imaging of living cells, Sensors and Actuators B: Chemical. 276(2018) 13-22.

[11] Ashok Kumar, S. L., et al, Novel heterocyclic thiosemicarbazones derivatives as colorimetric and "turn-on" fluorescent sensors for fluoride anion sensing employing hydrogen bonding, Spectrochimica Acta Part A: Molecular and Biomolecular Spectroscopy. 113(2013) 123-129.

[12] Liu, S.-y., et al, Fluorescent sensors for amino acid anions based on calix[4]arenes bearing two dansyl groups, Tetrahedron: Asymmetry. 16(8)(2005) 1527-1534.

[13] Zhou, T., et al, Synthesis and evaluation of a new furfuran-based rhodamine B fluorescent chemosensor for selective detection of Fe^{3+} and its application in living-cell imaging, Sensors and Actuators B: Chemical. 253(2017) 292-301.

Morphological, Structural and Electrochemical Studies of Conductive Polyaniline Coated Polyester Fabrics

Muhammad Faiz Aizamddin[1], Mohd Muzamir Mahat[1*], Mohd Azizi Nawawi[2*]

[1]*School of Physics and Materials Studies, Faculty of Applied Sciences, Universiti Teknologi MARA, 40450 Shah Alam, Selangor, Malaysia*
[2]*School of Chemistry and Environmental Studies, Faculty of Applied Sciences, Universiti Teknologi MARA, 40450 Shah Alam, Selangor, Malaysia*

*Corresponding author email: *mmuzamir@uitm.edu.my* and *azizi_nawawi@uitm.edu.my*

Abstract: *In this work, polyaniline (PANI) fabrics were fabricated using a facile method namely, immersion. Polyester (PES) fabrics were immersed in PANI solution followed by a drying process. In order to make the fabric conductive, p-*toluene sulfonic acid *(pTSA) was priory added into polymer solution as dopant. Different concentrations of dopant were used i.e. 0.3 wt%, 0.6 wt% and 0.9 wt%. Upon addition of the dopant, the colour of PANI fabric changed from blue (PANI Emeraldine Base) to green (PANI Emeraldine Salt) which indicates that the PANI fabric has transformed into the conductive state. Field Emission Scanning Electron Microscope (FESEM) and Fourier Transform Infrared Spectroscopy (FTIR) were used to analyse the morphology and reveal the chemical structure of doped and undoped PANI fabrics, respectively. Electrochemical Impedance Spectroscopy (EIS) was used to measure the conductivity of fabricated fabrics. FESEM analysis revealed the random distribution of PANI precipitates on PES which makes the surface rough. This provides a higher surface area and a more effective surface for chemical interaction with the acid. Fourier Transform Infrared Spectroscopy (FTIR) shows N-H stretching mode peak characterizing PANI appeared at 3436.18 cm^{-1} (PANI EB), 3444.02 cm^{-1} (0.3 wt% pTSA), 3428.34 cm^{-1} (0.6 wt% pTSA) and 3343.22 cm^{-1} (0.9 wt% pTSA) after the fabrication process. This indicates that PANI has been incorporated within the fabric. The EIS results revealed that doping with 0.9 wt% pTSA gives excellent conductivity of 3.30 x 10^{-3} S/m compared to undoped sample (1.06x10^{-7} S/cm) on PES fabric.*

Keywords: Polyaniline, conductive fabrics, Field Emission Scanning Electron Microscope (FESEM), Fourier Transform Infrared Spectroscopy (FTIR) and Electro Impedance Spectroscopy (EIS).

1. INTRODUCTION

Conducting polymer (CP) is the polymer that has the ability to conduct electricity. It is a popular basic material for advanced materials including electromagnetic shielding [1], batteries [2], biosensors [3] and electronic devices [4,5]. CPs are widely used by researchers because of their tunable properties and stability. Researchers have also shown certain polymers such as polyaniline, polyethylene or polypropylene which possess an extended π conjugation bonds or electrons along the polymer backbone, exhibit semiconducting behavior [6]. PANI can exist in three different forms which are leucoemeraldine base (LEB, fully reduced form), emeraldine base (EB, partially oxidized form) and base pernigraniline (PNB, fully oxidized form) [7]. In order to make the CP (PANI) conductive, it needs to undergo the process called doping and make them electrically conducting. Mahat *et al*., (2015) [8] reported that doping of PANI is a reversible process which depend on environmental conditions such as pH and temperature. They can simply be doped with reducing or oxidizing agent such as *p*-toluene sulfonic acid (*p*TSA), hydrochloric acid (HCl) and camphorsulfonic acid (CSA). Since then, there are many studies have been conducted to fit these requirements [9].

Fabric is one of the best candidates to have the flexibility and electronic properties. This can be achieved by incorporating CPs into a fabric. Different types of fabric can portray different properties of conductivity, surface morphology and physical. This is due to the nature of their physical structure. Gomes *et al.*, (2012) [10] reported that CPs coated polyester (PES) fabric can have conductivity up to high as 10 to 10^3 S/cm in conductivity. In another study, PES fabric can exhibit a high conductivity after incorporation of CPs that has more interlacement structure which shows higher resistivity [11].

In this study, we fabricate a conductive fabric using an immersion method. This is an approach to render the conductivity properties of fabrics utilizing PANI as the conductive agent. *p*-Toluene Sulfonic Acid (*p*TSA) was used as the dopant during the synthesis of PANI. Polyester (PES) fabrics were immersed in a PANI solution, followed by drying process. These fabrics were then characterized by Fourier Transform Infrared Spectroscopy, Field Emission Scanning Electron Spectroscopy (FESEM) and Electrochemical Impedance Spectroscopy (EIS) for their chemical structure, morphology and conductivity of PANI fabricated fabrics, respectively.

2. EXPERIMENTAL

2.1 Materials

Polyester fabric (50 cm × 60 cm) were purchased from Kamdar Sdn. Bhd. Aniline water base was purchased from Sigma-Aldrich. Hydrochloric acid (HCl), *p*-toluene sulfonic acid (*p*TSA), sodium hydroxide (NaOH), ammonium persulfate $(NH_4)_2S_2O_8$, sulfuric acid (H_2SO_4) and dimethylformamide (DMF) were purchased from ACROS, UK.

2.2 Synthesis of PANI

A 10 mL of aniline was mixed in 100 mL of HCl and stirred at room temperature. After that, a 22 g of ammonium persulfate (APS) was dissolved in distilled water. APS solution was added into aniline solution drop by drop at room temperature and stirred for 4 hours until a green solution obtained. Then, the green solution was filtered using filter paper, separating the solution and precipitate. The precipitate was then washed with HCl, acetone and distilled water followed by a drying process for 24 hours. The dried precipitate was mixed with 1M of NaOH and HCl, followed by stirring it for 4 hours. Next, they were dried in the furnace at 60 ^{o}C to obtain polyaniline emeraldine base (PANI EB) powder (blue colour). This process was repeated 2 times.

2.3 Preparation of doped and undoped PANI-EB with *p*-Toluene Sulfonic Acid (*p*TSA)

PANI EB powder was dissolved in a 60 mL of dimethylformamide (DMF). Then, 0.3 wt% of *p*TSA was added into the solution. The colour of solution turned from blue to green indicating its conductive state. The same step was repeated for different concentration of *p*TSA (0.6 wt%, 0.9 wt%). PANI without the addition of acid served as a control (undoped PANI). The PANI solutions were centrifuged for 30 minutes with 400 rpm of speed.

2.4 Immersion of cotton and PES fabric doped and undoped PANI

PES fabrics were cut into 5 cm × 5 cm. They were immersed in the PANI solution for 15 minutes followed by a drying process. They were kept in the dark place for further use.

2.5 Material Characterisations

2.5.1 Fourier Transform Infrared Spectroscopy (FTIR)

Perkin-Elmer Fourier Transform Infrared Spectroscopy (FTIR) was used to investigate the chemical structure of the sample using the attenuated total reflectance (ATR) FTIR technique. The FTIR spectra were recorded between 400-4000 cm^{-1} at the frequency of 20 kHz with resolution of 16 cm^{-1} by averaging 16 scans for each sample. A mirrored diamond surface were used under the spectroscopic conditions to produce each spectrum and BIO-RAD WIN-IR PRO software was used to analyse the spectrum.

2.5.2 Field Emission Scanning Electron Microscope (FESEM)

Field Emission Scanning Electron Microscope (FESEM) model TM3030 Plus was used for morphological analysis. The sample was firstly mounted on the sample stage by sticking with carbon tape and placed in the chamber. Sample were viewed and magnified at 1000×.

2.5.3 Electrochemical Impedance Spectroscopy (EIS)

HIOKI 3532-50LCR Hi Tester Electrochemical Impedance Spectroscopy was used and operated at 100 Hz to 1000 kHz frequency at room temperature. Two stainless steel disc electrodes with 2.0 cm diameter were used to sandwich PANI fabrics. The conductivity (σ) of the samples was calculated using the following formula:

$$\sigma = \frac{L}{R_B \times A}$$

Where L is the thickness of the fabric, R_B is bulk resistance and A is contact surface area of electrode with the fabric.

3. RESULTS AND DISCUSSION

3.1 Synthesis of PANI

In this work, PANI was synthesized by chemical polymerization of aniline according to the method reported by Tang, S. J. *et al.* (2011) [12]. Treating the synthesized polymer with an acid is known to cause change in chemical composition through modification of backbone chains of the polymer [13]. This change will has enhance the electrical properties of PANI as it could become a conductive polymer through protonation process. The transformation can be observed by looking at colour changes of the solution in which the blue colour of emeraldine base solution will turn into green colour emeraldine salt upon protonation by the acid [14]. The chemical equation illustrating the equilibrium between the two states is shown in Fig. 1.

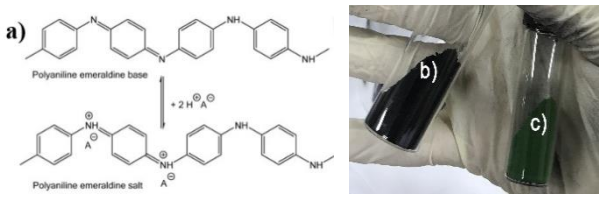

Fig. 1. a) Chemical structure of PANI EB and PANI ES. b) PANI EB Powder (Undoped State). C) PANI ES Powder (Doped State).

Following this, immersion process was carried out to transfer the PANI into the fabrics. Fig. 2. (b and c) shows the images of PANI on fabrics at different PANI states. These visual suggested that PANI fabrics can be fabricated using a facile immersion method, producing a conductive fabric.

Fig. 2. a) Bare PES Fabric. b) Undoped PANI-PES Fabric. c) Doped PANI-PES Fabric.

3.2 FESEM

Fig. 3. shows the morphology of bare polyester (PES) fabric and PANI coated PES fabric doped with 0.9 wt% *p*TSA.

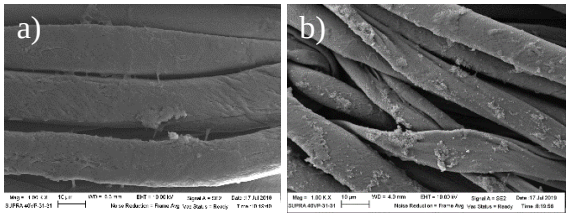

Fig. 3. Morphological surface through FESEM on a) bare cotton fabric b) 0.9 wt% of PANI PES fabric doped *p*TSA with 1000x magnification.

From the Fig. 3. (b), there were randomly distributed precipitate formed on the fibers. It may indicates that PANI powder have been successfully coated onto the fabric surface. This is in line with Bhat, N. *et al*., (2004), reported that PANI was greatly absorbed within the fibers and had rough with non-uniform surface after fabricated with fabric [15]. Further exploration has been conducted using FTIR analysis to confirm the chemical identity that exists on the fabrics.

3.3 FTIR Analysis

FTIR was used to detect the absorption of infrared radiation that pass through the sample. In this case, FTIR used to reveal the optical properties of doped and undoped PANI by the fingerprint that detect by the detector. Thus, the intensity and position of band of functional group of PANI can be detect in the spectra of IR. FTIR also may detect the foreign material that exist in the PANI thus giving all the information that match in the reference library in the program. Fig. 4. shows the FTIR spectra of PANI polyester fabrics at different concentration of *p*TSA (0.3 wt%, 0.6 wt% and 0.9 wt%).

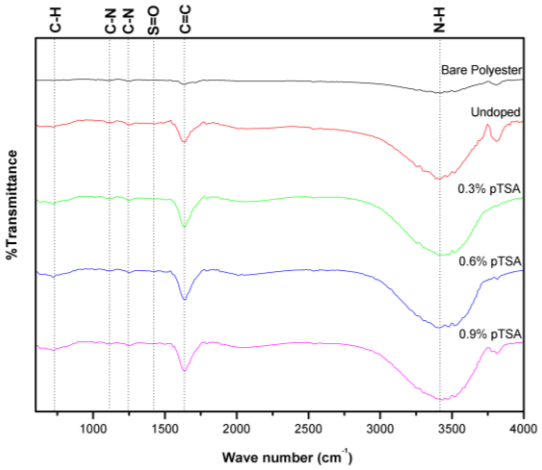

Fig. 4. FTIR spectra of bare PES fabric and polyaniline coated PES fabrics with different concentration of *p*TSA (0.3 wt%, 0.6 wt% and 0.9 wt%).

The main characteristic peak of PANI which is N-H stretches was observed at 3436.18 cm^{-1} (PANI EB), 3444.02 cm^{-1} (0.3 wt% *p*TSA), 3428.34 cm^{-1} (0.6 wt% *p*TSA), 3343.22 cm^{-1} (0.9 wt% *p*TSA). The C-C stretches in the aromatics ring was observed as a peak centered at 1644.32 cm^{-1} (0.3 wt% *p*TSA), 1632.23 cm^{-1} (0.6 wt% *p*TSA) and 1633.12 cm^{-1} (0.9 wt% *p*TSA). The S=O stretching peak of sulphate was observed at 1428.97 cm^{-1} (0.3 wt% *p*TSA), 1421.84 cm^{-1} (0.6 wt% *p*TSA) and 1415.25 cm^{-1} (0.9 wt% *p*TSA) indicating PANI EB was successfully doped with *p*TSA.

The fabrics coated with PANI doped with *p*TSA showed additional IR peaks at 1106.79 cm^{-1} (0.3 wt%), 1110.23 cm^{-1} (0.6 wt%) and 1128.90 cm^{-1} (0.9 wt%) correspond to C-N stretching of aliphatic amines or π electron displacement due to induction [16]. This indicates the C-H bond presence at the fabrics which increasing the bond of acids with the fabrics [17-18]. In addition, peak in range of 1607.23 cm^{-1} to 1654.92 cm^{-1} indicates C=C stretching of quinoid structure while 1340 cm^{-1} to 1366 cm^{-1} indicates the benzonoid rings.

3.4 EIS Measurements

Electrochemical Impedance Spectroscopy (EIS) was used as a technique to measure the conductivity of all fabricated fabrics. Fig. 5. shows the bar chart summarized the conductivity of PANI coated PES fabrics with different wt% of *p*TSA.

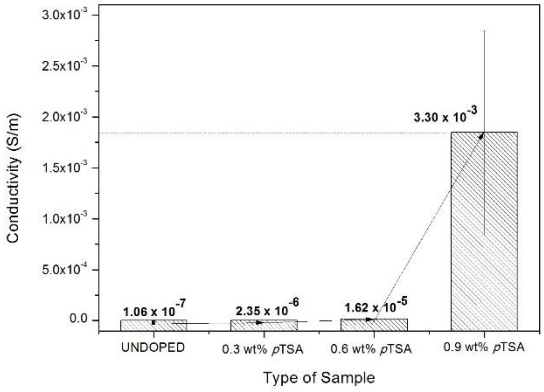

Fig. 5. Conductivity of PANI PES fabrics at different weight percentage of *p*TSA.

It can be seen that the sample doped with 0.9 wt% of *p*TSA showed the highest conductivity and undoped PANI give the lowest conductivity which 3.30×10^{-3} S/m and 1.6×10^{-7} S/cm respectively. Thus, as increasing the weight percentage (0.3 wt% to 0.9 wt%), the conductivity also increased. This indicates that PANI doped 0.9 wt% *p*TSA has very good electron mobility charge carrier. In addition, PANI doped with 0.9 wt% of *p*TSA in PES fabric shows majority of the polymer chain being connected to the PES fabric through hydrogen bonds [17-18]. This situation also showing that higher fraction of PANI chains are chemically grafted onto the PES fabric surface.

4. CONCLUSIONS

PANI was synthesized using chemical oxidation method. The conductivity of PANI can be increased by adding a dopant, *p*TSA at different concentration. PES fabric can be simply made conductive by incorporating a conducting polymer, PANI through a facile immersion technique. The morphological properties of the fabrics have shown randomly distributed precipitates suggesting that the PANI has incorporated within the PES fabric. It shows PANI PES fabric has a homogenous structure. From the FTIR analysis, the spectra shows the chemical structure of PANI (N-H) exist at the band of 3436.18 cm^{-1} (PANI EB), 3444.02 cm^{-1} (0.3 wt% *p*TSA), 3428.34 cm^{-1} (0.6 wt% *p*TSA), 3343.22 cm^{-1} (0.9 wt% *p*TSA) after the fabrication process. It was confirmed that PANI has incorporated within the fabric. Furthermore, S=O stretching sulphate peak was observed at 1428.97 cm^{-1} (0.3 wt% *p*TSA), 1421.84 cm^{-1} (0.6 wt% *p*TSA) and 1415.25 cm^{-1} (0.9 wt% *p*TSA) indicate that PANI EB was successfully doped with *p*TSA. The conductivity of the fabrics can be achieved at 3.30×10^{-3} S/m using 0.9 wt% ~~%~~ of *p*TSA concentration. Collectively, this study has presented a simple approach to produce a conductive fabrics utilizing PANI as the conducting agent.

5. ACKNOWLEDGEMENT

Authors are grateful for the funding from research management center Universiti Teknologi MARA (UiTM) under GIP grant (600-IRMI 5/3/GIP(010/2019))

6. REFERENCES

[1] A. Rochliadi, S. A. Akbar and V. Suendo, "Polyaniline/Zn as secondary battery for electric vehicle base on energy return factor," Proceedings of the Joint International Conference on Electric Vehicular Technology and Industrial, Mechanical, Electrical and Chemical Engineering (ICEVT & IMECE), Surakarta, 2015, 353-358. doi: 10.1109/ICEVTIMECE.2015.7496686

[2] Sengupta, P. P., Barik, S., & Adhikari, B. (2006). Polyaniline as a Gas-Sensor Material. Materials and Manufacturing Processes, 21(3), 263–270.doi:10.1080/10426910500464602

[3] Ibrahim, K. A. (2017). Synthesis and characterization of polyaniline and poly(aniline-co-o-nitroaniline) using vibrational spectroscopy. Arabian Journal of Chemistry, 10, S2668–S2674. doi:10.1016/j.arabjc.2013.10.010

[4] Heng Teo, C., Karode, N. S., Abid, K., & Rahman, F. (2011). Interfacial behaviour of polyaniline as an organic electronic material. Journal of Physics and Chemistry of Solids, 72(7), 886–890. doi:10.1016/j.jpcs.2011.04.010

[5] Erokhin, V., Berzina, T., & Fontana, M. P. (2005). Hybrid electronic device based on polyaniline-polyethyleneoxide junction. Journal of Applied Physics, 97(6), 064501. doi:10.1063/1.1861508

[6] Wang, H., Lin, J., & Shen, Z. X. (2016). Polyaniline (PANi) based electrode materials for energy storage and conversion. Journal of Science: Advanced Materials and Devices, 1(3), 225–255. doi:10.1016/j.jsamd.2016.08.001

[7] C. Gomes, E., & A. S. Oliveira, M. (2012). Chemical Polymerization of Aniline in Hydrochloric Acid (HCl) and Formic Acid (HCOOH) Media. Differences Between the Two Synthesized Polyanilines. American Journal of Polymer Science, 2(2), 5–13. doi:10.5923/j.ajps.20120202.02

[8] Mahat, M. M., Mawad, D., Nelson, G. W., Fearn, S., Palgrave, R. G., Payne, D. J., & Stevens, M. M. (2015). Elucidating the deprotonation of polyaniline films by X-ray photoelectron spectroscopy. Journal of Materials Chemistry C, 3(27), 7180–7186. doi:10.1039/c5tc01038a

[9] Olad, A & Azhar, F.F. (2013). Biomedical applications of polyaniline. *Trends in Polyaniline Research.* 361-384.

[10] C. Gomes, E., and A. S. Oliveira, M., (2012). Chemical polymerization of aniline in hydrochloric acid (HCl) and formic Acid (HCOOH) media. Differences between the two synthesized polyaniline. American Journal of Polymer Science, 2(2), 5–13.

[11] R. Neelakandan and M. Madhusoothanan. (2010) Electrical Resistivity Studies on Polyaniline Coated Polyester Fabrics. Journal of Engineered Fibers and Fabrics, 5(3), 2-5

[12] Tang, S. J., Wang, A.-T., Lin, S.-Y., Huang, K.-Y., Yang, C.-C., Yeh, J.-M., & Chiu, K.-C. (2011). Polymerization of aniline under various concentrations of APS and HCl. Polymer Journal, 43(8), 667–675. doi:10.1038/pj.2011.43

[13] Liao, G., Li, Q., & Xu, Z. (2019). The chemical modification of polyaniline with enhanced properties: A review. Progress in Organic Coatings, 126, 35–43. doi:10.1016/j.porgcoat.2018.10.018

[14] Yoo, J. E., Cross, J. L., Bucholz, T. L., Lee, K. S., Espe, M. P., & Loo, Y.-L. (2007). Improving the electrical conductivity of polymer acid-doped polyaniline by controlling the template molecular weight. Journal of Materials Chemistry, 17(13), 1268. doi:10.1039/b618521e

[15] Bhat, N. V., Seshadri, D. T., & Radhakrishnan, S. (2004). Preparation, Characterization, and Performance of Conductive Fabrics: Cotton + PANi. Textile Research Journal, 74(2), 155–166. doi:10.1177/004051750407400212

[16] Zhang, B., Xue, T., Meng, J., and Li, H., (2015). Study on property of PANI or PET composite conductive fabric. Journal of Materials Chemistry, 13(22), 0-7. He, J., Li, R., & Gu, F. (2012). Preparation of polyaniline/nylon conducting fabric by layer-by-layer assembly method. Journal of Applied Polymer Science, n/a–n/a. doi:10.1002/app.38331

[17] Prokeš, J., & Stejskal, J. (2004). Polyaniline prepared in the presence of various acids. Polymer Degradation and Stability, 86(1), 187–195. doi:10.1016/j.polymdegradstab.2004.04.012

[18] Murthy, N. S. (2006). Hydrogen bonding, mobility, and structural transitions in aliphatic polyamides. Journal of Polymer Science Part B: Polymer Physics, 44(13), 1763–1782. doi:10.1002/polb.20833

Interfacial magnetic properties of Fe deposited on MoS_2 flakes

Farhana Jesmin Tuli, Mohammad Tawheed Kibria, Takeshi Nakagawa* and Seigi Mizuno
*Department of Molecular and Material Sciences, Interdisciplinary Graduate School of Engineering Sciences, Kyushu University, Fukuoka, Japan
*Corresponding author email: naka@kyudai.jp

Abstract: *Analysis of magnetic behavior of Fe deposited on MoS_2 flakes was carried out by magneto-optic Kerr effect (MOKE). Small hysteresis loop was observed after depositing 12.5 Å of Fe on transferred MoS_2 flakes on clean SiO_2 substrate. Using thickness dependent study of Kerr rotation, it was found that magnetic dead layer (MDL) existed at the interface of Fe and MoS_2 up to 7 Å of Fe deposition. The presence of magnetically dead layer was due to the existence of small interaction between Fe and MoS_2 which led to the generation of antiferromagnetic coupling between atoms at the interface. With the increase of Fe deposition, interactivity of Fe and MoS_2 was decreased and prompted magnetism through ferromagnetic coupling between deposited Fe atoms.*

Keywords: deposition; hysteresis; magnetism; MOKE; MoS_2.

1. INTRODUCTION

Two dimensional (2D) materials have drawn tremendous attention after the invention of 'graphene' because of exhibiting unique chemical and physical properties [1]–[3]. Due to having zero bandgap, application of graphene in upcoming electronic devices is limited [4]. Thereafter, 2D layered transition metal dichalcogenides (TMD) with a sizeable bandgap of 1-2 eV are developed as an alternative of graphene for different applications in future [5]. Among the group of TMD, molybdenum disulfide (MoS_2) is a layered semiconductor containing covalently bonded S-Mo-S trilayers that are bound together by van der Waal forces, which has been achieved numerous interests because of its extraordinary physical properties [3]. Naturally available MoS_2 shows semiconducting properties and exists in 2H phase which is diamagnetic in nature and therefore, it is difficult to utilize this nonmagnetic material in spintronic devices [6]. Whereas, 1T phase of MoS_2 is metallic and paramagnetic which has been achieved after reducing the thickness of bulk 2H-MoS_2 to single layer [6]. Many theoretical and experimental works have been carried out to introduce magnetic properties in MoS_2, such as, controlling thickness, applying external strain, creating defects and doping MoS_2 with transitional metals or nonmetals. Among them, inducing magnetism by transition metal doping is considered as an effective and facile way [7].
To investigate the magnetic, electronic and structural properties of MoS_2 with the change of doping concentration, Fan *et al.*, performed first principle calculations after doping monolayer MoS_2 with Cu, Co, Fe, Mn and V. They found that doped transition metals preferred to remain in nearest neighboring configurations and exhibited ferromagnetic coupling at low concentration [5]. Tongay *et al.*, reported that the existence of ferromagnetism in bulk MoS_2 due to the presence of zigzag edges at the grain boundaries [8]. Xia *et al.*, observed that doping MoS_2 nanosheets with Fe would generate ferromagnetism which could be adjusted by altering the Fe concentration [9]. In our study, we observed the magnetic behavior of deposited Fe on transferred MoS_2 flakes on SiO_2 substrate by MOKE measurements.

2. EXPERIMENT

MoS_2 flakes were transferred to clean SiO_2 substrate by mechanical and thermal methods. Nonmagnetic sample holder was utilized to hold the sample and placed it in ultrahigh vacuum (UHV) chamber. Experiments were performed in UHV condition with a base pressure of 2×10^{-7} Pa. Then, e-beam evaporator was used to deposit Fe on MoS_2 flakes with a deposition rate of 1 Å/min, which was estimated by using quartz crystal microbalance (QCM). MOKE measurements were conducted to analyze the magnetic behavior of Fe/MoS_2 by applying a magnetic field along the longitudinal direction at room temperature.

3. RESULTS AND DISCUSSION

The magnetic properties of Fe on transferred MoS_2 flakes on SiO_2 substrate was studied by MOKE measurements in room temperature with a magnetic field applying in the in-plane direction. The hysteresis loops obtained from MOKE measurements for Fe/MoS_2 is shown in Fig. 1. When the thickness of Fe was increased to 12.5 Å on MoS_2 flakes, a small hysteresis loop was observed.

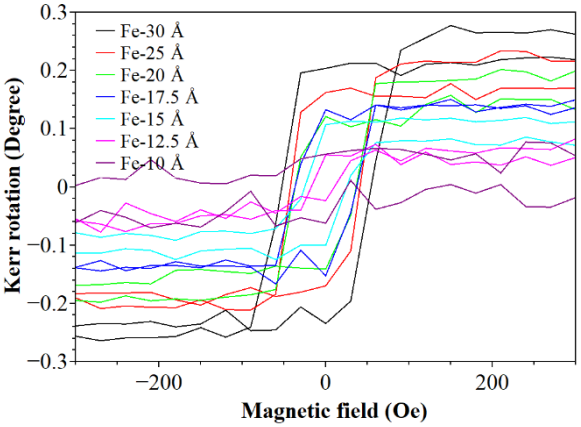

Fig. 1. MOKE hysteresis loops obtained after depositing various amount of Fe on transferred MoS_2 flakes on SiO_2 substrate at room temperature.

The absence of hysteresis loop after lower thickness of Fe deposition on MoS_2 flakes can be happened due to the low Curie temperature than room temperature or non-ferromagnetic behavior of material. As the Curie temperature of ferromagnetic material decreases with the decrease of its thickness, then there is a possibility of the absence of Kerr signal at room temperature due to the

deposited thickness of Fe was thinner than critical thickness [10]. Thus, a thickness-dependent study of Kerr rotation was carried out to determine the reason behind the non-ferromagnetic phase of the material at low coverage. Kerr rotation is related to the thickness of ferromagnetic material within the light penetration region. In this study, Kerr rotation would increase linearly with the Fe thickness up to around ~100 Å [10]. Fig. 2 shows the change of Kerr rotation for Fe/MoS_2 with Fe thickness. If the straight line extrapolation of these points intersects zero Kerr rotation at zero coverage of Fe, then there is no formation of magnetic dead layers at the interface of Fe/MoS_2 [11].

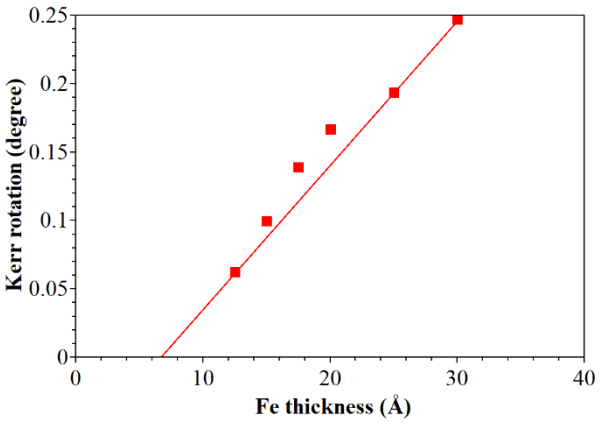

Fig. 2. Plot of Kerr rotation as a function of Fe thickness.

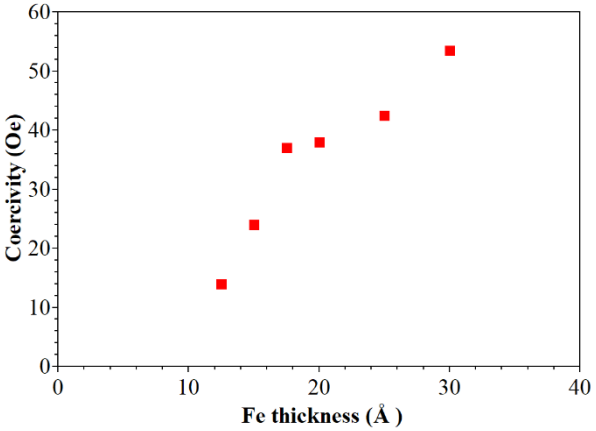

Fig. 3. Plot of coercivity as a function of Fe thickness.

In Fig. 2, it can be seen that straight line extrapolation intersects Fe thickness at 7 Å for Fe on MoS_2. Therefore, 7 Å of Fe was magnetically dead at the interface of Fe/MoS_2 instead of having low Curie temperature. Formation of magnetic dead layer (MDL) at the interface of Fe/MoS_2 might be due to the interaction between Fe and MoS_2 at lower thickness of Fe which could lead to the generation of antiferromagnetism because of the antiparallel spin alignment. Therefore, the formation of ferromagnetic phase after depositing more than 7 Å for Fe on MoS_2 flakes might be due to the absence of interaction between Fe and MoS_2, and the origination of ferromagnetic coupling between Fe atoms.

A plot of coercivity as a function of Fe thickness is shown in Fig. 3. It was found that coercivity was increased linearly with the increase of Fe thickness due to the pinning of domain wall and higher magnetic anisotropy.

4. CONCLUSIONS

We have analyzed the magnetic properties of MoS_2 flakes after depositing Fe on it by MOKE measurements. We found that hysteresis loop was appeared after 12.5 Å of Fe deposition as well as MDL was present at the interface up to 7 Å thickness of Fe. Deposited Fe interacted with MoS_2 flakes at lower thickness of Fe which might create antiparallel spin alignment between atoms and therefore, MDL was formed at the interface of Fe/MoS_2. Obtaining hysteresis loops at higher amount of Fe deposition might be due to the reduction of the interactivity of Fe and MoS_2 which could induce ferromagnetism.

5. REFERENCES

[1] A. P. S. Gaur, S. Sahoo, M. Ahmadi, S. P. Dash, M. J. F. Guinel, and R. S. Katiyar, Surface energy engineering for tunable wettability through controlled synthesis of MoS_2, Nano Lett. 14 (2014) 4314–4321.

[2] S. Qian, R. Yang, F. Lan, Y. Xu, K. Sun, and S. Zhang, Materials Science in Semiconductor Processing Growth of continuous MoS_2 film with large grain size by chemical vapor deposition, Mater. Sci. Semicond. Process. 93 (2019) 317–323.

[3] Q. Zhao, Q. Lu, Y. Liu, and M. Zhang, Two-dimensional Dy doped MoS_2 ferromagnetic sheets, Appl. Surf. Sci. 471 (2019) 118–123.

[4] Z. Cheng, M. Xia, S. Liu, R. Hu, and G. Liang, Applied Surface Science Role of rough substrate on the growth of large single-crystal MoS_2 by chemical vapor deposition, Appl. Surf. Sci. 476 (2019) 1008–1015.

[5] X. L. Fan, Y. R. An, and W. J. Guo, Ferromagnetism in Transitional Metal-Doped MoS_2 Monolayer, Nanoscale Res. Lett. 11 (2016).

[6] S. Jayabal, J. Wu, J. Chen, D. Geng, and X. Meng, Metallic 1T-MoS_2 nanosheets and their composite materials: Preparation, properties and emerging applications, Mater. Today Energy, 10 (2018) 264–279.

[7] B. Xia, P. Liu, Y. Liu, D. Gao, D. Xue, and D. Jun, Re doping induced 2H-1T phase transformation and ferromagnetism in MoS_2 nanosheets, Appl. Phys. Lett. 113 (2018) 1–6.

[8] S. Tongay, S. S. Varnoosfaderani, B. R. Appleton, J. Wu, and A. F. Hebard, Magnetic properties of ferromagnetism : Existence of ferromagnetism, Appl. Phys. Lett. 101 (2012).

[9] B. Xia, Y. Yang, J. Ma, K. Tao, and D. Gao, Adjustable ferromagnetic behavior in iron-doped two-dimensional MoS_2 multilayer nanosheets, Appl. Phys. Express. 10 (2017).

[10] J. Li, Z. Y. Wang, A. Tan, P. A. Glans, E. Arenholz, C. Hwang, J. Shi, and Z. Q. Qiu, Magnetic dead layer at the interface between a Co film and the topological insulator Bi_2Se_3, Phys. Rev. B - Condens. Matter Mater. Phys. 86 (2012) 2–5.

[11] M. Tawheed, R. Ishibashi, T. Nakagawa, and S. Mizuno, A Magneto-Optic Kerr Effect Study : Interfacial Magnetism of Iron / Graphene and Graphite Surfaces, Proc. Int. Exch. Innov. Conf. Eng. Sci. 4 (2018) 147–148.

Biomechanical Analysis of Hypertrophic Cardiomyopathy Behavior of Human Heart using Dynamic Finite Element Method

Shahrul Hisyam Marwan[1,2], Mitsugu Todo[3]
[1]Interdisciplinary Graduate School of Engineering Sciences, Kyushu University,
[2]Faculty of Mechanical Engineering, Universiti Teknologi MARA, Bukit Besi, Terengganu, Malaysia,
[3]Research Institute for Applied Mechanics, Kyushu University.
Todo@riam.kyushu-u.ac.jp

Abstract: *Hypertrophic cardiomyopathy (HCM) is the most familiar inherited cardiac disorder exhibits significantly by clinical heterogeneity and genetic. The aim of this research is to understand the effect of the wall thickness in terms of the performance of the human heart. In HCM symptoms, it is easy to understand with related to the wall thickness become thicker than normal size. In this study, a simple 3D human heart model is developed using 3D CAD software. Then, the simple 3D human heart model involved with the thicker thickness which is correlated with HCM. There are two thicknesses for HCM which are 14.0 mm and 22.0 mm and compared with the normal thickness which is 6.0 mm. After the simple 3D model of the human heart successfully developed, the simple 3D model of the human heart is exported to LS DYNA to undergo the simulation procedure. The results show the correlation between the wall thickness and the displacement of the human heart. With 14.0 mm and 22.0 mm of wall thickness, the results show 7.15 mm and 6.97 mm, respectively. Compared with 6.0 mm for normal thickness, the displacement is 7.30 mm.*

Keywords: Hypertrophic Cardiomyopathy; Human Heart; Wall Thickness; Finite Element Method

1. INTRODUCTION

Heart is the most important organ in our body. It is a very important organ to distribute blood throughout the circulatory system for surviving [1]. However, if the heart has a problem like Hypertrophic cardiomyopathy (HCM), it will give bad conditions to the patient. HCM is the symptom which increases ventricular wall thickness that is unexplained by myocyte enlargement and disarray, underlying condition, and increased myocardial fibrosis and also known as a primary disorder of the myocardium [2,3].

According to Hunter and Borg (2003) and Noble (2002), the research about heart investigation is involving integration based on computational sciences as a powerful tool [4,5]. Therefore, this study is aimed (1) to develop simple 3D model of the human heart and (2) to study the effect of different wall thickness of human heart correlate with HCM symptom.

2. METHODOLOGY

2.1 Development of simple 3D Model of Human Heart.

In this study, the simple 3D model of human heart has been done using 3D CAD application software which is known as JVision 3.6 software. Before the simple 3D model of human heart can be completely developed, it should be drawn in one layer which involved 93 number of nodes and 60 number of elements for this 3D model as shown in Fig. 1. The complete version of human heart in simple 3D model consists of 3603 number of nodes and 2400 number of element as shown in Fig. 2.

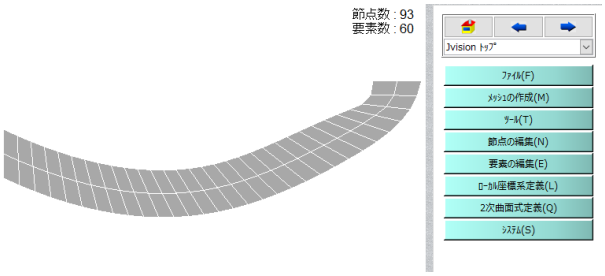

Fig. 1. One layer of 3D Model

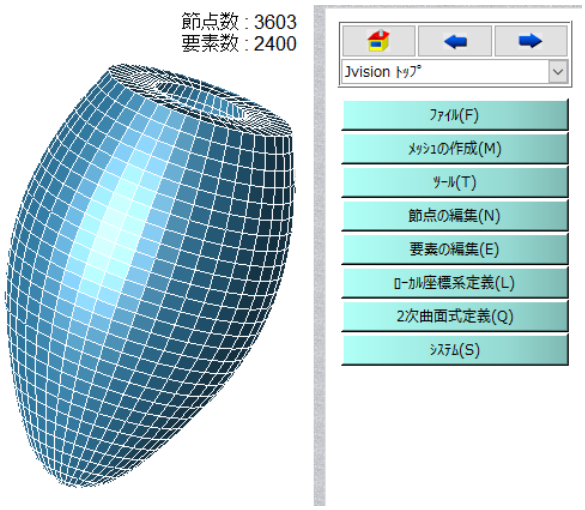

Fig. 2. Completely simple 3D Model of Human Heart

2.2 Simulation of simple 3D Model of Human Heart.

The completely simple 3D model was exported to LS DYNA (Liverware Software, Livermore, CA) software for conducting the simulation procedure as shown in Fig. 3. Post-processing was performed with LS-PREPOST.

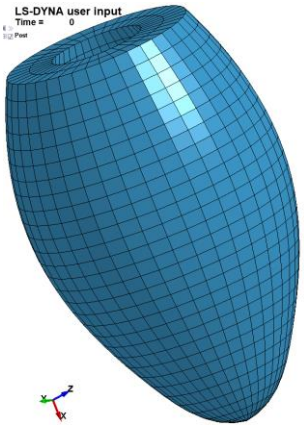

Fig. 3. 3D model in LS PREPOST software.

According to Iwamoto et al, in reality, the condition of lung, stomach, heart, intestine, and duodenum are not solid organs, but they are occupied with solid elements which are to represent air, blood, and other contents inside [6]. Therefore, in this study, it is considered as a solid element as well.

In this study, the material used is material type 128 (MAT_128) also known as MAT_HEART_TISSUE in LS DYNA material dictionary. Walker et al (2005) described in his paper this material model of a heart tissue model [7]. This current study uses the various number of wall thickness as shown in Table 1.

Table 1. Wall Thickness Involved in Simple 3D Model of Human Heart [8,9]

Wall Thickness (mm)		Authors
Normal	6.0	Kalsi et al (1999)
HCM 1	14.0	Kalsi et al (1999) Maron et al (2013)
HCM 2	22.0	Kalsi et al (1999) Maron et al (2013)

3. RESULTS AND DISCUSSION

3.1 Beating confirmation in 3D Model of Human Heart

This simple 3D of human heart model was successfully behave as systole condition as well as diastole condition as shown in Fig. 4 and Fig. 5, respectively.

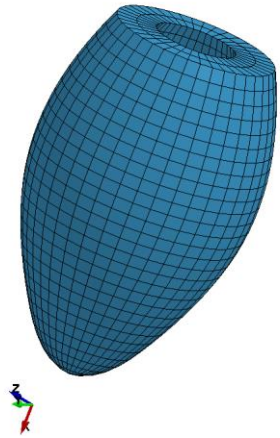

Fig. 4. 3D model in systole condition

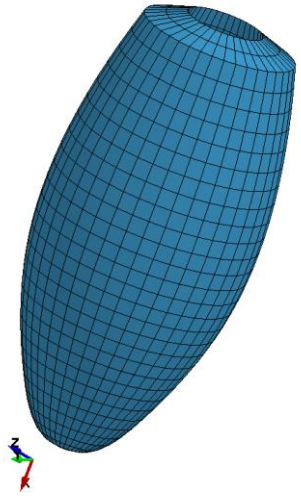

Fig. 5. 3D model in diastole condition

It is found that the total number of beating is 7 times in between 5 second as shown in Fig. 6. Therefore, in 60 seconds it will be 84 beatings. According to Bahar Gholipour (2018), the normal beating heart rate is between 60 and 100 beats per minute (bpm) for adults 18 and older [10]

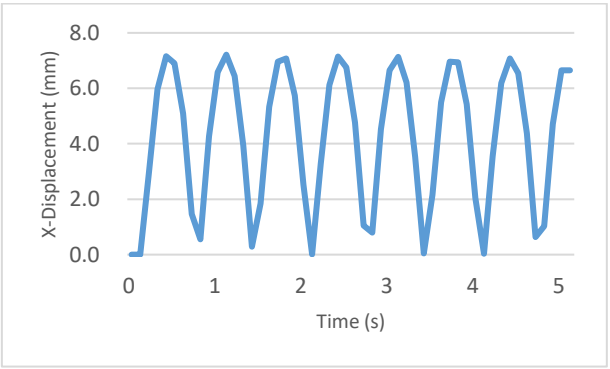

Fig. 6. Beating in the 3D model of Human Heart

3.2 Effect of wall thickness in beating behavior.

In this study, three different wall thicknesses (see Table 1) were involved in order to know the effect of the wall

thickness in terms of beating behavior. The graph can also be used as tool for predicting other thicknesses. The results for three different wall thicknesses are tabulated as shown in Fig. 7.

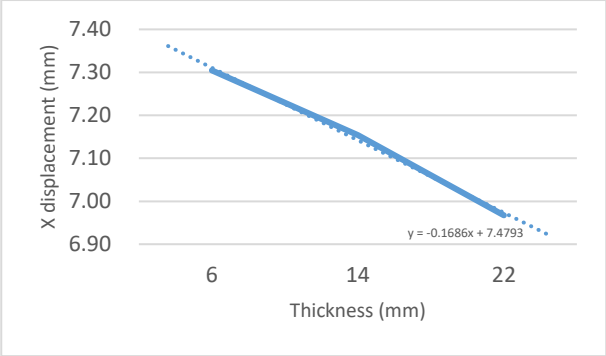

Fig. 7. The effects of wall thickness on displacement

Based on the result tabulated on the graph, it can be simplified that the thicker wall thickness will decrease the displacement of the 3D human heart model in terms of the mechanical point of view. If the displacement is smaller, the ability of the heart to pump will also be diminished.

According to Maron et al (2016), if the thickness of left ventricle (LV) equals or more than 30.0 mm, it is considered to be extreme LV wall thickness [11]. Kalsi et al (1999) mentioned that it is also known as HCM symptom if the thickness is (15.8 ± 5.5) mm [8]

In terms of medical point of view of the character human heart, the symptom of HCM will give short breath and from the results, if displacement is smaller, the heart will generally be weaker to pump the blood.

4. CONCLUSION

In conclusion, this study is important to know the effect of the wall thickness by using 3D model of human heart which involved with the finite element method. In normal thickness which is 6.0 mm, the displacement is 7.30 mm. In HCM patients, the thicknesses are 14.0 mm and 22.0 mm and the displacements are 7.15 mm and 6.97 mm, respectively. The displacement of the heart or the ability of the heart to pump blood will decrease as the wall thickness becomes thicker.

5. REFERENCES

[1] Hiroshi Watanabe, Seiryo Sugiura, Hidenobu Kafuku, and Toshiaki Hisada. Multiphysics Simulation of Left Ventricular Filling Dynamics Using Fluid-Structure Interaction Finite Element Method. Biophysical Journal (September 2004) Volume 87, 2074–2085.

[2] Tetsuo Konno, Stephen Chang, J. G. Seidman, and Christine E. Seidman. Genetics of Hypertrophic Cardiomyopathy, Curr Opin Cardiol. (2010 May) 25(3).

[3] Maron BJ, Gardin JM, Flack JM, et al. Prevalence of hypertrophic cardiomyopathy in a general population of young adults. Echocardiographic analysis of 4111 subjects in the CARDIA Study. Coronary Artery Risk Development in (Young) Adults. Circulation. 1995; 92:785–789. [PubMed: 7641357]

[4] Hunter, P. J., and T. K. Borg. Integration from proteins to organs: the physiome project. Nat. Rev. Mol. Cell Biol.(2003) 4:237–243.

[5] Noble, D. Modeling the heart: from genes to cells to the whole organ. Science.(2002) 295:1678–1682

[6] Masami Iwamoto, Yuko Nakahira, Atsutaka Tamura, Hideyuki Kimpara, Isao Watanabe and Kazuo Miki. Development of Advanced Human Models In Thums. 6th European LS-DYNA Users' Conference; 47-56.

[7] Walker JC, Ratcliffe MB, Zhang P, Wallace AW, Fata B, Hsu EW, Saloner D, Guccione JM. MRI-based finite-element analysis of left ventricular aneurysm. American Journal of Physiology-Heart and Circulatory Physiology. (2005) Wal289(2): 692-700.

[8] Kalsi KK, Smolenski RT, Pritchard RD, Khaghani A, Seymour AM, Yacoub MH. Energetics and function of the failing human heart with dilated or hypertrophic cardiomyopathy. European journal of clinical investigation. (Jun 1999) 29(6):469-77.

[9] Maron, B.J. and Maron, M.S., Hypertrophic cardiomyopathy. The Lancet. (2013) 381(9862):242-255.

[10]LIVESCIENCEwebsite:https://www.livescience.com/42081-normal-heart-rate.html (accessed 23.07.19).

[11] Maron BJ, Maron MS. Contemporary strategies for risk stratification and prevention of sudden death with the implantable defibrillator in hypertrophic cardiomyopathy. Heart Rhythm. (2016 May) 1;13(5):1155-65.

Modelling Low-Velocity Impact on Composite Laminate Considering Inter- and Intralaminar Damage

M.S. Meon[1,2], N.H. Mohamad Nor[1], S. Shawal[1], J.B. Saedon[1], M.N. Rao[2], K.-U. Schröder[2]
[1]Faculty of Mechanical Engineering, Universiti Teknologi MARA, Shah Alam, Selangor, Malaysia, [2]Institute for Structural Mechanics and Lightweight Design, RWTH Aachen University, Germany.
msuhairil@uitm.edu.my

Abstract: *Damage due to Low-Velocity Impact (LVI) in composite structures raises a maintenance concern because it can lead to invisible damage which contributes to catastrophic failure. Therefore, this study aims to investigate the LVI damage behaviour of CCF300/epoxy composite using three-dimensional Puck failure criteria and gradual degradation law. The finite element model was developed using solid elements, and the simulation was done in Abaqus/Explicit platform. The simplified boundary condition was employed in the model to analyse the significance of the clamping zone in predicting the contact-force diagram. The performance of proposed failure criteria and evolution law was compared with experimental results and damage morphologies of inter- and intralaminar were observed and discussed based on failure criteria used in this paper. The results revealed that the computational analysis agreed well with experimental data using a simple boundary condition.*

Keywords: Low-velocity impact (LVI); carbon fibre reinforced polymer (CFRP); finite element model (FEM); intralaminar damage; interlaminar damage

1. INTRODUCTION

Carbon-fibre reinforced plastic (CFRP) is an extremely strong and light fibre-reinforced plastic which contains carbon fibres. Thus, it can produce parts that are incredibly light and rigid. The application of the CFRP composite material can be seen in many engineering areas such as aerospace, the superstructure of ships and automotive due to its high strength and rigidity although the price is quite expensive compared to other composite materials.

Despite having such excellent characteristics, the composite structures experiencing low-velocity impact (LVI) typically confront the issue on the structural integrity. The LVI is caused by many factors such as bird strikes, tool drop during manufacturing and servicing, or runway debris. Those influencing factors may contribute to the variation of failure modes that can lead to a severe reduction in the strength and integrity of composite structures [1]. Also, the residual strength and stiffness of the structure can create internal defects in the form of delamination, matrix failure and fibre breakage.

Modelling the progressive damage of composite laminates under low-velocity impact become a critical research field, especially in the fabrication of aircraft structural components where barely visible impact damage can be a critical issue [2]. Many analytical studies [3–6] have focussed on integrating the progressive damage model into the numerical calculation. Finite element method (FEM) is thus convenient and efficient tools to use in many engineering types of research, also for the sake of cost-saving. To minimize the computational time, boundary conditions (i.e. clamping zone) and layup arrangement, especially at the interface between layers were crucially emphasized in the FE model. Full-scale geometry, including gripping areas, was modelled explicitly as described in the paper of Lou et al. [3], Tie et al. [4] and Riccio et al. [7]. Cohesive elements were used to capture the onset and propagation of inter-laminar failure. Long et al. [8] simplified the clamping areas to boost the numerical calculation. The results obtained were close proximity with experimental data. The areas between the laminate and cut-out region on both sides were the targeted clamping zones.

To achieve better prediction, a robust and efficient progressive damage model (PDM) which consists of failure criteria to identify the onset of failure and material degradation model (MDM) to capture the damage progression until final failure is crucially required since the architecture of the composite is complex and not isotropic. In many publications, a three dimensional (3D) Hashin failure criteria [9] has extensively used as initiation criteria to detect the failure, especially for uni-directional (UD) composite laminates because of its credibility to isolate different mode of failures. Long et al. [8] and Tie et al. [10] performed the damage analysis of the LVI using Hashin formulation and linear degradation scheme for progression law. Tie et al. [4] predicted the failure in laminates due to impact loading using Hashin criteria together with continuum damage mechanics (CDM) degradation law. The study shows that the approach is in line with test results.

Despite the efforts of many researchers in this field, there are no single criteria that can predict well in all cases, which describes that this research is inconclusive. Therefore, the proper process guideline in establishing the boundary condition and implementation of progressive damage law in impact laminates is highlighted and considered as the primary research topic. This article aims to provide the detail of modelling and failure prediction strategies. The effect of simplification of clamping areas together with Puck failure criteria to predict the intralaminar damage in the laminates for such type of loading is emphasized here. The cohesive contact formulation was employed to predict the initial

and growth of intra-laminar damage. The validation of the proposed damage model agreed well with the numerical simulation. Besides, the boundary condition plays a significant role to evaluate the performance of the finite element model.

2. METHODS

2.1 Finite element

The FE model of the LVI test was simulated using Abaqus/Explicit software. The laminates were produced from CCF300/epoxy composite material which consists of $[45/0/-45/90]4_s$ stacking sequences having a total thickness of 4 mm and meshed with eight-node linear brick reduced integration elements (C3D8R). The layup configuration was simplified to $[45_4/0_4/-45_4/90_8/-45_4/0_4/45_4]$ in order to achieve low computational time, as shown in Figure 1. This approach was employed successfully by Han et al. [11] and is called the global-local approach. To predict the failure behaviour of the interlaminar damage, six cohesive interfaces were developed in the model, and the cohesive contact formulation was used to predict the delamination. The delaminated region is discretised using eight-node three-dimensional cohesive elements (COH3D8). The region nearby impacted areas were modelled with finer mesh size compare with areas further away from the impacted zone. Table 1 shows the mechanical properties of CCF300/epoxy composite, while the cohesive material properties are depicted in Table 2.

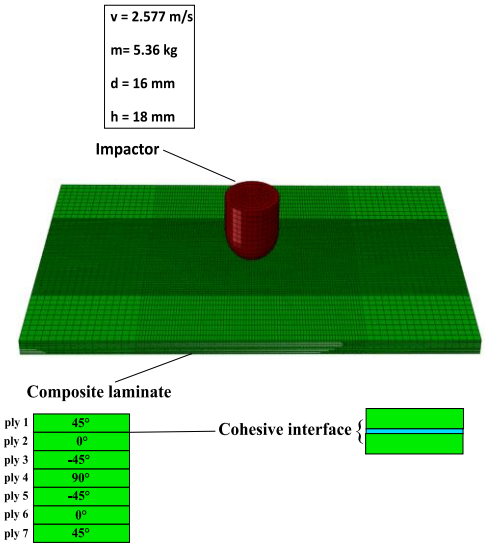

Fig. 1. The local-global approach in defining the stacking sequences and meshing strategy for the LVI plate.

The steel impactor was modelled with rigid body elements since the stiffness of the punch is much higher than the laminate. The spherical punch has a diameter of 16 mm, and 5.36 kg lumped mass was specified using rigid body reference point. The large value of the moment of inertia was applied to prevent rotation of the punch. The punch was constrained in all directions except in the direction of applied initial velocity as shown in Figure 2.

Table 1. The Mechanical properties of CCF300/epoxy

Category	Properties[11]
Elastic	E_1 = 123.91 GPa, $E_2 = E_3$ = 9.72 GPa $G_{12} = G_{13}$ = 4.53 GPa, G_{23} = 2.56 GPa $v_{12} = v_{13}$ = 0.288, v_{23} = 0.347
Strength	X_t = 1762.3 MPa, X_c = 1362.2 MPa, Y_t = 71.1 MPa, Y_c = 218.3 MPa, $S_{12} = S_{13} = S_{23}$ = 83.5 MPa
Density	ρ = 1.5 x 10^{-9} ton/mm^3

Table 2. The Cohesive Properties of CCF300/epoxy

Cohesive Properties [11]
$K_{nn} = K_{ss} = K_{tt}$ = 1 x 10^5 MPa
$t_n^o = t_s^o = t_t^o$ = 80 MPa
G_n^c= 556 J/m^2, $G_s^c = G_t^c$ = 1497 J/m^2

To mimicked the clamping behaviour, the displacement in the vertical direction of the bottom was constrained, and all vertical corner edges were clamped to simulate the fixation of clamping force. Finally, the contact force between the impactor and the laminate were recorded and compared with test data.

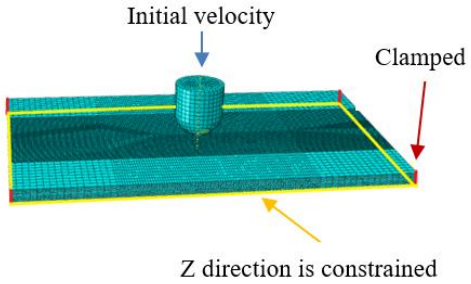

Fig. 2. Boundary condition applied on the LVI laminate

2.2 Puck's intralaminar damage model

Puck failure criteria were used [12] to capture the initiation of intralaminar damage on the composite laminate. The damages are classified into fibre-failure (FF) and inter-fibre failure (IFF) in both tension and compression. The equation of FF can be written in the following term:

Fibre failure in tension:

$$f_{FF}^t = \frac{1}{X_t}[\sigma_1 - \alpha\,(\sigma_2 + \sigma_3)] \text{ for } [\ldots.] \geq 0 \qquad (1)$$

Fiber failure in compression:

$$f_{FF}^c = \frac{1}{X_c}|\sigma_1 - \alpha\,(\sigma_2 + \sigma_3)| \text{ for } |\ldots.| < 0 \qquad (2)$$

With

$$\alpha = v_{12} - v_{12f} m_{\sigma f} \frac{E_{11}}{E_{11f}}$$

Where X_t and X_c are the tensile and compressive

strengths of a UD layer in the longitudinal direction and v_{12} and v_{12f} are the Poisson's ratio for UD lamina and fibre, respectively. The mean stress magnification factor, $m_{\sigma f}$ is 1.3 for glass fibre and 1.1 for carbon fibre.

For inter-fibre failure (IFF), also referred to as matrix cracking assumes that fracture in the laminate is resulted by the stresses acting on the fracture plane (FP) (σ_n, τ_{nl} and τ_{nt}) inclined θ_{FP} with respect to the material plane.

Inter-fiber failure in tension:

$$f^t_{IFF(\theta)} = \sqrt{\left(\left(\frac{1}{R_\perp} - \frac{P^+_{\perp\psi}}{R_{\perp\psi}}\right)\sigma_n(\theta)\right)^2 + A^2 + B^2} + \frac{P^+_{\perp\psi}}{R_{\perp\psi}}\sigma_n(\theta) \quad \text{for } \sigma_n \geq 0 \tag{3}$$

Inter-fiber failure in compression:

$$f^c_{IFF(\theta)} = \sqrt{\left(\frac{P^-_{\perp\psi}}{R_{\perp\psi}}\sigma_n(\theta)\right)^2 + A^2 + B^2} + \frac{P^+_{\perp\psi}}{R_{\perp\psi}}\sigma_n(\theta) \quad \textit{for } \sigma_n < 0 \tag{4}$$

With,

$$A = \frac{\tau_{nt}(\theta)}{R_{\perp\perp}} \quad \text{and} \quad B = \frac{\tau_{nl}(\theta)}{R_{\perp\parallel}} \tag{5}$$

The parameter ψ denotes the shear angle in an action plane, $R_\perp$ is failure resistance normal to fibres direction, and $R_{\perp\psi}$, $R_{\perp\perp}$ and $R_{\perp\parallel}$ are the fracture resistances of the action plane due to the shear stressing.

The damage progression is predicted based on the reduction of the stiffness matrix and is written as:

$$C^d = \begin{bmatrix} \beta C_{11} & \kappa C_{12} & \kappa C_{13} & 0 & 0 & 0 \\ \kappa C_{21} & \kappa C_{22} & \kappa C_{23} & 0 & 0 & 0 \\ \kappa C_{31} & \kappa C_{32} & \kappa C_{33} & 0 & 0 & 0 \\ 0 & 0 & 0 & \beta\omega G_{12} & 0 & 0 \\ 0 & 0 & 0 & 0 & \beta\omega G_{13} & 0 \\ 0 & 0 & 0 & 0 & 0 & \beta\omega G_{23} \end{bmatrix} \tag{6}$$

where C_{ij} is an undamaged stiffness component, and G_{12}, G_{13} and G_{23} are the in-plane and out-of-plane shear modulus of composite material. The multiplication factors β, κ, and ω were defined as follows:

$$\begin{aligned} \beta &= 1 - d_f \\ \kappa &= (1 - d_f)(1 - d_m) \\ \omega &= (1 - S_{mt}d_{mt})(1 - S_{mc}d_{mc}) \end{aligned} \tag{7}$$

Where $d_i (i = f, m)$ is the global damage variables corresponding to fibre and inter-fibre failure respectively. The relationship between global and local variables is defined as $d_f = 1 - (1 - d_{ft})(1 - d_{fc})$ and $d_m = 1 - (1 - d_{mt})(1 - d_{mc})$ where $d_{ij} (i = f, m; j = t, c)$ are the internal damage variables for tension and compression. The control parameters, S_{mt} and S_{mc} are 0.9 and 0.5, respectively as suggested in Abaqus manual.

2.3 Interlaminar damage model

Damage in composite structures is not only dominated by in-plane failures but also produces out of plane failure mode, especially in the case of LVI. Delamination is predicted using cohesive which already available in the software. Delamination was simulated by cohesive surface behaviour using a cohesive contact interface as discussed thoroughly in the publication of Han et al. [11].

3. NUMERICAL RESULT AND DISCUSSION

The numerical simulation is focused on CCF300/epoxy composite with the simplified boundary condition of clamped areas based on impact energy of 4.45 J/mm.

3.1 Structural response

Figure 3 demonstrates the comparison of the simulated impact force-time curves with the experiment. The duration of impact force for the simulation is in line with experimental data. However, the peak load was predicted slightly lower than the real ultimate load which probably caused by the gradual degradation law employed in the analysis. It can be concluded that the proposed progressive damage model works well with the experimental curve even though the configuration of the lay-up and boundary condition used has been simplified to reduce the computational cost.

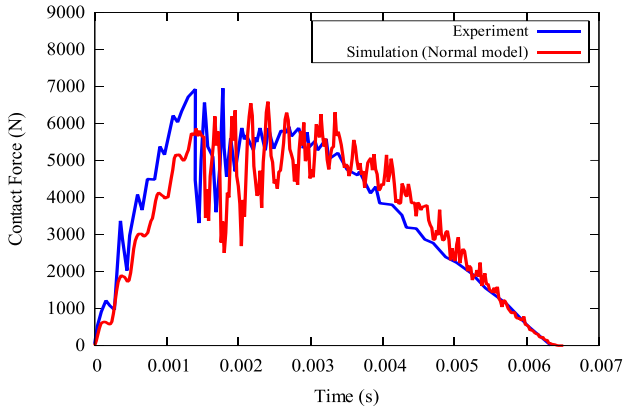

Fig. 3. Comparison of simulation and experimental data for contact force vs time of CCF300/epoxy laminate.

3.2 Damage initiation and growth

Due to the low initial impact energy applied to the laminate, only matrix failure observed in the analysis. Figure 4 illustrates the damage morphologies of IFF in tension and compression direction. Red colour indicates full damage, while other colour exhibit no failure area. Matrix damage radius increases for matrix failure in tension measured from impacted point to the bottom layer of the laminates, while decreases for compressive matrix failure. These trends similarly observed in the original publication [7]. No fibre failure found here because of the inadequacy of impact energy of the impactor to break the fibre in the composite laminate.

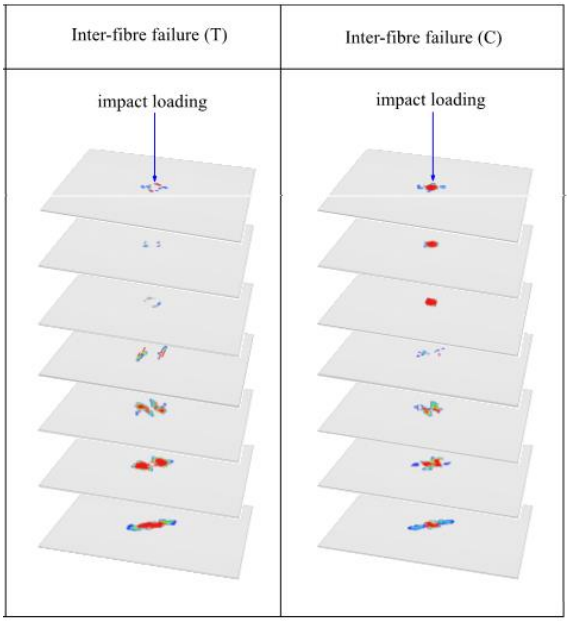

Fig. 5. Intralaminar morphology for the impact energy of 4.45 J/mm

Delamination or interlaminar damage is another area of interest in predicting total failure due to impact loading. As can be seen in Fig. 6, the damage morphology indicates the area of delamination getting more prominent towards the 90º layups, and slowly decreases approaching the last bottom layers. The existence of delamination boosts the process of damage accumulation by degrading the stiffness of the laminate.

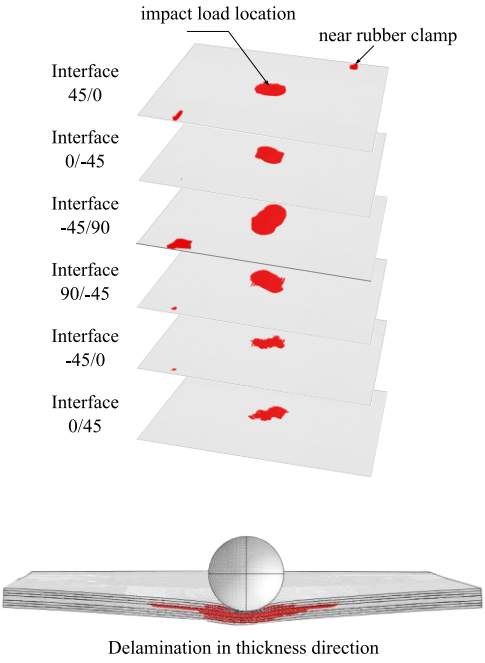

Fig. 6. Interlaminar morphology for the impact energy of 4.45 J/mm

4. CONCLUSIONS

In this paper, Puck damage criteria incorporated with a gradual degradation scheme and cohesive damage formulation were proposed to study the failure mechanism of fibre and matrix components as well as the structural response of CCF300/epoxy composite laminate subjected to low-velocity impact loading. The proposed damage model agreed well with the experiment, and the simplification made on the FE model has the least significant in determining the quality of the simulation.

5. REFERENCES

[1] Jagtap KR, Ghorpade SY, Lal A, and Singh BN, Finite Element Simulation of Low Velocity Impact Damage in Composite Laminates . *Mater. Today Proc.* 4 (2017) 2464–9.

[2] Hillermeier K, Prospects of Aramid as a Substitute for Asbestos . *Text. Res. J.* 54 (1984) 575–80.

[3] Lou X, Cai H, Yu P, Jiao F, and Han X, Failure analysis of composite laminate under low-velocity impact based on micromechanics of failure . *Compos. Struct.* 163 (2017) .

[4] Tie Y, Hou Y, Li C, Zhou X, Sapanathan T, and Rachik M, An insight into the low-velocity impact behavior of patch-repaired CFRP laminates using numerical and experimental approaches . *Compos. Struct.* 190 (2018) 179–88.

[5] Liu G, Bao H, and Tang K, Damage prediction in notched fiber-reinforced composite laminates . *Compos. Interfaces* 24 (2017) 279–90.

[6] Puck A, and Schürmann H, Failure analysis of FRP laminates by means of physically based phenomenological models . *Fail. Criteria Fibre-Reinforced-Polymer Compos.* (2004) .

[7] Riccio A, De Luca A, Di Felice G, and Caputo F, Modelling the simulation of impact induced damage onset and evolution in composites . *Compos. Part B Eng.* 66 (2014) 340–7.

[8] Long S, Yao X, and Zhang X, Delamination prediction in composite laminates under low-velocity impact . *Compos. Struct.* 132 (2015) 290–8.

[9] Hashin Z, Fatigue Failure Criteria for Unidirectional Fiber Composites . *J. Appl. Mech.* 48 (2009) 846.

[10] Du J, Tie Y, Li C, and Zhou X, Numerical and experimental study for damage characterization of composite laminates subjected to low-velocity impact . *Mater. Phys. Mech.* 27 (2016) 195–204.

[11] Han G, Guan Z, Li X, and Du S, Failure analysis of carbon fiber reinforced composite subjected to low velocity impact and compression after impact . *J. Reinf. Plast. Compos.* 35 (2016) 727–46.

[12] Puck A, Failure Analysis of Frp Laminates By Means of Physically Based Phenomenological Models . *Compos. Sci. Technol.* 58 (1998) 1045–67.

Adsorption Characteristics of CO_2 onto Carbon Nanotube for Adsorption Cooling/Capturing Applications

Kaiser Ahmed Rocky[1,2,3], Animesh Pal[2], Bidyut Baran Saha[1,2,*]
[1]Department of Mechanical Engineering, Kyushu University, 744 Motooka, Nishi-ku, Fukuoka 819-0395, Japan
[2]International Institute for Carbon-Neutral Energy Research (WPI-I2CNER), Kyushu University, 744 Motooka, Nishi-ku, Fukuoka 819-0395, Japan
[3]Department of Physics, University of Dhaka, Dhaka-1000, Bangladesh
[*]Corresponding author: saha.baran.bidyut.213@m.kyushu-u.ac.jp

Abstract: *This article focuses on the possible applications of multi-walled carbon nanotube (MWCNT) in CO_2 capture and adsorption cooling applications. In this study, surface properties namely surface area and porosity of MWCNT are assessed employing N_2 adsorption/desorption method. It is observed that surface area and total pore volume of MWCNT are about 640 m^2 g^{-1} and 1.151 cm^3 g^{-1}, respectively. Moreover, adsorption isotherms of CO_2 onto MWCNT are investigated at temperature ranging from 30 to 70 °C and pressures up to 5000 kPa. Experimental adsorption uptake data are fitted with well-known Tóth and modified Dubinin-Astakhov (D-A) adsorption models. Adsorption characteristic analysis reveals that 1 gram MWCNT can adsorb up to 0.631cm^3 amount of CO_2.*

Keywords: Adsorption; CO_2; MWCNT; Porosity; Surface area.

1. INTRODUCTION

The concentration of CO_2 in atmosphere is rising promptly for rapid urbanization and industrialization. This excess concentration causes an imbalance in the carbon cycle, and results global warming. Hence, special care should be adopted to reduce CO_2 level in the atmosphere.

To control the CO_2 level in the atmosphere, CO_2 capture and storage have been attracted to the researchers. Several authors [1–6] investigated the adsorption of CO_2 onto different porous materials such as activated carbon (AC), zeolite, metal organic framework (MOF), silica gel etc for capture and storage applications. Nowadays, researchers are focusing on the utilization of the captured CO_2. Gustav Lorentzen [7] firstly utilized CO_2 as refrigerant. Besides, Saha et al. [8], Pal et al. [9,10], Singh et al. [11], Mahbubul et al. [12] and many other researchers showed the exploitation of CO_2 as refrigerant for adsorption cooling and heating (ACH) system. CO_2 as refrigerant can mitigate the environmental adverse effect of conventional refrigerants (HFCs, CFCs).

Environmentally benign ACH system along with CO_2 as refrigerant is becoming popular for compact system design. Porous adsorbent materials are the key elements of adsorption system. However, the widely used adsorbents such as AC, zeolite, silica gel and MOF exhibit low thermal conductivity and packing density, which render the ACH system bulky. Therefore, porous materials having high thermal conductivity and adsorption capacity will be very promising for ACH applications. Multi-walled carbon nanotube (MWCNT) may be a good candidate for ACH system due to its pore like structure and high thermal conductivity. The key contributions of this article are:

i) Investigation of N_2 adsorption/desorption onto MWCNT and estimating porous properties employing BET and NLDFT methods.
ii) Measurement of adsorption characteristics of CO_2 onto MWCNT at temperature ranging from 30–70 °C and pressures up to 5000 kPa.
iii) Experimental data are correlated with well-known adsorption models

2. MATERIAL

Carbon nanotubes (CNT) are widely used in various electrical applications specially in VLSI interconnection [13,14] due to their high electrical conductivity. Nevertheless, they possess high thermal conductivity [15] which leads them to be used in ACH systems. In this study, MWCNT has been used which was provided by Raymor Nanotech, Canada.

3. N_2 ADSORPTION/DESORPTION AND POROUS PROPERTIES OF MWCNT

3Flex™ Surface Characterization Analyzer is widely used to investigate the N_2 adsorption/desorption isotherm which is one of the standard methods to estimate the porous properties of any material. Fig. 1 shows the N_2 adsorption/desorption isotherm of MWCNT.

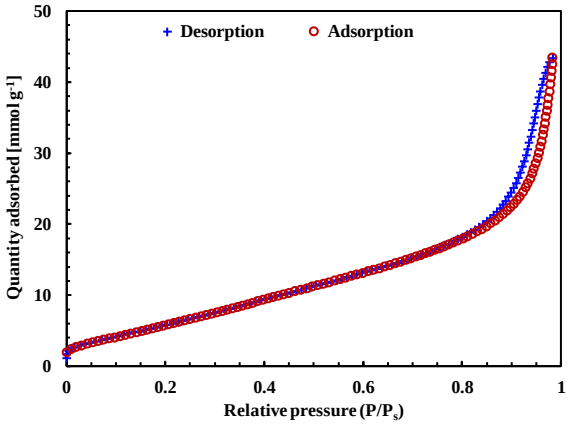

Fig. 1. N_2 adsorption/desorption isotherm of MWCNT.

From Fig. 1, it is seen that N_2 adsorption increases gradually at low relative pressure, and rises sharply at high relative pressure, which correspond to Type II isotherm. The intermediate flat region of the isotherm indicates monolayer and multilayer formations. At high

relative pressure, hysteresis is observed which restricts MWCNT to be used in ACH system at 0 to 0.8 relative pressure range.

Using the N_2 adsorption data, surface area analysis is carried out adopting Brunauer-Emmett-Teller (BET) method, and Fig. 2 shows the BET plot. It is observed that MWCNT exhibits surface area about 640 m^2/g.

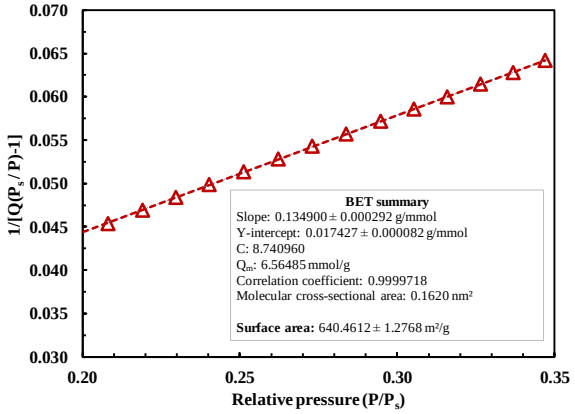

Fig. 2. BET plot of MWCNT

Pore size distribution (PSD) is a fundamental information of any porous material. The PSD analysis is performed employing Non-Local Density Functional Theory (NLDFT). Fig. 3 shows the incremental and cumulative pore volume of MWCNT.

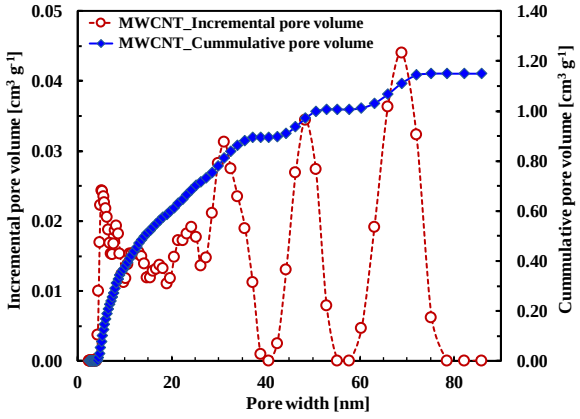

Fig. 3. Pore size distribution analysis of MWCNT

From Fig. 3 it is observed that most of the pores lie in the mesoporous and macroporous region, and the pore volume is 1.151 $cm^3\ g^{-1}$.

4. ADSORPTION OF CO_2 ONTO MWCNT

To check the feasibility of MWCNT for the application of ACH system, adsorption isotherms of CO_2 onto MWCNT are investigated employing Magnetic suspension adsorption measurement unit (MSB-GS-100-10M) supplied by BEL Japan. The details of this unit are available in literature [9]. This unit provides excess adsorption uptake data. The absolute adsorption uptake can be determined using the following equation.

$$C = C_{excess} + \rho_{CO_2} \times v_p \qquad (1)$$

where, C is the absolute adsorption uptake [g g^{-1}], C_{excess} denotes excess adsorption uptake [g g^{-1}], ρ_{CO_2} refers to the density of CO_2 [g cm^{-3}], and v_p represents total pore volume [$cm^3\ g^{-1}$].

In this study, Tóth and modified Dubinin Astakhov (D-A) equations are employed to correlate the CO_2 adsorption uptake data onto MWCNT as given by equations (2) and (3).

$$\frac{C}{C_0} = \frac{b_0 e^{\frac{Q_{st}}{RT}} P}{\left(1+\left(b_0 e^{\frac{Q_{st}}{RT}} P\right)^t\right)^{1/t}} \qquad (2)$$

$$C = \frac{W_0}{v_a} exp\left[-\left(\frac{RT\,ln\left(P_S/P\right)}{E}\right)^n\right] \qquad (3)$$

where, C_0 represents saturated amount of adsorption uptake [g g^{-1}], b_0 is equilibrium constant [kPa^{-1}], Q_{st} denotes isosteric heat of adsorption [J mol^{-1}], R stands for the molar gas constant [J $mol^{-1}\ K^{-1}$], T refers to adsorption temperature [K], P denotes the equilibrium pressure [kPa], t refers to Tóth parameter, W_0 is the maximum volumetric adsorption capacity [$cm^3\ g^{-1}$], E stands for adsorption characteristic energy [J mol^{-1}] and n represents structural heterogeneity.

The adsorbed phase specific volume of adsorbate is defined as-

$$v_a = v_t\, exp\left[\alpha\left(T - T_t\right)\right] \qquad (4)$$

where, v_t is the specific volume of the liquid adsorbate [$cm^3\ g^{-1}$] at triple point (v_t = 0.84858 $cm^3\ g^{-1}$ for CO_2), α (= 0.0025 K^{-1} [16], 1/T [17]) is the thermal expansion coefficient [K^{-1}] of the superheated liquid, and T_t refers to triple point temperature [K].

Beyond the critical temperature, saturated vapor pressure is replaced by pseudo saturated vapor pressure, and can be expressed as-

$$P_S = \left(\frac{T}{T_C}\right)^k P_C \qquad (5)$$

here, k is a fitting parameter, T_c and P_c represent critical temperature and pressure of CO_2, respectively.

Fig. 4 shows the experimental adsorption uptake data and the correlation between experimental data and adsorption models. Moreover, all the fitting parameters of the models and the root-mean square deviation (RMSD) values are listed in Table 1.

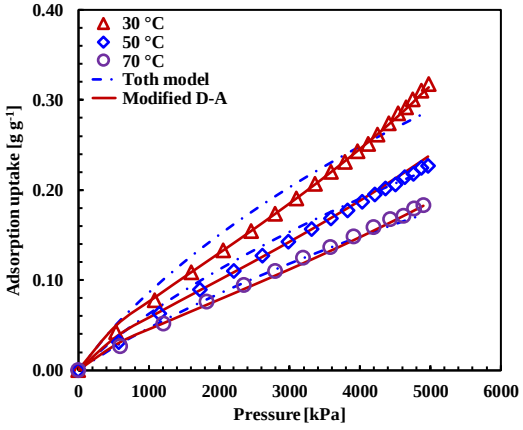

Fig. 4. Adsorption isotherms of CO_2 onto MWCNT.

From Fig. 4, it is observed that modified D-A equation shows good agreement with the measured adsorption isotherm data.

Table 1. Fitting parameters and RMSD values of the studied isotherm models.

Model	Fitting parameters	MWCNT/CO_2 pair
Tóth	C_0 [g g^{-1}]	1.530
	b_0 [kPa^{-1}]	1.72×10^{-07}
	Q_{st} [J mol^{-1}]	15297.479
	t [-]	0.630
	RMSD [%]	1.095
Modified D-A	W_0 [cm^3 g^{-1}]	0.631
	E [J mol^{-1}]	1753.740
	n [-]	0.694
	k [-]	2.362
	RMSD [%]	0.368

5. CONCLUSIONS

In this study, the possible applications of MWCNT in CO_2 capture and ACH system are investigated. From the N_2 adsorption/desorption analysis, it is observed that most of the pores of MWCNT are mesoporous and macroporous, and total pore volume is 1.151 cm^3 g^{-1}. Besides, adsorption characteristic analysis reveals that MWCNT exhibits significant CO_2 adsorption capacity, and it can adsorb up to 0.631 cm^3 g^{-1}. From this result, it is evident that MWCNT cannot replace highly porous AC as adsorbent in ACH application. However, it can be used as thermal conductive material along with activated carbon to enhance the heat transfer of adsorbent.

6. REFERENCES

[1] L. Jiang, A. Gonzalez-Diaz, J. Ling-Chin, A.P. Roskilly, A.J. Smallbone, Post-combustion CO 2 capture from a natural gas combined cycle power plant using activated carbon adsorption, Appl. Energy. 245 (2019) 1–15. doi:10.1016/j.apenergy.2019.04.006.

[2] Z. Zhang, Y. Xiao, B. Wang, Q. Sun, H. Liu, Waste is a Misplayed Resource: Synthesis of Zeolites from Fly Ash for CO2 Capture, Energy Procedia. 114 (2017) 2537–2544. doi:10.1016/j.egypro.2017.08.036.

[3] A. Modak, S. Jana, Advancement in porous adsorbents for post-combustion CO2 capture, Microporous Mesoporous Mater. 276 (2019) 107–132. doi:10.1016/j.micromeso.2018.09.018.

[4] S. Loganathan, M. Tikmani, S. Edubilli, A. Mishra, A.K. Ghoshal, CO2 adsorption kinetics on mesoporous silica under wide range of pressure and temperature, Chem. Eng. J. 256 (2014) 1–8. doi:10.1016/j.cej.2014.06.091.

[5] Y. Shen, W. Shi, D. Zhang, P. Na, B. Fu, The removal and capture of CO2 from biogas by vacuum pressure swing process using silica gel, J. CO2 Util. 27 (2018) 259–271. doi:10.1016/j.jcou.2018.08.001.

[6] N.A.A. Qasem, R. Ben-Mansour, M.A. Habib, An efficient CO2 adsorptive storage using MOF-5 and MOF-177, Appl. Energy. 210 (2018) 317–326. doi:10.1016/j.apenergy.2017.11.011.

[7] G. Lorentzen, 1-S2.0-0140700794900590-Main, Int. J. Refrig. 17 (1994) 292–301.

[8] B.B. Saha, S. Jribi, S. Koyama, I.I. El-Sharkawy, Carbon dioxide adsorption isotherms on activated carbons, J. Chem. Eng. Data. 56 (2011) 1974–1981. doi:10.1021/je100973t.

[9] A. Pal, K. Uddin, K.A. Rocky, K. Thu, B.B. Saha, CO2 adsorption onto activated carbon-graphene composite for cooling applications, Int. J. Refrig. (2019). doi:10.1016/j.ijrefrig.2019.04.022.

[10] A. Pal, S. Mitra, K. Thu, B.B. Saha, Improved adsorption uptake of ethanol and CO2 onto biomass based activated carbons, Proc. Int. Exch. Innov. Conf. Eng. Sci. 3 (2017) 127–128. http://hdl.handle.net/2324/1906402.

[11] V.K. Singh, E.A. Kumar, Experimental investigation and thermodynamic analysis of CO2adsorption on activated carbons for cooling system, J. CO2 Util. 17 (2017) 290–304. doi:10.1016/j.jcou.2016.12.004.

[12] M. Muttakin, A. Pal, K. Uddin, K. Thu, K. Ito, B. Baran Saha, Experimental study of CO_2 adsorption kinetics onto activated carbon, Proc. Int. Exch. Innov. Conf. Eng. Sci. 4 (2018) 48–49. doi:10.15017/1960664.

[13] P.K. Mahanta, K.A. Rocky, S.M. Ullah, Latency analysis of metallic single walled carbon nanotube (SWCNT) in circuit interconnections for VLSI, in: 2012 Int. Conf. Informatics, Electron. Vision, ICIEV 2012, 2012. doi:10.1109/ICIEV.2012.6317325.

[14] P.K. Mahanta, P. Adhikari, K.A. Rocky, Skin effect analysis for carbon nano material based interconnects at high frequency, in: 2013 Int. Conf. Informatics, Electron. Vision, ICIEV 2013, 2013. doi:10.1109/ICIEV.2013.6572717.

[15] E. Pop, D. Mann, Q. Wang, K. Goodson, H. Dai, Thermal conductance of an individual single-wall carbon nanotube above room temperature, Nano Lett. 6 (2006) 96–100. doi:10.1021/nl052145f.

[16] S. Ozawa, S.E.I.I.C.H.I.R.O. Kusumi, Y. Ogino, 1976-OzawaKusumiOgino-Physical adsorption of gases at high pressure. IV.pdf, J. Colloid Interface Sci. 56 (1976) 83–91.

[17] B.B. Saha, S. Koyama, I.I. El-Sharkawy, K. Habib, K. Srinivasan, P. Dutta, Evaluation of adsorption parameters and heats of adsorption through desorption measurements, J. Chem. Eng. Data. 52 (2007) 2419–2424. doi:10.1021/je700369j.

Preparation and Characterization of Yttrium Doped Barium-Zirconates at High Temperature Sintering

*M. Khalid Hossain[1,2], **Kenichi Hashizume[1]
[1]Department of Advanced Energy Engineering Science, Interdisciplinary Graduate School of Engineering Science, Kyushu University, Fukuoka 816-8580, Japan,
[2]Atomic Energy Research Establishment, Bangladesh Atomic Energy Commission, Dhaka 1349, Bangladesh.
Correspondences: *khalid.baec@gmail.com, ** hashi@nucl.kyushu-u.ac.jp

Abstract: *In this study, yttrium (Y) doped barium-zirconates ($BaZr_{0.9}Y_{0.1}O_{3-\alpha}$ (BZY10)) disc sample was prepared with high temperature sintering (1650℃, 20 h) to evaluate the structural and morphological properties by using X-Ray Diffraction (XRD) and Scanning Electron Microscope (SEM) respectively. The XRD analysis confirmed the cubic perovskite structure for both powder and sintered samples, and the SEM analysis showed a surface with small-sized grains and pores of the sintered sample.*

Keywords: Proton-conducting oxide, Barium-zirconate; Oxide ceramics; High temperature sintering; XRD analysis; SEM analysis.

1. INTRODUCTION

Successful production of energy from nuclear fusion reactor by using deuterium (D) and tritium (T) reaction as a fuel is still under research by the nuclear scientists as a clean and sustainable energy source for next generations [1]. As tritium is a radioactive material, it's necessary to recover the tritium gas and tritiated water from the nuclear reactor system, and to purify them to reuse as fuel [2]. Kawamura *et al.* propose that, perovskite-type proton conductive oxide is one of the good candidates for hydrogen pump for tritium recovery and purification system as shown in Fig. 1 [3]. It is known that the characteristics of the proton conductive oxides depend on its micro-structure. Therefore, it is necessary to study the structural and morphological properties of typical proton conductive materials after high temperature sintering.

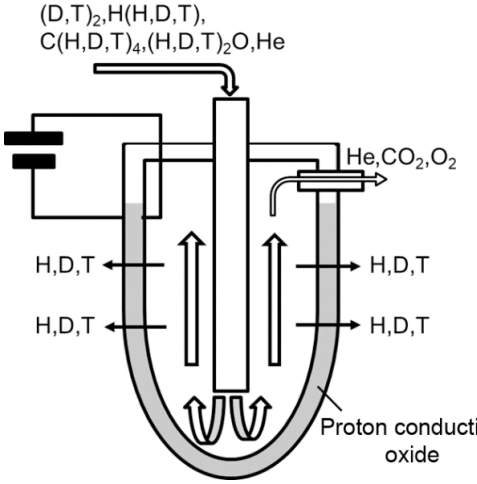

Fig. 1. Conceptual diagram of hydrogen recovery and separation system used in nuclear reactor. Reprinted with permission from Ref. [3].

In this study, barium-zirconates ($BaZrO_3$) which is one of typical proton conductor oxides was used as a specimen, in which10% of Zr^{4+} was substituted by Y^{3+} ($BaZr_{0.9}Y_{0.1}O_{3-\alpha}$, hereafter BZY10) to get a proton conducting. The powder of BZY10 was die-pressed, isostatically pressed, and then high temperature sintering was done to get a sintered sample for structural and morphological analysis. BZY10 has a perovskite structure (chemical composition ABO_3), where trivalent cation like yttrium sits in a part of the B-site of the crystal after doping as shown in Fig. 2 [4].

2. EXPERIMENTAL

2.1 Sample preparation

As a raw material, $BaZr_{0.9}Y_{0.1}O_{3-\alpha}$ powder supplied by TYK Co. was used. After an appropriate amount of the powder was weighed, it was pressed uniaxially (100 MPa) with a die of 10 mm in diameter and formed into a disc shape. Next, the disc-shaped sample was put into a rubber tube, evacuated by a diaphragm-type dry vacuum pump, and then an isostatic press (200 MPa) was applied. The compact was sintered in air at 1650℃ for 20 hours using a molybdenum (Mo) heater furnace. The sample obtained after sintering had a black surface, and its size was 7 to 8 mm in diameter and about 2.5 mm in thickness. The sintered sample surface was wet-polished with four different silicon carbide (SiC) abrasive papers (#400, #600, #800, and #1200) sequentially, and finally mirror polished with an alumina (Al_2O_3) slurry solution.

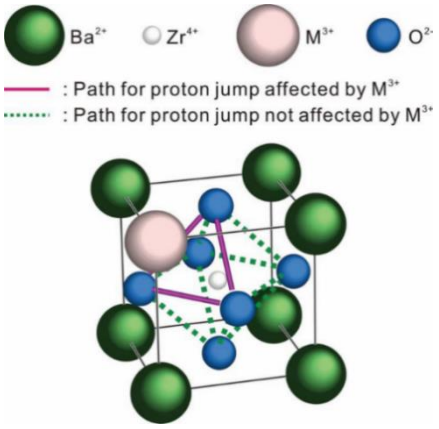

Fig. 2. Schematic presentation of the crystal structure of a single unit cell of barium zirconate, where trivalent cation (where M^{3+} = Y, In, Yb, Tm, Er, Ho, Gd etc.) doped in the B-site of perovskite structure. Reprinted with permission from Ref. [4].

2.2 Characterization

X-ray diffraction analysis was performed on both sintered body and powder of BZY10 at room temperature by using an X-ray diffractometer (MultiFlex, RIGAKU) at 40kV. The measurement was performed by using Cu-Kα radiation in the range of 20° to 80° at 2θ position, where step width was 0.01 degree. Then both polished and non-polished surface of the sintered sample was analyzed by using a SEM (JSM-6010LA, JEOL) in different magnifications at 20kV accelerating voltage.

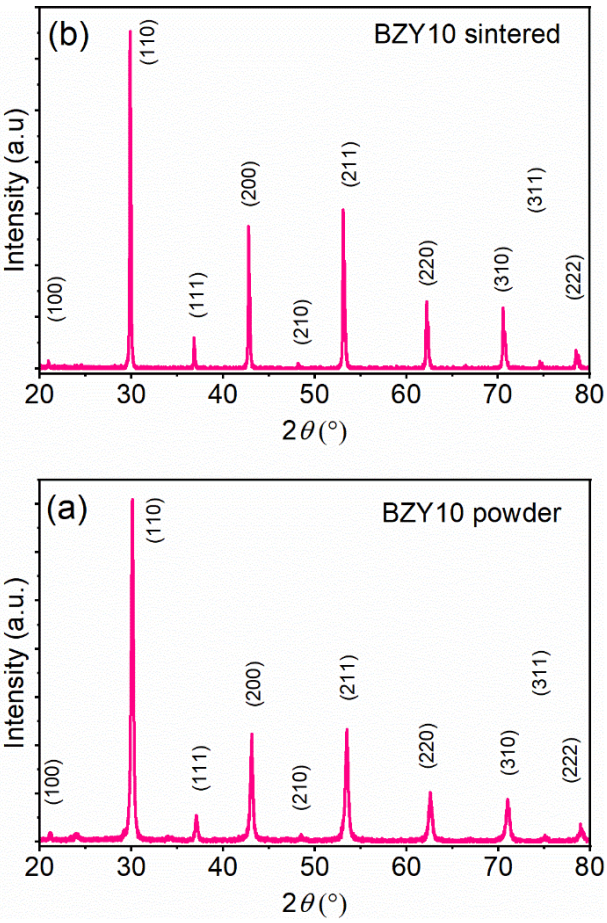

Fig. 3.XRD patterns for the (a) powder, and (b) sintered samples of BZY10.

3. RESUTS AND DISCUSSION

3.1 Structural analysis

Fig. 3 shows the XRD patterns for the powder and sintered samples of BZY10, and the characteristics peaks

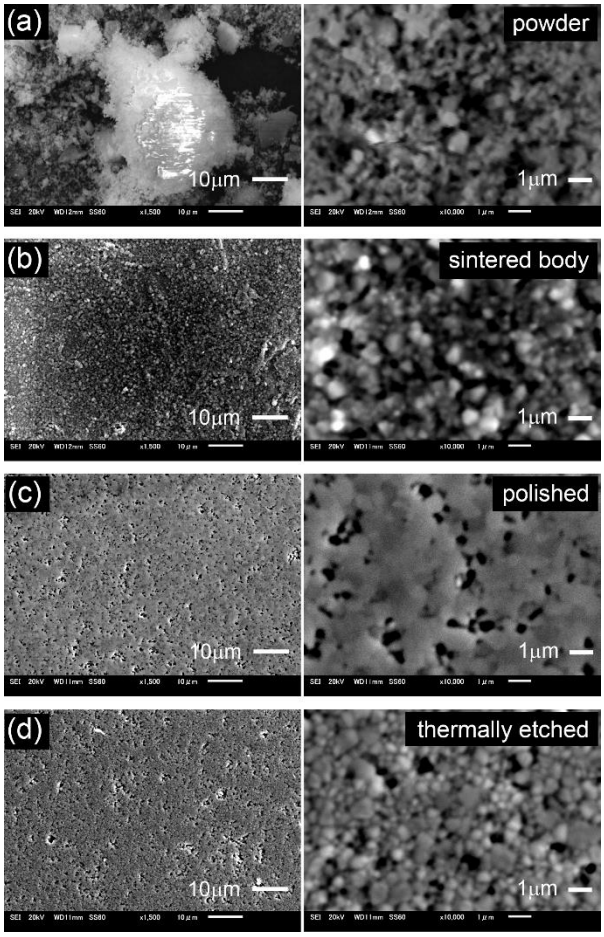

Fig. 4. SEM images at low and high magnifications of (a) powder BZY10, (b) sintered BZY10 before polishing, (c) after polishing, and (d) after thermal etching of polished sample.

properties are summaries in Table 1. The BZY10 samples were confirmed as the cubic crystal structure of barium-zirconates based on the obtained peak pattern and DB card number of 01-070-3667. The peaks were assigned as the diffractions of (100), (110), (111), (200), (210), (211), (220), (310), (311), and (222) planes. From Table 1 it is clear that, each peak position of the powder and sintered sample shifts to lower degrees. A decreasing trend is also observed for the full width at half maximum (FWHM) value between the powder and sintered sample. As a result, the inter-planner distance *d* shows opposite trend for the sintered sample, i.e. its value increases after sintering BZY10 powder. It is found that lattice constant

Table 1. Structural parameters for the powder and sintered samples of BZY10 obtained from XRD patterns analysis.

Index	2θ (deg)		d (Å)		FWHM		Crystallite size (nm)	
	BZY10 powder	BZY10 sintered	BZY10 powder	BZY10 sintered	BZY10 powder	BZY10 sintered	BZY10 powder	BZY10 sintered
(100)	21.1	20.9	4.2	4.24	0.26	0.17	33	51
(110)	30.1	29.9	2.97	3	0.281	0.11	31	78
(111)	37.1	36.8	2.42	2.44	0.348	0.137	25	64
(200)	43	42.8	2.1	2.11	0.295	0.138	30	65
(210)	48.5	48.2	1.88	1.88	0.37	0.15	24	60
(211)	53.5	53.1	1.71	1.72	0.344	0.114	27	82
(220)	62.6	62.2	1.48	1.49	0.385	0.127	25	76
(310)	70.9	70.6	1.33	1.33	0.397	0.148	26	69
(311)	75	74.6	1.27	1.27	0.42	0.15	25	70
(222)	79	78.5	1.21	1.22	0.56	0.164	19	65

a value increases after sintering the BZY10 powder. Using the lattice constants, the calculated density for the powder sample (6.210 g/cm^3) was found higher than that of the sintered sample (6.099 g/cm^3). The obtained powder sample density is exactly same as the literature value [5]. The reason of differences of lattice constants between powder and sintered samples is not clear at present, but it is found that the bulk density (obtained by applying Archimedes method) of the present samples exceeds 96% of theoretical density even for adopting the powder's value. In the present sintering process, dense samples were obtained, and as listed in Table 1, the crystallite size increases after sintering, but it was just double of the powder sample's value [6].

3.2 Morphological analysis

Fig. 4 shows the SEM images for both powder and sintered samples. In the SEM images (Fig. 4(a)) of powder sample, the particles are agglomerated with each other the size of primary grains is not clear but the size of the particles seems to be 0.1 ~1.0 μm. From the sintered surface as shown in Fig. 4(b), surface grains seem to stick together, and their size ranges approximately 0.5-1.0 μm. The polished sample's surface (Fig. 4(c) is flat but not clear for its grain size. After polishing, the sample was thermally etched at high temperature condition (1650℃ for 1 hour) using the same furnace of sintering. After the etching as shown in Fig. 4(d), the grains and pores are clearly visible: size of grains and pores range 0.3~1.0 μm as appearing in literature [7–10]. The grain of the sample did not seem to grow very much in the sintering process.

4. CONCLUSIONS

10% yttrium doped barium-zirconate ($BaZr_{0.9}Y_{0.1}O_{3-\alpha}$) proton conducting oxide sample was prepared by powder metallurgy method at high temperature sintering. The sintered sample shows cubic lattice structure with comparatively similar sized grains as the powder one. Grains and pores of about 0.3~1.0 μm were observed in the sintered sample and the bulk density exceeds 96% of theoretical density.

ACKNOWLEDGEMENTS

The authors wish to acknowledge the kind support from the Center of Advanced Instrumental Analysis, Kyushu University for XRD analysis.

5. REFERENCES

[1] J.L. Tuck, Outlook for Controlled Fusion Power, Nature. 233 (1971) 593–598.

[2] K. Katayama, M. Nishikawa, Safety Confinement System, in: Tritium Fuel Fusion React., Springer Japan, Tokyo, 2017: pp. 297–329.

[3] Y. Kawamura, K. Isobe, T. Yamanishi, Mass transfer process of hydrogen via ceramic proton conductor membrane of electrochemical hydrogen pump, Fusion Eng. Des. 82 (2007) 113–121.

[4] S. Imashuku, T. Uda, Y. Nose, G. Taniguchi, Y. Ito, Y. Awakura, Dependence of Dopant Cations on Microstructure and Proton Conductivity of Barium Zirconate, J. Electrochem. Soc. 156 (2009) B1.

[5] M.D. Gonçalves, R. Muccillo, Properties of yttrium-doped barium zirconate ceramics synthesized by the oxidant-peroxo method, Ceram. Int. 40 (2014) 911–917.

[6] F. Iguchi, T. Yamada, N. Sata, T. Tsurui, H. Yugami, The influence of grain structures on the electrical conductivity of a $BaZr_{0.95}Y_{0.05}O_3$ proton conductor, Solid State Ionics. 177 (2006) 2381–2384.

[7] H. Bae, J. Choi, K.J. Kim, D. Park, G.M. Choi, Low-temperature fabrication of protonic ceramic fuel cells with $BaZr_{0.8}Y_{0.2}O_{3-\delta}$ electrolytes coated by aerosol deposition method, Int. J. Hydrogen Energy. 40 (2015) 2775–2784.

[8] Y. Yamazaki, P. Babilo, S.M. Haile, Defect Chemistry of Yttrium-Doped Barium Zirconate: A Thermodynamic Analysis of Water Uptake, Chem. Mater. 20 (2008) 6352–6357.

[9] Y. Liu, Y. Guo, R. Ran, Z. Shao, A new neodymium-doped $BaZr_{0.8}Y_{0.2}O_{3-\delta}$ as potential electrolyte for proton-conducting solid oxide fuel cells, J. Memb. Sci. 415–416 (2012) 391–398.

[10] H. Bae, G.M. Choi, Novel modification of anode microstructure for proton-conducting solid oxide fuel cells with $BaZr_{0.8}Y_{0.2}O_{3-\delta}$ electrolytes, J. Power Sources. 285 (2015) 431–438.

Coupling Approach of Lattice Boltzmann Fluid Simulation and Finite Element Analysis of Geophysical Properties: Application to Natural Rock Fracture in Geothermal Area

Kazuki Sawayama[1,*], Takeshi Tsuji[2,3], Yasuhiro Fujimitsu[3]
[1]Department of Earth Resources Engineering, Graduate school of Engineering, Kyushu University
[2]International Institute for Carbon-Neutral Energy Research, Kyushu University
[3]Department of Earth Resources Engineering, Faculty of Engineering, Kyushu University
[*]Corresponding author email: k.sawayama0926@mine.kyushu-u.ac.jp

Abstract: *This study develops a new approach which can simultaneously calculate the hydraulic permeability, electrical resistivity and elastic wave velocity from the digital image of natural rock fracture. The digital fracture simulation is applied to natural single fracture which was cored from geothermal area and validate that performance by comparing experimental results. The fluid-flow experiment is conducted in a pressure vessel which simulates the pressure condition of the geothermal area. As a result, resistivity and velocity show thresholds at the same pressure condition (~5 MPa in our study) while decreasing rates of them with aperture opening were different at 0.8 mm or higher aperture condition (decreasing rate of resistivity is ~60 Ωm while that of velocity is ~80 m/s per 0.1 mm aperture change). These behaviors may be controlled by connection or disconnection of the fluid pathway and will be used for subsurface monitoring by using velocity and/or resistivity.*

Keywords: Digital rock physics; Lattice Boltzmann Method; Fracture permeability; Electrical resistivity; Elastic wave velocity.

1. INTRODUCTION

The hydraulic property of crustal fluid is essential to understand the mechanisms of earthquake and fluid reservoir formation (e.g., petroleum and geothermal reservoir). As one of the time-dependent models of earthquake recurrence, fault-valve model has been well known [1]. The fault-valve model describes that the mineral precipitation within faults controls the pore pressure change which can trigger the earthquake recurrence. For estimating this valve-like behavior of faults, fracture permeability plays a key role because the mineral precipitation may preferentially occur at slower fluid-velocity zone. In terms of fluid reservoir development, the permeability estimation is crucial for predicting the fluid production. In addition to permeability, local behavior of fluid-flow (e.g., fluid pathway) within fractures controls preferential-flow and total thermal response in geothermal area [2, 3]. Since permeability decreases with aperture closure [4, 5], fracture aperture condition (opening or closing) should be monitored.

Taira et al. recently observed seismic wave velocity changes in Salton sea geothermal area and interpreted that velocity changes were caused by crack aperture changes [6]. Some magnetotelluric surveys also revealed subsurface aperture opening or closure (e.g., [7]). However, it is unknown that how much aperture changes can demonstrate these changes of geophysical properties. Although there is an enormous amount of studies about electric and elastic properties of rocks (e.g., [8–14]), these geophysical properties of rock fractures have not been well investigated. Recently, Kirkby et al. investigated permeability-resistivity relationship of the rock fracture [15]. Pyrak-Nolte and Nolte proposed universal relationship between elastic and hydraulic properties [16]. However, to the best of our knowledge, relationships between fracture permeability, electrical resistivity and elastic wave velocity have not been revealed yet. Since fracture is anisotropic, these three geophysical parameters should be investigated simultaneously.

In this study, a new approach of Digital Rock Physics is developed that can simultaneously calculate hydraulic permeability, electrical resistivity and elastic wave velocity from the digital image of natural rock fracture by coupling approach of Lattice Boltzmann Method and Finite Element Method. Although there is a great interest of such numerical approach using digitalized rock (so-called Digital Rock Physics), these works mostly uses porous rocks (e.g., sandstone). Present study proposes that Digital Rock Physics can also be applicable to natural rock fracture and confirmed good agreements with experimental results. From the estimated hydraulic permeability, electrical resistivity and elastic wave velocity, the relationships between them as well as mean aperture in the fracture are further discussed.

2. METHOD

2.1 Sample preparation

The numerical simulation and fluid-flow test were carried out using a cylindrical fractured sample (35 mm in diameter and 70 mm long). The sample was obtained from geothermal area and has a natural sheared fracture [17]. For the numerical simulation, a fracture of the sample was digitalized. This digitalized fracture model was created from the surface roughness data of hangingwall and footwall which were obtained by One-shot 3D Measuring Macroscope.

2.2 Numerical simulation

From the digitally created fracture model, three-dimensional fluid flow was calculated by Lattice Boltzmann Method (LBM; e.g., [18–20]). Model sizes of simulations is 224 x 32 x 576 grids. Each grid of x, y and

z directions are 0.1 mm. Fluid-flow direction driven by the pressure gradient is along z-direction with periodic boundary. The initial aperture model is determined by assuming that footwall and hangingwall contact at only one point. Consequently, different digital fracture models were prepared by made them closer. After simulating fluid distribution in the fractures by LBM fluid-flow simulation, then elastic wave velocity and electrical resistivity in fluid-saturated fractures were calculated by Finite Element Method (FEM, [21]). Elastic wave velocity (P-wave velocity, V_p) was calculated by following equations;

$$V_p = \sqrt{\frac{K + {}^4/_3\ \mu}{d}}$$

where d denotes density, K and μ is bulk modulus and shear modulus which were estimated from stress-strain relationship with engineering triaxial stress by FEM. Electrical resistivity simulation applies 30 mV of electrical field in z-direction (same as fluid-flow direction) and calculates electric current. From this applied voltage (V) and calculated electric current (I), resistivity (ρ) can be calculated as;

$$\rho = \frac{\mathrm{V}}{I}\frac{\pi D^2}{4L}$$

where D and L is diameter and length of the sample, respectively. Detailed simulation input parameters are summarized in Table1.

Table 1. Input parameters of numerical simulation by FEM

Parameters	Rock	Fluid
Conductivity [S/m]	0.001	1.75
Bulk modulus [GPa]	34	2.2
Shear modulus [GPa]	35	0
Density [kg/m^3]	2900	997

2.3 Experimental validation

Fluid-flow tests were performed under confining pressure ranging between 6 and 20 MPa. Pore pressures of upstream and downstream were fixed as 5 and 4 MPa, respectively. During the test, flow rate (Q) was monitored by a digital logger and thereby permeability (k) is calculated by following equation (Darcy's law),

$$\frac{Q}{A} = \frac{k}{\mu}\frac{dp}{dx}$$

while A, μ and dp/dx is cross sectional area, viscosity and pressure gradient, respectively. Consequently, from this calculated permeability, we estimated fracture permeability (k_f) as follows [22];

$$k_f = \frac{e^2}{12}$$

where hydraulic aperture (e) is written by

$$e^3 = \frac{12\mu Q}{D}\frac{dx}{dp}$$

while D is the width of fracture.

During this fluid-flow experiment, electrical resistivity and elastic wave velocity were simultaneously measured by using four electrodes-method and pulse transmission method, respectively [23]. These measured permeability, resistivity and velocity were compared with calculated results for the validation of simulation results.

3. RESULTS AND DISCUSSION

Fig. 1 shows hydraulic permeability, electrical resistivity and elastic wave velocity of both of experimental and simulated results as a function of effective confining

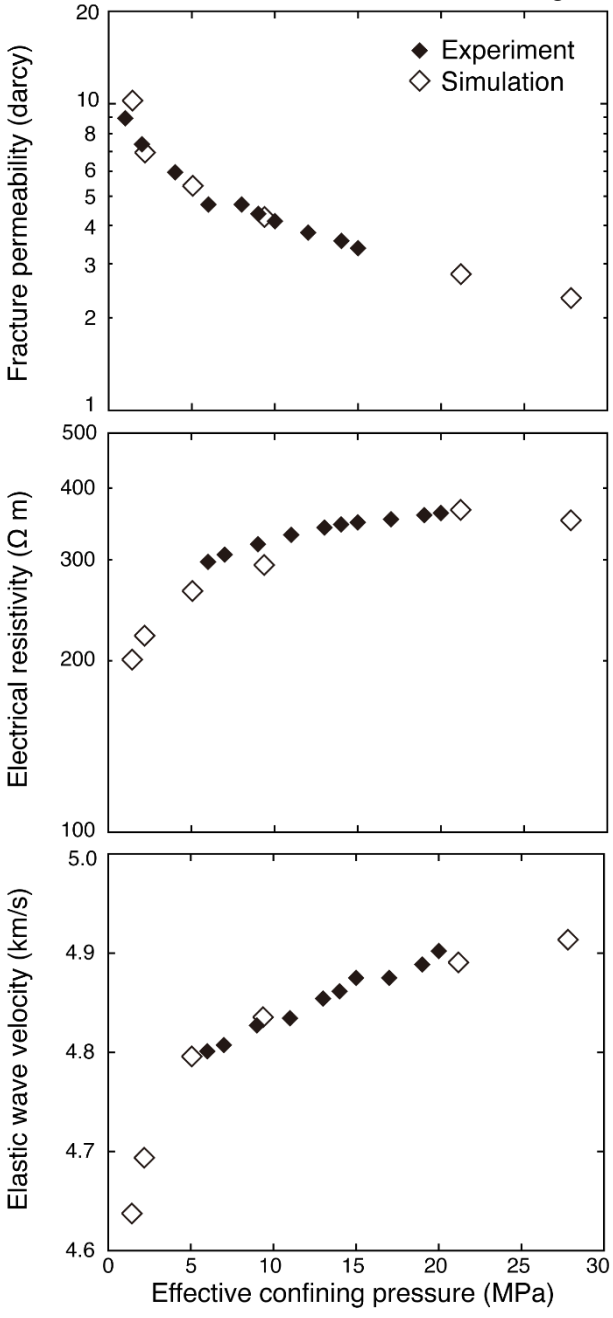

Fig. 1. Changes of hydraulic permeability, electrical resistivity and elastic wave velocity against the effective confining pressure. Note that pressure condition of

numerical simulation was estimated by using aperture-pressure relationship based on permeability matching approach.

pressure. Although simulated results originally calculated these parameters as a function of mean aperture, effective confining pressure was estimated in each aperture condition from aperture-pressure relationship based on the permeability matching approach [4, 5]. Despite the fact that only permeability was used for the matching, calculated resistivity and velocity also show good agreements with experimental results. Furthermore, the threshold of resistivity and velocity changes appeared at ~5 MPa of effective confining pressure.

For further investigation of resistivity and velocity changes with aperture closure, these properties are plotted against the mean aperture of fracture (Fig. 2). Mean aperture values during the experiment were estimated from aperture-pressure relationship at each pressure condition. Whereas both resistivity and velocity decrease with increasing mean aperture, the decreasing rate of them becomes different after ~0.8 mm of mean aperture. This ~0.8 mm of aperture condition is consistent with ~5 MPa of effective confining pressure where resistivity and velocity show thresholds. In addition to these thresholds, fluid pathway is disconnected after this pressure condition. In other words, connective fluid pathway may be formed at ~0.8 mm of aperture condition. Once connective fluid pathway is formed, resistivity may not change while velocity shows continuous changes against the aperture opening. This suggests that velocity has higher sensitivity against the aperture opening whereas resistivity can be useful for detecting connection or disconnection of fluid pathways with aperture changes.

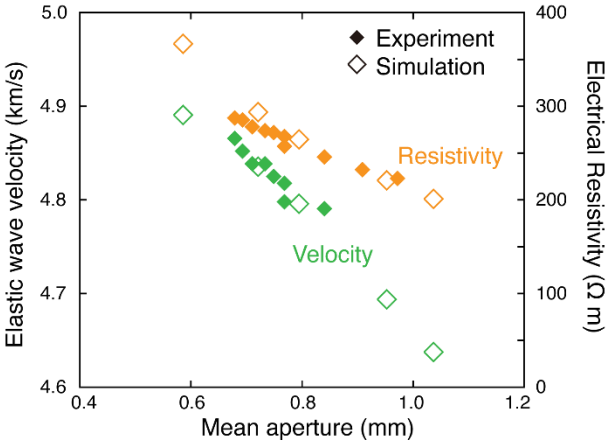

Fig. 2. Elastic wave velocity and electrical resistivity changes as a function of mean aperture. Note that mean aperture during the experiment was estimated by using aperture-pressure relationship based on permeability matching approach.

4. CONCLUSSION

The present study developed experimentally-validated numerical approach that can simultaneously investigate hydraulic permeability, electrical resistivity and elastic wave velocity from the digital image of natural rock fracture. From the permeability matching approach, we estimated mean aperture during the experiment and also pressure condition in each numerical simulation which could not be determined by only the experiment or simulation. As a result, resistivity and velocity shows threshold at the same pressure condition (~5 MPa in our study) while decreasing rates of them with aperture opening would be different after 0.8 mm of aperture condition (decreasing rate of resistivity is ~60 Ωm while that of velocity is ~80 m/s per 0.1 mm aperture change). These behaviors may be controlled by connection or disconnection of the fluid pathway which was observed by Lattice Boltzmann fluid-flow simulation. Our new approach can reveal the resistivity and velocity changes with aperture closure or opening and our results suggest that resistivity monitoring can be useful for detecting connection or disconnection of the fluid pathway while aperture opening can be monitored by velocity measurement.

5. REFERENCES

[1] R. H. Sibson, Earthquake rupturing as a mineralizing agent in hydrothermal systems, Geology, 15 (1987) 701–704.

[2] A. J. Hawkins, M. W. Becker, J. W. Tester, Inert and adsorptive tracer tests for field measurement of low-wetted surface area. Water Resour. Res., 54 (2018) 53415–5358.

[3] E. R. Okoroafor, R. N. Horne, The Impact of Fracture Roughness on the Thermal Performance of Enhanced Geothermal Systems, GRC Transactions, 42 (2019).

[4] N. Watanabe, N. Hirano, N. Tsuchiya, Determination of aperture structure and fluid flow in a rock fracture by high resolution numerical modeling on the basis of a flow-through experiment under confining pressure, Water Resour. Res., 44 (2008).

[5] T. Ishibashi, N. Watanabe, N. Hirano, A. Okamoto, N. Tsuchiya, Beyond-laboratory-scale prediction for channeling flows through subsurface rock fractures with heterogeneous aperture distributions revealed by laboratory evaluation, J. Geophys. Res. Solid Earth, 120 (2015) 106–124.

[6] T. Taira, N. Avinash, F. Brenguier, M. Manga, Monitoring reservoir response to earthquakes and fluid extraction, salton sea geothermal field, California. Science Advances, 4 (2018).

[7] J. R. Peacock, S. Thiel, P. Reid, G. Heinson, Magnetotelluric monitoring of a fluid injection: Example from an enhanced geothermal system. Geophysical Research Letters, 39 (2012), 3–7.

[8] W. F. Brace, A. S., Orange, T. R. Madden, The effect of pressure on the electrical resistivity of water-saturated crystalline rocks. J. Geophys. Res., 70 (1965), 5669–5678.

[9] A. Nur, G. Simmons, The effect of saturation on velocity in low porosity rocks. Earth and Planetary Science Letters, 7 (1969), 183–193.

[10] A. Revil, N. Florsch, Determination of permeability from spectral induced polarization in granular media, Geophysical Journal International, 181(2010), 1480–1498.

[11] K. Zaima, I. Katayama, Evolution of Elastic Wave Velocities and Amplitudes During Triaxial Deformation of Aji Granite Under Dry and Water - Saturated Conditions. J. Geophys. Res. Solid Earth, 123 (2018), 9601-9614.

[12] T. Watanabe, A. Higuchi, Simultaneous measurements of elastic wave velocities and electrical conductivity in a brine-saturated granitic rock under confining pressures and their implication for interpretation of geophysical observations, Progress in Earth and Planetary Science, 37 (2015).
[13] Guéguen, Y., and Palciauskas, V. Introduction to the physics of rocks, Princeton, New Jersey, 1994, 294p.
[14] G. Mavko, T. Mukerji, J. Dvorkin, The Rock Physics Handbook: Tools for Seismic Analysis of Porous Media. Cambridge University Press, Cambridge, 2009, 511p.
[15] A. Kirkby, G. Heinson, L. Krieger, Relating permeability and electrical resistivity in fractures using random resistor network models, J. Geophys. Res. Solid Earth, 121 (2016).
[16] L. J. Pyrak-Nolte, D. D. Nolte, Approaching a universal scaling relationship between fracture stiffness and fluid flow. Nat. Commun. 7 (2016).
[17] K. Sawayama, K. Kitamura, Y. Fujimitsu, Laboratory measurements on electric and elastic properties of fractured geothermal reservoir rocks under simulated EGS conditions. GRC Transactions, 42 (2018) 2459–2475.
[18] F. Jiang and T. Tsuji, Changes in pore geometry and relative permeability caused by carbonate precipitation in porous media, Physical Review E 90 (2014).
[19] N. Mohd, C. Hu, X, Li, WAVE-STRUCTURE INTERACTION USING FREE SURFACE LATTICE BOLTZMANN METHOD (FSLBM), IEICES (2015) 11–12.
[20] N. A. C. Sidek, A. A. Kihan, Experimental and Numerical Simulation Investigation of Flow Over a Cavity Using Multi- Relaxation Time Lattice Boltzmann Method, IEICES (2016) 45–48.
[21] E, J. Garboczi, Finite Element and Finite Difference Programs for Computing the Linear Electric and Elastic Properties of Digital Images of Random Materials (1998).
[22] P. A. Witherspoon, J. S. Y. Wang, K. Iwai, J. E. Gale, Validity of cubic law for fluid flow in a deformable rock fracture, Water Resour. Res., 16 (1980).
[23] K. Sawayama, K. Kitamura, Y. Fujimitsu, Relationship between Complex Resistivity, Elastic Wave and Water Saturation of Cracked Andesite under Laboratory Fluid-Flow Test. BUTSURI-TANSA (Exploration Geophysics), 71 (2018) 71–85.

Integrating 3D- Printing Technology in Assistive Adaptive Device Prescription in Rehabilitation Medicine: A Conceptual Framework

NM Hashim[1]*, NAC Zakaria[2], S Shukor[2], MZ Amin[2], NS Mahdzir[2], NM Mustafah[1], NF ARoslan[1]
[1]Department of Rehabilitation Medicine, Faculty of Medicine, Universiti Teknologi MARA Selangor
[2] Faculty of Mechanical Engineering, Universiti Teknologi MARA Selangor
*Corresponding author: natiara@uitm.edu.my

Abstract: *Prescription of assistive adaptive device (AAD) is one of the interventions to assist person with disabilities (PWD) in performing activities of daily living and reduce their dependency level. PWD possess a unique set of disabilities which differ from one to another. Customization of AAD is important to conform toward various disabilities. However, production of AAD in our local clinical setting is limited in customization due to lack of technical expertise and out- dated method of production. The objective of this project is to propose a new conceptual framework of introducing 3D printing technology in AAD prescription. 3D- printing technology allows shorter lead times, mass customization, reduced parts count, more complex shapes, parts on demand and less material waste. This paper will illustrate a conceptual framework to integrate 3D Printing Technology in AAD Prescription process.*

Keywords: Disabilities; Assistive Adaptive Device; 3D Printing Technology; Rehabilitation.

1. INTRODUCTION

The ultimate goal of rehabilitation medicine for person with disabilities is to achieve optimize functional status [1]. Assistive adaptive device (AAD) (Figure 2 and Figure 3) is one of the means to assist person with disabilities (PWD) to assist in performing activities of daily living [2]. Every patient possesses a set of unique disabilities depending on the nature of the diseases and other biopsychosocial factors as described by International Classification of Functional Framework, depicted by Figure 1 [3]. Hence, the adaptive devices must be customized individually to conform towards specific disability in achieving specific functional goal. Globally, more than 1 billion people need 1 or more assistive products. It is interestingly to state many low-income and middle-income countries, people who have access to required AAD is limited to only 5-15% (4). Recent United Nations resolutions has included the accessibility to assistive technology into its action plan in order to realizing towards the targets in Sustainable Development Goals relating to universal health coverage (5). There are six criteria that should be assessed in ensuring a good assistive technology delivery; availability, accessibility, acceptability, adaptability, affordability and quality [6].

In an optimum condition, adaptive device prescription process should be able to conform, amiable to customization, adjustable to more complex parts in order to produce a functioning AAD that address specific different needs [2]. Current local clinical setting, the fabrication of upper limb AAD is very much reliance towards what is available in the market or produced by conventional way by occupational therapist which is limited to only molding or sewing with very few materials options that can be utilized. More complex design of AAD are unable to be produced due to limited technology in modelling, fabrication and production [7].

3D- printing technology allows shorter lead times, mass customization, reduced parts count, more complex shapes, parts on demand and less material waste [8]. The popularity and low cost of 3D printing technology, it has driven a Do-It- Yourself (DIY) movement created by the consumers and hobbyists via online communities [8]. However, there are limited evidence to support DIY AAD production in terms of how the rehabilitation professional should response to this kind of movement [9]. Their AAD production is not supervised or monitored by the rehabilitation professionals, which may not meet acceptable standards. Additionally, the benefits of multidisciplinary team are lost during this DIY process. 3D printing products should be monitored for its adverse effect which is not occurring during DIY process. A proper mechanism on how the 3D printing technology should be conducted in rehabilitation setting is crucial that include the work process and products. In terms of the process, we should examine the CAD/CAM program usability, material variability/availability, costs of 3DP for rehabilitation-related endeavors, identify appropriate professional other than rehabilitation health professional that should be recruited into the multidisciplinary team to assist in the development of new innovative ideas [9]. In terms of product, research should be directed in examining potential improvement in function, aesthetic and quality. Effectiveness of the end product should be examined by administering validated functional outcome measure such Functional Independence Measure (FIM), Modified Barthel Index (MBI) or Goal Attainment Scale [10].

This proposed project is to construct a multidisciplinary framework to conceptualize 3D-printing technology into rehabilitation medicine services, pertaining to the invention of customized AAD.

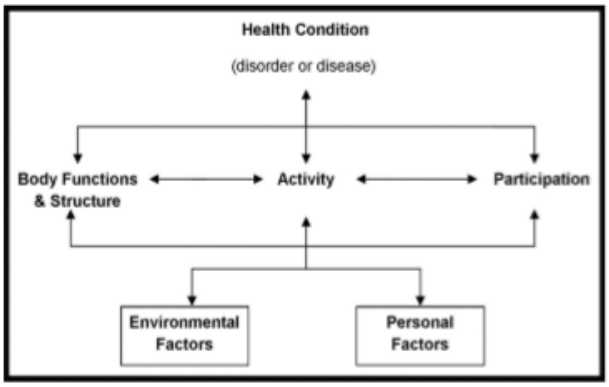

Figure 1: International Classification of Functional Framework describing factors that contribute to the diversity of disabilities.

Figure 2: Example of conventional AAD for feeding function for tetraplegic hand

Figure 3: Example of conventional AAD for writing function for tetraplegic hand

The central focus of this paper is to discuss the conceptual framework in analyzing the work process of integrating 3D printing technology into assistive adaptive device prescription in rehabilitation medicine. In this newly developed framework, the bio-mechanic features, designs, material selection and cost of fabrication and production of assistive adaptive devices is explored. Trial project is conducted to test the effectiveness and safety of the produce AAD in improving function in spinal cord injured patients with tetraplegia, stroke patients with hemiparesis of the limbs, rheumatoid arthritis patients with joint problems, patient with progressive motor neuron diseases and other diseases that may presented with variable pattern of disabilities especially affecting the upper limb function.

2. OPERATIONAL FRAMEWORK

The framework is composed of two phases, begins with constructing a trans-disciplinary framework in AAD prescription and measurement of the effectiveness and safety of the invented functional AAD.

Formation of trans-disciplinary team member consist of rehabilitation physician (RP), occupational therapist (OT) and a new addition of technical expertise (engineer) is a new vital step that will be introduced into the existing AAD prescription process. Patients who require AAD are examined by RP and OT to identify the impairment and disabilities that need to be addressed. The patient's clinical condition and disabilities are demonstrated to the technical expertise. Discussion among the team members and patient are held to achieve a collective decision on setting the functional goal specifically pertaining to upper limb function as illustrate in Figure 4. Appropriate specification of design and desired features of AAD that will be produced in order to achieve the functional goal are discussed. This process is crucial, which enable the synchronization of information and understanding of patient's disabilities and theirs needs, hence, ideal solutions can be proposed pertaining to AAD designs.

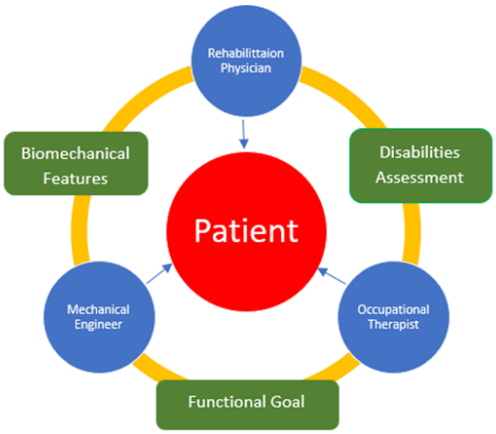

Figure 4: Transdisciplinary Team Proposition

The recruitment of a technical expertise as a new member in the existing multi- disciplinary team allows exploration of a new method utilizing 3D printing technology in customizing AAD. The new method of fabrication and production of customized AAD includes several stages: **Scanning**: Using a handheld scanner to scan the anatomy of the hand to ensure the shape, any deformity and size of the hand are captured. The scan model will be uploaded to the CAD software for further modelling for AAD. **Design:** Using CAD model, modelling involve planning of the AAD blueprint. The process may include modifying, refining or upgrading existing available AAD blueprint or inventing or creating of a new product. AAD for upper limb should possess important features which are required in order to adapt and customize towards patient impairment. **Printing:**

Identification and selection of the appropriate material for the desired strength, durability, strength, usage properties and cost estimation. **Finishing:** This process involves cooling, removing residual debris, polishing, drilling or cutting to prepare the product for further testing on patient. **Product Testing:** The newly produced AAD will be tested on its function onto patients and any adverse event will be monitored which include pressure injury, pain or AAD malfunctions. During this process, any problem or product malfunction will be modified accordingly which may involve re-designing, material re-selection or re-printing. At the end of this process, the finalized product will be analyzed for its characteristics and level of function. **Product Outcome**: CAD designs, bio-mechanical features, material characteristics, cost involve, limitations and advantages of the process framework. **Level of Function Outcome:** Goal Attainment Scale and Modified Barthel Index. **Service Quality**: Orthotics and Prosthetics Users' Survey (OPUS) Questionnaire.

3. CONCLUSION

3D printing technology for advanced medical device applications encompasses a versatile, growing array of technologies for generating AAD products. Identifying correct expertise, formation of a trans- disciplinary team and conceptualizing a new framework to utilize 3D printing technology in rehabilitation services are mandatory to ensure good outcomes. Thus, this will ensure a new upgraded and up-to-date rehabilitation medical service that is cost-effective can be set- up, in order to improve PWD current medical rehabilitation management and may further reduce time and waste materials.

4. REFERENCES

[1] Rimmer JH. Use of the ICF in identifying factors that impact participation in physical activity/rehabilitation among people with disabilities. Disability and rehabilitation. 2006;28(17):1087-95.

[2] Yeung K-T, Lin C-H, Teng Y-L, Chen F-F, Lou S-Z, Chen C-L. Use of and self-perceived need for assistive devices in individuals with disabilities in Taiwan. PloS one. 2016;11(3): e0152707.

[3] Stucki G, Cieza A, Melvin J. The international classification of functioning, disability and health: A unifying model for the conceptual description of the rehabilitation strategy. Journal of rehabilitation medicine. 2007;39(4):279-85.

[4] World report on disability. Geneva: World Health Organization; 2011.

[5] Resolution WHA71.8. Improving access to assistive technology Geneva: World Health Organization; 21-26 May 2018 [Available from:http://www.whoseajph.org/(http://apps.who.int/gb/ebwha/pdf_files/WHA71/A71_R8-en.pdf.

[6] Tangcharoensathien V, Witthayapipopsakul W, Viriyathorn S, Patcharanarumol W. Improving access to assistive technologies: challenges and solutions in low-and middle-income countries. WHO South-East Asia journal of public health. 2018;7(2):84.

[7] Mavroidis C, Ranky RG, Sivak ML, Patritti BL, DiPisa J, Caddle A, et al. Patient specific ankle-foot orthoses using rapid prototyping. Journal of neuroengineering and rehabilitation. 2011;8(1):1.

[8]Thingiverse: Digital Design for Physical Objects [Available from: https://www.thingiverse.com/

[9] Sharma S, Goel SA. 3D Printing and its Future in Medical World. Journal of Medical Research and Innovation. 2019;3(1): e000141-e.

[10] Lunsford C, Grindle G, Salatin B, Dicianno BE. Innovations with 3-dimensional printing in physical medicine and rehabilitation: a review of the literature. PM&R. 2016;8(12):1201-12.

Non-uniform Sintering Behavior of Y_2O_3 Ceramics

Ji-Hwoan Lee[1], Byung-Nam Kim[2], Byung-Koog Jang[1,*]
[1]Interdisciplinary Graduate School of Engineering Science, Kyushu University, Kasuga 816-8580, Japan
[2]Research Center for Functional Materials, National Institute for Materials Science, Tsukuba 305-0047, Japan
*Corresponding author email: jang.byungkoog@kyudai.jp

Abstract: *The densification of Y_2O_3 was carried out by spark plasma sintering (SPS) technique with various heating rates (5, 10, 20, and 50°C/min) and holding times (2, 5, 20, and 60 mins) at 1000°C. Among the entire specimens, uniform or non-uniform sintering behavior was divided based on the heating rate of 20°C/min like Fig. 1. At the heating rate of 20°C/min, the center was totally translucent and densified, and the boundary of the specimen was opaque. On increasing the holding time, the center became opaque and the periphery became translucent. It is special result that the sintering is conducted thoroughly and the regions were divided. As a result of the microstructural analysis, the grain size in the center of all specimens was larger than the periphery. Especially, at the high heating rate (20 and 50°C/min), the difference in grain size between the center and periphery was significantly increased around 3.5 times on average. In addition, there was a difference of the pore size and distribution.*

Above non-uniform sintering behavior could be explained by setting the assumption (the mass transfer occurred from center to periphery). The densification was carried out with lots of defects in sintered bodies and coarsening was significantly induced in the center due to the assumption and the dynamic grain growth on increasing the heating rate [1]. The evidence to demonstrate the assumption will be obtained by additional experiments.

Keywords: Spark plasma sintering; Non-uniform sintering behavior; Translucent; Opaque; Y_2O_3.

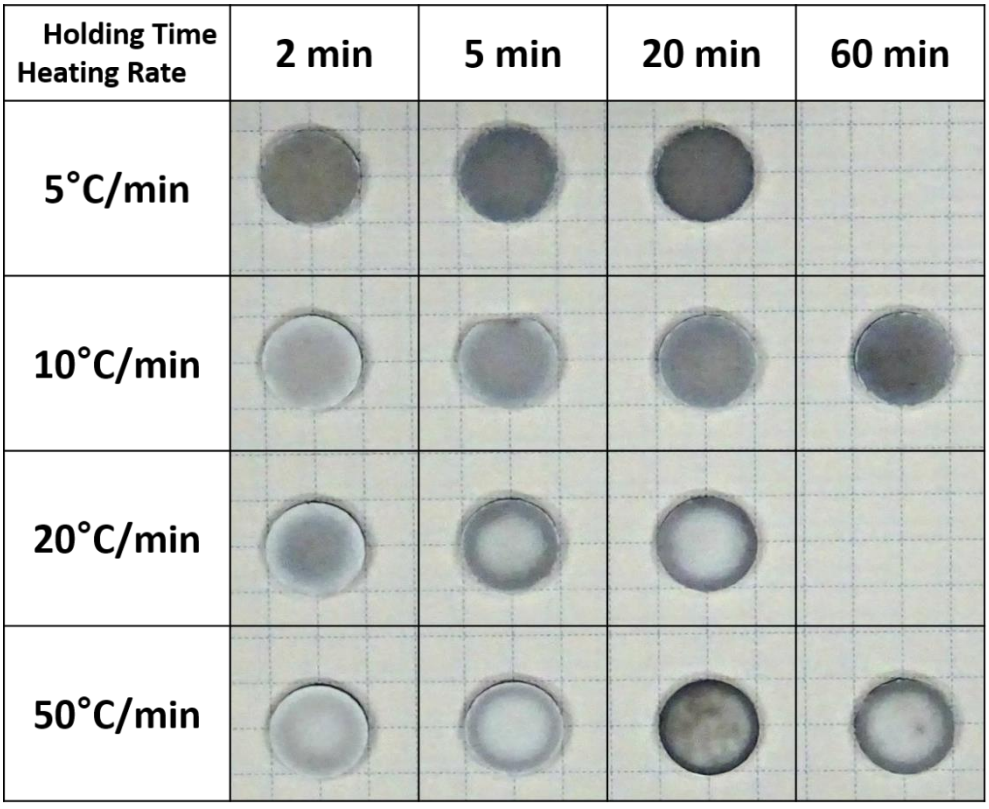

Fig. 1 Optical image of the sintered bodies with different appearance depending on holding times (2, 5, 20 and 60 min) and heating rates (5, 10, 20 and 50°C/min).

References

[1] B.N. Kim, K. Hiraga, K. Morita, H. Yoshida, Y.J. Park, Y. Sakka, *Scripta Mater.* 80 (2014) 29-32.

Propagation Mode Retention Using Strongly Coupled Multi-Core Fiber

Mahmoud Nasef[1*], Kantaro Fujimoto[1], Haisong Jiang[1], Kiichi Hamamoto[1]
[1]Interdisciplinary Graduate school of Engineering Sciences, Kyushu University, Japan
[*]Corresponding author email: mmnasef@kyudai.jp

Abstract: *This paper deals with the research proposal and evaluation of Strongly coupled MCF which is studied in propagation mode retaining capability as regular multi-mode fiber has an issue of mode crosstalk. As a result, mode retention characteristics of 5 dB at 80 mm bending radius has been confirmed successfully.*

Keywords: Strongly coupled fiber; Mode crosstalk; Multi-core fiber; Mode division multiplexing.

1. INTRODUCTION

Data center traffic is already estimated to become 20 ZB by the year 2021 about twice as much as in 2019 [1]. MDM (mode division multiplexing) can expand transmission capacity within data center [2]; therefore, we propose to introduce an optical network system utilizing MDM into data centers [3]. It has; however, a problem of mode crosstalk in the fiber that prevents proper preservation of individual mode transmission. One main cause of this crosstalk has been mode excitation phenomenon at the bending region of the fiber [4]. MIMO (Multi-input multi-output) is exploited to demonstrate MDM transmission capability; however, it is ideal in the case of utilizing mode retaining that leads to MIMO less transmission. In this paper, we study and demonstrate strongly coupled MCF to verify the mode retaining capability. We simulated and estimated the transmittance of input mode by using BPM (beam propagation method) simulation. As a result, we verified the mode retention characteristics of 5 dB at 80 mm bending radius, compared to regular multi-mode fiber.

2. CONCEPTS

2.1 Propagation Mode in Strongly Coupled MCF

In MDM, LP (linear polarization) mode has mainly been researched in recent years; however, LP mode has some problems in applying it to transmission within data centers, especially, the existence of mode degeneration [5]. Thus, it normally requires the use of MIMO processing which is not suitable for data centers. One way to avoid the mode degeneration issue is to use single dimensional mode and strongly coupled MCF for the transmission line.

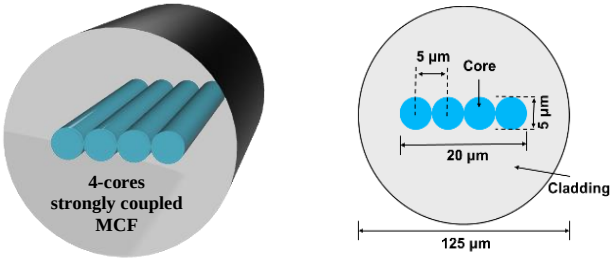

(a) (b)

Fig. 1. Strongly coupled MCF which propagates strongly coupled beams. (a) Schematic; (b) Cross-sectional structure view.

A schematic view of the fiber being used is shown in Fig.1. Here, the fiber used is a coupled multi-core fiber which consists of 4 single-mode cores strongly coupled together as shown in Fig.1 (a). This strongly coupled MCF propagates strongly coupled beams with each core width of 5 µm as illustrated in Fig.1 (b). The fiber length used is about 4 m long. In the coupled MCF, cores with small diameter are adjacent in horizontal directions (the refractive indices of core and cladding are n_1 =1.45886 and n_2 =1.43824, respectively) [6].

2.2 Mode Crosstalk in Fiber

Mode crosstalk may occur in the transmission line. This may be caused at the bending region of the fiber. This phenomenon is explained in Fig.2. This figure shows one example of the simulation by using beam propagation method (BPM). Higher mode may be excited especially in the case of small bending radius. This leads to mode crosstalk. In the case of Fig.2, LP_{01} mode is injected whereas LP_{11} mode is excited at the bending region [5]. Because of the mode crosstalk, MIMO is essential when we want to distinguish the modes; however, MIMO is not

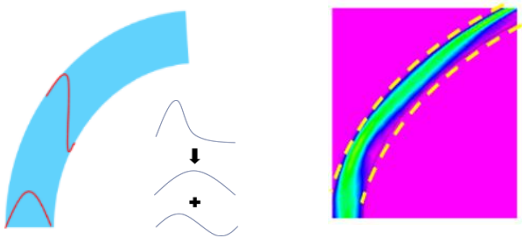

(a) (b)

Fig. 2. Light un-centered and higher mode excitation at bending region of regular multi-mode fiber. (a) Schematic; (b) Simulation.

desired in short distance transmissions such as within data centers due to the latency in addition to the cost issues.

2.3 Concept of Mode Retention

The beam going outside at the bending region (fiber or waveguide) may be prevented in the strongly coupled MCF (multi-core fiber) as shown in Fig.3. The strongly coupled MCF may prevent higher order mode excitation at the bending region as the core spacing may prevent beam deflection toward bending outside.

Fig. 3. Mode propagation at bending waveguide/region in proposing slit waveguide.

3. RESULTS AND DISCUSSION

3.1 Simulation Results

We estimated the 0^{th} mode transmittances of the strongly coupled MCF and regular MMF by BPM simulation. Input light used was 1550 nm TE 0^{th} mode. In order to verify mode retention characteristics in bending strongly coupled MCF, we estimated 0^{th} mode transmittance per one turn (custom reel) after calculating and standardizing the 0^{th} mode transmittance in 5 degree bending fiber. The overall results of four different bending radii are shown in Fig. 6. (a). In the case of strongly coupled MCF, the 0^{th} mode transmittance was improved to about 3 dB in 40 mm bending radius, so we confirmed mode retention characteristics of strongly coupled MCF. Note that the simulation was done for the parallel direction bending against the core-arrangement line as shown in Fig.4.

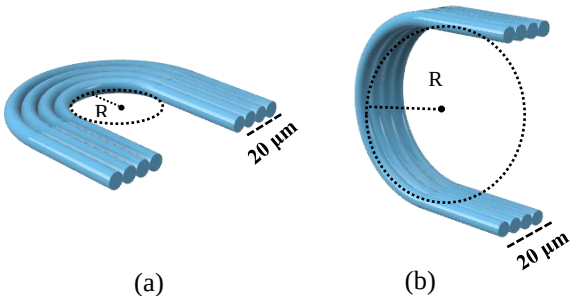

(a) (b)

Fig. 4. Bending directions of the strongly coupled MCF against core-arrangement line. (a) Parallel arrangement, (b) Perpendicular arrangement.

3.2 Experimental Results

Firstly, Fig. 5 below illustrates the far field pattern (FFP) intensity measurement of 0^{th} mode and 1^{st} mode. We conducted an experimental setup that demonstrates the effect of bending radius of strongly coupled MCF and observed the findings. We could change the bending radius of the fiber by turning the fiber one turn using a custom made reel. In addition, four different bending radius measuring points (50 mm, 80 mm, 110 mm, 150 mm) were considered in order to observe the changes in the propagation mode retention and suppression of any mode excitation.

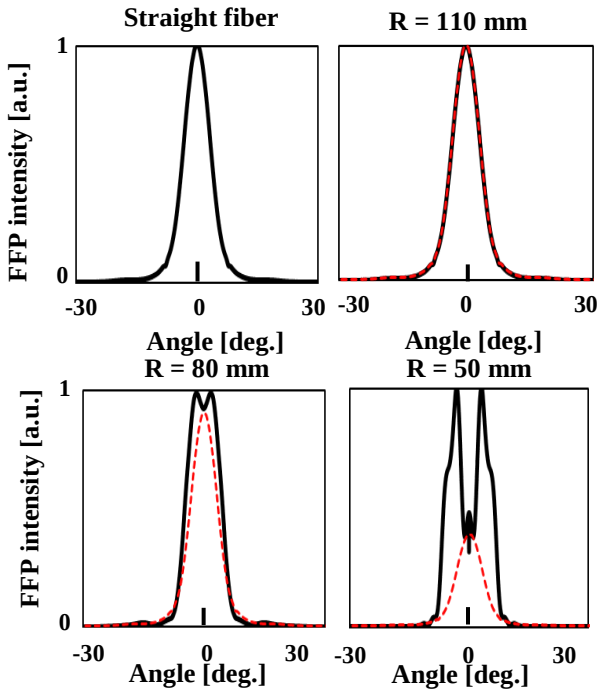

Fig. 5. FFP intensity measurement of strongly coupled MCF at different bending radii (R).

We validated the FFP intensity profiles along the horizontal center axis and the results are shown in Fig. 5. Initially, by observing Fig. 6. (b) below, 0^{th} mode transmittance of the strongly coupled MCF is higher than those of the few mode fiber (FMF). When the bending radius of the fiber is at 80 mm, mode retaining effect of 5 dB was confirmed. Furthermore, by comparing both results of Fig. 6. (a) and (b), both data show that strongly coupled MCF looks better in mode retention than the regular FMF when it comes to mode retention along the bending region.

However, the 0^{th} mode transmittance of the strongly coupled MCF of the experiment seems higher than that of the simulation results. The reason may be due to the different fiber bending directions. For the experimental work, the direction of the fiber could not be arranged to only parallel direction. Since mode retention is better in the perpendicular bending arrangement case in Fig.4 (b), the experiment resulted in better mode retaining capability than that of the simulation.

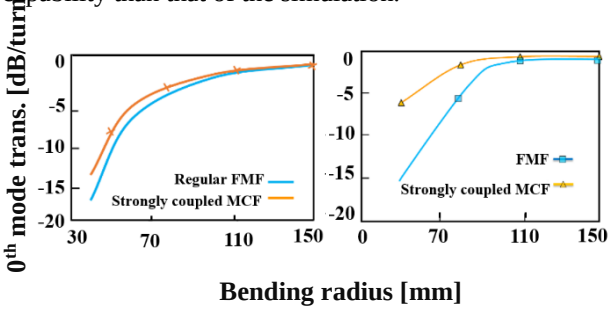

(a) (b)

Fig. 6. (a) Simulation results, (b) Experimental results of 0^{th} mode transmittance and mode retaining effect by reeling the strongly coupled MCF.

4. CONCLUSION

By using strongly coupled MCF, the simulation data estimated that the 0^{th} mode transmittance is about 3 dB better at the bending radius of 40 mm and the mode retention effect may be higher as the bending radius is smaller for the regular multimode fiber.

Additionally, the experimental results verified and improved on the simulated work. We verified mode retention characteristics of 5 dB at 80 mm bending radius, compared to the regular multi-mode fiber. Therefore, the experimental measurement results suggested the propagation mode retention characteristics of strongly coupled MCF.

5. ACKNOWLEDGMENT

This work has been financially supported by JSPS and technical support with fiber implementation by Fujikura Ltd, are all gratefully acknowledged.

6. REFERENCES

[1] "Cisco Global Cloud Index: Forecast and Methodology, 2016-2021 White Paper" https://www.cisco.com/c/en/us/solutions/collateral/service-provider/global-cloud-index-gci/white-paper-c11-738085.html

[2] Y. Kokubun, T. Komo, K. Takenaga, S. Tanigawa and S. Matsuo, "Quantitative mode discrimination and bending crosstalk of four-core homogeneous coupled multi-core fiber," *OFC/NFOEC*, Los Angeles, CA, 2012, pp. 1-3.

[3] Y. Kokubun, M. Koshiba, "Novel multi-core fibers for mode division multiplexing: proposal and design principle". *IEICE Electronics Express*, *6*(8), 2009, pp.522-528.

[4] T. Hayashi, T. Nagashima, O. Shimakawa, T. Sasaki and E. Sasaoka, "Crosstalk variation of multi-core fibre due to fibre bend," 36th European Conference and Exhibition on Optical Communication, Torino, 2010, pp. 1-3.

[5] K. Hamamoto, H. Jiang, "Optical mode switch and mode selective light source toward flexible mode-division multiplexing network." pp. PTh1D-4. *Photonics in Switching*. Optical Society of America, 2017.

[6] Snyder, A.W. and Love, J.D., 1986. Optical waveguide theory. *J. Opt. Soc. Am. A*, *3*, p.378.

The Effect of Post Treatment in Pore Development of Activated Carbon Prepared from Rice Husk

Chairunnisa[1], Kyaw Thu[2], Takahiko Miyazaki[3], Jin Miyawaki[4], Koji Nakabayashi[5], Muhammad Hamid Mahmood[6], Muhammad Sultan[7]
[1]Department of Energy Environmental Engineering, IGSES, Kyushu University, [2,3]International Institute for Carbon-Neutral Energy Research, Kyushu University, [4,5]Department of Advanced Device Materials, Institute for Material Chemistry and Engineering, Kyushu University, [6,7]Department of Agricultural Engineering, Bahauddin Zakariya University, Multan, Pakistan
chairunnisa.365@s.kyushu-u.ac.jp

Abstract: *The silica removal by post-treatment of activated carbon derived from rice husk has been conducted. Effect of post-treatment was observed by measuring the change of pore properties of carbon materials. Activated carbon prepared by steam activation has total surface area 285.5 m^2/g. After post-treatment, the total surface area of activated carbon is increased to 1170.9 m^2/g. From the Scanning Electron Microscope (SEM) images, it is found that the activated carbon derives from rice husk has non-uniform carbon frame shape and this frame was broken after post-treatment.*

Keywords: activated carbon; rice husk; steam activation; post-treatment.

1. INTRODUCTION

Rice is a major food crop for many countries and its husk has been produced in large quantity. Unfortunately, due to high silica content and low nutrition, rice husk is not suitable as animal feedstock or as compost materials. Therefore, recent method to reduce rice husk is by burning it in the open air which causing environmental pollution [1]. In order to decrease the rice husk amount without adding more environmental problems, it is necessary to convert this biomass into another material with a higher value.

Activated carbons are very important adsorbents which are used for many applications such as CO_2 adsorption [2] and air conditioning [3]. They have been prepared from various kinds of precursors such as biomass [3], fabric waste [4], and coals [5]. The utilization of biomass is promising because it is sustainable and low cost. Rice husk has been used as an activated carbon precursor in some previous studies[6][7]. However, rice husk contains 15% of ash which 90% of the ash is SiO_2 [8][9]. SiO_2 in carbon materials is needed to be removed in order to increase the surface area and impurity of activated carbon [10]. Several methods to remove SiO_2 from the surface of carbon materials have been reported in prior researches[11][12]. Therefore, in the present study, the activated carbon from rice husk had prepared by steam activation then the effect of post-treatment of activated carbon on its pore development was studied.

2. MATERIALS AND METHOD

2.1 Materials

Rice husk was pretreated by soaking in warm water (60°C) for 3 h to remove some ash content. The rice husk was then dried in an oven at 100°C for overnight. Dried rice husk was carbonized at 900°C for 1 h by a 15°C/min heating rate and 200 cm^3/min of N_2 gas flow rate. The carbonization product was activated by using steam at 900°C for 30 minutes. The activated carbon then was post-treated using KOH 2M and warm water at 90°C for 24 h to reduce silica content that can still block the pores of activated carbon [13]. The prepared materials were labeled as RHC (carbonized material), RHAC (activated carbon without post-treatment), RHAC-DW (activated carbon post-treated with distilled water), and RHAC-KOH (activated carbon post-treated with KOH).

2.2 Characterization

The pore properties of char and activated carbon before and after post-treatment was characterized by N_2 adsorption-desorption at 77K (Fig. 2) using Quantachrome NOVA3200e, SA and Pore Size Analyzer (USA). All pore properties were calculated by using NLDFT (non-localized density functional theory). The surface morphology of activated carbon was observed by the Scanning Electron Microscope JFM-6700, JEOL.

3. RESULTS AND DISCUSSION

Before biomass was converted into carbon materials, it was pretreated by 60°C of distilled water to reduce the mineral contents**.** There was a 9% mass loss of rice husk after being pretreated using warm water. It might be due to the dissolution of some inorganic materials such Al_2O_3, SiO_2, Fe_2O_3, CaO, MgO, Na_2O, and K_2O from rice husk into the water[14]. The pre-treated biomass then were carbonized and activated by steam. The yield of activation is 44.7% with an overall yield is 13.5%.

Fig. 1 Demonstrates that before activation, char derives from rice husk possess some pores. More pores were formed after activation (b) and it is shown that activated carbon derives from rice husk has non-uniform pores and cavities, different pore size and shapes. The structure of activated carbon was broke after post-treatment with both distilled water (c) and KOH (d).

The post-treatment by warm water broke the carbon structure and causing the decrease in the total surface area (Table 1). On the other hand, the post-treatment by KOH at 90°C not only broke the structure of activated carbon but also broadened the pores. Post-treatment by KOH were able to produce more micropores and enlarging the

existed micropores into bigger pores. This phenomenon can be observed from the pore size distribution graph (Fig. 3).

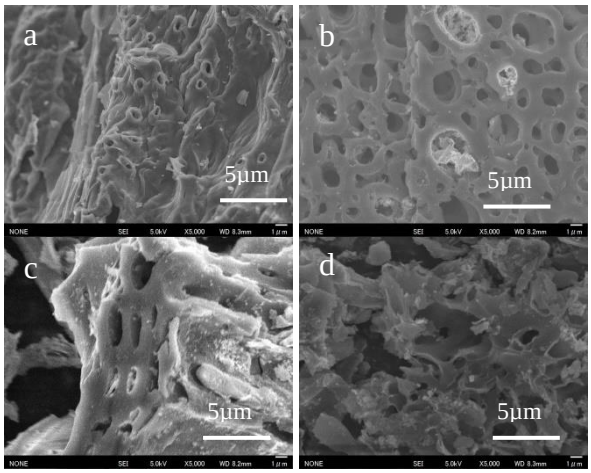

Fig. 1. SEM images of: (a) RHC, (b) RHAC, (c) RHAC-DW, and (d) RHAC-KOH.

Fig. 2 shows the nitrogen adsorption-desorption isotherm of all materials. From Fig. 2, it can be seen that adsorption of N_2 onto RHAC and RHAC-KOH were following the combination of type I and IV which is typically for microporous (type I) and developed mesopores (type IV) according to the classification of IUPAC [15]. On the other hand, N_2 adsorption onto RHC and RHC-DW are following the combination of type I and type II which indicate that both materials have a small number of micropores and nearly to the non-porous material.

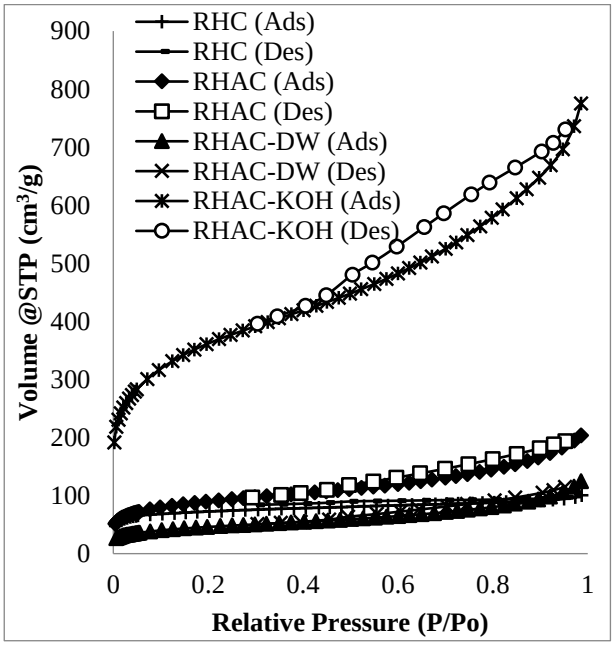

Fig. 2. N_2 adsorption-desorption isotherms of carbon materials at 77K.

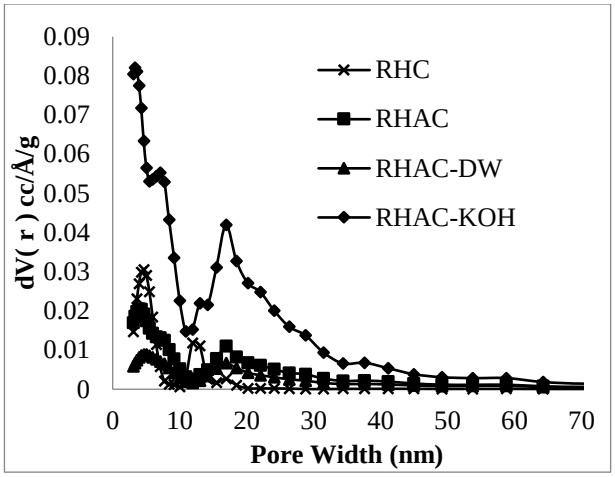

Fig. 3. Pore size distribution of the carbon materials.

Fig. 3 demonstrates how the pore development happened. It is shown that RHC has a small number of micropores. After activation (RHAC), the peak intensity at around 5 nm was decreased. Moreover, there is broadened and shift peak into bigger pore width which indicates after activation, instead of producing new micropores, the steam reacts with existed pores to created bigger pores. After being post-treated with deionized water, the number of pores and surface area of RHAC-DW reduced. Surface area of RHDAC-DW (140.7 m^2g^{-1}) is smaller than RHC (239.5 m^2g^{-1}) and RHAC (285.5 m^2g^{-1}) which means that post-treatment by warm deionized water was not favored to increase the porosity of activated carbon. On the other hand, bigger and higher peaks were produced after post-treatment by KOH (RHAC-KOH) which demonstrate that more blocked pores of activated carbon opened [13]. This result also supporting by the total surface area of RHAC-KOH which is 1170.9 m^2/g with total pore volume is 1.07 cm^3/g. This value shows that post-treatment of activated carbon by KOH can effectively enrich the porosity of activated carbon.

The pore properties of all carbon materials are represented at Table 1. From that table, it is confirmed that RHAC-KOH has the highest total surface area, total volume, and micro-porosity compare with other prepared carbon materials. This result is higher compare with prior research that produced activated carbon by chemical activation[16][6].

Table 1. Pore properties of carbon materials.

Samples	S_{total}[a] ($m^2\ g^{-1}$)	V_{total}[b] ($cm^3\ g^{-1}$)	S_{micro}[c] ($m^2\ g^{-1}$)	V_{micro}[d] ($cm^3\ g^{-1}$)
RHC	239.5	0.14	238.11	0.13
RHAC	285.5	0.28	254.3	0.16
RHAC-DW	140.7	0.17	120.84	0.09
RHAC-KOH	1170.9	1.07	1064	0.69

4. CONCLUSIONS

The study investigated the effect of post-treatment of activated carbon prepared from rice husk by steam. As treated by KOH, the surface area of activated carbon increased more than 4 times of the surface area of activated carbon without post-treatment. The pore volume raised more than 7 times compare to before post-treatment.

5. REFERENCES

[1] E. Menya, P. W. Olupot, H. Storz, M. Lubwama, and Y. Kiros, "Production and performance of activated carbon from rice husks for removal of natural organic matter from water: A review," *Chem. Eng. Res. Des.*, vol. 129, pp. 271–296, 2018.

[2] M. Muttakin, A. Pal, K. Uddin, K. Thu, K. Ito, and B. Baran Saha, "Experimental study of CO_2 adsorption kinetics onto activated carbon Experimental study of CO2 adsorption kinetics onto activated carbon," vol. 4, pp. 2018–2028, 2018.

[3] A. Pal, S. Mitra, K. Thu, and B. B. Saha, "Improved adsorption uptake of ethanol and CO2 onto biomass based activated carbons," *Proc. Int. Exch. Innov. Conf. Eng. Sci.*, vol. 3, pp. 127–128, 2017.

[4] T. L. Silva, A. L. Cazetta, P. S. C. Souza, T. Zhang, T. Asefa, and V. C. Almeida, "Mesoporous activated carbon fibers synthesized from denim fabric waste: Efficient adsorbents for removal of textile dye from aqueous solutions," *J. Clean. Prod.*, vol. 171, pp. 482–490, 2018.

[5] A. H. Jawad, K. Ismail, M. A. M. Ishak, and L. D. Wilson, "Conversion of Malaysian low-rank coal to mesoporous activated carbon: Structure characterization and adsorption properties," *Chinese J. Chem. Eng.*, no. xxxx, 2019.

[6] N. Yalçin and V. Sevinç, "Studies of the surface area and porosity of activated carbons prepared from rice husks," *Carbon N. Y.*, vol. 38, no. 14, pp. 1943–1945, 2000.

[7] S. Sugashini and K. M. M. S. Begum, "Preparation of activated carbon from carbonized rice husk by ozone activation for Cr(VI) removal," *Xinxing Tan Cailiao/New Carbon Mater.*, vol. 30, no. 3, pp. 252–261, 2015.

[8] M. S. Masoud, W. M. El-Saraf, A. M. Abdel - Halim, A. E. Ali, E. A. Mohamed, and H. M. I. Hasan, "Rice husk and activated carbon for waste water treatment of El-Mex Bay, Alexandria Coast, Egypt," *Arab. J. Chem.*, vol. 9, pp. S1590–S1596, 2016.

[9] C. B. Majumder, M. Sharma, and G. Soni, "A simple non-conventional method to extract amorphous silica from rice husk," *Bioresour. Technol.*, pp. 0–4, 2014.

[10] N. M. Hieu, V. V. Korobochkin, and N. V. Tu, "A Study of Silica Separation in the Production of Activated Carbon from Rice Husk in Viet Nam," *Procedia Chem.*, vol. 15, pp. 308–312, 2015.

[11] M. Rhaman, M. Haque, M. Rouf, M. Siddique, and M. Islam, "Preparation and characterization of activated carbon & amorphous silica from rice husk," *Bangladesh J. Sci. Ind. Res.*, vol. 50, no. 4, pp. 263–270, 2015.

[12] M. Li, S. Ma, and X. Zhu, "Preparation of activated carbon from pyrolyzed rice husk by leaching out ash content after Co2 activation," *BioResources*, vol. 11, no. 2, pp. 3384–3396, 2016.

[13] J. H. Lee, Y. J. Heo, and S. J. Park, "Effect of silica removal and steam activation on extra-porous activated carbons from rice husks for methane storage," *Int. J. Hydrogen Energy*, vol. 43, no. 49, pp. 22377–22384, 2018.

[14] W. Xu *et al.*, "Comparative study of water-leaching and acid-leaching pretreatment on the thermal stability and reactivity of biomass silica for viability as a pozzolanic additive in cement," *Materials (Basel).*, vol. 11, no. 9, 2018.

[15] K. Stafford, W. Sing, and J. Rouquerol, "Reporting Physisorption Data for Gas / Solid Systems INCLUDING CATALYSIS * REPORTING PHYSISORPTION DATA FOR GAS / SOLID SYSTEMS with Special Reference to the Determination of Surface Area and Porosity," *Pure Appl. Chem.*, vol. 57, no. January 1985, pp. 603–619, 2016.

[16] W. Zhang *et al.*, "Direct carbonization of rice husk to prepare porous carbon for supercapacitor applications," *Energy*, vol. 128, pp. 618–625, 2017.

Design and Analysis of 3D Printed Prosthetic Hand for Symbrachydactyly Patients

Mohammad Azeeb Mazlan, Wan Fatimatul Aifaa Wan Fadzil, Helmi Rashid, Abdul Halim Abdullah*
Faculty of Mechanical Engineering, Universiti Teknologi MARA, 40450 Shah Alam, Selangor, Malaysia
*halim471@uitm.edu.my

Abstract: *A symbrachydactyly is a genetic problem which also synonym as a person with fingerless condition. The patients will have difficulties in daily activities such as to hold an item. To ease the constraints, a customized and patient-specific prosthetic hand is needed with a minimum cost. This project covers the designing process for the prosthetic hand, including computational analysis. Parametric study on the different thickness of the palm cover was conducted to evaluate the performance of the product. Then, the prosthetic hand is fabricated using 3D printing technology. The simulation study suggested that the 5mm thickness of the palm cover was sufficient to the product. The resulting maximum stress variation and total displacement were the indicator in proposing the optimum design.*

Keywords: 3D Printing; Finite Element Analysis; Prosthetic Hand; Symbrachydactyly.

1. INTRODUCTION

Three out of ten thousand newborns are born with symbrachydactyly according to a statistic by Latin-American Collaborative Study of Congenital Malformations [1]. Symbrachydactyly is a genetic problem which caused the finger of the newborn to be underdeveloped or shorten as shown in Figure 1 [2]. There are also cases of fingerless due to accident such as power-tool accident and also finger crushed between door.

Figure 1 Example of Symbrachydactyly Condition [2]

Due to non-life-threatening condition, not much solutions are available for them to improve their life quality or help them with the problems. These problems could hinder them from interacting like a normal person as even a simple task such as holding an item or pushing a button is very hard for them.

Current prosthetic that are available in the market such as the myoelectric or electrical-powered prosthetic hand are not suitable for these conditions due to limited space to place electrical component. It will be too bulky if implemented for people with these conditions [3].

The one solution that was proposed is to design and fabricate a prosthetic hand that do not uses any electrical component. The idea came from a company called E-Nable which uses the wrist to control the prosthetic hand [4]. By using 3D printing technology, a prosthetic hand could be fabricated in a cheaper and faster way compared to other method such as injection molding technique [5]. The 3D printer that will be used for the project is Fused Deposition Modelling (FDM) type which uses plastic filament as it is cheapest type and are easy to handle by anyone with minimal training [6].

The project will cover on the design of prosthetic hand using a Computer Aided Design (CAD) software and analyzed the design on the most critical part for different thickness. Different thickness of design would result in different behavior toward energy absorption [7]. Analysis is done to know the behavior of the design toward real life situation [8]. Finally, the prosthetic hand would then be fabricated using a 3D printer. The project would help to improve the life of those people with fingerless conditions.

2. METHODOLOGY

This project consists of three (3) major steps which are: (a) design process, (b) analysis process and (c) fabrication process.

2.1 Design Process

The first step is to scan the hand of the one with the fingerless patient to model the prosthetic hand from to have better fitment and better comfort for the user. The prosthetic hand would then be designed based on the scanned hand as per shown in Figure 2.

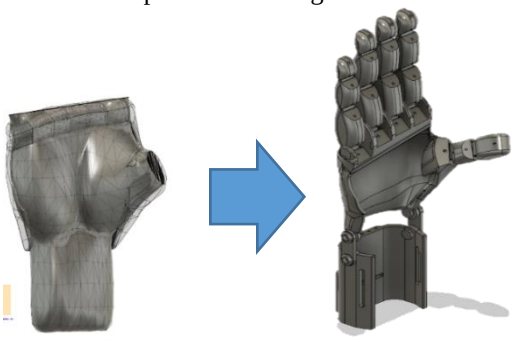

Figure 2 Process of Producing Prosthetic Hand from 3D Scanned File

2.2 Computational Analysis

The computational analysis was conducted using commercial finite element software, Ansys v19. The static analysis was focused on the most critical part which is the cover palm. Five different thickness of cover palm were considered which were 3mm, 4mm, 5mm, 6mm and 7mm. The model was discretized into tetrahedral

elements to predict the behavior of each section. The load of 10kg were assigned to the palm as illustrated in Figure 3. The performance of the model was predicted on the resulting total deformation and stress distribution of the model.

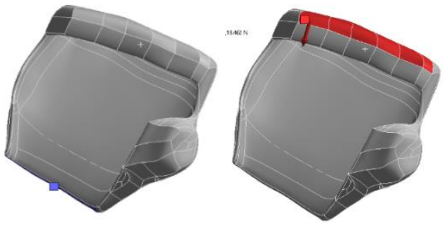

Figure 3 Loading and Boundary Conditions in the analysis. Constraints(Left) and Loading of 10kg (right) Conditions

2.3 Fabrication Process

The design would then be reworked if needed. The prosthetic hand design would then be exported to a slicing software for the 3D printer to read before it could fabricate the prosthetic hand. Once it is done printing, it would then be assembled to make a functional prosthetic hand.

3. RESULTS AND DISCUSSION

The design of the prosthetic hand was successfully developed and analyzed. The result for the analysis is as follow. For stress, it improved significantly when increasing the thickness of palm cover until 5mm. It shows minimal improvement when exceeding 5mm thickness as shown in Figure 4. The maximum stress that the material (Polylactic Acid) used could handle was 37.45MPa [5]. Similar case goes for the results of total deformation as per shown in Figure 5. All thickness would not fail but the best design would be of 5mm thickness with the safety factor of around 7.2. The deformation occur is insignificant as the deformation is too low under 1mm for 5mm thickness.

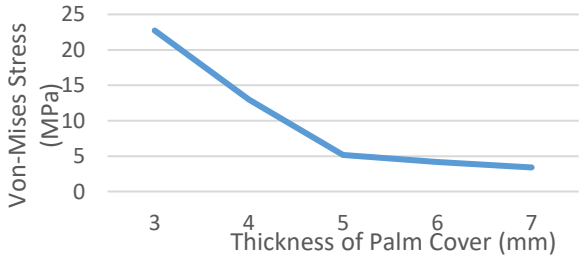

Figure 4 Maximum von Mises Stress in the Palm Cover

Once the best thickness was picked which is 5mm which has the suitable safety factor without increasing too much on the weight of the prosthetic hand, the design is ready for fabrication using 3D printer. The design need to be set-up according to the findings of the analysis. The setting used is of 1.2mm wall thickness with 100% infill. The 3D printer would then fabricate the prosthetic hand part by part. Once completed, it would be assembled into a working model as shown in Figure 6. The working model could be worn by the patient for its intended purpose straight away after assembly.

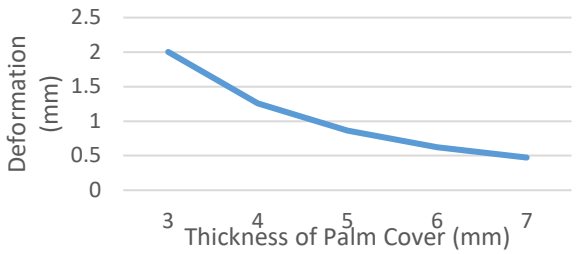

Figure 5 Deformation of Palm Cover

Figure 6 3D Printed Model of the Prosthetic Hand

4. CONCLUSION

The project's objective was successfully achieved which is to design a prosthetic hand, analyze the critical part and lastly to fabricate the prosthetic hand. The best thickness determined for the palm cover is 5mm with the safety factor of 7.2. The prosthetic hand also works as intended.

ACKNOWLEDGMENT

This research was supported by Universiti Teknologi MARA, UiTM under Grant No. 600-IRMI/PERDANA 5/3 BESTARI (103/2018). We also thank and acknowledge to Ministry of Education, Malaysia for the financial support.

5. REFERENCES

[1] Eduardo E Castilla, "Syndactyly: Frequency of specific types", American Journal of Medical Genetics, 1980;5(4),pp 357-364

[2] Julie C. Woodside and Terry R Light, "Symbrachydactyly — Diagnosis, Function, and Treatment", The Journal of Hand Surgery, 2015;41(1), pp. 135-143

[3] Robert S Kistenberg, "Prosthetic Choices for People with Leg and Arm Amputations", Physical Medicine and Rehabilitation Clinics of North America, 2014;25(1), pp 93-115.

[4] Jelle Ten Kate, "3D-Printed Upper Limb Prostheses: A Review", Disability and Rehabilitationl Assistive Technology, 2017;12(3), pp 300-314

[5] Matthew B Burn, Anderson Ta, Gloria R Gogola, "Three-Dimensional Printing of Prosthetic Hand for Children", Journal of Hand Surgery, 2016;41(5), pp 103-109.

[6] Mohd A Salim, Zarif H Termiti, Adzni Md Saad, "Mechanical Properties on ABS/PLA Materials for Geospatial Imaging Printed Product using 3D Printer Technology", Reference Module in Materials Science and Materials Engineering, 2019.

[7] Z. Darmawan, S. Haruyama, K. Kaminishi, "Investigate Effect of Thickness and Additional Supporting Frame on Rollover Protective Structure', International Exchange and Innovation Conference on Engineering and Sciences (IEICES), 2017, pp 109-111.

[8] A. M. M. Ismaiel, S. M. Metwalli, B. M. N. El-Hadidi, "Fatigue Analysis of an Optimized HAWT Composite Blade", International Exchange and Innovation Conference on Engineering and Sciences (IEICES), 2016, pp 49-50.

Effects of Varus and Valgus Implant Malposition in Resurfacing Hip Arthroplasty

Nor Aiman Nor Izmin[1], Mitsugu Todo[2], Abdul Halim Abdullah[1,*]
[1]Faculty of Mechanical Engineering, Universiti Teknologi MARA, 40450 Shah Alam, Selangor, Malaysia
[2]Research Institute for Applied Mechanics, Kyushu University,6-1 Kasuga-koen, Kasuga 816-8580, Japan
*halim471@uitm.edu.my

Abstract: *Resurfacing Hip Arthroplasty is a widely known method despite having complications that lead to implant failure. This study aims to determine the displacement values from several implant malposition hence to identify the maximum principal stress of the femur bone by using finite element analysis. A 3D bone model was generated by using Computed Tomography (CT) image of an osteoarthritis patient. Mechanical Finder v10 software was employed in this study. The bone model generated as an inhomogeneous bone model. A separate RHA implant model with Cobalt Chromium (CoCr) alloy was inserted towards the bone. The implant was placed to the selected angles of varus and valgus position. The patient's body weight is 87.6 kg while the loading and boundary condition simulated the normal walking condition. The highest displacement value was recorded when the implant was placed at the varus position and lowest value on the valgus position.*

Keywords: Resurfacing Hip Arthroplasty: Femoral Bone; Implant Malposition; Maximum Principal Stress; Displacement.

1. INTRODUCTION

Resurfacing Hip Arthroplasty (RHA) is known as the hip replacement method that has high similarities with the condition of the normal person on its outcomes especially on the walking movement. Resurfacing Hip is a hip replacement method that can solve the end-stage of osteoarthritis disease. This method has its priority towards the young and active patient and highly recommended to the patient with age below 50 years old with a good quality of bone [1,2]. Although this method has a good outcome in terms of movement similarities, however, there is a high potential of implant malposition to occur. One of the factors of occurrence on implant malposition in RHA is the limitation during the surgery. The limitation on the difficulty to visualize the acetabular caused by the femoral resection has been giving the technical challenge to the surgeon thus increasing the potential risk of implant malposition [3].

Implant malposition has given an awful impact towards the femur bone and as consequences from that, it affects the patient lifestyles. The bad consequence of implant malposition has been proven by a national review of 50 cases regarding the femoral neck fracture happened to the first 3429 Birmingham Hip Resurfacing. Over the four years period, 50 fractures of the neck of the femur were found and over 45 cases with complete data, 22 occurred in women and 23 in men [4]. Most of the patients with femoral neck fracture can be concluded by the specific errors of operative technique or in other words error in surgical with referring to the implant malposition [5].

The existence of implant malposition might contribute to the incompatibility of stresses and displacement which can be determined through the findings by using finite element analysis. Thus, this study aims to determine the total displacement and maximum principal stress values exerted on the femur bone as the results from the presence of the implant malposition.

2. MATERIALS AND METHODS

As the requirement recommended by the clinical studies for patients suitability to perform Resurfacing Hip Arthroplasty (RHA) [6], a CT image of a patient with age 47 years old has been chosen. The patient bodyweight recorded was 87.6 kg. The patient was having an osteoarthritis disease which was acting on his left femur. Therefore, from the CT Image, a 3D bone model has been developed by using a biomedical software, Mechanical Finder v10.

The CT image was extracted into the biomedical software, Mechanical Finder v10 and the 3D bone model was developed by using its features. Previously, researchers who conducted studies in finite element analysis that related to hip arthroplasties assumed a homogeneous bone model which stated as one of the limitations in their study [7,8,9]. Hence, in this study, the limitation was solved since the inhomogeneous bone model has been developed according to the study made by Keyak et al. [10,11] by assuming a linear relationship between the element 'apparent density' and gray data values which in Hounsfield units (HU). Tetrahedron elements were applied towards the bone model and the implant inserted into the bone was assumed perfectly bonded.

2.1 Prosthesis of the Resurfacing Hip

The RHA implant was imported based on previous study by Abdullah et al [12] and assigned as Cobalt Chromium Alloy (CoCr) material. The mechanical properties of the implant are shown in Table 1.

2.2 Implant Malposition

In this study, the implant malposition was categorized into two positions namely, varus position where the implant pin angle is positioned more than 130° and valgus position for the case of implant pin that less than 130° as in Fig.1. Angle 130° was referred to the

normal angle which measured from the femoral neck and shaft.

Properties	Unit	Value
Elastic Modulus	GPa	230
Critical Stress	GPa	0.94
Yield Strength	GPa	2.70
Density	(g/cm^3)	8.28
Poisson Ratio	-	0.30

Table 1. Mechanical properties of Cobalt Chromium

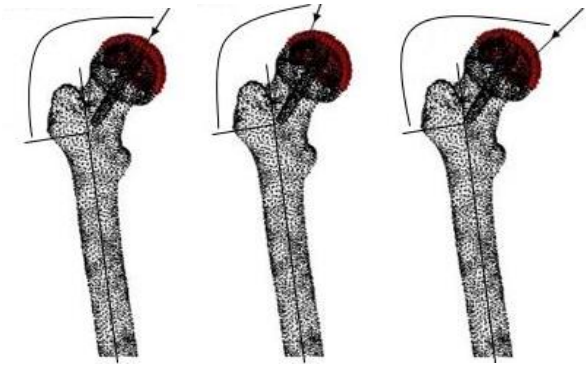

(a) (b) (c)

Fig. 1. Implant Malposition of varus and valgus (a) straight implant with 130º(b) valgus zone with <130º (c) varus zone with >130º.

To analyze the displacement and stress on the bone as consequences from implant malposition, there were few angles of varus and valgus have been selected upon this study. The selected orientation of the implant malpositions are as shown in Table 2.

Implant Malposition	Angle
Valgus position (<130°)	122°
	120°
	118°
Varus position (>130°)	138°
	140°
	142°

Table 2: Orientation of implant malposition

2.3 Loading and boundary conditions

The aim of this study is to identify the effects of implant malposition of RHA to the displacement and stress concentration towards the bone, where loading and boundary condition selected in the simulation was based on the physiological loading of a human. Physiological loading of a normal walking condition was selected in this study. The normal walking condition also tends to give a contact force at human joint about 238% of the human body weight [13]. During the normal walking condition, the compressive force will exert on the hip joint and the tensile force will occur at the greater trochanter. As suggested in the study made by Heller et al. [9], the tensile force acted on the greater trochanter during normal walking is around 104% of the human body weight. Thus, these parameters were selected to be performed in this simulation study while the force directions (Fig.2) conducted were as the same as the previous published works [9,14,15].

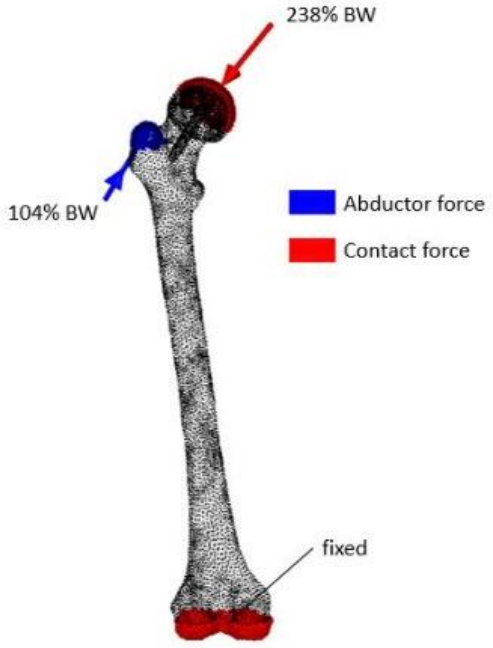

Fig. 2. Loading & Boundary Conditions

3. RESULTS AND DISCUSSION

The findings of the analysis is discussed based on the resulting total displacement and maximum principal stress.

3.1 Total displacement in femoral bone

The highest displacement value was obtained on the angle of varus 140° position where the bone elements displace about 0.11194 mm, while the lowest displacement value in varus group is on the varus 138° position with only 0.06338 mm. The displacement pattern increased significantly after the implant being titled by 2° from 138° to 140° and decreased as the implant moves towards 142°.

In the valgus group, there is a significant difference on the displacement result. The bone elements displaced much lower than the varus group which the highest displacement is around 0.02626 mm acting on the valgus 120° position. The displacement pattern on the valgus group is similar to the varus group where the displacement increased after the addition of 2° and then decreased when the implant moves to another 2°. The lowest displacement among all implant malposition is on the valgus 122° which around 0.01633 mm.

It is suggested that the RHA implant affected the displacement result since the only variable parameter in this study is on the implant angles. However, the displacement values did not increase consistently, hence, it can be assumed that the pin positioning of the RHA implant might contribute to the displacement results based on the applied force direction. Fig. 3 and Fig. 4 show the lowest and highest displacement for valgus and varus malposition groups, respectively.

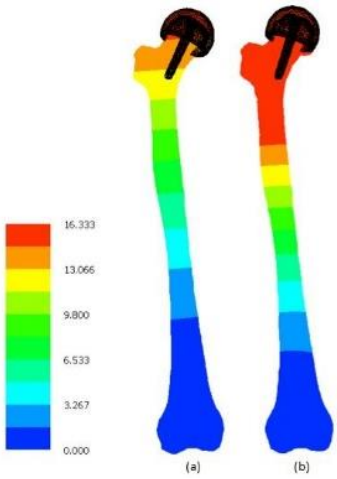

Fig. 3. Comparison contour of the lowest and highest bone displacement value for valgus malposition group (a) valgus 122° (b) valgus 120°

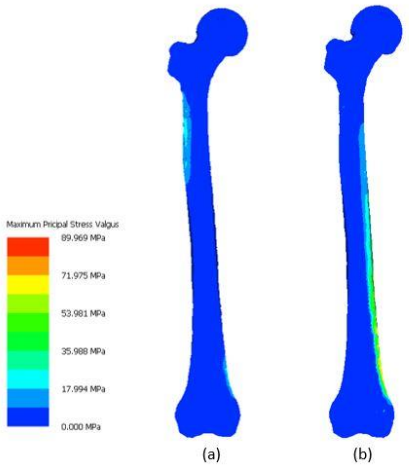

Fig. 5. Comparison contour of the lowest and highest maximum principal stress on valgus malposition group (a) valgus 122° (b) valgus 120°

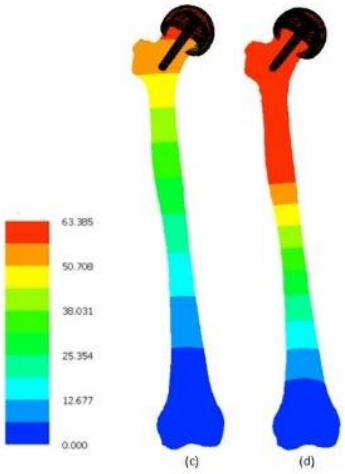

Fig. 4. Comparison contour of the lowest and highest bone displacement value for varus malposition group (c) varus 138° and (d) varus 140°

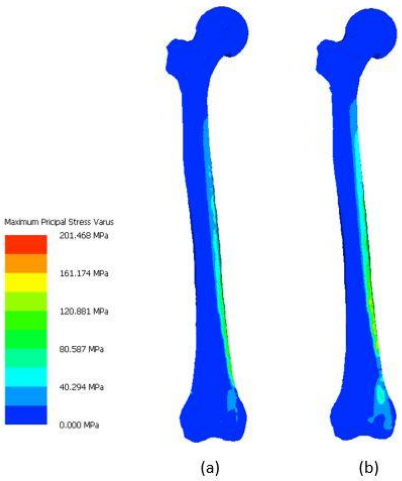

Fig. 6. Comparison contour of the lowest and highest maximum principal stress on varus malposition group (a) varus 138° (b) varus 140°

3.2 Maximum principal stress analysis on the femur bone model

The pattern of maximum principal stress observed in this study was similar to that predicted in the total displacement. The highest maximum stress value among the six implants position occurred at the varus 140° position with 264.622 MPa while the lowest maximum principal stress occurred at valgus 122° position with only 89.968 MPa. The highest and lowest values of maximum principal stress were also acting at the same implant malposition as in the displacement results. Overall, there is a huge difference on the mean value of maximum principal stress on varus position group compared to the valgus position group.

The maximum principal stress result shown on the bone explained that the highest stress value experienced the highest tensile condition by referring to the force direction applied as in Fig. 2.

The variation of the maximum principal stress for valgus and varus malposition groups are shown in Fig. 5 and Fig. 6, respectively.

The presence of implant malpositions has affects the displacement and stress variation. The comparison of the maximum values for both findings is summarized in Fig. 7. Malposition at varus angle indicated higher displacement and principal stress as compared to valgus malposition. Different angles or orientations also contribute to significant changes for the findings.

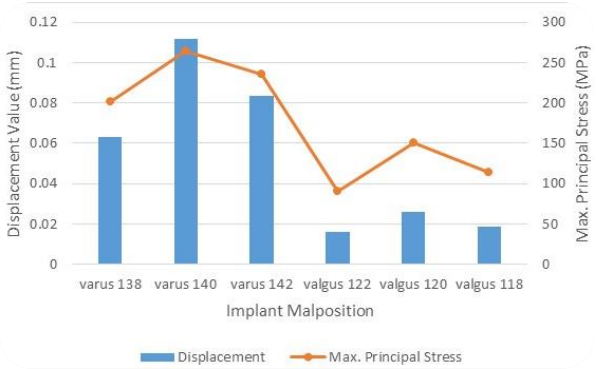

Fig. 7. Bone displacement and Maximum Principal Stress values

Since the RHA implant malposition always occurred on the patient after the post-operative surgery, it might lead to the other factors hence increased the tendency of femoral bone and neck fracture. Nonetheless, the simulation results on displacement value and maximum principal stress value obtained in this study shows a positive impact to reduce any damage formation towards the bone. Also, the results obtained on the valgus position were similar to the conclusion made by the previous works [7,16].

4. CONCLUSION

The analysis suggests that the implant malposition affects the performance of the resurfacing hip arthroplasty. Malposition at varus angle indicated higher displacement and principal stress as compared to valgus malposition with varus 140^{o} indicated the highest principal stress and total displacement.

5. ACKNOWLEDGMENT

This research was supported by Universiti Teknologi MARA, UiTM under Grant No. 600-IRMI/PERDANA 5/3 BESTARI (103/2018). We thank and acknowledge Ministry of Education, Malaysia and to our colleagues from Faculty of Medicine, UiTM who provided insight and expertise that greatly assisted the research.

6. REFERENCES

[1] A. J. Shimmin, J. Bare, and D. L. Back, "Complications associated with hip resurfacing arthroplasty," *Orthop. Clin. North Am.*, vol. 36, no. 2, pp. 187–193, 2005.

[2] D. F. Amanatullah, Y. Cheung, and P. E. Di Cesare, "Hip Resurfacing Arthroplasty: A Review of the Evidence for Surgical Technique, Outcome, and Complications," *Orthop. Clin. North Am.*, vol. 41, no. 2, pp. 263–272, 2010.

[3] J. R. Romanowski and M. L. Swank, "Imageless navigation in hip resurfacing: avoiding component malposition during the surgeon learning curve.," *J. Bone Joint Surg. Am.*, vol. 90 Suppl 3, pp. 65–70, 2008.

[4] A. J. Shimmin, "Femoral neck fractures following Birmingham hip resurfacing: A NATIONAL REVIEW OF 50 CASES," *J. Bone Jt. Surg. - Br. Vol.*, vol. 87-B, no. 4, pp. 463–464, 2005.

[5] T. London, "ICLH Surface Replacement Of The Hip: An Analysis of the first 16 years," vol. 65, no. 4, pp. 704–813, 1983.

[6] P. R. Kim, P. E. Beaulé, G. Y. Laflamme, and M. Dunbar, "Causes of Early Failure in a Multicenter Clinical Trial of Hip Resurfacing," *J. Arthroplasty*, vol. 23, no. 6 SUPPL., pp. 44–49, 2008.

[7] I. A. J. Radcliffe and M. Taylor, "Investigation into the effect of varus-valgus orientation on load transfer in the resurfaced femoral head: A multi-femur finite element analysis," *Clin. Biomech.*, vol. 22, no. 7, pp. 780–786, 2007.

[8] E. T. Davis, M. Olsen, R. Zdero, M. Papini, J. P. Waddell, and E. H. Schemitsch, "A Biomechanical and Finite Element Analysis of Femoral Neck Notching During Hip Resurfacing," *J. Biomech. Eng.*, vol. 131, no. 4, p. 041002, 2009.

[9] I. O. Rizzoli, "Strain distribution within the human femur due to physiological and simpli ed loading : nite element analysis using the muscle standardized femur model," vol. 217, pp. 173–189, 2012.

[10] J. H. Keyak, S. A. Rossi, K. A. Jones, and H. B. Skinner, "Prediction of femoral fracture load using automated finite element modeling," *J. Biomech.*, vol. 31, no. 2, pp. 125–133, 1997.

[11] J. H. Keyak, H. B. Skinner, and J. A. Fleming, "Effect of force direction on femoral fracture load for two types of loading conditions," *J. Orthop. Res.*, vol. 19, no. 4, pp. 539–544, 2001.

[12] A.H. Abdullah, M. Todo and Y. Nakashima, "Prediction of damage formation in hip arthroplasties by finite element analysis using computed tomography images," *Med. Eng. Phys.*, vol. 44, pp. 8–15, 2017.

[13] B. G. *et al.*, "Hip contact forces and gait patterns from routine activities," *J. Biomech.*, vol. 34, no. 7, pp. 859–871, 2001.

[14] I. A. J. Radcliffe and M. Taylor, "Investigation into the affect of cementing techniques on load transfer in the resurfaced femoral head: A multi-femur finite element analysis," *Clin. Biomech.*, vol. 22, no. 4, pp. 422–430, 2007.

[15] M. O. Heller, G. Bergmann, J. P. Kassi, L. Claes, N. P. Haas, and G. N. Duda, "Determination of muscle loading at the hip joint for use in pre-clinical testing," *J. Biomech.*, vol. 38, no. 5, pp. 1155–1163, 2005.

[16] C. Anglin, B. A. Masri, J. Tonetti, A. J. Hodgson, and N. V. Greidanus, "Hip resurfacing femoral neck fracture influenced by valgus placement," *Clin. Orthop. Relat. Res.*, no. 465, pp. 71–79, 2007.

Feasibility study of theophylline solution in water and sodium carboxy-methylcellulose

Jannatul Fardous[1,2,*], A H M Saifuddin[3], Sultana Amena[3], Sakina Sultana[3]
[1]Department of Chemical Engineering, Kyushu University, Fukuoka 819-0395, Japan
[2]Department of Pharmacy, Comilla University, Cumilla-3506, Bangladesh
[3]Department of Pharmacy, Jahangirnagar University, Dhaka-1342, Bangladesh
[*]fardousj11@cou.ac.bd

Abstract: *Solution is a liquid dosage form that ensures better bioavailability of drug upon oral administration. In this study an attempt was taken to prepare theophylline solution (20mg/ml) using sodium carboxy-methylcellulose as a vehicle. Feasibility of Na-CMC as drug vehicle was tested and compared with widely used vehicle water. Effect of different storage conditions on organoleptic and physicochemical properties was tested for a period of three months. Drug potency was found 9-13 mg/ml and 14-16 mg/ml in water and Na-CMC respectively and was consistent with time. Viscosity of the solution was good with easy pourability for both of the vehicles used. Theophylline solution in water showed changes in color after two months. However, no changes in organoleptic properties with CMC-Na as vehicle within the experimental time period irrespective of storage condition. Moreover, good stability of the theophylline solution was seen with Na-CMC at 1% (w/v) concentration.*

Keywords: Solution; carboxymethylcellulose sodium; asthma; theophylline.

1. Introduction

Solution is one of the most common dosage forms for oral administration. It is a clear homogenous system where the solid substances remain dissolved in a liquid phase [1]. It has several advantages like rapid onset of action, faster absorption rate, simple method of preparation and so on compared to solid dosage form. Along with this liquid dosage forms are best choice for children and elderly patients for ease of swelling [2]. Use of sweeteners, flavoring agents, coloring agents make this dosage form palatable and results in increased patient compliance [3]. Syrup, suspension, elixir, emulsion are other forms of oral liquid dosage forms. In spite of these liquid dosage forms, solution has some additional advantages. Solution is free from sedimentation and ensures uniform dose than suspension or emulsion which requires shaking [4]. Besides this gastric irritation caused by some drugs can be avoided when administered as solution because of immediate dilution by gastric contents. However this dosage form is not denied of problems. Major disadvantages of solution are poor stability, prone to microbial growth, difficulties in storage and transportation and not suitable for poorly soluble drugs [5]. Although solution has some problems, it is one of the widely used dosage form still now. Depending on drug solubility, both aqueous and organic solvents are used as vehicle or drug carrier in solution. Water is widely used vehicle for solution due to its easy availability and better biocompatibility [6].

Sodium carboxymethylcellulose (Na-CMC) is sodium salt form of a cellulose derivative having carboxymethyl group. It is widely used in both food and pharmaceutical industry. Na-CMC is widely used in oral and topical pharmaceutical formulations, primarily for its viscosity-increasing properties. Varying on its concentration Na-CMC can be used as emulsifying agent, gelling agent in oral and topical solutions. Usually in oral solution Na-CMC is used at a concentration of 0.1-1% (w/v) [7]. Its higher aqueous solubility, good swelling properties and erosion characteristics make it a good candidate for use as a carrier in solution [6]. Na-CMC is easily dispersible that ensures better solubility of drug and uniform distribution in a preparation. At the same time use of Na-CMC may retard drug release that helps to improve patient compliance by reducing dosing frequency [8].

Asthma is inflammation of airways that causes bronchoconstriction and one of the leading causes of death in Bangladesh [9]. Regrettably asthma is only manageable, not curable. Different types of bronchodilators are mainly used in the treatment of asthma. One of them is theophylline which is a second line drug used in addition with steroids in chronic asthma. This drug has been using over the last 50 years or so [10]. It acts by phosphodiesterase inhibition followed by increased cAMP level that causes airways relaxation [11]. Most of the commercially available theophylline preparations in Bangladesh are solid dosage forms. A few of the manufacturers prepare theophylline as syrup and injection [12]. Unfortunately all the available preparations of theophylline are not suitable for all kinds of patients. The solid and liquid forms contain glycogenic materials like sorbitol, glycerol, sugar etc. which make it unsuitable for asthma patients with diabetes [13]. Similarly high content of sugar in syrup causes dental carries and sometimes gastrointestinal problems in children due to their underdeveloped digestive system [14]. Therefore it will be useful if theophylline is formulated in liquid form without glycogenic materials and high sugar content.

In this study we are focusing on formulation and preparation of theophylline solution using water and Na-CMC (1% w/v). Different quality tests were performed along within stability study in different storage conditions to determine the feasibility of theophylline solution. If the results found good and acceptable, it will be a new hope for both pediatric and geriatric patients with chronic asthma.

2. Materials and methods

2.1 Materials

Theophylline anhydrous was gift from Square Pharmaceuticals Ltd., Bangladesh. Citric acid, ascorbic acid (antioxidants), aspartame (sweetener), methyl paraben (preservative) and sodium carboxymethylcellulose (Na-CMC) were gift from Department of Pharmacy, Jahangirnagar University, Bangladesh.

2.2 Methods

2.2.1 Theophylline solution preparation: All the excipients were added to water gradually and mixed well by magnetic stirring. After that theophylline was added in a concentration of 20mg/ml and stirred until a clear solution was formed. The same was followed when using 1% Na-CMC as a vehicle. All the prepared solutions were filled in glass container and stored in two different conditions- a) at room temperature, b) dark and cool place (20ºC).

2.2.2 Quality control tests

i) Aesthetic properties: Aesthetic properties of prepared solutions namely color, odor, transparency were observed visually during the experimental time period of three months. Quality of solution based on aesthetic properties was evaluated according to the typical thermometer scale of consumer acceptability.

ii) Assay: For assay of theophylline solution, 0.1ml of solution was withdrawn and diluted 1000 times with water. Then absorbance of diluted solution was determined using UV-visible spectrophotometer (Shimadzu 1601 PC, Japan) at 214nm wavelength. The concentration of theophylline in solution was determined by using standard calibration curve from 1µg/ml to 32µg/ml. This test was done for all solutions and from all storage condition.

iii) Viscosity: Viscosity of prepared theophylline solution at different storage conditions was tested using Ostwald viscometer. Viscosity of prepared solutions was compared with viscosity of water at room temperature.

3. Results

i) Aesthetic properties: Physical stability of solutions was usually determined by its changes on organoleptic properties with time and environmental conditions i.e. light, temperature, humidity etc. [15]. Results of aesthetic properties for theophylline solution in water and Na-CMC are given on Table 1 and Table 2 respectively.

Table 1: Stability of theophylline solution in water

Day	Solution in water					
	Room temperature			Dark and cool place		
	Color	Odor	Ppt↓	Color	Odor	Ppt↓
1	○	√	×	○	√	×
7	○	√	×	○	√	×
15	○	√	×	○	√	×
30	○	√	×	○	√	×
60	◯	√	×	○	√	×
90	◯	√	×	◯	√	×

Note: Ppt↓- Precipitation, ○- Colorless, ◯-Yellowish color, √-Good, × - Absent.

Table 2: Stability of theophylline solution in 1% Na-CMC

Day	Solution in water					
	Room temperature			Dark and cool place		
	Color	Odor	Ppt↓	Color	Odor	Ppt↓
1	○	√	×	○	√	×
7	○	√	×	○	√	×
15	○	√	×	○	√	×
30	○	√	×	○	√	×
60	○	√	×	○	√	×
90	○	√	×	○	√	×

Note: Ppt↓- Precipitation, ○ - Colorless, √-Good, ×- Absent

ii) Assay: Assay of the prepared solutions was done to determine quality, efficacy and safety of drug therapy [16]. Result of assay for prepared solution is given in figure 1.

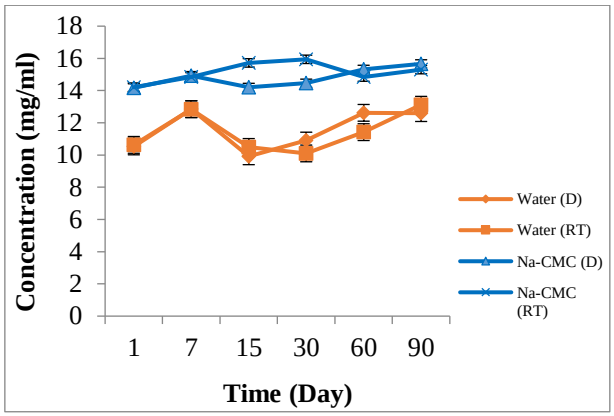

Figure 1: Theophylline concentration in different vehicle with time. D = Dark and cool place, RT= Room temperature.

iii) Viscosity: Viscosity of solution changes with temperature and also depends on excipients used [15]. Effect of storage condition on theophylline solution during experimental time period is shown in figure 2.

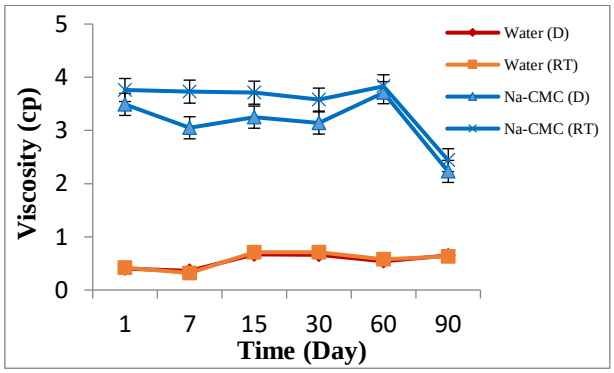

Figure 2: Viscosity of theophylline solution with time. D = Dark and cool place, RT= Room temperature.

4. Discussion

As we make an effort to prepare theophylline solution with a better carrier, therefore theophylline solution was prepared using both water and Na-CMC as carrier. At the same time effect of light and temperature was also tested for the prepared solutions for a time span of three months. Results of different quality tests show the possibility of theophylline solution.

In case of aesthetic properties, changes in color, odor was observed. No changes took place for theophylline

solution in 1% Na-CMC (w/v) regardless of storage condition. But in case of solution in water, preparation turns slight yellowish after second and third month at room temperature and dark and cool place respectively (table 1 and 2). This may be due to photolytic reaction which affects the structural conformation of any component used in the solution. In case of Na-CMC its viscosity imparting property protects the components from such conformation change. No sedimentation as well as precipitation of drug particles took place for all the solutions during the stability period. Assay of theophylline solution gives useful information for how much drug will be dispensed on unit dose. For solution in water drug concentration was found 9-13 mg/ml and 14-16 mg/ml for solution in Na-CMC during experimental time period (figure 1). Drug concentration was not affected by storage condition and showed a consistency with time mainly for 1% Na-CMC. In case of water as a solvent, drug concentration showed a discrepancy with time which may be a result of poor solubility of theophylline in water. Theophylline was used at a concentration of 20 mg/ml of concentration and our assay results are very close to this amount for 1% Na-CMC. Therefore dosage uniformity can be maintained if theophylline is administered as solution. Further study is needed in this regard. On the other hand viscosity of theophylline solution was same regardless of light and temperature. Viscosity of solution in water was lower (0.5 on average) than solution in Na-CMC (3.0 on average) because of viscosity imparting nature of Na-CMC (figure 2). But no problem was found during dispensing of solution from bottle for its viscous nature. This property can be used to get sustained drug release from theophylline solution. Usually viscosity decreases with temperature. In our study we stored solutions in both dark and cool condition and room temperature. As the temperature difference was not so high between the two storage conditions, viscosity of the solution remain almost same for both of the carriers. Although in case of Na-CMC, a fall in viscosity was found after 3 months for all storage conditions. Further study is needed to determine the reason behind this. As our results are found good for assay, viscosity and organoleptic properties, it is possible to formulate theophylline as solution for oral administration. Depending on the results of assay and stability study at different storage conditions we can assume that Na-CMC at a concentration of 1% w/v is a good vehicle for theophylline solution compared to water. Such preparation will be better for both pediatric and geriatric patients and also for diabetic patients as our solution devoid of any sugar or glycogenic substances.

5. Conclusion

This study has shown promising data for potency and viscosity of theophylline solution. At the same time data showing effect of light and temperature on solution quality is also encouraging. Therefore it can be concluded that it is possible to formulate and prepare theophylline solution and data can be simulated to in-vivo study for further progression of research.

6. References

[1] G. Binson, K. Beuzit , V. Migeot, L. Marco, B. Troussier, N. Venisse, A. Dupuis, Preparation and physicochemical stability of liquid oral dosage forms free of potentially harmful excipient designed for pediatric patients, Pharmaceutics, 11(4) 190 (2019); DOI:10.3390/pharmaceutics11040190

[2] V. Ivanovska, Carin M.A. Rademaker, L.V. Dijk, A. K. Mantel-Teeuwisse, Journal of American Academy of Pediatrics, 134 (2014): 361-372
DOI: 10.1542/peds.2013-3225

[3] M. E. Aulton. Aulton's Pharmaceutics: The design and Manufacture of Medicines. Third ed. UK: Churchill Livingstone Elseiver; 2007.

[4] L Lachman, H. A. Lieberman, J. L. Kanig, The Theory and Practice of Industrial Pharmacy, Third ed. India: Varghese Publishing house; 2010.

[5] L. Shargel, A. H. Mutnick, P. F. Souney, L. N. Swanson, Comprehensive Pharmacy Review Seventh ed.: Lipincott Williams and Wilkins Philadelphia; 2009

[6] D. B. Troy, P. Beringer, Remington, The Science and Practice of Pharmacy- Volume II; 21st ed.: India: Lippincott Williams & Wilkins, 2006

[7] R. C. Rowe, P. J Sheskey, M. E. Quinn, Handbook of Pharmaceutical Excipients, Sixth edition. Pharmaceutical Press, London, 2009

[8] D. Palmer, M. Levina, A. Nokhodchi, D. Douroumis, T. Farrell, A. R. Siahboomi, The influence of sodium carboxymethylcellulose on drug release from polyethylene oxide extended release matrices, AAPS PharmSciTech, 12:3, (2011): 862-871.
DOI: 10.1208/s12249-011-9648-4

[9] M. M. Mamun, A.S. A. Salauddin, M. F. Hossain, M. Afrin, M. Asaduzzaman, M. E. Kabir, S. Mahmud, Prevalence of asthma and its associated factors among the undergraduate students of Bangladesh Agricultural University. International Journal of Natural and Social Sciences, 3:1 (2016):32–36.

[10] J. Fardous , F. F. Perveen , M. S. Hossain , P. K. Baral, S. Sultana, Formulation and Preparation of Theophylline "Sonophoric Gel", Galore International Journal of Health Sciences and Research, 4:1(2019): 91-97

[11] LL Brunton, JS Lazo, KL Parker. Goodman & Gilman's The Pharmacological basis of Therapeutics. Eleventh ed.: McGRAW– HILL: Medical Publishing Division, New Delhi, 2006.

[12] J. Fardous , F. F. Perveen, AHM Saifuddin, M. Akter, S. Sultana , Preparation and evaluation of an anti-asthmatic gel of theophylline with diclofenac sodium. Journal of Anaytical and Pharmaceutical Research, 8:2(2019):65–69.
DOI: 10.15406/japlr.2019.08.00314.

[13] L.V. Allen jr, N. G. Popovich, H. C. Ansel, Ansel's Pharmaceutical Dosage Forms and Drug Delivery Systems. Eighth ed. Philadelphia: Lippincott Williams & Wilkins; 2005

[14] J. E. Thompson, L. W. Davidow, A Practical Guide to Contemporary Pharmacy Practice, Third ed.: Philadelphia: Wolters Kluwer Health/ Lippincott Williams & Wilkins; 2009 pp.267-276

[15] M. S. Uddin, A. A. Mamun, N. Akter, M. S. Sarwar, M. Rashid, M. S. Amran, Pharmacopoeial Standards and Specifications for Pharmaceutical Oral Liquid Preparations, Archives of Current Research International 3(2), 2016: 1-12, DOI: 10.9734/ACRI/2016/22675

[16] W. Misiuk, The role of assay methods in characterizing the quality of bulk pharmaceuticals**,** J Pharm Bioallied Sci. 2(2), 2010: 88–92.

doi: 10.4103/0975-7406.67007

Comparison of LCL and LCLC Compensation Circuit for Capacitive Power Transfer System

Suziana Ahmad[1], Aam Muharam[2], Reiji Hattori[3],
[1,2,3]Interdisciplinary Graduate School of Engineering Sciences, IGSES, Kyushu University,
[1]FTKEE, Universiti Teknikal Malaysia Melaka.
[2]Research Centre for Electrical Power and Mechatronics, Indonesian Institute of Sciences (LIPI)
binti.ahmad.suziana.748@s-kyushu-u.ac.jp

Abstract: *Capacitive power transfer is one of the techniques to transfer power wirelessly. In this paper, LCL compensation topology and LCLC compensation topology were studied and simulated. The aims of this study are to determine the parameter value of the LCL and LCLC compensation topologies, simulate and compare both circuits. The operating frequency of 1Mhz was used in all topologies and had been simulated in LTspice XVIII simulation software. The value of parameters were obtained and simulated successfully. The comparison result is presented.*

Keywords: Wireless power transfer; Capacitive Power Transfer.

1. INTRODUCTION

Wireless power transfer (WPT) becomes one of the interesting topics in engineering and technology industry due the WPT promises an energy sustainability in delivering energy. WPT transfers power between the supply source and electronic devices without using cables and it is more reliable and convenient.

Capacitive power transfer (CPT) in wireless power transmission is using electric field coupling between electrodes for transferring energy between transmitter and receiver. Meanwhile Inductive power transfer (IPT) is using magnetic field coupling between cores. Both methods become an interesting subject for delivering power without cable and can be applied in many electrical and electronics appliances such as wireless vehicle charging [1], unmanned aerial vehicle [2], machine[3] and others.

There are many advantages and disadvantages between IPT and CPT in wireless power transfer. CPT has advantages in relatively low cost and weight, negligible eddy-current lost and excellent misalignment performance [4].

The main factor in WPT is its efficiency. The factor that effected to the efficiency of WPT systems are coupling factor between transmitting and receiving elements, load current, fire angles of rectifier switch and semiconductor devices.

2. CAPACITIVE W POWER TRANSFER (CPT) SYSTEM

Capacitive power transfer consists of capacitor plate as a main part for transferring power and others component. Size of capacitive plates and the distance between the plates give the value of coupling capacitance.

Fig. 1 shows the wireless power transfer system in which contains a supply, primary and secondary part, load and capacitive interface. The plates are arranged in parallel for transferring power and produce the capacitance effect.

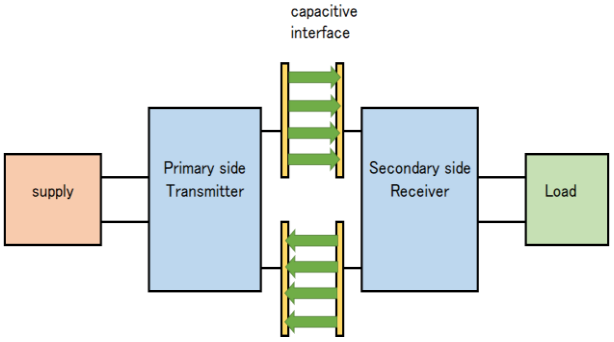

Fig. 1. Wireless power transfer system.

There are a lot of compensation topologies proposed by researcher, including series L, LC, LCL and LCLC compensation and these compensation circuits determine the system power capabilities, frequency properties with output and input condition and power capabilities [4]. A compensation circuit able to increase the voltages and maximize the output efficiency. At the secondary side, additional DC-DC converter can be used to achieve better performance [5].

2.1 LCL double compensated CPT system

By combining LC and series inductor, it can result in a double sided LCL compensation topology as shown in Fig. 2.

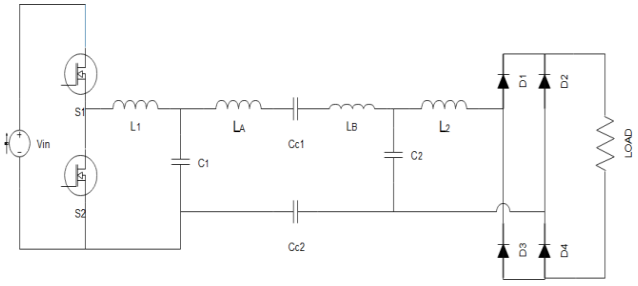

Fig. 2. LCL compensated CPT system.

The LCL compensation circuit can able to tune the system power in flexibility, but needs the larger value of series inductor [4].

2.2 LCLC double compensated CPT system

LCLC double compensated circuit gives an advantages of power regulation through the circuit without affecting coupling coefficient [4] and LCLC network can helps both output and input to achieve unity power factor [6].

Fig. 3 shows the arrangement of inductor and capacitor for LCLC compensated CPT system

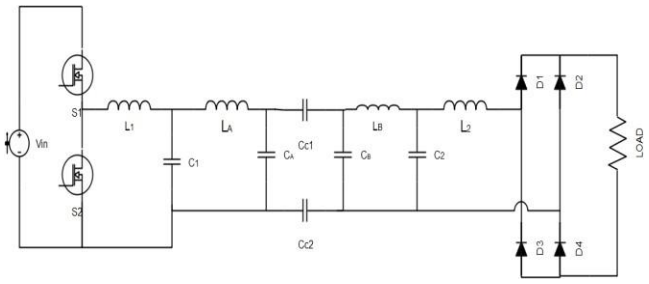

Fig. 3. LCLC compensated CPT system.

3. DESIGN OF THE CIRCUIT

In order to simulate LCL and LCLC double compensated circuit, the value of duty cycle, D and Inductor, L_1 were determined firstly. After the both value of D and L_1 were obtained, others parameter value was calculated based on resonance at the same frequency by using the formula given by [6]. Then, the LCL and LCLC topologies were proposed and simulated in LTspice XVII simulation

3.1 Determination of Duty cycle and Inductor L1 value of maximizing output

Duty cycle, D of the power MOSFET contributes to the high efficiency. Thus, the variation value of D and inductor L_1 are taken into consideration for finding better output. Thus, this study was done to find the suitable value for both inductor and inverter duty cycle for producing maximum efficiency. Fig. 4 shows a circuit which is used to determine the value of D and L_1.

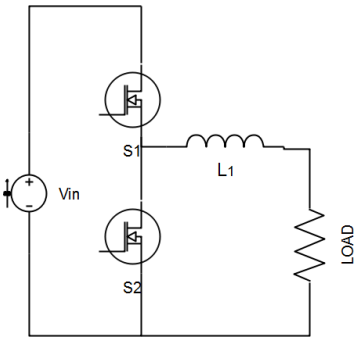

Fig. 4. A circuit to determine the value of Duty cycle and Inductor L_1

The higher value of inductor will result in the bigger size of inductor and internal series resistance as well as higher cost. Thus, these factors also need to take into consideration for choosing the value of inductor even though the efficiency is the most important factor for the circuit.

The circuit was simulated by using DC voltage supply and operating frequency of 60V and 1MHz respectively. First, the duty cycle value was changed with 0.4, 0.45 and 0.5 and inductor value was 4µH. Secondly, the inductor value was changed with 0.4µH, 4µH and 40µH. The result of the simulations is presented in Fig. 5 and Fig. 6.

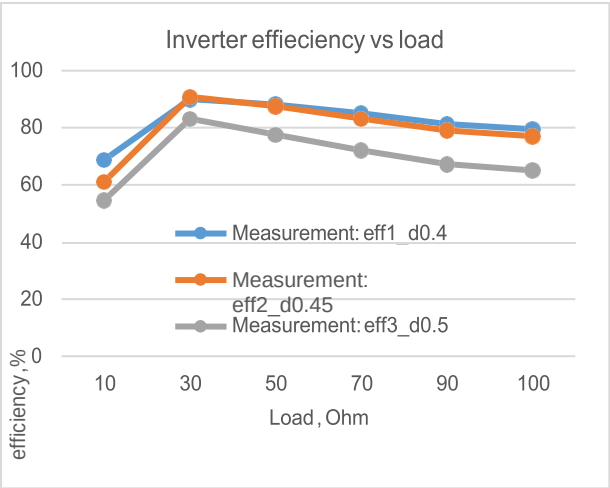

. Fig. 5. Fixed Inductor (4µH) with changing of duty cycle, D

Fig. 5 shows duty cycle of 0.4 is the best in comparison with D = 0.45 and 0.5. Thus, the value of 0.4 is chosen for the duty cycle.

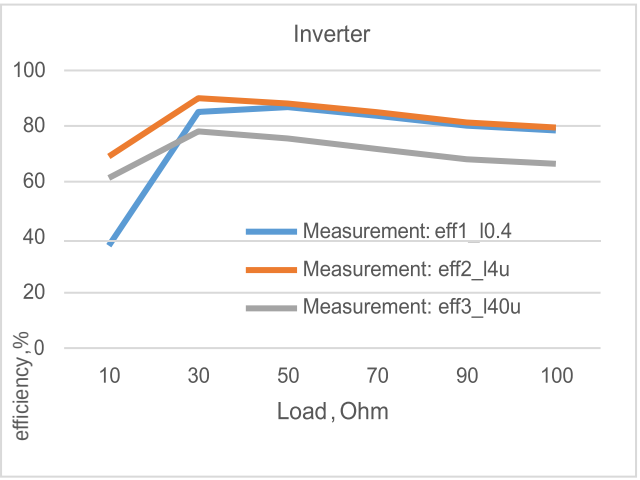

Fig. 6. Fixed duty cycle, D (0.4) with changing of inductor.

Fig. 6 shows the inductor value of 4µH is the best in comparison of 0.4µH and 40µH. Thus, 4µH is selected for the value in LCL and LCLC topologies. Duty cycle of 0.4 and inductor L_1 of 4µH is chosen in this study. Others parameter was calculated based on these values and presented in simulation to analyze the output.

3.2 Simulation of LCL and LCLC topologies

Both LCL and LCLC circuit are simulated in LTspice XVII simulation with the operating frequency and duty cycle of 1MHz of 0.4 respectively. The DC supply is 60 V. The components were arranged as in Fig. 2 and Fig. 3 for LCL and LCLC circuit respectively. The inductor value of L1 and L2 were based on previous simulation result and other components value were determined by calculation. The parameters for both LCL and LCLC is presented in Table 1.

Table 1. Specifications of the system

Components	LCL	LCLC
$C_{1,} C_{2}$	6.33nF	6.33nF
L_1 , L_2	4µH	4µH
L_A , L_B	257µH	50.4µH
$C_{A,} C_{B}$	-	500pF
$C_{C1,} C_{C2}$	100pF	100pF

4. RESULT AND DISCUSSION

The result for both circuits were obtained successfully. The efficiency of the both circuits were presented, and it was found that the efficiency of LCLC circuit are better in comparison with LCL. Fig. 7 shows the efficiency of proposed LCL and LCLC compensation circuit.

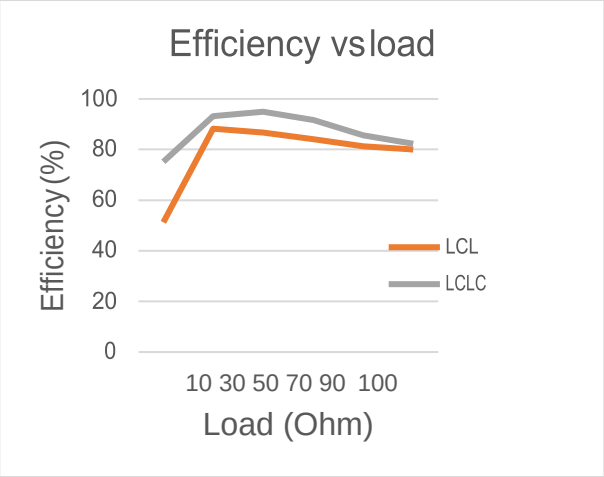

Fig. 7. LCL and LCLC compensated CPT system efficiency.

Fig. 7 shows LCLC topology has better efficiency compared to LCL topology with various value of load from 10Ω to 100Ω. The simulated and output efficiency will be used as reference for further work. The efficiency graph for both topologies show almost similar pattern.

5. CONCLUSION

The parameters of the LCL and LCLC compensation circuit were determined and simulated successfully. The efficiency of the both circuits was obtained, compared and presented. It shows that the selected inductor value of 4µH is suitable for both topologies. In comparison, LCLC compensation topology is better than LCL in term of efficiency for various load from 10Ω to 100Ω. However, further analyze need to be done to find details output data for both LCL and LCLC topologies. The simulated and output efficiency will be used as reference for further work in wireless power transfer system.

6. REFERENCES

[1] A. Ahmad, M. S. Alam, and R. Chabaan, "A Comprehensive Review of Wireless Charging Technologies for Electric Vehicles," *IEEE Trans. Transp. Electrif.*, vol. 4, no. 1, pp. 38–63, 2017.

[2] T. M. Mostafa, A. Muharam, and R. Hattori, "Wireless battery charging system for drones via capacitive power transfer," *2017 IEEE PELS Work. Emerg. Technol. Wirel. Power Transf. WoW 2017*.

[3] D. C. Ludois, J. K. Reed, and K. Hanson, "Capacitive power transfer for rotor field current in synchronous machines," *IEEE Trans. Power Electron.*, vol. 27, no. 11, pp. 4638–4645, 2012.

[4] F. Lu, H. Zhang, and C. Mi, "A review on the recent development of capacitive wireless power transfer technology," *Energies*, vol. 10, no. 11, 2017.

[5] A. H. M. Z. Alam, "Three Phase DC-DC Converter with Six Inverter for EV Application," *Proceedings of International Exchange and Innovation* Conference on Engineering & Sciences (IEICES). 3, pp. 141 - 144, 2017-10-19. pp. 141–144, 2017.

[6] F. Lu, H. Zhang, H. Hofmann, and C. Mi, "A Double-Sided LCLC-Compensated Capacitive Power Transfer System for Electric Vehicle Charging," *IEEE Trans. Power Electron.*, vol. 30, no. 11, pp. 6011–6014, 2015.

Significant Propagation Loss Reduction on Silicon High-Mesa Waveguides Using Thermal Oxidation Technique

Yu Han*, Wenying Li, Haisong Jiang, and Kiichi Hamamoto
I-EggS (Interdisciplinary Graduate School of Engineering Sciences), Kyushu University
6-1, Kagugakouen, Kasuga, Fukuoka 816-8580, Japan
*E-mail: han.yu.926@s.kyushu-u.ac.jp

Abstract: *Breath sensing system based on cavity ring-down spectroscopy (CRDS) technique is attractive due to its real time sensing in addition to the capability of high sensitivity. Utilizing waveguide for CRDS may realize ppm-order components into a compact area. This work have exploited thermal oxidation technique to silicon high-mesa waveguides for sensing-application. Significant propagation loss reduction from 1.45 to 0.84 dB/cm at a waveguide width of 500 nm has been achieved by the technique successfully.*

Keywords: Loss reduction, High-mesa waveguide, Thermal oxidation, CRDS.

1. INTRODUCTION

Breath sensor is a noninvasive and convenient fashion for health-monitoring [1]. In order to detect ppm-order breath content in addition to the real time sensing, breath sensing system based on cavity ring-down spectroscopy (CRDS) technique has been researched as a candidate [2]. Compared to the conventional bulk CRDS system [3], utilizing waveguide as the gas sensing cell may realize several meters sensing path which is needed for measuring ppm-order components in human breath within a compact area [4]. This brings the possibility of integrating CRDS system into a cell phone or other mobile equipment for powerful in-situ and real-time health-monitoring. One issue is the propagation loss of the waveguide as it may prevent ppm-order gas detection.

In a CRDS system, the length of a regular sensing cell is about 1 meter needed for measuring ppm-order breath content [3, 5]. If the propagation loss of the waveguide exceeds 0.2 dB/cm, the total loss of the waveguides is higher than 20 dB. This high loss causes the waveguide impossible to be used even if an optical amplifier is introduced in the CRDS system [5]. A 1 m-long waveguide with the propagation loss ≤ 0.2 dB/cm is required to be applied as the sensing cell. Recently, a novel high-mesa waveguide structure has been proposed by our group for the compact and high-sensitive CRDS system [4, 6, 7]. Compared to the slot waveguide [8] and the conventional channel waveguide, it not only provides the evanescent field sufficient touching the breath gas, but also avoids the surface to be contaminated by particles in air. A high-mesa silicon-on-insulator (SOI) waveguide with 260-nm thick silicon (Si) as the core has been fabricated [6, 7], but its propagation loss (α) was still too high to be as the sensing cell [9].

In order to decrease α, this work designed and fabricated a 100 nm thick Si high-mesa waveguides in this work. After fabrication, This work applied dry thermal Si oxidation technique for further reduction. After thermal oxidation, the propagation loss was effectively reduced from 1.45 to 0.84 dB/cm for width=0.5 μm and from 0.29 to 0.2 dB/cm for width= 3μm. The reduction of α was attributed to the decrease of the sidewall scattering loss and the absorption loss from the damaged Si.

2. EXPERIMENTS and RESULTS

The designed 100 nm thick Si high-mesa waveguide is shown in Fig. 1 (a). The device layer of the SOI is 100 nm and the top SiO2 cladding is 2 μm. The bottom SiO2 cladding is etched with a thickness of 1 μm. The width of the waveguide is variable to optimize α.

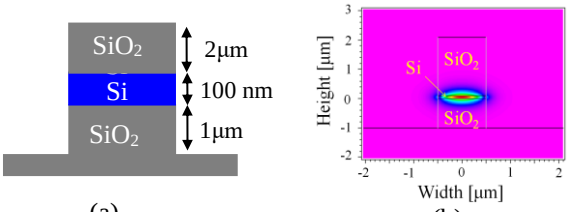

Fig. 1 Designed 100 nm-thick Si high-mesa waveguide. (a) Cross-section and (b) TE mode light profile when width=1 μm

The propagation loss α of a waveguide is generally attributed to three different mechanisms: radiation loss, absorption loss and scattering loss. The simulated TE mode in Fig. 1(b) indicates that the optical field is well-confined in the waveguide. In addition, the materials, Si and SiO_2, are highly transparent around 1550 nm. As a result, the main reasons of α in our case are the scattering loss $\alpha_{scattering}$ origining from the rough sidewall and the absorption loss $\alpha_{absorption}$ from damaged Si caused by the ICP etching. Oxidation of Si has been shown to be effective at reducing the sidewall scattering and recovering the damaged Si [4]. After oxidation, a thin Si layer near the sidewall is oxidized into SiO_2, so that the effective refractive index (n_{eff}) of waveguide is reduced and the damaged Si is recovered. According to the Payne-Lacey model [5], a lower n_{eff} indicates a lower $\alpha_{scattering}$. In addition, the $\alpha_{absorption}$ from damaged Si is also reduced due to the transformation to SiO_2.Based on the design and analysis above, high-mesa waveguides were fabricated on a SOI wafer. A 2 μm-thick SiO2 top cladding was deposited on the SOI wafer via chemical vapor deposition. The wafer was coated with electron beam (EB) resist SU-8 and patterned by EB lithography. The exposed wafer was etched in an inductively coupled plasma (ICP) etching machine by using CHF3 gas.

Finally, This work applied dry thermal oxidation at 1000 ℃ from 1 to 4 hours (hrs) under the gas condition as O2:N2=1:4 (mole ratio). The propagation loss α was evaluated by using Fabry–Perot interferometric method [14]. Light from a distributed feedback laser source was coupled into the waveguide in TE mode through a polarization-maintaining lensed fiber. A polarizer was used to align the input light polarization between the laser and the fiber. Output optical power of the waveguide is collected using a photo-detector and the detected data were recorded automatically by a computer.

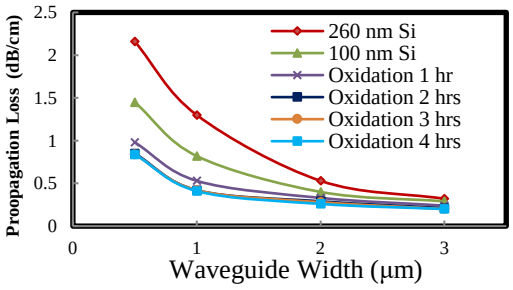

(a)

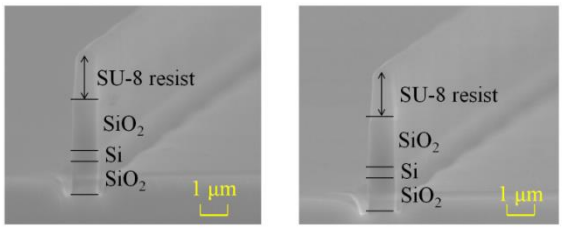

(b) (c)

Fig. 2 Optical properties of the high-mesa waveuides (a) Measured propagation loss before and after oxidation (260 nm data for comparison) and Captured SEM images (b) before oxidation and (c) after 4 hrs oxidation.

The estimated α as a function of the waveguide width is shown in Fig. 2 (a). The loss of 100 nm Si waveguides at the wavelength of 1550 nm even without oxidation are lower than those of 260 nm-Si waveguides. This is because that the effective refractive index (neff) is lower when the Si core is thinner and thus the αscattering is lower according to the Payne-Lacey model. After sufficient oxidation (⩾3 hrs), α is effectively reduced from 1.45 to 0.84 dB/cm for width=0.5 μm and from 0.29 to 0.2 dB/cm for width= 3μm, which follows our above analysis of the oxidation of Si. Longer time oxidation (4 hrs) does not induce obvious further reduction of α, which is attributed to the formation of SiO2 preventing oxygen from diffusing through the grown oxide film into the Si [15]. Figure 2(b) and (c) show the SEM images of the 1 um wide waveguide before oxidation and after 4 hrs oxidation, respectively. The waveguide structure seems to be secure even after long oxidation process as shown in Fig. 2(b) and (c).

3. DISCUSSIONS

From Fig. 2(a), the curve slope of the measured α becomes lower and lower with the increasing waveguide width. When the width reaches around 3 μm, the curve seems to be almost flat, which indicates that α goes constant when the width > 3 μm. Therefore, α at the width of 3 um is considered to be totally caused by the damaged Si absorption αabsorption. By using thermal oxidation, αabsorption has been reduced down from 0.29 to 0.2 dB/cm. Subsequently, αscattering at each waveguide width is readily obtained just by using αscattering = α - αabsorption. According to the Payne-Lacey model [13], αscattering is given as follows

$$\alpha_{scattering} \propto (n_{eff} - n_0)^2 \sigma^2 \Gamma_{air} \quad (1)$$

where n0 is the refractive index of the cladding, σ the sidewall roughness and Γair the portion of the guided light out of the waveguide. This work fitted the αscattering according to Eq. 1 by continuously changing σ until the fitted curve overlaps with the measured result. When the σ is 11.5 nm, for the un-oxidated waveguides, This work find that the fitted and measured curves overlap each other well. After sufficient oxidation (⩾3 hrs), the fitted and measured curves overlap each other well when the σ is 9.4 nm, which means that the oxidation improves the σ as high as 2.1 nm. This 2.1 nm can not be observed in Fig. 2(b) and (c) obviously because of the limilted resolution of the SEM.

Based on the 3 μm wide waveguide, This work design a photonic integrated circuit for the CRDS system as schematically shown Fig. 3. On the chip, it integrates a tunable laser (TL), a semiconductor optical amplifier (SOA), an optical coupler (CP) with a splitting ratio 9:1, a 1 m long waveguide gas sensing (WGS) cell and a photo-detector (PD) [4]. In this work, This work take CH4 for the targeted gas as an example and use the 3 μm wide waveguide with the measured α=0.2 dB/cm and the calculated Γair =2.6%. In the CRDS system, the ring-down times are 200, which means the effective sensing path is 200 m [4]. Consequently, the sensitivity of the integrated CRDS circuit is determined by the α and Γair of the WGS and the CH4 absorption cross section. The detailed calculation method has been demonstrated in our previous work [4]. Based on this method, the calculated sensitivity of the CRDS is ranging from 104 to 10 ppm depending on the gain of the SOA [5]. Since the CH4 concentration in exhaled breath of 2-10 ppm indicates a buerger disease [4], our waveguide has a promising potential to be applied in an integrated CRDS system.

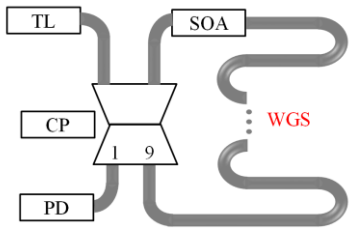

Fig. 3 Schematic of designed photonic integrated circuit for the CRDS systerm

4. CONCLUSIONS

Authors have designed and fabricated 100 nm-thick Si core high-mesa waveguides for breath sensors. By using dry thermal oxidation, $\alpha_{scattering}$ and $\alpha_{absorption}$ are reduced effectively and the final achieved α satisfies the requests of the low loss of a compact CRDS system.

5. ACKNOWLEDGMENT

This work is supported in finance by SECOM Science and Technology Foundation.

6. REFERENCES

[1] T. H. Risby and S. F. Solga, Current status of clinical breath analysis, Appl. Phys. B, vol. 85, 2006, pp. 421-426.

[2] G. Berden, R. Peeters, and G. Meijer, Cavity ring-down spectroscopy: Experimental schemes and applications, Int. Rev. Phys. Chem., vol. 19, 2000, pp. 565-607.

[3] J. Manne, O. Sukhorukov, W. Jager, and J. Tulip, Pulsed quantum cascade laser-based cavity ring-down spectroscopy for ammonia detection in breath,Appl. Opt., vol. 45, 2006, pp. 9230–9237.

[4] J. Chen, H. Hokazono, D. Nakashima, M. Tsujino, Y. Hashizume, M. Itoh and K. Hamamoto, Low loss silica high-mesa waveguide for infrared sensing, Jpn. J. Appl. Phys., vol. 53, 2014, pp. 022502.

[5] W. Li, Y. Han, Z. Chen, H. Jiang, and K. Hamamoto, Amplifier Assisted CRDS (Cavity Ring-down Spectroscopy) toward Compact Breath Sensing, IEICE vol. 118, no. 399, 2019, pp. 251-254.

[6] A. Intekhab, SOI-based Si/SiO2 High-mesa Waveguide for Optical Absorption Sensing, Thesis, Kyushu Univ., 2013.

[7] D. Nakashima and K. Hamamoto, Proposal of novel strip high-mesa waveguide for infrared absorption sensing, Appl. Phys. Express, vol. 5, 2012, pp. 062202.

[8] F. D. Olio and V. M. Passaro, Optical sensing by optimized silicon slot waveguides, Opt. Express, vol. 15, 2007, pp. 4977-4993.

[9] Y. Han, W. Li, H. Jiang and K. Hamamoto, Thin core (100nm) silicon high-mesa waveguide for high quality breath sensors, IEICE Tech. Rep., vol. 118, 2018, pp. 87-92.

[10] K. K. Lee, D. R. Lim, and L. C. Kimerling, Fabrication of ultralow-loss Si/SiO2 waveguides by roughness reduction, Opt. Lett., vol. 26, 2001, pp. 1888–1890.

[11] A. Yahata, S. Urano, T. Inoue, and T. Shinohe, Smoothing of Si trench sidewall surface by chemical dry etching and sacrificial oxidation, Jpn. J. Appl. Phys., vol. 37, p. 7, 1998.

[12] F. P. Payne and J. P. R. Lacey, A theoretical analysis of scattering loss from planar optical waveguides, Opt. and Quantum Electron., vol. 26, 1994, pp. 977-986.

[13] S. Taebi, M. Khorasaninejad, and S. S. Saini, Modified Fabry-Perot interferometric method for waveguide loss measurement, Appl. Opt., vol. 47, 2008, pp. 6625–6630.

[14] M. Liu, P. Jin, Z. Xu, D. A. H. Hanaor, Y. Gan, and C. Chen, Two-dimensional modeling of the self-limiting oxidation in silicon and tungsten nanowires, Theor. Appl. Mech. Lett., vol. 6, 2016, pp. 195–199.

Compact and Highly Sensitive Methane Sensor Based on Two Tangent Air Hole Structure

Zan Hui Chen*, Haisong Jiang and Kiichi Hamamoto
I-Eggs, Kyushu University, 6-1, Kagugakouen, Kasuga, Fukuoka 816-8580,
*zan.hui.861@s.kyushu-u.ac.jp

Abstract: *We propose and numerically investigate a silicon bus waveguide with two tangent air hole structure, to improves the detection sensitivity of methane gas (2.16 nm/%). The spectral feature of the proposed methane sensor with two tangent air hole structure for the change of structure parameters and methane gas concentration is analyzed. The result shows that the proposed two tangent hole structure as a methane sensor can realize an overall figure of merit of 1.2×10^4 compared to the previous studies. The proposed structure is one of the alternatives for detecting low concentration methane gas environment.*

Keywords: Silicon Waveguide; Methane Sensor; Highly Sensitive; Two Tangent Hole.

1. INTRODUCTION

Integrated on-chip sensors play an important role in industrial and environmental monitoring application [1, 2]. Up to now, photonic crystal (PhC)-based resonators are widely used as gas refractive index (RI) sensors due to a strong light-matter interaction between the optical field and gaseous analytes. Because the gaseous molecules are usually located in the air region where the pinched optical field can fully overlap with the gaseous analytes. However, these above PhC-based sensors, the optical field of resonance mode is concentrated inside the dielectric region (silicon material) [3]. As this result, the sensitivity of the above structures is low. The sensitivities (S) of most above device structures are generally located to the range of 100–200 nm/RIU [4]. On the other hand, the trade-off between S and Q also lead to the low figure of merit (FOM∼300-400) for those structures [5].

In this paper, a silicon bus waveguide consisting of the tangent air hole array has been proposed. To the contrary to the previously reported structure, the proposed structure improves the detection sensitivity of methane to 2.16nm/%. Additionally, a high figure of merit (FOM=1.2×10^4) was realized. The results imply the possibility of ppb-order methane detection which is one of the alternatives for detecting low concentration methane gas environment.

2. CONCEPT AND OPERATE PRINCIPLE

2.1 Concept

The structure of the unit cell consists of two holes, of which corresponds to one-dimensional lattice each, inside a straight bus waveguide. As shown in Fig. 1 (a), the unit cell structure is consisting of two etched holes. A silicon dioxide cladding of 2 μm is formed under Si-core layer of 0.26 μm. By inducing periodicity in the RI variation, a photonic bandgap is generated variation along waveguide direction because the periodic RI contrast diffracts the propagating light. Frequencies falling in the bandgap are not allowed to propagate due to the inexistence of the optical modes. For the above result, a resonance peak or dip will appear in the transmission spectrum. It is well known that a fractional change in the RI of the device structure results in a fractional change in the frequency of the resonance mode. This property has been utilized in sensing purposes, as infiltration of various methane concentration will change the RI contrast of the two tangent hole structure.

Next, one uses the finite-difference time-domain (FDTD) method to simulate the designed structure. Here, light is incident into the bus waveguide in the silicon layer from the z-direction, as shown in Fig. 1 (a). Figure 1 (a), (b), and (c) shows the change of electric field intensity profile with the varied gap. Figure 1 (c), the optical field is concentrated inside the gap between two air holes, and the optical energy is fully compressed into smaller volume with the decrement gap. That to say, the proposed structure can tightly pinch light inside the air region where it can fully overlap with the gaseous analytes, to improve the detection sensitivity of gas. That means a minute difference in the RI of various ethanol concentration is even enough for detection as two tangent hole structure enables light localization that enhances the light-matter interactions and thus the sensitivity.

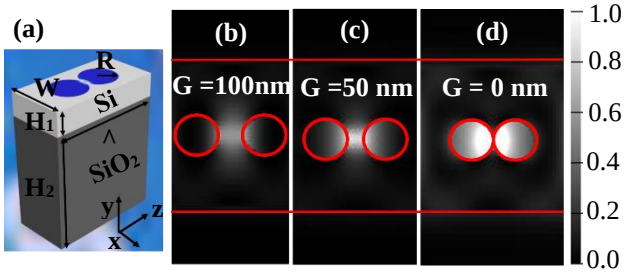

Fig. 1. Light intensity profile in different gap distance. (a) 3D schematic of two tangent hole structure; the periodicity of the tangent hole is 600 nm (Λ), and the width of bus waveguide is 700 nm (W), H_1=0.26 μm, H_2=2 μm. The simulated electric field energy contribution with different gap distance100 nm (b), 50 nm (c), 0 nm (d).

2.2 Operate Principle

A 2D schematic of the design of this two tangent hole waveguide (named, TTHW) is shown in Fig. 2 (a). In this structure, there are 21 unit cells between the central cavity and the 10 unit cells as a mirror on each side of the cavity, as shown in Fig. 2 (b). Note that not all unit cells are patterned in Fig. 2 (b). The cavity is consisting of a central unit cell of 100 nm radii (R_1) and mirror unit cells

of 120 nm radii (R_2) on both sides of the cavity. The photonic crystal lattice spacing is Λ=600 nm and the width of the waveguide is 700 nm. The structure can be directly fabricated on SOI wafer, which consisting of a 260 nm device layer (silicon) and 2 μm thick active layer (silicon dioxide). Finally, the proposed device thickness is determined by the choice of the wafer. Note also that the design can allow the light field confine in the gap between two open space holes, which corresponding to the optical energy is progressively squeezed into a smaller volume to improve the sensitivity of gas detection. It was reported that the parameter of periodicity, hole radius and mirror numbers can be optimized by using the algorithm [6].

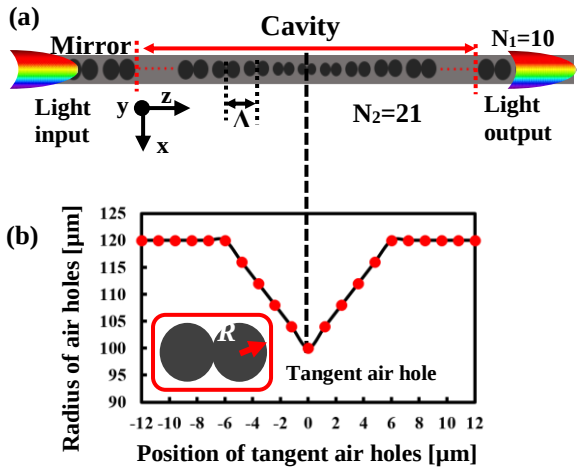

Fig. 2. Design of the TTHW structure. (a) Schematic illustration of the TTHW; the periodicity of the tangent hole is 600 nm (Λ), and the width of bus waveguide is 700 nm (W). (b) The plot of the air hole radius with the position change of the tangent air holes.

3. RESULT AND DISCUSSION

To quantitatively evaluate the performance of the gas sensor, the sensitivity as the shift of the resonance wavelength per gas concentration is be define. Figure 3(a) shows the transmission spectra of the TTHW sensor as a function of methane gas concentration. The resonance property of the structure shows a distinct blue-shift as the methane gas concentration changes from 0% to 3%. As shown in Fig. 3(b), which compares the wavelength shift for the resonant cavity mode between the proposed two tangent air hole and single air hole structures for varied methane gas concentrations. As shown, the methane gas detection sensitivity calculated by $S=\Delta\lambda/\Delta C$ is 2.16 nm/%, which corresponds to a RI sensitivity ($S=\Delta\lambda/\Delta RI$) of 353 nm/RIU. The proposed two tangent air hole structure improves the sensitivity to 2.16 nm/% compared to the single air hole structure (0.67 nm/%) [3]. Considering the optical performance of other refractive index sensors based on the PhC, it can be seen that the proposed TTHW can simultaneously achieve high sensitivity (353 nm/RIU) and figure of merit (FOM=12,006) than these report results, which is useful for high sensitivity refractive index sensing.

4. CONCLUSION

In conclusion, a silicon bus waveguide with two tangent air hole structure has been proposed and numerically investigated, to achieve highly sensitive methane gas detection. The spectral feature of the TTHW as a function of methane gas concentration is also investigated.

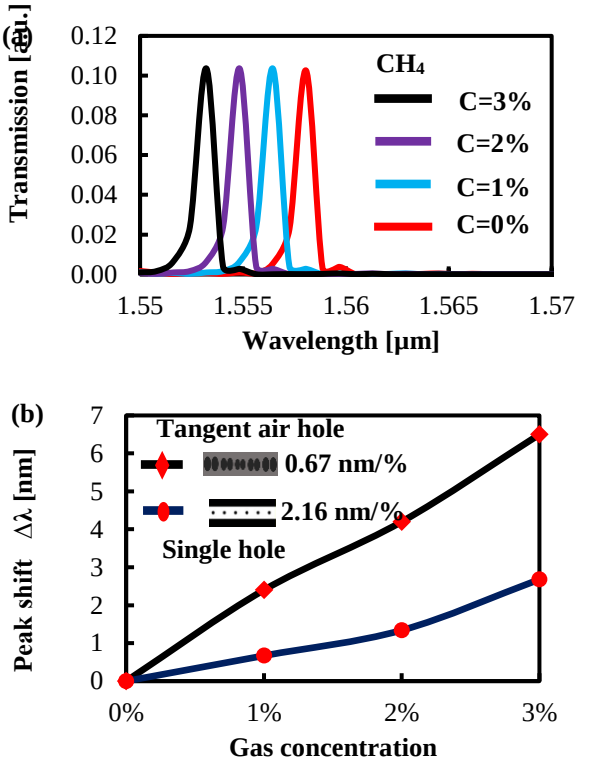

Fig. 3. The sensitivity properties of the methane gas sensor based on TTHW structure. (a) Transmission spectra for the proposed TTHW as a function of the methane gas concentration from 0% to 3%. (b) The shift of resonant wavelength between the tangent air hole and single air hole structures for the increased methane gas concentration.

Theoretical analysis reveals that methane gas detection sensitivity can be significantly improved to 2.16 nm/% (corresponding to a RI sensitivity of 353 nm/RIU). A high figure of merit ($FOM=1.2\times10^4$) was realized for the TTHW compared to previous studies. As demonstrated by these results, the proposed TTHW is potentially an ideal platform for RI-based breath gas analysis and environmental monitoring.

5. REFERENCES

[1] M. A. Islam, B. B. Saha, S. Jribi, K. Thu, T. Miyazaki, S. Koyama3, IEICES. 2 (2016) 21–24.
[2] S. ALrsheedi, B. B. Saha, A Chakraborty, T._Miyaziki, K Thu, S Jribi, Ibrahim I. El-Sharkawy, S. Koyama, IEICES. 2 (2016) 29–32.
[3] S. Tomljenovic-Hanic, A. Rahmani, M. J. Steel, and C. Martijn de Sterke, Opt. Express 17 (2009), 14552-14557.
[4] K. Hirai, T. Araki, J. Cai, K. Hayashi, T. Horiuchi, Y. Iwasaki, Y. Ueno, E. Tamechika, K. Wada, and Y. Ishikawa, Jpn. J. Appl. Phys. 53 (2014), 04EG09.
[5] B. Wang, M. A. Dündar, R. Nötzel, F. Karouta, S. He, and R. W. van der Heijden, Appl. Phys. Lett. 97 (2010), 1511505.
[6] Q. Quan, and M. Loncar, Opt. Express 19 (2011), 18529.

Proposal of 1×N Optical Mode Switch Based on Spatial Single Dimensional Mode

Satoshi Ogawa[1]*, Haisong Jiang[1], and Kiichi Hamamoto[1]
[1]I-EggS (Interdisciplinary Graduate School of Engineering Sciences), Kyushu University
6-1, Kasuga-Koen, Kasuga, Fukuoka 816-8580, Japan
*E-mail: ogawa.satoshi.851@s.kyushu-u.ac.jp

Abstract: *For a rapid increase of the recent data traffic, 1×N optical mode switch based on spatial single dimensional mode is newly proposed in this paper. Simulated results of this new switch show all 64 switching among 8 modes (0th – 7th) under low excess loss (1.6 dB) due to the precise eigen-mode realization.*

Keywords: Spatial division multiplexing (SDM) devices; SDM technologies for photonic switching and networking

1. INTRODUCTION

For a rapid increase of the recent data traffic, ROADM (Reconfigurable Optical Add/Drop Multiplexer), based on spatial single dimensional mode, has been proposed [1, 2]. We have also proposed the N×N optical mode switch which is able to switch modes as the key device of the space-mode- (SM) ROADM [3]. In this paper, the 1×N mode switch is newly proposed, regarding evolution for higher order mode: scalability. We have designed 1×8 optical mode switch and simulated all 64 switching among 8 modes (0th – 7th) under low mode switching loss (< 1.6 dB).

2. HIGHER ORDER MODE EVOLUTION OF N×N OPTICAL MODE SWITCH

In the proposing SM-ROADM system, mode information of optical signal is used as "addressing". In the SM-ROADM concept, there are no direct communication lines between transmitters and receivers. Instead, there is a whole communication channel, which is able to circulate information. For the traffic control of multiple mode signals, it is important that the mode of each signal is switched to another mode by optical mode switch.

2.1 Eigen-mode realization issue of the N×N optical mode switch

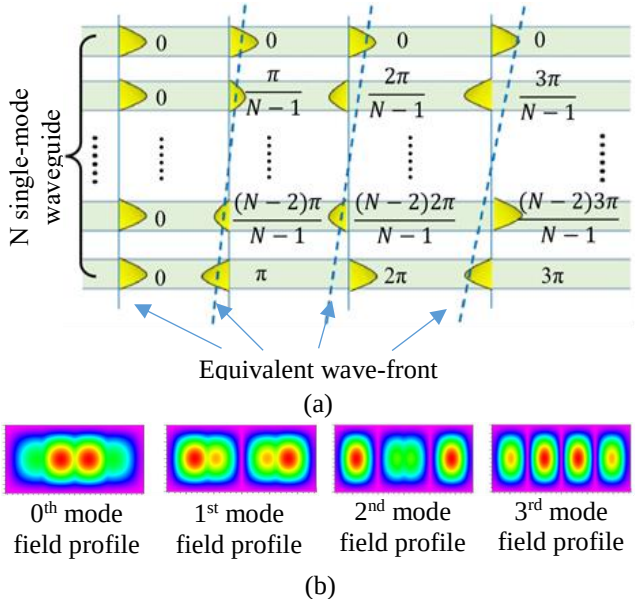

Fig. 1. (a) Phase profiles of spatial single mode in a waveguide and (b) field profiles of modes (0th – 3rd).

If only based on spatial single dimensional mode, optical mode switch is easier in the device-design rather than LP mode. Figure 1 shows the phase and field profiles of spatial single mode.

We have already reported the 4×4 optical mode switch based on the single dimensional mode [3]. Whereas the 4×4 optical mode switch can switch modes to any other different modes among 0th, 1st, 2nd and 3rd order modes, this switch configuration had a problem of precise eigen-mode realization, which is important for MIMO (multi-in / multi-out) less operation.

2.2 Operation principle of the 1×N optical mode switch

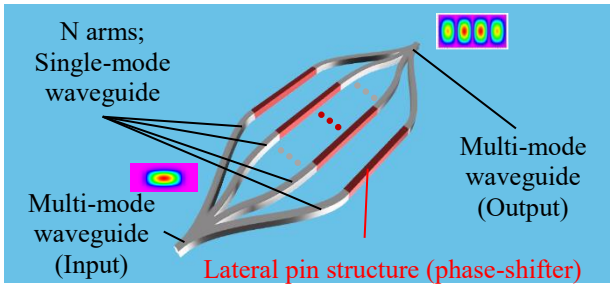

Fig. 2. Schematics of 1×N optical mode switch.

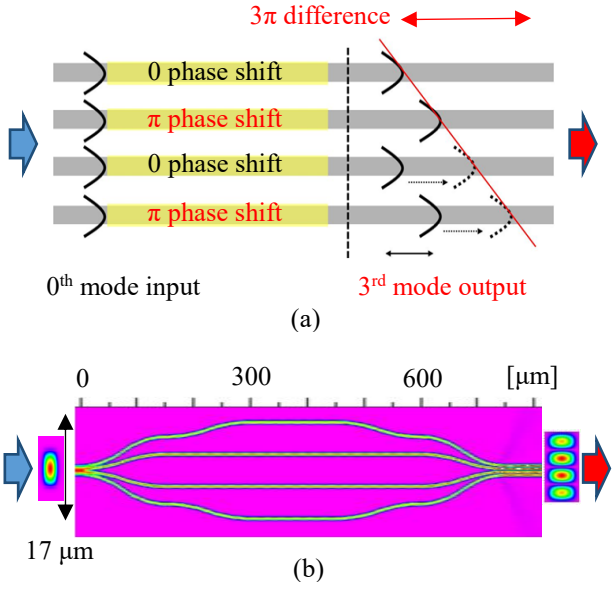

Fig. 3. (a) Switching mechanism and (b) simulation result from 0th order mode to 3rd order mode).

We propose the 1×N optical mode switch which enable precise eigen-mode realization. The schematic diagram of the 1×4 optical mode switch configuration is shown as an example in Fig. 2. Multimode input waveguide is connected to a 1×4 power splitter which separates eigen-mode into N-fold single mode in each arm. Each arm possesses mode sifting region which realizes mode conversion. Then the separated light is coupled toward output multimode waveguide. This 1×N optical mode switch secures the switching from one mode to another one. The 1×N optical mode switch is operated by electric current injection into pin phase-shifters. Lateral pin structure make π difference of phase-shift at each arm, which leads to mode-change in the output signal.
For example, when we shift π as shown in Fig.3, we get 3rd order mode output. Wave-fronts drawn in broken-lines are imaginary wave-fronts (2π difference).

3. SIMULATION RESULTS OF 1×8 OPTICAL MODE SWITCH AND DISCUSSIONS

We designed 1×8 optical mode switch and confirmed fundamental switching among 8 modes (0th – 7th order mode). Beam propagation method (BPM) was used for the simulation.
For confirmation of the switching quality, we have estimated mode switching loss. Mode switching loss Lm is defined as the ratio of output mode power Po versus input mode power Pi (see equ. (1)).

$$L_m = -10 \log \frac{P_o}{P_i} \quad [\mathrm{dB}] \tag{1}$$

Table 1. Mode switching loss of 1×8 optical mode switch simulation. Input mode (vertical axis) vs. output mode (lateral axis).

Input mode \ Output mode	0th	1st	2nd	3rd	4th	5th	6th	7th
0th	0.2	0.2	0.9	0.9	0.3	0.4	0.3	0.3
1st	0.2	0.01	1.6	1.4	0.4	0.4	0.2	0.2
2nd	0.4	0.4	0.2	0.3	0.3	0.3	0.3	0.2
3rd	0.8	0.7	0.5	0.1	0.2	0.1	0.2	0.1
4th	0.3	0.1	0.6	0.4	0.1	0.08	0.08	0.07
5th	0.3	0.1	0.4	0.2	0.08	0.04	0.07	0.04
6th	0.2	0.08	0.5	0.4	0.09	0.07	0.03	0.02
7th	0.2	0.3	0.4	0.2	0.07	0.04	0.02	0.004

Mode signal noise ratio (SNR_m) is also estimated. Definition of SNR_m is as follow:

$$SNR_m = 10 \log \frac{P_o}{P_N} \quad [\mathrm{dB}] \tag{2}$$

where P_N is the power of other mode components.

Table 2. Mode signal noise ratio (S/N) of 1×8 optical mode switch simulation. Input mode (vertical axis) vs. output mode (lateral axis)

Input mode \ Output mode	0th	1st	2nd	3rd	4th	5th	6th	7th
0th	13.5	14.4	6.3	6.3	10.9	10.6	11.2	11.4
1st	14.4	27.0	3.7	4.1	10.1	10.5	13.2	13.5
2nd	10.1	9.9	13.9	12.1	11.2	11.9	12.3	12.9
3rd	7.1	7.5	9.4	15.2	14.0	14.9	14.5	14.9
4th	12.2	15.1	8.6	10.0	14.7	17.1	17.1	18.2
5th	12.1	15.7	10.4	12.6	17.4	20.0	18.2	20.4
6th	14.2	17.4	9.1	10.4	16.7	17.9	20.9	24.0
7th	12.4	15.6	10.3	12.6	17.6	20.0	24.0	30.0

As shown in Table. I and Table II, we could successfully confirm that the configuration proposed realize relatively precise eigen-mode for all switching state. The estimated worst mode switching loss was 1.6 dB. We will plan to implement the proposed 1×N optical mode switch in the future.

4. CONCLUSIONS

We have proposed and simulated new configuration of 1×N optical mode switch. We have designed 1×8 optical mode switch and simulated all 64 switching among 8 modes (0th – 7th) by BPM simulation. Mode switching losses and mode of less than 1.6 dB has been successfully confirmed.

5. ACKNOWLEDGEMENT

This work has been financially supported by SCAT. Also, a part of this work was financially supported by JSPS KAKENHI Grant Number JP19K05308.

6. REFERENCES

[1] K. Hamamoto and H. Jiang,"Active Opto-Electronic Devices Based on Multi-Mode Interference among Spatial Single Dimensional Modes," IEICE Electronics, J100-C, 72, (2017).
[2] R. Takakura, M. Jizodo, A. Fujino, T. Tanaka, and K. Hamamoto "Proposal of optical mode switch," Japanese Journal of Applied Physics, 53, 08MB10 (2014).
[3] Y. Matsunaga, S. Yano, K. Kameyama, H. Wado, Y. Takeuchi and K. Hamamoto "SOI-based Si/SiO_2 high-mesa waveguides for a compact infrared sensing system," Engineering Sciences Reports Kyushu University, 30, 1, (2008).

Compact Breath Sensing using Amplifier Assisted CRDS (Cavity Ring-down Spectroscopy)

Wenying Li , Yu Han, Zanhui Chen, Haisong Jiang, and Kiichi Hamamoto
I-EggS (Interdisciplinary Graduate School of Engineering Sciences), Kyushu Univ.,
Email: ri.uenin.271@s.kyushu-u.ac.jp

Abstract: *Amplifier assisted CRDS (cavity ring-down spectroscopy) is proposed to realize ppm-order gas sensing using optical waveguide with telecom wavelength band. One issue of the amplifier assisted CRDS system is that the self-lasing may happen when optical amplifier is at high pumping condition. Self-lasing light takes away the gain of amplifier from the signal light, limits the sensing sensitivity. To stop the self-lasing, we proposed the polarization direction control scheme in this work. The experimental results show the light intensity of self-lasing light is suppressed down below -50 dBm, and the gain of signal light improved 24dB.*

Keywords: Gas sensing; CRDS system; Waveguide.

1. INTRODUCTION

Breath sensing system based on CRDS (Cavity ring-down spectroscopy) method is attractive because human-breath contains various disease-markers, as well as its real time and high sensitivity sensing. Compact breath sensing system is desired for daily health care and optical waveguide gas-cell [1-2] has been proposed to realize such that compact system. The propagation loss of the waveguide, however, may prevent the low gas concentration sensing. We have proposed the optical amplifier assisted CRDS system scheme to compensate the waveguide propagation loss [3]. One issue is that when optical amplifier is at high pumping condition, self-lasing may happen. Self-lasing light takes away the gain of amplifier from the signal light, limits the sensing sensitivity. To stop the self-lasing, we proposed the polarization direction control scheme in this work. The experimental results show the light intensity of self-lasing light is suppressed down below -50 dBm, and the gain of signal light improved 24dB.

2. SELF-LASING ISSUE IN AMPLIFIED CRDS SYSTEM

The amplifier assisted CRDS system we use is shown in Fig. 1 (a). Two couplers and sensing-waveguide [3] form sensing "cavity". Couplers work like mirrors to reflect signal light back into the cavity except a portion of monitor-light leak out via the coupler. In this system, we used an EDFA (Erbium-doped fiber amplifier) as an optical amplifier to compensate the propagation loss of the waveguide. An EDFA inside a closed ring loop, however, may form the structure of fiber ring laser [4-5], when optical amplifier is at high pumping condition, self-lasing happens. Figure 1 (b) shows an example of this self-lasing. 1572 nm wavelength (Absorption wavelength of CO_2) light is introduced into the CRDS system, however, another wavelength of 1564 nm starts lasing. The self-lasing light takes most of the gain from amplifier, signal light loses its gain, which limits the sensing sensitivity.

The ASE (Amplified spontaneous emission) that generated by EDFA works as the "first seed" and travelling inside the CRDS system. This travelling light keeps the same phase, polarization and frequency, coherency is secured [6], thus self-lasing happens. To stop the self-lasing, we propose the polarization direction control scheme. By changing the polarization of the travelling light, destroy the coherency condition, prevent the self-lasing.

3. RESULT AND DISSCUSSION

The configuration of polarization direction control is shown in Fig. 2 (a). A polarization controller is set inside the CRDS system. The "first seed" of self-lasing, the ASE of EDFA is circular polarization light. When it propagates through the polarization controller, it is changed to linear polarization light, a portion of light intensity of this "first seed" is cut. As the polarization condition is changed from circular polarization to linear polarization, the coherency condition is weakened, thus the self-lasing is suspended. The spectrum of the amplifier assisted CRDS system after polarization direction control is shown in Fig. 2 (b). The self-lasing power is suppressed to be below -50 dBm. We estimate that the gain of signal improved 24dB.

Figure 3 shows the cavity ring-down waveform after the polarization direction control. As is shown in the figure, more than 200 pulses are achieved, which is available for ppm-order gas detection.

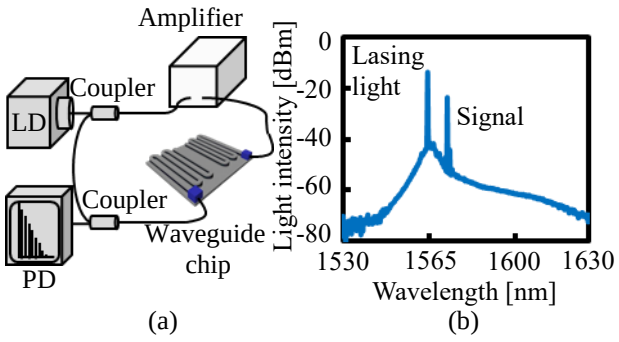

Fig. 1 (a) Amplifier assisted CRDS system configuration. (b) Spectrum of amplifier assisted CRDS system.

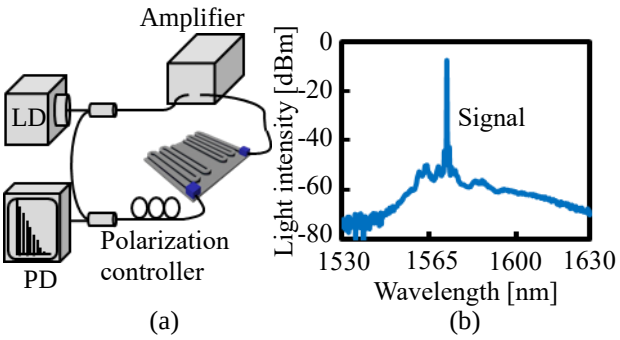

Fig. 2 (a) Configuration of polarization direction control in amplifier assisted CRDS system. (b) Spectrum of polarization direction controlled CRDS system.

4. CONCLUSIONS

In amplifier assisted CRDS system, when optical amplifier is at high pumping condition, self-lasing may happen. The self-lasing light consumes most of the gain and the signal light hardly get gain from amplifier. We introduced the polarization direction control scheme to suspend the self-lasing, the experiment results show the light intensity of self-lasing light is suppressed down below -50 dBm, and the gain of signal light improved 24dB.

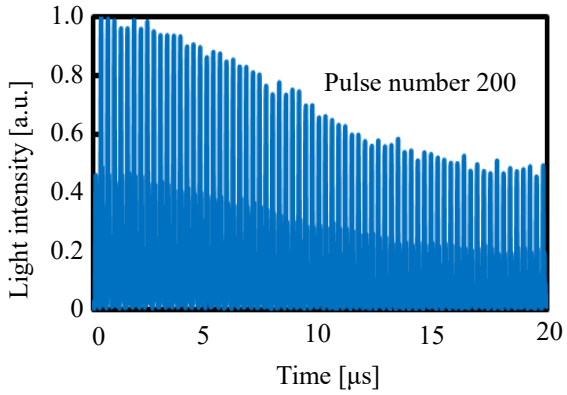

Fig. 3. Cavity ring-down waveform after polarization direction control.

5. ACKNOWLEDGEMENT

This research was financially supported by SECOM Science and Technolygh Foundation.

6. REFERENCE

[1] A. Wilk, F. Swichter, S. Kim, E. Tutuncu, B. Mizaikoff, J.A. Vogt, U. Wachter, and P. Radermacher, Toward the quantification of the $^{13}CO_2/^{12}CO_2$ ratio in exhaled mouse breath with midinfrared hollow waveguide gas sensors, J. Analy. Bioanaly. Chem., 402 (2012) 397-404.

[2] W. Lai, S. Chakravarty, X. Wang, C. Lin, R. Chen, On-chip methane sensing by near-IR absorption signatures in a photonic crystal slot waveguide, J. Opt. Lett., 36 (2011) 984-986.

[3] H. Hokazono W. Li, S. Enami, H. Jiang, and K. Hamamoto, Gas sensing demonstration by using silica high-mesa waveguide with amplified cavity ring down spectroscopy technique, J. ELEX, 12 (2015) 20150574.

[4] C. Chang, and A. Amrullah, A steady-gain C-band EDFA for multi-wavelength fiber optical transport networks, Int. J. of Optoelectron. Eng. 3 (2013) 6-11.

[5] X. Liu, Z. Li, S. Luo, Z. Gu, J. Liu, Y. Wang, and Q. Shen, Multiwavelength erbium-doped fiber laser based on a nonlinear amplifying loop mirror assisted by un-unpumped EDF, J. Opt. express 20 (2012) 7088-7094.

[6] Ter-Mikirtychev, and Vartan, *Fundamentals of fiber lasers and fiber amplifiers*, Springer, Swizerland, 2014, pp. 79-98.

Observation of 60 GHz and 20 GHz Multiple Photon-Photon Resonances Using Active Multimode Interferometer Laser Diodes

Shingo Murakami, Bingzhou Hong, Haisong Jiang, and Kiichi Hamamoto
Interdisciplinary Graduate School of Engineering Sciences, Kyushu University.
murakami.shingo.050@s.kyushu-u.ac.jp

Abstract: *1 × N active multimode interferometer laser diodes to achieve two photon-photon resonances (PPRs) have been designed and fabricated. Very high frequency of 60 GHz in addition to 20 GHz PPR peaks were confirmed.*

Keywords: Active MMI-LD; Photon-Photon resonance; High speed modulation

1. INTRODUCTION

Optical inter-connection is highly developed due to computer technology advancing [1], and direct modulation laser diode (DML) may be one of the transmitter candidates especially for the future mobile IT-devices which speed is required around 100 Gbps [2, 3], whereas the modulation speed of DML has been limited up to around 50 Gbps. One way to improve the maximum modulation rate beyond 100 Gbps is photon-photon resonance (PPR) [2-7]. In this paper, the design concept and the experimental results of multiple photon-photon resonances based on active-MMI configuration is reported. This scheme of multiple photon-photon resonances enables plural PPR peaks which may achieve higher modulation speed in the future. As a result, two PPR resonance frequencies of around 20 GHz, and 60 GHz have been successfully confirmed experimentally.

2. CONCEPT OF ACTIVE-MMI LDs

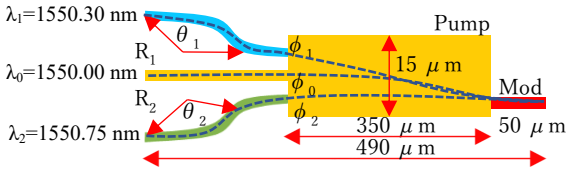

Fig. 1. Schematic view of active-MMI LD

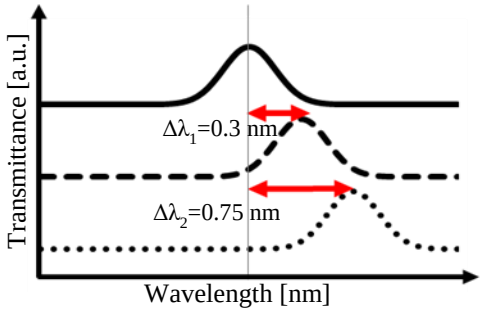

Fig. 2. Schematic concept of PPRs using 1×N active-MMI

The PPR peak is designed using wavelength differences between center wavelengths of each arm at *N*-side of MMI [8]. As shown in Fig. 1, there are three arms at LHS of the 1 × *N* active-MMI configuration. In case of $N \geq 3$, the phase must be matched at the MMI edge to avoid non self-image at the RHS of the MMI. This phase-matching requirement causes free spectral range in the transmission spectrum of the 1 × *N* MMI. To secure this phase-matching condition, bending regions in the both top and bottom arms are introduced. The bending region also induces wavelength dependency which gives the center wavelengths of each arm. Each center wavelength slightly different as indicated in Fig. 1 as to achieve two different PPR peaks in the emission wavelength is designed.

The relation between three different center wavelengths are schematically illustrated in Fig. 2. In the case of center wavelengths arranged as Fig. 1, two different peak shifts are designed. The corresponding wavelength differences are derived in the following equation (1);

$$\Delta\lambda = \lambda_m - \lambda_{center} = \frac{2\Delta L}{n_{eq}} \cdot \frac{1}{2\phi + 2\pi m} - \lambda_{center} \qquad (1)$$

Here, λ_{center}: the center wavelength, which is given by the transmittance peak wavelength of the MMI waveguide, ΔL: Path length difference between center and bending waveguide, n_{eq} : equivalent refractive index of waveguide, λ_m: wavelength, m: positive integer, and ϕ: initial phase for 1 × *N* MMI waveguide (For instance in case of 1 × 3 MMI shown in Fig. 1, $\phi = 1/3\pi$.). From eq. (1), ΔL is derived as eq. (2):

$$\Delta L = \frac{n_{eq}}{2} \cdot (\lambda_{center} + \Delta\lambda) \cdot (2\phi + 2\pi m) \qquad (2)$$

And according to the eq. (2), to obtain two different PPR peaks are designed as summarized in Table 1. PPR frequency F_{PPR} corresponded according to the following eq. (3);

$$F_{PPR} = \frac{\Delta\lambda \cdot c}{\lambda^2} \qquad (3)$$

Table 1. The PPR designs in this work

λ_{center} [nm]	ΔL [mm]	Δλ [nm]	F_{PPR} [GHz]
1550.00	-	-	-
1550.30	0.02	0.30	35
1550.75	0.04	0.75	80

As shown in Tab.1, PPR frequencies at around 35 GHz and 80 GHz, respectively, were designed for the devices.

3. RESULTS AND DISCUSSIONS

For the implemented devices, InGaAsP multi-quantum well was used for the active layer. The waveguide

structure was a high mesa are formed by using dry-etching.

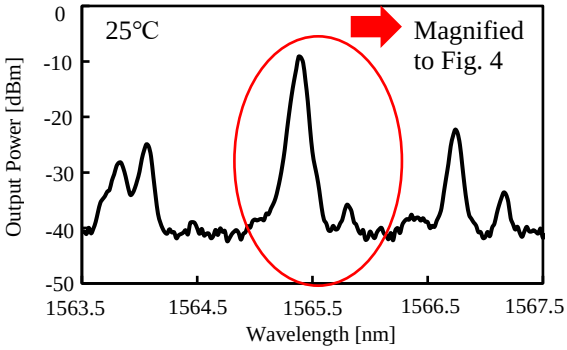

Fig. 3. Emission spectrum

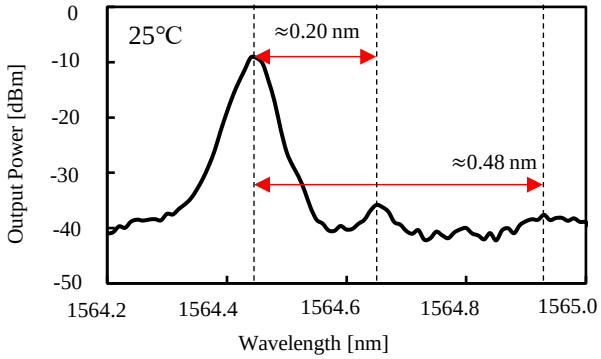

Fig. 4. Emission spectrum

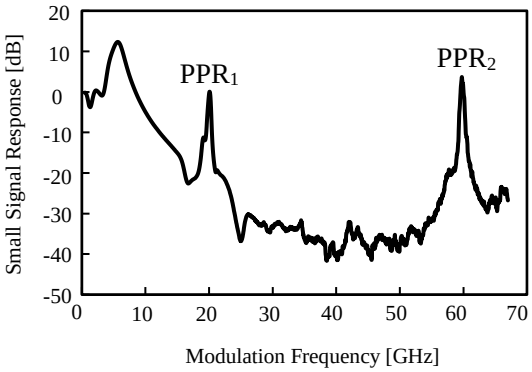

Fig. 5. Small signal response of the fabricated active-MMI LD

Figure 3 shows the emission spectra of the implemented 1 × N active multimode interferometer laser diodes. DC currents were injected as follows; pumping region (MMI section): 172 mA, bias: 53 mA, lower arm: 57 mA, upper arm: 43 mA respectively. As shown in Fig. 4, two peaks beside the main peak were observed at 1564.65 nm and 1564.93 nm, respectively. The wavelength difference between main emission peaks are 0.20 nm and 0.48 nm, respectively. These wavelength differences are not exactly same with the designed ones, however, relatively agreeable. From eq. (3), FPPR appears at the positions of 25 GHz and 59 GHz from these wavelength differences. Figure 5 shows the evaluated small signal frequency response of the fabricated devices. As shown in the figure, the limitation of resonance frequency of LD (CPR peak) at 6 GHz, and two PPR peaks of 20 GHz and 60 GHz were clearly observed successfully. There PPR peaks were corresponding to the emission spectrum in Fig. 4, therefore, these two peaks are concluded that came from photon-photon resonances. In addition, the intensity of the second PPR at higher frequency of 60 GHz are high of more than 0 dB in the response, whereas the response between two peaks completely dropped down below -30 dB. Right now, the determination factors of PPR peak intensity are not so clear, however, we hope we may keep the frequency response flat at entire frequency band by introducing this effect.

Table 2. Design and evaluated PPR frequencies

	PPR_1	PPR_2
Monitored wavelength	1564.65 nm	1564.93 nm
Calculated F_{PPR}	25 GHz	59 GHz
F_{PPR} in Fig. 3	20 GHz	60 GHz

4. CONCLUSION

Two PPRs of 20 GHz and 60 GHz based on 1 × N active-MMI LDs configuration was be able to successfully confirm. Presently, we still investigate the reason of the intensity recovery mechanism especially at high frequency. This approach of multiple PPRs is hoped that will realize flat frequency response up to very high frequency region of more than 100 GHz in the future.

ACKNOWLEDGEMENT

This work has been financially supported by SUPOIN and Kakenhi-B 19H02201. The authors greatly thank to Dr. Yasuhiro Matsui, Finiser Corp., for the future discussion.

Reference to a journal publication:

[1] S. Rumley, et al., "Optical interconnects for extreme scale computing systems," Parallel Computing, Vol. 64, 65-80, 2017.
[2] U. Troppenz et al., "40 Gbit/s directly modulated lasers: physics and application," SPIE 2011, Vol. 7953, 79530F1-F10, 2011.
[3] Y. Matsui, et al., "55-GHz bandwidth short-cavity distributed reflector laser and its application to 112-Gb/s PAM-4," OFC2016, PDP Th5B.4, 2016
[4] M. Dumitrescu, et al., "High-speed directly-modulated lasers with photon-photon resonance," OFC2013, JW2A.33, 2013.
[5] B. Hong, et al., "Bandwidth enhancement scheme demonstration (from 5 GHz to 34 GHz) on direct modulation laser diode using multiple PPR (photon-photon resonance) active MMI," ECOC 2017, P1.SC2.22, 2017.
[6] B. Hong, et al., "Mode selective active multimode interferometer laser diode with over 40 GHz Direct Modulation Bandwidth," OFC 2018, Th3B.4. 2018.
[7] K. Hamamoto, et. al., "Active-MMI laser diode toward high-speed direct modulation based on multiple photon-photon resonance," SPIE 10682, Semiconductor Lasers and Laser Dynamics VIII, 106820X; doi: 10.1 1 17/12.2306018, 2018.
[8] K. Hamamoto, et. al., "Mode-selective active-multimode-interferometer laser diode -mode-selection principle and high-speed modulation-," IEICE Tans. Electron., Vol. E102-C, No.4, pp. 364-370, 20

Transition of Initiative from Ubiquitous City to Sustainable Smart City by Korea: Focusing on the Case of Songdo City

Myung Hee Kim
Smith College, Sahmyook University
kmh@syu.ac.kr

Abstract: *The purpose of this paper is to compare the conceptual difference between the past U-city and the recent smart city in Korea, analyzing the reasons for initiative paradigm shift from U-city to smart city in Songdo city, and to provide insights into the success of new smart initiatives. In conclusion, the Songdo initiative, which reflects the U-city paradigm centered on infrastructure construction, has exposed limitations to sustainable growth as a smart city. To solve these limitations Korea has been revised the related law and is promoting smart city initiative in the form evolved from U-city.*

Keywords: Smart City; Sustainability; Ubiquitous City; ICT Convergence; Urban Smartization.

1. INTRODUCTION

UN expects that by 2030 more than 60% of the global population will live in cities, particularly surge in Africa, Asia and Latin America [1-2]. Thus, the urbanization of the 21st century is a clear global phenomenon. However, since urbanization produces a variety of urban problems, unlike U-city, which is centered on urban infrastructure, smart city must be a real alternative to solve the urban problems such as traffic congestion, energy shortages, environmental pollution, and crime. This is because smart city is emerging as a new growth engine for countries, utilizing ICT technologies such as AI, Big Data, and 5G [2].

Developed countries are promoting smartization for the purpose of regenerating the existing cities, while developing countries [22] are introducing smartization for the purpose of constructing new cities. Uniquely, the smart city project under way by Japan is to promote disaster recovery and energy efficiency after the Fukushima nuclear power plant accident and to designate Yokohama, Kyoto, Toyota and Kitakyushu as demonstration areas and plan to export smart city technology [3-5] [21].

Korea has been promoting a ubiquitous city project in the early 2000s by installing communication networks and CCTVs in new cities earlier than other countries to efficiently manage urban infrastructure such as traffic signals, waterworks, and sewage systems. However, since Ubiquitous city (U-city) was a project mainly focused on infrastructure construction such as integrated control system, there was a limit to achieve sustainable growing city due to insufficient participation of private actors and little provision of sustainable service based on citizen demand [6-7]. Moreover, as the real estate market has been stagnated due to the global financial crisis, construction companies have been reluctant to build infrastructures, which made the U-city project more difficult [2][8].

Ultimately, owing to the rapid growth of the global smart city market, Korea acknowledged smart city as a growth innovation engine of the fourth industrial revolution and supported it in the strategic level of the country. But the transition from U-city was made in 2015. In 2017, the Korean government revised the related law in line with the proliferation trend of smart city, and pursued smart ubiquitous urban projects [19-20].

The purpose of this paper is to compare the conceptual difference between the past U-city and the recent smart city, analyzing the reasons for initiative paradigm transition from U-city to smart city in Songdo city, and to provide insights into the success of new smart initiatives. The findings of the paper will also provide meaningful implications for other projects that are pursuing initiatives similar to those of Korea.

2. METHODOLOGY

2.1 Review of Literature

This paper to achieve the research aims applies a literature review of relevant theoretical and empirical research articles such as papers, periodicals, annuals, statistics yearbooks, conference proceedings, government reports, world-level dataset. For the comparative analysis of two conceptual frameworks, Lee et al's research data [23] is applied to case analysis of Songdo U-city will be used to compare the concept of U-city and smart city in this study.

2.2 Research Composition

This research is largely conducted in three stages. First, it reviews domestic and overseas literature dealing with the conceptual frameworks of U-city and smart city respectively. Second, for research findings and discussion it compares conceptual characteristics between U-city and smart city. It also analyzes the reasons for transition from U-city initiative by Songdo city, which was a pilot city of project. Finally, it concludes with summary starting new initiative.

3. RESEARCH AND DISCUSSION

3.1 Conceptual Frameworks of a Ubiquitous City

Korea Smart City Association (KSCA) [10] defines a U-city concept, based on Basic Plans for U-city from the Ministry of Information and Communication as follows: U-city is a future high-tech city where IT infrastructure, technology and service are integrated into housing, economy, traffic, and other facilities.

- Quality of life is improved by U-Traffic, U-Home

(convenient city), U-Security, U-Facility Management (safe city), U-Environment (clean city), and U-Health Care (healthy city) service.
-The new IT market is created where hardware/middleware/platform technologies involved with sensors, tags, and terminals; and communications and applications services related to software, BcN, USN, Wibro, and HSDPA are integrated.

Lee et al. [11] defines U-city as a space where information exchange can be freely combined with service, information communication, and infrastructure management systems.

U-city's brand name in Korea was be coined from the combination of the word 'city' and the word 'ubiquitous'. There, sensors or CCTV cameras are built into urban infrastructures such as roads and bridges, or networks are built to avoid school crime or disaster (Fig 1).

In 2003, Korea applied the concept of U-city, which means a livable city made of ICT, to Songdo new city, and as a result, a project for the construction of a new city that fuses ICT technology to urban infrastructure was started. “Act on the Construction, ETC. of Ubiquitous Cities” (in brief, Ubiquitous Act) was enacted (March 3, 2008) to form the legal basis of U-city initiative, construction and managements afterwards [9] [12].

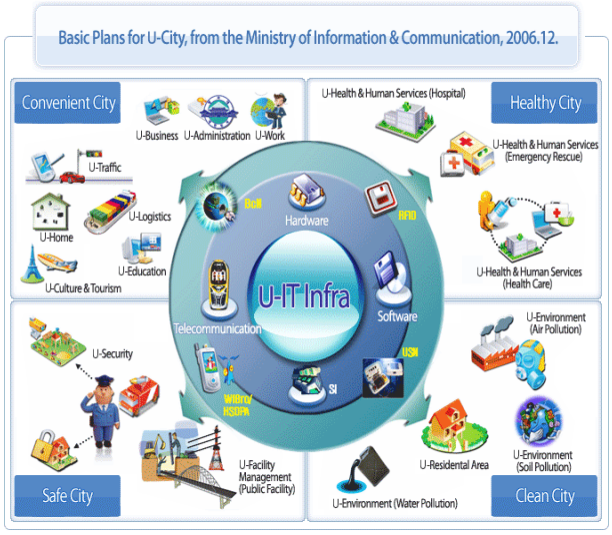

Fig. 1 Basic Plans for U-city (2006)

3.2 Conceptual Frameworks of a Smart City

There is no single commonly standardized definition of a smart city and various definitions have been used [1-2].

Frost and Sullivan [13] has defined a smart city as one that has an active presence and plan in at least five of the eight criteria below and has clearly demonstrated projects in place: smart governance, smart energy, smart building, smart mobility, smart infrastructure, smart technology, smart healthcare, smart citizen.

A smart city from the functional point of view is defined as a configuration of six primary functions: smart economy, smart mobility, smart environment, smart people, smart life, and smart governance [2]

Euro-Cities proposed the smart cities concept is accomplished by state-of-the art ICT, such as broadband networks being closely correlated with global competitiveness, sustainability, diversification of functions(or authority) and quality of life [14-15]

Deakin [16] considered a characteristic feature of smart cities as follows: ubiquitous ICT to play a crucial role in interconnection between the human and social networks of the intellectual capital of universities, the wealth creation of industries and the democratic government of civil society.

Fig.2 Songdo Public Transportation and Information Service

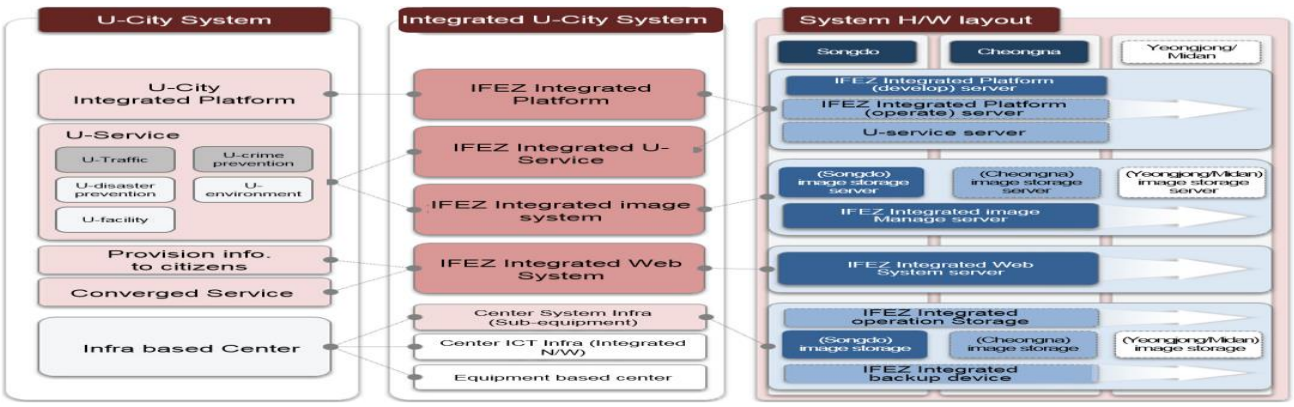

Fig. 3 Songdo & IFEZ U-city System Layout

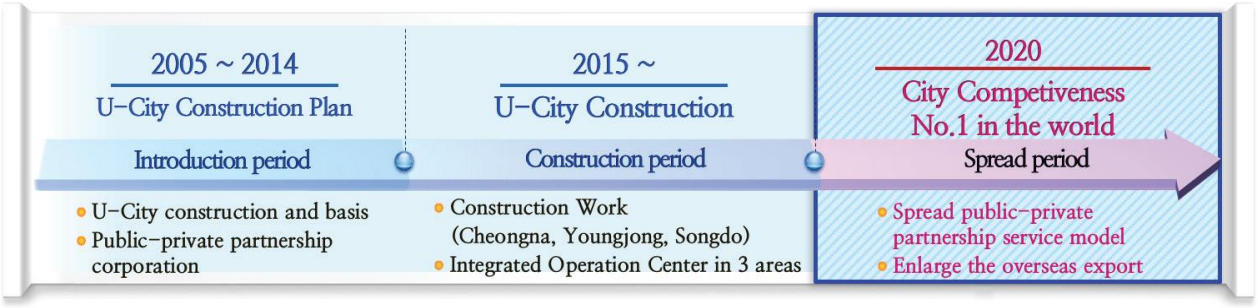

Fig. 4 Target for Each Step of Establishing Songdo U-city

3.3 A Comparison between U-city and Smart City Based on Respective Initiatives in Korea

The viewpoints on U-city and smart city in Korea are diverse, but this paper will consider smart city as an extended concept from U-city. Thus, smart city means that systems are functionalized, interconnected, and intelligentized. While U-city is accompanied by local information through the combination of infrastructure-oriented IT and city, smart city focuses on the development of services closely related to the lives of urban residents [17].

To be brief, in Korea, U-city is being driven by the government and focuses on building a system for efficient use of information based on ICT infrastructure. Smart city is being driven by private firms and focuses on creating low-cost, high-efficiency spaces for building social capital (Table 1).

Table 1. A Conceptual Comparison of U-city & Smart City

Category	U-city	Smart City
Concept	a city to use advanced technology according to the needs of the citizens.	a city with an interconnected system between intelligent systems
Direction	ICT-based infrastructure construction	developing services related to the life of citizens
	integrated system for efficient use of information	creating low-cost, high-efficiency space for building social capital
Promoting Actor	government, public institutions	private firms

Lee et. al. [23] presented a smart city evaluation index through comparison of smart city indicators of San Francisco and Seoul as shown in the following table (Table 2). According to them, U-city is an idea as a convergence of ICT services that are accessible regardless of time and space and under this concept, social infrastructure is less emphasized in terms of human and social capital. They also describe Smart city as an urban city that has evolved from an ICT-centered city and now uses immense mobile network infrastructures and services.

Table 2. Summary of Proposed Case Framework for Smart City Analysis

Category	Detailed Index
Urban openness	Participatory service design
	Open data platform availability
Service innovation	Service diversity
	Service integration
Partnership formation	Private-public partnerships types
	Funding resources
Urban proactiveness	Intelligent technology embedded in smart city services
	Smart green services related to environment and energy
Smart city infrastructure Integration	Multiple-device/platform availability
	City's own network infrastructure
	Data center availability and integration
Smart governance	Smart city leadership
	Smart city strategy
	Dedicated organization for promoting smart city
	Smart city development and management processes
	Smart city principles
	Performance measurement

Eight comparisons (eight stylized facts) derived from their analysis are applied as a conceptual framework as shown in the following table (Table 3).

Table 3. A Conceptual Framework of Smart City

1	Movement towards more interactive services engaging citizens
2	Open data movement facilitates open innovation
3	Diversifying service development: exploit or explore?
4	How to accelerate adoption: top-down public driven vs bottom-up market driven partnerships
5	Advanced intelligent technology supports new value-added smart city services
6	Smart city services combined with robust incentive systems empower engagement
7	Multiple device & network accessibility can create network effects for smart city services
8	Centralized leadership implementing a comprehensive strategy boosts smart initiatives

3.4 A Transition of Songdo U-city Initiative

A concept of U-city in Korea was first introduced in Songdo U-city project. In fact, U-city is derived from the brand name of Songdo new city. "Songdo" U-city, covering 53.4 km^2 in the Incheon Free Economics Zone (IFEZ), into which 308.4 million dollars has been invested for construction [6]. In 2008, the validity of the

project was examined and a ubiquitous service platform (USP) was established, and in 2009 the working design was completed. Based on this, 5-step Intelligent Transport System (ITS) pilot project was implemented between 2009 and 2014. In 2012, Incheon U-city Corporation, which is a private and public joint corporation, was established to exclusively take care of the IFEZ's U-City business [18].

However, according to the smart city conceptual framework (Table 3) the following problems were raised in the course of its implementation. Songdo U-city initiative has been successful in expanding public infrastructure by applying ICT to new city development. [2]. On the other hand, citizen participation was inadequate despite the necessity to become a smart city, and even if it was government-led at the beginning of the initiative, it should have strengthened the decentralized governance setting at the stage of growth. Besides, firms with small-scale and scarce industrial capacities participated in the construction of infrastructure related to the development of Songdo city, and large-scale companies participated only in the limited supply of some services such as information & communications. In short, during the implementation of the plan, Songdo U-city failed to catch up with the rapid development of smart technologies and the level and standards of improved citizen demand [18].

Korea, which is an IT powerful nation, was not able to incorporate these innovative technologies into Songdo city, which was a U-city paradigm, despite having the world's best technology for 5G, IoT and mobile [17].

4. CONCLUSION

As seen so far, U-city initiatives in Korea began with a construction-oriented project in 2003, but after a period of temporary stagnation, it is evolving into a smart city initiatives to create a cutting-edge multifunctional urban model and solve realistic urban problems. Smart city is a platform securing urban sustainability, which is characterized by energy efficiency, data opening, efficiency of urban management, and citizen participation based on the hyper connectivity of urban infrastructure with ICT technology. Therefore, the Songdo initiative, which reflects the U-city paradigm centered on infrastructure construction and top-down governance perspective has exposed limitations to sustainable growth as a smart city.

To overcome those limitations, Korea revised the existing ubiquitous law into the “Act on Smart City Creation and Industrial Promotion” (in brief, Smart City Act) in December 2017 [19]. And the revised act defines a smart city as a sustainable city wherein various city services are provided based on city infrastructure constructed by converging and integrating construction technologies, information and communication technologies, etc. to enhance its competitiveness and livability. According to the revised Smart City Act, smart city is a city evolved from the existing U-city, and is recognized as an urban platform to solve various urban problems and improve the quality of life by combining new technologies such as ICT and Big Data [20]. Thereafter, Songdo city which have finished its establishment and development in 2016 are continuously developing smart service (such as such as RFID/USN, U-bike, U-street, and smart CCTV) models and establishes through efficient integration between public and private sectors.

5. REFERENCES

[1] UN World Urbanization Prospects, The 2014 Revision, 2014, pp.1-32. Website: https://esa.un.org/unpd/wup/publications/files/wup2014-report. pdf (accessed 19. O3. 12)

[2] K. N. Kim, J. K. Jung, J. Y. Choi, Impact of the Smart City Industry on the Korean National Economy: Input-Output Analysis, Sustainability. 8 (2016)

[3] United Nations Economic and Social Council, Smart Cities and Infrastructure. Website: https://unctad.org/meetings/en/SessionalDocuments/ecn162016d2_en.pdf (accessed 19. 02. 05)

[4] Smart Cities Navigant Research. Website: https://www.navigantresearch.com/research/smart-cities(accessed on 19. 03. 20)

[5] H. Kudo, Quality of Life and Resilience: Japanese Smart City Projects After the 3.11 Great East Japan Earthquake, The European Group of Public Administration, Proceedings. Website: https://www.scss.tcd.ie/disciplines/information_systems/egpa/docs/2013/Kudo.pdf

[6] S, Han, current Status of the Smart Cities, Korea Internet and Security Agency(KISA) Power Review, Seoul, South Korea (2015) 3-18

[7] H.Y. Jang, Y. M. Im, J.Y. Lee, A Study on Development Directions of System for the Level Diagnosis of U-city for U-city Activation, Journal of the Korean Society for Geospatial Information System, 23(2), (2015) 49-58.

[8] S. T. Shwayri, A Model Korean Ubiquitous Eco-city” The Politics of Making Songdo, Journal of Urban Technology 20 (2013) 39-55.

[9] Act on the Construction, ETC. of Ubiquitous Cities. Website: http://law.go.kr/engLsSc.do?tabMenuId=tab45&query=%EC%9C%A0%EB%B9%84%EC%BF%BC%ED%84%B0%EC%8A%A4%EB%8F%84%EC%8B%9C%EC%9D%98%20%EA%B1%B4%EC%84%A4%20%EB%93%B1%EC%97%90%20%EA%B4%80%ED%95%9C%20%EB%B2%95%EB%A5%A0#

[10] Korea Smart City Association, Website: http://www.smartcity.or.kr/en/ucity/concept.php

[11] S. H. Lee, Y. T. Lim, B. S. Song, K. I. C, Comparative Analysis on the U-City Strategies’ Characteristics in Terms of Tendency, Philosophy, Vision, and Concept, Journal of Korea Planning Association 44(2) (2009) 247-259.

[12] C. M. Cho, J. H. Kim, Study on the Legal Establishment of u-City Management Center; Focusing on its Function and Location, Journal of GIS Association of Korea 17(3), 2009, 269-276

[13] Frost and Sullivan, Global Smart City Market, 2013. https://ww2.frost.com/wp-content/uploads/2019/01/SmartCities.pdf

[14] H. Schaffers, C. Ratti, N. Komninos, Special Issue on Smart Applications for Smart Cities: New Approaches to Innovation: Guest Editors’

Introduction, Journal of Theoretical and Applied Electronic Commerce Research 7 (2012) 2-5
[15] Euro-Cities Website: http://www.eurocities.eu
[16] M. Deakin, Smart Cities: The State-of-the Art and Governance Challenge. Triple Helix 1 (2014) 1-7
[17] S. H. Lee, Y. T. Leem., U-city Overseas Expansion Strategy through Comparison of U-city with Smart City, Journal of Korea Planners Association 49(4) (2014) 243-252
[18] S. K. Lee, H. R, Kwon, H. A. Cho, J. B. K, D. J. Lee, International Case Studies of Smart Cities, Inter-American Development Bank June (2016).
[19] Act on Smart City Creation and Industrial Promotion. Website: http://law.go.kr/engLsSc.do?tabMenuId=tab45&query=%EC%9C%A0%EB%B9%84%EC%BF%BC%ED%84%B0%EC%8A%A4%EB%8F%84%EC%8B%9C%EC%9D%98%20%EA%B1%B4%EC%84%A4%20%EB%93%B1%EC%97%90%20%EA%B4%80%ED%95%9C%20%EB%B2%95%EB%A5%A0#
[20]Telecommunications Technology Association, The Case of Core Fusion of the Fourth Industrial Revolution: Smart City Concept and Standardization, Website: http://www.itfind.or.kr/publication/regular/periodical/read.do?selectedId=02-001-180920-000002
[21]H. Farabi-Asl, A. Chapman, K. Itaoka, Y. Noorollahi, Zero Emission Building, Proceedings of International Exchange and Innovation Conference on Engineering & Sciences (IEICES). 4 (2018).96-101
[22] S. Maharjan, N. Tsurusaki, P. Divigalpitiya, The Influence of Urban Form on Travel Energy Consumption in Kathmandu, Proceedings of International Exchange and Innovation Conference on Engineering & Sciences (IEICES). 4 (2018) 90-95,
[23] J. H. Lee, M. G. Hancock, M-C Hu, Towards an Effective Framework for Building Smart Cities: Lessons from Seoul and San Francisco, Technological Forecasting and Social Change 89 (2014) 80-99

"Can People Detect Dilemma Strength in A 2 Player 2 Strategy Game?": A Survey Game

Md. Ahsan Habib
Interdisciplinary Graduate School of Engineering Sciences, Kyushu University, Japan
Corresponding Author E-mail: emonape@gmail.com

Abstract: *The objective of this study is to get data from the answers to calculate the dilemma strength for partners and strangers. A questionnaire field survey has been conducted on 28 individuals considering different games such as Prisoners Dilemma (PD), Trivial (TR), Chicken (CH) and Shag Hunt (SH) at Kyushu University, Japan. It is observed that the dilemma strength of Prisoners Dilemma is higher than Trivial. But on the other hand, the cooperation level of Chicken has been found better than that of Shag Hunt.*

Keywords: Dilemma strength; Cooperation; Defection; Game; Survey.

1. INTRODUCTION

2×2 game or 2-player 2-strategy game is one of the important paradigms for explaining our biological system. In case of 2×2 game, players are selected randomly and made to play the game where each player has 2-strategies: cooperation and defection [1]. However, if everybody defects, the mean population payoff is lower than if everybody cooperates, thus creating a social dilemma[2]. Von Neumann and Morgensteri's statement on game theory that the game are classified into 4 classes; the Trivial game with no dilemma i.e. 100% cooperation, the Prisoner's dilemma(PD) with entire dilemma means 100% defection, the Chicken (CH) game has coexistence of cooperation and defection members, the Shag Hunt (SH) game converge to either complete defection or complete cooperation depending upon the initial fraction of cooperators[3]. Thus, the objective of this study is to evaluate the dilemma strength of Friends and unknown with the base of this game theory.

2.RESEARCH MATERIALS & METHODOLOGY

To set forth the survey, questions are created by logical thinking to be as transparent as possible and so as not to be vexing for participants. There are 28 individuals participated at Kyushu University, Fukuoka, Japan who eligible persons in a sense are to answer the question paper. For each questionnaire, it comprises 8 questions and each question has multiple-choice answers which represented as 1 & 0 for the calculation of the result. Based on the responds from the fc (cooperation fraction), SD(standard deviation), Dg(dilemma strength), Dg/(normalized dilemma strength), fc ± SD(maximum or minimum value with the reference of fc and SD),the result is calculated.

3.RESULTS AND DISCUSSION

This segment represents the results from our survey. There is no consistency from the responses as a result no data is omitted. Results obtained from the survey are represented in figure 1,2,3 & 4 in which PD & TR game are played. Figure1 & 2 describe the interactions with 28 friends whereas figure 3 & 4 depict interactions with 28 unknown persons. In the case of friends, total average cooperation fraction for the PD & TR is successively 0.25(PD) & 0.85 (TR) but the natural characteristics of PD & TR game are 100% defection in PD but still have cooperation tendency where TR should have 100% cooperation but have some defection also. So, it can be said that, people are not able to recognize given dilemma strength exposed but they are able to recognize dilemma class. Most of the people can correctly recognize but some of the people are not. It is exposed that PD has high dilemma situation than TR game. Again From the figure 3 & 4, the total average cooperation fraction for the 28 unknown persons is 0.18(PD game) & 0.80(TR game) which represented that PD game has higher dilemma strength than TR game where noticing the fact people here being very generous, optimistic in PD and it can be said that defection is happened in trivial game also. For the case of friends and unknown persons the dilemma strength of PD is higher than SH.

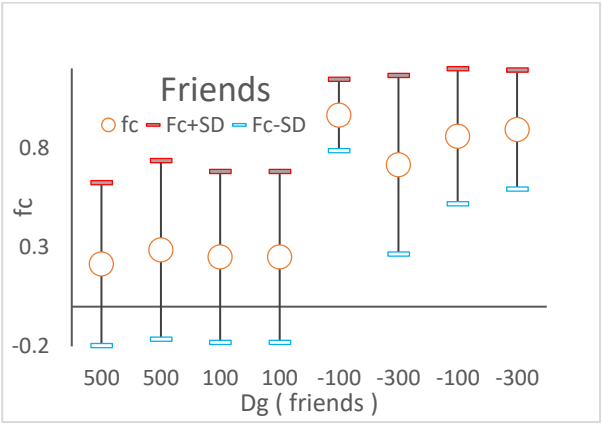

Fig.1: Game with 28 friends (PD & TR game) where Dg (dilemma strength) vs fc (cooperation fraction) is shown.

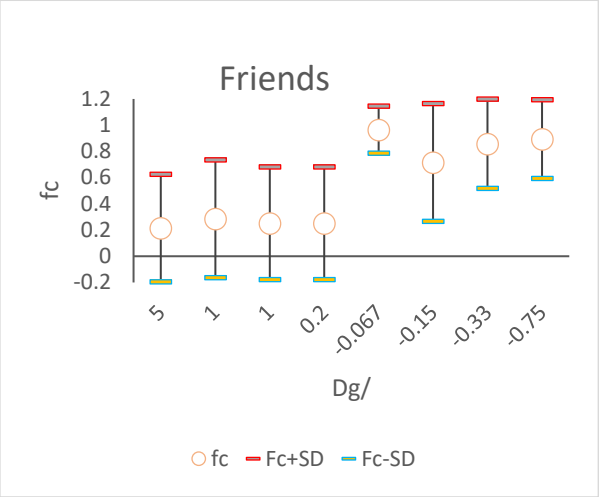

Fig.2: Game with 28 friends (PD & TR game) Where Dg/ (normalized dilemma strength) vs fc (cooperation fraction) is exhibited.

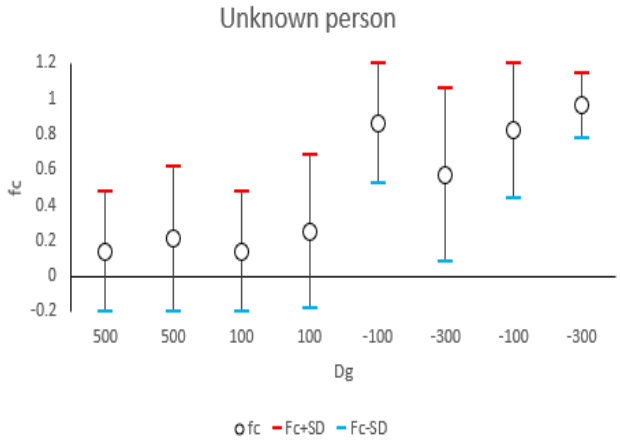

Fig. 3: Game with 28 unknown person (PD & TR game) where Dg (dilemma strength) vs fc (cooperation fraction) is shown.

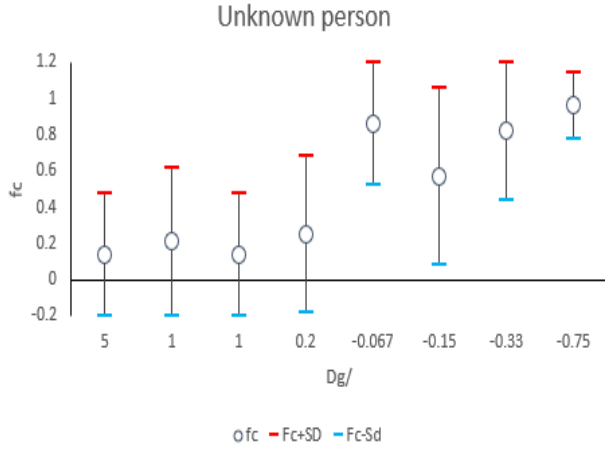

Fig. 4**:** Game with 28 unknown people (PD & TR game) where Dg/ (normalized dilemma strength) vs fc (cooperation fraction) is exhibited.

Playing with CH & SH, It is found that the total average cooperation fraction for the 28 friends is consecutively 0.59 (CH) and 0.54(SH) and again with 28 unknown people, is 0.65 (CH) and 0.61 (SH). Ideally the total cooperation fraction should be 0.5 but a little bit higher for every case. Precisely speaking, it's not very close, a little bit higher cooperation in CH than SH.

4.CONCLUSION

To recognize dilemma class and dilemma strength, this survey represents that people can detect PD, Trivial, CH & SH game. PD has cooperative situation and Trivial has less defection level. In the same time, cooperation fraction of CH is higher than SH.

REFERENCES

[1]. Ryo Matsuzawa, Jun Tanimoto. (2016). A social dilemma structure in diffusible public goods. EPL. doi: 10.1209/0295-5075/116/38005

[2] Zhen Wang,Satoshi kokubo,Marko Jusup,Jun Tanimoto .(2015). Universal scaling for dilemma strength in evolutionary games.Physics of life reviews 14(2015) 1-30.

[3] Jun Tanimoto (2015) Fundamentals of evolutionary Game Theory and its Applications. Springer.Evolutionary Economics and Social Complexity Science 6.